

Biomechanical Modeling and Analysis of Manual Wheelchair Propulsion

by

Mohammadreza Mallakzadeh

B.Sc., Sharif University of Technology, 1992

M.Sc., Sharif University of Technology, 1995

A DISSERTATION SUBMITTED IN PARTIAL FULFILLMENT OF
THE REQUIREMENTS FOR THE DEGREE OF

DOCTOR OF PHILOSOPHY

in

THE FACULTY OF GRADUATE STUDIES

(Mechanical Engineering)

THE UNIVERSITY OF BRITISH COLUMBIA

October 2007

© Mohammadreza Mallakzadeh, 2007

Abstract

Users of manual wheelchairs depend on wheelchairs for most of their daily activities. Manual Wheelchair Propulsion (MWP) is an inefficient and physically straining process, which in the long term can cause injury. However, wheelchair users do benefit greatly from cardiovascular exercise with the use of manual wheelchairs.

The first step in improving the low efficiency and/or preventing injuries during MWP is to be able to measure these factors. To do this, we have proposed an Equivalent Biomedical Index (EBI) and two Wheelchair Users' Joint Injury Indices (WUJII and WUJII') for gross mechanical efficiency and injury assessments.

We have fabricated and validated an instrumented wheel to measure the user's applied loads on the handrim during MWP as part of the data required for calculating the proposed indices. The wheel system has been verified by using general uncertainty analysis, and its specifications have been determined using both static and dynamic experiments. The results have ensured the reliability of the system. Also, a procedure has been developed to determine the angular position of the contact point between the hand and the handrim by using the applied loads and without the use of cameras.

This study also focuses on proposing a novel method to determine the optimum seat position of the wheelchair to minimize the values of the injury indices and/or maximize the value of EBI for each user. Eight male wheelchair user subjects were recruited for the experiments. Statistical analysis showed that horizontal seat position was significantly related to all three indices ($p < 0.05$). The response surfaces of the indices for two users were determined by using the proposed method and a Bivariate Quadratic Function.

We developed and elaborated “Method I” for analysis of the dynamics of user joints and to calculate the joint loads as part of the factors required to define the optimum seat position. A 3D rigid-body inverse dynamic method was used to calculate the joint loads. “Method II” for analysis of the kinetics of the upper limbs was developed and validated to simplify the experimental procedure and decrease the required post-processing. Method II showed to be reliable for measuring the joint forces.

Table of Contents

Abstract	ii
Table of Contents	iv
List of Tables	xi
List of Figures	xiii
List of Symbols	xix
List of Abbreviations	xxvii
Acknowledgements	xxx
Dedication	xxxi
CHAPTER 1 Introduction	1
1.1 Foreword	1
1.2 Research Questions, Hypothesis, Objectives and Limitations	3
1.3 An Overview of the Upper Limb Joints' Anatomy	6
1.3.1 Shoulder Girdle Joints	6
1.3.2 Elbow Joint	8
1.3.3 Wrist Joint	10
1.4 Terminology	10
1.5 Previous Studies	11
1.5.1 Kinetics of MWP	12

1.5.2 Injuries Due to MWP.....	16
1.5.3 Effect of Seat Position on MWP	17
1.5.4 Metabolic Energy Expenditure during MWP	19
1.5.5 Instrumented Wheel	22
1.6 Possible Solutions	23
1.7 Thesis Organization	25
1.8 Concluding Remarks	26
CHAPTER 2 The Instrumented Wheel	28
2.1 Introduction	28
2.2 Instrumentation	30
2.2.1 Wheelchair	30
2.2.2 The Instrumented Wheel	31
2.2.3 Roller-rig	32
2.2.4 AC Motor	34
2.2.5 Computers	34
2.2.6 Data Acquisition Board	35
2.2.7 Static and Dynamic Loading Setup	35
2.3 Preliminary Experimental Protocol	37
2.4 Derivation of Dynamic Equations	37
2.4.1 System Calibration	38
2.4.2 Preload Equations	38
2.4.3 Local and Global Forces and Moments	39

2.4.4 Important Kinetic Factors	45
2.4.5 Determining the Position of the Hand on the Handrim	47
2.5 Uncertainty Analysis	53
2.5.1 General Uncertainty Analysis	54
2.5.2 Uncertainty of Preloads	55
2.5.3 Uncertainty of Local Loads	57
2.5.4 Uncertainty of Global Loads	59
2.5.5 Uncertainty of ϕ	62
2.5.6 Uncertainty of Hand Contact Loads	64
2.6 System Verification	65
2.6.1 Experimental Setup	65
2.6.1.1 First Vertical Loading Setup	66
2.6.1.2 Second Vertical Loading Setup	67
2.6.1.3 Horizontal Loading Setup	68
2.6.1.4 Dynamic Loading Setup	69
2.6.2 Verification Tests Protocol	70
2.6.2.1 Static Verification	70
2.6.2.2 Dynamic Verification	74
2.7 Conclusions	80
CHAPTER 3 Efficiency and Injury Assessment	83
3.1 Introduction	83
3.2 Efficiency Assessment	85

3.3 Injury Assessment	87
3.4 Chapter Summary	93
CHAPTER 4 Optimum Seat Position	95
4.1 Introduction	95
4.2 Modeling and Analysis Approach	96
4.2.1 An Overview	97
4.2.2 Study Population	98
4.2.3 Study Design	99
4.2.4 Test Protocol	100
4.2.5 Anthropometric Data	104
4.2.6 Experimental Setup	104
4.2.6.1 Motion Analysis System	104
4.2.6.2 Heart Rate Monitor	106
4.2.6.3 Blood Pressure Monitor	106
4.2.6.4 Fat Caliper	107
4.2.6.5 Speedometer	107
4.2.6.6 Weight Scale	107
4.2.6.7 Global View of the Experimental Setup	109
4.2.7 Modeling	110
4.3 Analytical Methodology	112
4.3.1 Design of Experiments	115
4.3.1.1 Grid-base Design	115

4.3.2 Response Equation	116
4.3.2.1 Artificial Neural Network	117
4.3.2.2 Local Interpolation	117
4.3.2.3 Bivariate Quadratic Function	118
4.3.3 The Big Picture	119
4.4 Results and Discussion	121
4.4.1 Heart Rate, Blood Pressure, and Anthropometric Data.....	121
4.4.2 Fixed Seat Position	123
4.4.2 Constant Wheelchair Velocity	127
4.4.2.1 Seat Height Y1	127
4.4.2.2 Seat Height Y2	132
4.4.2.3 Horizontal Seat Position X1	138
4.4.2.4 Horizontal Seat Position X2	140
4.4.2.5 Horizontal Seat Position X3	142
4.4.2.6 Optimum Seat Position	144
4.5 Conclusions	149
CHAPTER 5 Injury Assessment for the Upper Limb Joints	152
5.1 Introduction	152
5.2 Method I	153
5.2.1 The Kinematics of the Upper Limb	154
5.2.1.1 Velocity of the Segment	156
5.2.1.2 Z-Y-X Euler Angles	156

5.2.1.3 Determining the Directional Cosines	158
5.2.1.4 Acceleration of a Segment	161
5.2.2 Kinetics of the Upper Limbs	163
5.2.3 Mass Distribution	163
5.2.4 Modeling	167
5.3 Results	175
5.4 Conclusions	185
CHAPTER 6 A New Method for Dynamic Analysis of the Upper Limb.....	187
6.1 Introduction	187
6.2 Method II	188
6.2.1 Link Parameters	189
6.2.2 Link Parameters of the Model	190
6.2.3 Calculating the Joints Angles	192
6.2.4 Kinetics of Wheelchair Propulsion	201
6.3 Comparison of Methods I and II.....	201
6.4 Conclusions	206
CHAPTER 7 Conclusions	208
7.1 Introduction	208
7.2 Conclusions	208
7.2.1 Research Questions and Answers	209
7.3 Limitations of the Study	214

7.3 Contributions	215
7.4 Future Research Directions	217
References	219
Appendix	232

List of Tables

Table 2.1 Constants for different preload equations	40
Table 2.2 Primary uncertainties for measured variables	56
Table 2.3 Primary uncertainties for measured loads	56
Table 2.4 Primary uncertainties for constants	56
Table 2.5 Pearson correlation coefficient r (static verification)	72
Table 2.6 Mean coefficient of variation of measured loads (%; static verification)	73
Table 2.7 Mean errors as percentage of loads (static verification)	74
Table 2.8 Pearson correlation coefficient r (dynamic verification)	77
Table 2.9 Mean coefficient of variation of measured loads (%; dynamic verification)	77
Table 2.10 Mean errors as percentage of loads (dynamic verification)	78
Table 4.1 Demographic data for the manual wheelchair user subjects	99
Table 4.2a Heart rate and blood pressure for the subjects	121
Table 4.2b Anthropometric data for the subjects	122
Table 4.3 Mean and Std. Dev. of WUJII for the subjects for three velocities	124
Table 4.4 Mean and Std. Dev. of WUJII' for the subjects for three velocities	125
Table 4.5 Mean and Std. Dev. of EBI for the subjects for three velocities	126
Table 4.6 Mean and Std. Dev. of WUJII for the subjects at three X-ratios and seat height Y1	129
Table 4.7 Mean and Std. Dev. of WUJII' for the subjects at three X-ratios and seat height Y1	130
Table 4.8 Mean and Std. Dev. of EBI for the subjects at three X-ratios and seat height Y1	130
Table 4.9 Mean and Std. Dev. of WUJII for the subjects at three X-ratios and seat height Y2	135
Table 4.10 Mean and Std. Dev. of WUJII' for the subjects at three X-ratios and seat height Y2	135
Table 4.11 Mean and Std. Dev. of EBI for the subjects at three X-ratios and seat height Y2	136

Table 4.12 The coefficients and constants for the response equations that determine the indices at different seat positions for subject 7	146
Table 4.13 The coefficients and constants for the response equations that determine the indices at different seat positions for subject 8	149
Table 5.1 The coefficients and constants for the response equations that determine \overline{WUJII} for the upper limb joints at different seat positions for subject 7	180
Table 5.2 The coefficients and constants for the response equations that determine \overline{WUJII}' for the upper limb joints at different seat positions for subject 7	180
Table 5.3 The coefficients and constants for the response equations that determine \overline{WUJII} for the upper limb joints at different seat positions for subject 8	184
Table 5.4 The coefficients and constants for the response equations that determine \overline{WUJII}' for the upper limb joints at different seat positions for subject 8	185
Table 6.1 Link parameters of the model	191
Table 6.2 Average rates of over-estimation for upper limb joint loads	205
Table 6.3 Mean and Std. Dev. of the relative error (%) for upper limb joint loads	206

List of Figures

Figure 1.1 Front view of acromioclavicular and glenohumeral joints (Image courtesy of medicalmultimediasgroup.com [14])	7
Figure 1.2 Front view of the bones of the right shoulder girdle, and sternoclavicular and scapulothoracic joints (Image courtesy of medicalmultimediasgroup.com [14])..	7
Figure 1.3 Side view of the bones and ligaments of the shoulder girdle, and section view of glenohumeral joint capsula (Image courtesy of medicalmultimediasgroup.com [14])	8
Figure 1.4 Medial view of the bones of the right elbow joint (Image courtesy of medicalmultimediasgroup.com [14])	9
Figure 1.5 Lateral view of the bones of the right elbow joint (Image courtesy of medicalmultimediasgroup.com [14])	9
Figure 1.6 Back view of the right wrist joint (Image courtesy of medicalmultimediasgroup.com [14])	10
Figure 1.7 Different phases of a complete stroke cycle and related terminology	11
Figure 1.8 Illustration of forces and moments applied on the handrim during wheelchair propulsion: (a) side view; (b) front view	13
Figure 1.9 The relationships among the direction of the applied force, joint torques, and rotation around the shoulder and elbow (modified from [9] with permission)	15
Figure 2.1 Instrumented wheel: (a) side view; (b) front view	32
Figure 2.2 Initial position and orientation of global and two local coordinate systems on the instrumented wheel	33
Figure 2.3 Encoder gear system	33
Figure 2.4 AC motor and its coupling to a shaft of the roller-rig	34
Figure 2.5 Global schematic rear view of the physical data acquisition system	36
Figure 2.6 Measurement signal flow diagram for: (a) load; (b) angular position	36
Figure 2.7 Illustration of local loads after θ degrees of wheel rotation	42
Figure 2.8 Propulsion force components with respect to global and hand local	

coordinate system	43
Figure 2.9 Propulsion moment components with respect to global coordinate system	44
Figure 2.10 F_{total} and TEF with respect to the global coordinate system, and the FEF during the propulsion phase	46
Figure 2.11 Calculated ϕ using kinetic and kinematic methods, and the exponential of curve fit of the kinetic method	49
Figure 2.12 Mean absolute error and Std. Dev. for calculated ϕ using the kinetic method	50
Figure 2.13 Mean absolute error and Std. Dev. for calculated ϕ using the exponential curve fit for the kinetic method	51
Figure 2.14 Global propulsive and hand moments in z direction	51
Figure 2.15 Components of the user's hand moment	52
Figure 2.16 Uncertainties for local force components during possible range for propulsion phase	58
Figure 2.17 Uncertainties for local moment components during possible range for propulsion phase	59
Figure 2.18 Uncertainties for local and global force components during propulsion phase	61
Figure 2.19 Uncertainties for local and global moment components during propulsion phase	62
Figure 2.20 First vertical loading setup for static tests	66
Figure 2.21 Second vertical loading setup for static tests	67
Figure 2.22 The horizontal loading setup for static tests	68
Figure 2.23 The dynamic loading set-up	69
Figure 2.24 Measured and predicted global sample force components	79
Figure 2.25 Measured and predicted global sample moment components	79
Figure 3.1 Variation of heart rate versus time, from start to completion of a steady-state exercise and back to rest	86
Figure 4.1 A subject on the instrumented wheelchair and roller-rig during blood pressure measurement. The marker on the left hip is not shown	102
Figure 4.2 Possible seat heights and backrest horizontal positions. The wheelchair	

variables are set at X1 and Y1 in this figure. Dimensions are not to scale	103
Figure 4.3 VICON infrared camera	105
Figure 4.4 Positions of six infrared cameras, a subject, the wheelchair and the roller-rig for stationary MWP	105
Figure 4.5 HR-polar heart rate monitor: (a) Heart rate sensor and transmitter; (b) recorder	106
Figure 4.6 Blood pressure monitor	106
Figure 4.7 Fat caliper	107
Figure 4.8 Speedometer: (a) Cycling computer; (b) Holding magnet; (c) Wiring kit and sensor	108
Figure 4.9 The setup for measuring the wheelchair user weight	108
Figure 4.10 Global schematic rear view of the kinetic and kinematic data acquisition system and its connections	109
Figure 4.11 The Model of the upper limbs: (a) Sagittal view of the half body; (b) the linkage model. Numbers 1–3 represent upper arm, forearm, and hand, respectively	110
Figure 4.12 Landmark positions on the upper limbs and trunk of the subject, and the wheel	111
Figure 4.13 A 3D model of the upper body and wheel, developed by using the VICON system	112
Figure 4.14 Grid-base design for two variables with four sub-areas and nine data Points. Dimensions are not to scale	116
Figure 4.15 Flowchart for the entire test process to determine the optimum positions of a wheelchair for a MWU	120
Figure 4.16 Variation of \overline{WUJII} versus velocity	124
Figure 4.17 Variation of \overline{WUJII}' versus velocity	125
Figure 4.18 Variation of \overline{EBI} versus velocity	126
Figure 4.19 Variation of \overline{WUJII} against X-ratio at Y1. Minimum values encircled	128
Figure 4.20 Variation of \overline{WUJII}' against X-ratio at Y1. Minimum values encircled	128

Figure 4.21 \overline{EBI} with respect to the X-ratio at Y1. Maximum values encircled	129
Figure 4.22 Maximum and minimum values of \overline{WUJII} and its Std. Dev. against X-ratio at Y1, among the subjects	131
Figure 4.23 Maximum and minimum values of \overline{WUJII}' and its Std. Dev. against X-ratio at Y1, among the subjects	131
Figure 4.24 Maximum and minimum values of \overline{EBI} and its Std. Dev. against X-ratio at Y1, among the subjects	132
Figure 4.25 Variation of \overline{WUJII} against X-ratio at Y2. Minimum values encircled	133
Figure 4.26 Variation of \overline{WUJII}' against X-ratio at Y2. Minimum values encircled ...	134
Figure 4.27 Variation of \overline{EBI} against X-ratio at Y2. Maximum values encircled	134
Figure 4.28 Maximum and minimum values of \overline{WUJII} and its Std. Dev. against X-ratio at Y2, among the subjects	136
Figure 4.29 Maximum and minimum values of \overline{WUJII}' and its Std. Dev. against X-ratio at Y2, among the subjects	137
Figure 4.30 Maximum and minimum values of \overline{EBI} and its Std. Dev. against X-ratio at Y2, among the subjects	137
Figure 4.31 Variation of \overline{WUJII} against Y-ratio at X1	139
Figure 4.32 Variation of \overline{WUJII}' against Y-ratio at X1	139
Figure 4.33 Variation of \overline{EBI} against Y-position at X1	140
Figure 4.34 Variation of \overline{WUJII} against Y-ratio at X2	141
Figure 4.35 Variation of \overline{WUJII}' against Y-ratio at X2	141
Figure 4.36 Variation of \overline{EBI} against Y-ratio at X2	142
Figure 4.37 Variation of \overline{WUJII} against Y-ratio at X3	143
Figure 4.38 Variation of \overline{WUJII}' against Y-ratio at X3	143
Figure 4.39 Variation of \overline{EBI} against Y-ratio at X3	144
Figure 4.40 Variation of \overline{WUJII} versus wheelchair variables, for subject 7	145
Figure 4.41 Variation of \overline{WUJII}' versus wheelchair variables, for subject 7	145
Figure 4.42 Variation of \overline{EBI} versus wheelchair variables, for subject 7	146

Figure 4.43 Variation of \overline{WUJII} versus wheelchair variables, for subject 8	147
Figure 4.44 Variation of \overline{WUJII}' versus wheelchair variables, for subject 8	148
Figure 4.45 Variation of \overline{EBI} versus wheelchair variables for subject 8	148
Figure 5.1 Local and global frames for a rigid body	154
Figure 5.2 General transformation of a vector	155
Figure 5.3 Directional cosines of rotation matrix for the axes of {B} with respect to {A}	158
Figure 5.4 Frustum of conic rigid body with local frame on its center of mass	165
Figure 5.5 Rectangular prism rigid body with local frame at its center of mass	166
Figure 5.6 Free body diagram of a segment in sagittal plane	168
Figure 5.7 Free body diagram of a segment in frontal plane	168
Figure 5.8 Free body diagram of a segment in transverse plane	169
Figure 5.9 Position vectors for r_{pd} , proximal end (p), distal end (d), and COM of the segment	172
Figure 5.10 Variation of \overline{WUJII} versus X and Y-ratios for subject 7 at wrist joint	176
Figure 5.11 Variation of \overline{WUJII}' versus X and Y-ratios for subject 7 at wrist joint	176
Figure 5.12 Variation of \overline{WUJII} versus X and Y-ratios for subject 7 at elbow joint	177
Figure 5.13 Variation of \overline{WUJII}' versus X and Y-ratios for subject 7 at elbow joint	178
Figure 5.14 Variation of \overline{WUJII} versus X and Y-ratios for subject 7 at shoulder joint	178
Figure 5.15 Variation of \overline{WUJII}' versus X and Y-ratios for subject 7 at shoulder joint	179
Figure 5.16 Variation of \overline{WUJII} versus X and Y-ratios for subject 8 at wrist joint	181
Figure 5.17 Variation of \overline{WUJII}' versus X and Y-ratios for subject 8 at wrist joint	182
Figure 5.18 Variation of \overline{WUJII} versus X and Y-ratios for subject 8 at elbow joint	182
Figure 5.19 Variation of \overline{WUJII}' versus X and Y-ratios for subject 8 at elbow joint	183
Figure 5.20 Variation of \overline{WUJII} versus X and Y-ratios for subject 8 at shoulder joint	183
Figure 5.21 Variation of \overline{WUJII}' versus X and Y-ratios for subject 8 at shoulder joint	184
Figure 6.1 Link frames and link parameters	189
Figure 6.2 Half-body Linkage model for the upper limb with all coordinate reference systems	190

Figure 6.3 Forces, moments and inertial loads on a generic link i	200
Figure 6.4 Total applied force on the wrist joint	201
Figure 6.5 Total applied moment on the wrist joint	202
Figure 6.6 Total applied force on the elbow joint	202
Figure 6.7 Total applied moment on the elbow joint	203
Figure 6.8 Total applied force on the shoulder joint	203
Figure 6.9 Total applied moment on the shoulder joint	204

List of Symbols

a	Constant
a_i	Distance From Z_i to Z_{i+1} Measured Along X_i
$a_{x,y,z}$	Linear Acceleration Components of a Segment
a_{COM}	Linear Acceleration of Center of Mass of a Segment
a_T	Combined Linear Acceleration Matrix
A	Frame A
A'	First Intermediate Frame for Euler Transformation
A''	Second Intermediate Frame for Euler Transformation
A_0	First Constant in Durnin's Equation
$Atan2$	Return the Arctangent
b	Constant
b_0	Lumped Parameter
$b_{i=1-6}$	Constants
B	Frame B
B_0	Second Constant in Durnin's Equation
c_{1-7}	$\cos(\eta_{1-7})$
c_{34}	$\cos(\eta_3 + \eta_4)$
$c\alpha$	$\cos(\alpha)$
$c\varphi$	$\cos(\varphi)$
C_i	Frame at the Center of Mass of a Link with Direction and Orientation of Link Frame i
d_1	Distance between Data Point P_1 and Query Point P
d_2	Distance between Data Point P_2 and Query Point P
d_{12}	Distance between Two Data Points P_1 and P_2
d_i	Link Displacement
D	Lumped Parameter
D_{1-10}	Lumped Parameters
e	Random Vector

E_1	Position Vector between Points 3 and 1
E_2	Position Vector between Points 3 and 2
\hat{E}_1	Unit Vector of E_1
\hat{E}_2	Unit Vector of E_2
\hat{E}_3	Unit Vector Perpendicular to Plane of \hat{E}_1 and \hat{E}_2
f_0	Function
${}^i f_i$	Exerted Force on Link i by Link $i-1$ with Respect to Frame i
f_p	Pushing Frequency
$F_{x,y,z}$	Measured Force Components
$F_{c-x,y,z}$	Force Components with Respect to Wheel Center Coordinate System
$F_{d-x,y,z}$	External Force Components on Distal End of Segment
$F_{g-x,y,z}$	Applied Force with Respect to Global Coordinate System
$F_{h-x,y,z}$	Force Components with Respect to Hand Coordinate System
F_i	Inertial Force Acting on Center of Mass of a Segment
F_{Iij}	Maximum Joint Force of Propulsion Cycle i for Subject j Calculated Using Method I
F_{IIij}	Maximum Joint Force of Propulsion Cycle i for Subject j Calculated Using Method II
$F_{L-x,y,z}$	Applied Local Force Components
F_m	Maximum Total Force Applied on the Hub During Propulsion Phase
F_{mi}	Maximum Total Force Applied on the Joint i during Propulsion Phase
$F_{p-x,y,z}$	External Force Components on Proximal End of Segment
$F_{P-x,y,z}$	Force Preload
F_s	Centripetal Force
$F_{s-x,y}$	Components of Centripetal Force
g	Gravitational Acceleration
g_i	Function i
h	Height of Center of Mass of Frustum of Cone

h_1	Weight of Query Point with Respect to Data Point P_1
h_2	Weight of Query Point with Respect to Data Point P_2
H	Height of Frustum of Cone
H_h	Thickness of the Hand.
\hat{i}	Unit Vector of X-axis of Local Coordinate System
\hat{I}	Unit Vector of X-axis of Global Coordinate System
$^A I$	Inertia Tensor of a Rigid Body with Respect to Frame A
$^C I$	Inertia Tensor of a Rigid Body with Respect to Local Frame C at Its Center of Mass
I_T	Combined Mass and Inertia Matrix
$I_{xx,yy,zz}$	Mass Moment of Inertia Components
$I_{xy,xz,yz}$	Mass Product of Inertia Components
\hat{j}	Unit Vector of Y-axis of Local Coordinate System
\hat{J}	Unit Vector of Y-axis of Global Coordinate System
k	Weight Factor of Length
$K_{1,2,3,4}$	Lumped Parameters
K_{11-44}	Lumped Parameters
\hat{k}	Unit Vector of Z-axis of Local Coordinate System
\hat{K}	Unit Vector of Z-axis of Global Coordinate System
L_{11-44}	Lumped Parameters and Components of 2T_7
L_a	Length of Upper Arm
L_{ai}	Length of Segments Connected to Distal part of Joint i
L_d	Combined Distal Load Matrix
L_f	Length of Forearm
L_g	Matrix of Global Force and Moment Components
L_h	Length of Hand
L_L	Matrix of Local Force and Moment Components
L_p	Combined Proximal Load Matrix
m	Mass of a Segment
m_w	Mass of a Weight

$M_{x,y,z}$	Measured Moment Components
$M_{c-x,y,z}$	Moment Components with Respect to Wheel Center Coordinate System
$M_{d-x,y,z}$	External Moment Components on Distal End of Segment
$M_{g-x,y,z}$	Applied Moment with Respect to Global Coordinate System
$M_{h-x,y,z}$	Moment Components with Respect to Hand Coordinate System
M_{Iij}	Maximum Joint Moment of Propulsion Cycle i for Subject j Calculated Using Method I
M_{IIij}	Maximum Joint Moment of Propulsion Cycle i for Subject j Calculated Using Method II
$M_{L-x,y,z}$	Applied Local Moment Components
M_m	Maximum Total Moment Applied on Hub during Propulsion Phase
M_{mi}	Maximum Total Moment Applied on Joint i during Propulsion Phase
$M_{p-x,y,z}$	External Moment Components on Proximal End of Segment
$M_{P-x,y,z}$	Moment Preload
\overline{M}_z	Average Propulsive Moment Applied on Hub
n	Number of Variables
${}^i n_i$	Exerted Moment on Link i by Link $i-1$ with Respect to Frame i
N	Number of Cases
N_i	Inertial Moment Acting on Center of Mass of a Segment Preload
p	p -value, The Probability of the Null Hypothesis
P_0	Query Point
${}^A P_{BORG}$	Position Vector of Origin of Frame B with Respect to Frame A
${}^i P_{Ci}$	Position Vector of Origin of Center of Mass with Respect to Frame i
${}^A P_E$	Position Vector of Point E with Respect to Frame A
${}^B P_E$	Position Vector of Point E with Respect to Frame B
P_i	Data Point i
${}^i P_{i+1}$	Position Vector of Origin of Frame $i+1$ with Respect to Frame i

$P_{wx,wy,wz}$	Position Components of Wrist
q	Random Vector
Q	Skew-symmetric Matrix of Vector q
r	Pearson Correlation Coefficient
r_0	Smaller Radius of Frustum of Cone
r_{11-33}	Components of Rotation Matrix—Directional Cosines
r_h	Mean Radius of Handrim
r_{ij}	Directional Cosines
R	Larger Radius of Frustum of Cone
${}^A_B R$	Rotation Matrix Describing Frame B in Frame A
${}^A_C R$	Rotation Matrix Describing Frame C in Frame A
$R(P_0)$	Response at Query Point P_0
$R(P_1)$	Response at Data Point P_1
$R(P_2)$	Response at Data Point P_2
R^{-1}	Inverse of Matrix R
R^T	Transpose of Matrix R
s_{1-7}	$\sin(\eta_{1-7})$
s_{34}	$\sin(\eta_3 + \eta_4)$
s_x	Standard Deviation of Independent Variable
s_x^2	Variance of Independent Variable
s_y	Standard Deviation of Dependent Variable
$s\alpha$	$\sin(\alpha)$
$s\phi$	$\sin(\phi)$
S_{total}	Total Value for Skinfold Test
${}^{i-1}_i T$	Denavit-Hartenberg Matrix for Links $i-1$ and i
u	Function
U_i	Uncertainty of Parameter i
${}^i V_{i+1}$	Linear Velocity of Link $i+1$ with Respect to Frame i
${}^i \dot{V}_{i+1}$	Linear Acceleration of Link $i+1$ with Respect to Frame i
${}^i \dot{V}_{C_i}$	Linear Acceleration of Center of Mass of Link i with Respect

	to Frame i
${}^A V_E$	Linear Velocity of Point E with Respect to Frame A
${}^A \dot{V}_E$	Linear Acceleration of Point E with Respect to Frame A
${}^B V_E$	Linear Velocity of Point E With Respect to Frame B
${}^B \dot{V}_E$	Linear Acceleration of Point E with Respect to Frame B
\bar{V}_l	Average Linear Wheelchair Velocity
w_1	Normalized Weight of Query Point with Respect to Data Point P_1
w_2	Normalized Weight of Query Point with Respect to Data Point P_2
W_h	Width of Hand
$x_{1,2,3}$	X-position of Points 1, 2 and 3
x_c	X-position of Center of Mass
x_{dp}	Distance between Points d and p in X-direction
x_i	Case Value for Independent Variable
\ddot{x}_{COM}	Linear Acceleration of Center of Mass in X-direction
\bar{x}	Mean of Independent Variable
X	Horizontal Seat Position with Respect to Wheel Axle
\hat{X}_B	Unit Vector for X-axis of Frame B
${}^A \hat{X}_B$	Unit Vector for X-axis of Frame B With Respect to Frame A
\hat{X}_i	Unit Vector for X-axis of Frame i on the Link i
$y_{1,2,3}$	Y-position of Points 1, 2 and 3
y_c	Y-position of Center of Mass
y_{dp}	Distance between Points d and p in Y-direction
y_i	Case Value for Dependent Variable
\ddot{y}_{COM}	Linear Acceleration of Center of Mass in Y-direction
\bar{y}	Mean of Dependent Variable
Y	Vertical Seat Position with Respect to Wheel Axle
\hat{Y}_B	Unit Vector for Y-axis of Frame B
${}^A \hat{Y}_B$	Unit Vector for Y-axis of Frame B With Respect to Frame A
\hat{Y}_i	Unit Vector for Y-axis of Frame i on the Link i

$z_{1,2,3}$	Z-position of Points 1,2 and 3
z_c	Z-position of Center of Mass
z_{dp}	Distance between Points d and p in Z-direction
\ddot{z}_{COM}	Linear Acceleration of Center of Mass in Z-direction
Z_{0-9}	Z-direction of Local and Global Coordinate Systems for Upper Limb Model
\hat{Z}_B	Unit Vector for Z-axis of Frame <i>B</i>
${}^A\hat{Z}_B$	Unit Vector for Z-axis of Frame <i>B</i> with Respect to Frame <i>A</i>
\hat{Z}_i	Unit Vector for Z-axis of Frame <i>i</i> on the Link <i>i</i>
\bar{z}	Average Value for Index
Δz	Offset Distance between Plane of Handrim and Origin of Global Coordinate System in Z-direction
α	First Euler Angle
$\dot{\alpha}$	Time Derivative of α
α_i	Link Angle
β	Second Euler Angle
$\dot{\beta}$	Time Derivative of β
γ	Third Euler Angle
$\dot{\gamma}$	Time Derivative of γ
δ_i	Partial Derivative of Function f_0 with Respect to Ψ_i
η_i	Joint Variable of Frame <i>i</i>
$\dot{\eta}_i$	First Derivative of Joint Variable of Frame <i>i</i>
$\ddot{\eta}_i$	Second Derivative of Joint Variable of Frame <i>i</i>
θ	Angular Position of Wheel during Test
$\dot{\theta}$	Angular Velocity of Wheel during Test
$\Delta\theta$	Angular Displacement of Wheel during Test
λ	Transformation Matrix from Local to Global Coordinate System
ξ	Phase Difference
ρ	Radius in Polar Coordinate System

σ_z	Standard Deviation of Index z
τ_d	Induced Moment Due to External Forces at Distal Point of Segment.
τ_p	Induced Moment Due to External Forces at Proximal Point of Segment.
φ	Instantaneous Angular Position of Hand on Handrim in Global Coordinate System (x-y plane) Measured Clockwise with Respect to the +x Axis
φ_0	Angle in Polar Coordinate System
φ_c	Calculated φ
Φ	Formatted Skew-symmetric Segment Length Matrix
${}^i\omega_{i+1}$	Angular Velocity of Link $i+1$ with Respect to Frame i
$\omega_{x,y,z}$	Angular Velocity Components of a Segment
ω_T	Formatted Angular Velocity Matrix
${}^i\dot{\omega}_{i+1}$	Angular Acceleration of Link $i+1$ with Respect to Frame i
${}^C\dot{\omega}_{x,y,z}$	Angular Acceleration Components of a Segment With Respect to Frame C
Ψ_i	Measured Variables
${}^A\Omega_B$	Angular Velocity of Frame B with Respect to Frame A
${}^A\Omega_C$	Angular Velocity of Frame C with Respect to Frame A
${}^B\Omega_C$	Angular Velocity of Frame C with Respect to Frame B
${}^A\dot{\Omega}_B$	Angular Acceleration of Frame B with Respect to Frame A
${}^A\dot{\Omega}_C$	Angular Acceleration of Frame C with Respect to Frame A
${}^B\dot{\Omega}_C$	Angular Acceleration of Frame C with Respect to Frame B
Ω_T	Formatted Skew-symmetric Angular Velocity Matrix

List of Abbreviations

3D	3 Dimensional
{A}	Frame <i>A</i>
AD	Autonomic Dysreflexia
A/D	Analog-To-Digital
%BF	Percentage of Body Fat
ANN	Artificial Neural Network
ANOVA	Analysis of Variance
{B}	Frame <i>B</i>
BMI	Body Mass Index
BQF	Bivariate Quadratic Function
cm	Centimeter
{C}	Frame <i>C</i>
{C _{<i>i</i>} }	Frame <i>C_{<i>i</i>}</i>
COM	Center of Mass
CT	Contact Time
CTS	Carpal Tunnel Syndrome
d	Distal End of a Segment
DEXA	Dual Energy X-ray Absorptiometry
E	A Randomly Selected Point on a Segment
EBI	Equivalent Biomedical Index
$\overline{\text{EBI}}$	Mean value of EBI
EMG	Electromyogram
FEF	Fractional Effective Force
GME	Gross Mechanical Efficiency
h	Hour
HC	Hand Contact
HR	Hand Release
IV	Intravenous

kg	Kilogram
kHz	KiloHertz
km	Kilometer
log	logarithm
m	Meter
m'	Number of Unknown Constants in Response Equation
m ³	Cubic Meter
M	Male
MEE	Metabolic Energy Expenditure
Min	Minute
MWP	Manual Wheelchair Propulsion
MWUs	Manual Wheelchair Users
n	Number of Subjects
n'	Number of Data Points or Tests
N	Newton
N.m	Newton.Meter
p	Proximal End of a Segment
PCI	Physiological Cost Index
PEF	Partial Effective Force
rad	Radian
ROM	Range of Motion
ROT	Rotation
RSI	Repetitive Stress (Strain) Injury
RT	Release Time
s	Second (Time Unit)
SCI	Spinal Cord Injury
SPADI	Shoulder Pain and Disability Index
ST	Stroke Time
Std. Dev.	Standard Deviation
T3	Third Vertebrae of the Thoracic Part of Vertebral Column
T4	Forth Vertebrae of the Thoracic Part of Vertebral Column

T5	Fifth Vertebrae of the Thoracic Part of Vertebral Column
T6	Sixth Vertebrae of the Thoracic Part of Vertebral Column
TEF	Total Effective Force
THB	Total Heart-Beats
THBI	Total Heart-Beats Index
T _n	n th Vertebrae of the Thoracic Part of Vertebral Column
UBC	University of British Columbia
USB	Universal Serial Bus
VICON	Brand Name of a Motion Analysis System
WPSR	Wheelchair Propulsion Strength Rate
WUJII	Wheelchair User Joint Injury Index (using BMI)
$\overline{\text{WUJII}}$	Mean Value of WUJII
WUJII'	Wheelchair User Joint Injury Index (using %BF)
$\overline{\text{WUJII}'}$	Mean Value of WUJII'
WUSPI	Wheelchair User's Shoulder Index
X ₀₋₉	X-direction of the Local and Global Coordinate Systems for Upper Limb Model
X1	First Horizontal Seat Position with Respect to Wheel Axle
X2	Second Horizontal Seat Position with Respect to Wheel Axle
X3	Third Horizontal Seat Position with Respect to Wheel Axle
X-ratio	Ratio of X-position to Arm length
Y ₀₋₉	Y-direction of Local and Global Coordinate Systems for Upper Limb Model
Y1	First Vertical Seat Position with Respect to Wheel Axle
Y2	Second Vertical Seat Position with Respect to Wheel Axle
Y3	Third Vertical Seat Position with Respect to Wheel Axle
Y-ratio	Ratio of Y-position to Arm length

Acknowledgements

In the name of God, the Compassionate, the Merciful

First I would like to express my gratitude to my supervisor Dr. Farrokh Sassani. I am deeply indebted for the endless help, support and guidance he has given me, and his countless efforts in advising me throughout the different stages of this research. His profound knowledge and spirit of scientific exploration, have contributed significantly to the fulfillment of my academic goals, and will benefit me in my future pursuits.

I am particularly grateful to my very active supervisory committee member, Dr. Bonita J. Sawatzky, for her invaluable support and many hours of engaging and inspiring discussions about this study.

I would like to thank Dr. Thomas R. Oxland, Dr. Antony J. Hodgson, and Dr. Michiel van de Panne for supporting this research and providing access to facilities. I am also grateful to Dr. Thomas R. Oxland and Dr. A. William Sheel for their great suggestions for this dissertation.

I would also like to thank, Mr. Mohammad Sepasi, Mr. Amin Karami and Mr. Edward Cheung for their kind assistance during the tests.

I wish to thank my colleagues in the Process Automation and Robotics Laboratory: Dr. Reza Tafreshi, Dr. Reza Ghodsi, Dr. Tao Fan, Ms. Pirmoradi, for their moral support.

I am grateful to my dear parents, for their constant encouragement and prayers, and to my sisters and brother for their great emotional support when I was far from them. I wish to thank my wife's family for their endless moral support, too.

Last but not least, I wish to express my deepest gratitude to my dear wife, Sima Sajjadi, for her understanding, patience, encouragement and support during all the hard times that I went through; and my adorable children, Amirali and Melika, who were inexhaustible sources of motivation for me, and without whose sacrifices I would never have been able to complete this project.

To my dear parents

To my dear wife and lovely children

CHAPTER 1

Introduction

1.1 Foreword

A survey conducted by Canadian Community Health reported that about 155,000 Canadians were using a wheelchair for mobility in 2000/01 [1]. In the USA, statistics reported by researchers and official sources indicated that the number of wheelchair users had grown from 1.2 million in 1987 [2] to approximately 2.1 million in 2003 [3]. These people rely on wheelchair for locomotion and other daily activities.

Manual Wheelchair Propulsion (MWP) is inefficient and physically straining. It is a natural expectation for Manual Wheelchair Users (MWUs) to be comfortable, when they use their wheelchairs for mobility and accomplishing various activities. Normally, upper limbs are used for prehensile and manipulation tasks, whereas MWUs have to use their upper limbs for additional functions such as moving between the wheelchair and

other essential locations (bed, car seat, bathtub etc.), the pressure-relief raising to eliminate the pressure sore, reaching overhead objects, and propelling wheelchair.

The nature of wheelchair propulsion is such that MWUs are essentially walking with their upper limbs [4]. It has been reported that, on average, a MWU performs about 3,500 propulsive strokes per day [5]. Considering the millions of strokes during the lifetime, MWP can be categorized as a serious repetitive motion.

Repetitive Stress (or strain) Injuries (RSI) are “a variety of musculoskeletal disorders, generally related to tendons, muscle, or joints, as well as some common peripheral-nerve-entrapment and vascular syndromes [6, pp. 943]”. It is known that the repetitive stroke to manually propel a wheelchair is related to RSI in the shoulder, wrist, and elbow [2].

It has also been reported that the propulsion technique plays a role in the mechanical efficiency of the propulsion [7, 8]. MWP is a form of ambulation, whose mechanical efficiency is about 10% at best [8–10]. As a consequence, MWP is associated with a high mechanical load on the upper limb joints, which may lead to overuse injuries in shoulder, elbow and wrist. A reliable efficiency assessment must consider both the mechanical and biological aspects of MWP [9]. Therefore, Gross Mechanical Efficiency (GME) must be used to determine the efficiency of the physiological systems.

The position of the wheelchair seat with respect to the wheel axle is one of the most important factors that is related to MWP [11], and can cause injuries to the upper limbs [12, pp. 270–271]. Simply stated, changing the seat position will change the joint loads [13]. The subsequent chapters will have more detailed review for each section to extend the discussion and make connection to the chapters’ contents.

This study considers that a major part of RSI incidences in wheelchair users is the result of forceful motions and awkward postures that MWUs experience during wheelchair propulsion, and proposes a method to determine the optimum seat position to minimize injury for individual users. To accomplish this, an instrumented wheel as part of the required experimental setup was designed, fabricated and validated to measure the loads applied on the hand of the user during MWP. Also, two methods were developed and elaborated to determine the dynamic loads on the user's joints as part of the parameters needed by the proposed method to define the optimum seat positions. The thesis layout is presented at the end of this chapter.

1.2 Research Questions, Hypotheses, Objectives and Limitations

This study was performed to assess the feasibility of answering the following research questions in a cross-sectional study:

- Is the PY6 load transducer a suitable and sufficiently accurate measuring device for determining 3-Dimensional (3D) forces and moments in the handrim of a wheelchair during propulsion?
- How can the optimum horizontal and vertical seat positions with respect to the wheel axle (X,Y) be determined for each wheelchair user?
- Can one propose some generic rules to estimate the optimum seat position for various users?

- Is there a relationship between the average linear wheelchair velocity (simply referred to as velocity) and the degree of injury of the wheelchair user?
- Is there a relationship between the velocity and the propulsion efficiency of the wheelchair users?
- How can one estimate the probable injuries to upper limb joints?
- To what extent will a 3D simulation of the upper limb joints be reliable, if in a vision system only two markers are used for kinematic tracking and analysis?
(A smaller number of markers allows a convenient and speedy process.)

To answer these research questions, we considered and focused on the following hypotheses and objectives, respectively:

We hypothesized that:

- The fabricated instrumented wheel system, using the PY6 load sensor, will prove to be a reliable and valid instrument for measuring 3D forces and moments at the hub of a standard wheelchair during MWP.

This hypothesis is based on the assumption that the specifications reported by the manufacturer are dependable.

- Changing the seat position of the wheelchair can alter the Gross Mechanical Efficiency and the upper limb joint loads of MWUs.

This hypothesis is based on the assumption that the combination of the human and the manual wheelchair presents a closed-loop linkage-system during the propulsion. Changing the seat position, will change the length of the virtual link between the center of the wheel hub and the hip of the user. This apparently

simple kinematic change affects the kinetics of the system during propulsion and has a host of other influences.

The objectives of this study were then set to:

- Develop, fabricate and validate a versatile instrumented wheel.
- Propose three new indices for efficiency and injury assessment, which consider both mechanical and biological aspects of MWP.
- Propose a method to prescribe the optimum wheelchair seat position for a user, based on the efficiency and injury indices.
- Assess the injury at upper limb joints during MWP by using the inverse dynamic method and the new injury indices.
- Develop and verify a new model for analysis of the dynamics of the upper limb.

The limitations of this study are as follows:

- Small sample size of the subjects. Eight MWUs were recruited in this study.
- The study was focused on male subjects with Spinal Cord Injury (SCI) and lesion below the fifth thoracic vertebrae (T5).
- The subjects used the instrumented wheelchair not their own.
- The data from the dominant side of the subjects were used for the analysis.
- The propulsion techniques were not necessarily the same for all subjects.
- Limited range of variation for the seat position.

1.3 An Overview of the Upper Limb Joints' Anatomy

In this section, the important joints of the upper limb, which are: shoulder girdle, elbow, and wrist joints are introduced. The hand joints are not discussed here, as minimal concerns and injuries have been reported by MWUs.

1.3.1 Shoulder Girdle Joints

The shoulder girdle consists of three true joints and one articulation or false joint: glenohumeral, acromioclavicular, sternoclavicular, and scapulothoracic joints, respectively. The glenohumeral joint is formed where the ball of the humerus fits into a shallow socket on the scapula, which is called the glenoid cavity (Figure 1.1). The acromioclavicular joint is where the clavicle meets the acromion. The sternoclavicular joint provides the only connection of the arms and shoulders to the main skeleton on the front of the chest (Figure 1.2). The scapulothoracic joint helps to keep the glenoid cavity lined up during shoulder movements.

The glenohumeral joint is the most important joint in the shoulder girdle and the most mobile ball-and-socket joint in the human skeleton because the size of the semi-spherical humeral head is much larger compared to the shallow and relatively flat cavity of the glenoid [15] (Figure 1.3).

The possible movements and Range of Motion (ROM) of this joint are as follows: Flexion (0–90°), extension (0–45°), internal rotation (0–40°), external rotation (0–55°), adduction (0–45°) and abduction (0–180°) [16, page 87].

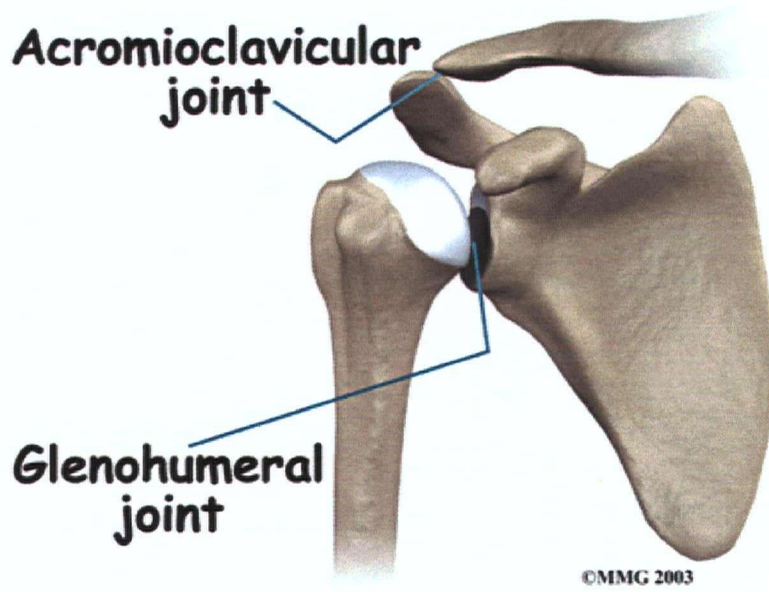


Figure 1.1 Front view of acromioclavicular and glenohumeral joints (Image courtesy of medicalmultimedigroup.com [14]).

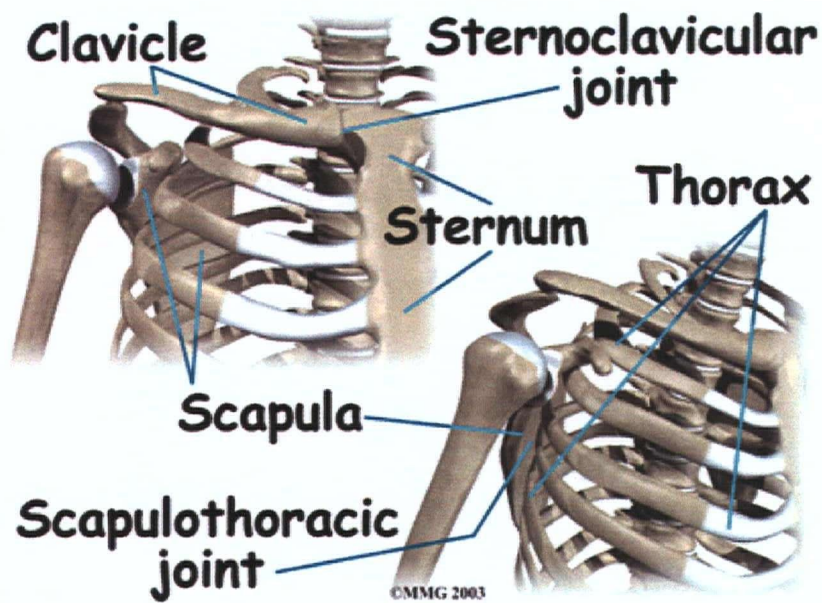


Figure 1.2 Front view of the bones of the right shoulder girdle, and sternoclavicular and scapulothoracic joints (Image courtesy of medicalmultimedigroup.com [14]).

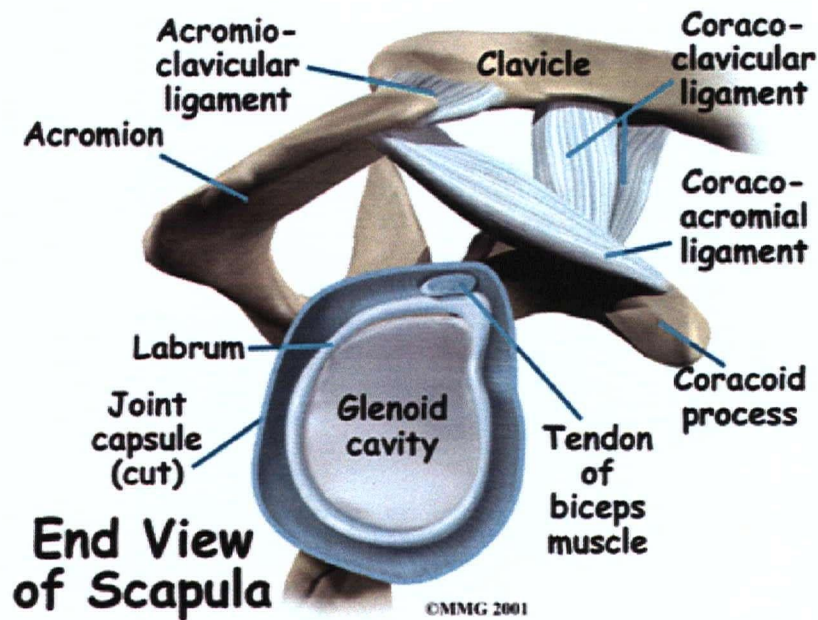


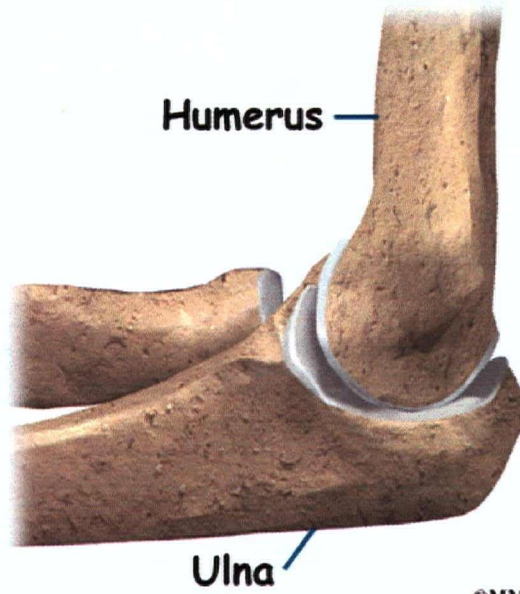
Figure 1.3 Side view of the bones and ligaments of the shoulder girdle, and section view of glenohumeral joint capsula (Image courtesy of medicalmultimedigroup.com [14]).

1.3.2 Elbow Joint

The elbow joint is a hinge joint composed of three separate joints: humeroradial, humeroulnar and proximal radioulnar (Figures 1.4 and 1.5). The joints between the humerus and both the ulna and radius (Figure 1.5) act as a typical hinge joint, allowing only flexion and extension, but the head of the radius and ulna is a pivot joint [16, pp. 91–93].

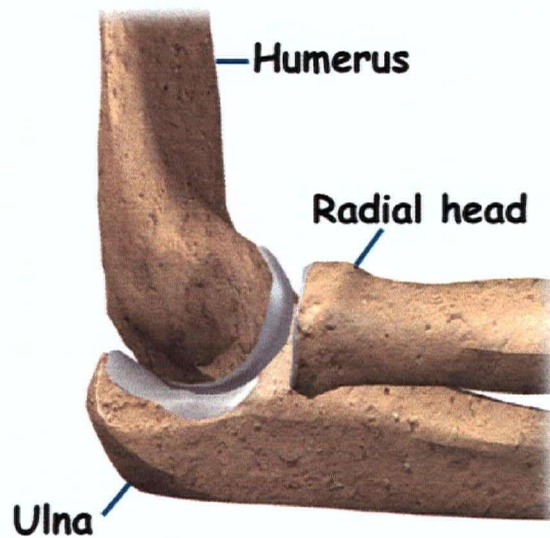
The possible movements and ROM of this joint are as follow:

Flexion (140°), extension (0°), pronation (90°), and supination (90) [16, pp. 91].



©MMG 2001

Figure 1.4 Medial view of the bones of the right elbow joint (Image courtesy of medicalmultimedigroup.com [14]).



©MMG 2001

Figure 1.5 Lateral view of the bones of the right elbow joint (Image courtesy of medicalmultimedigroup.com [14]).

1.3.3 Wrist Joint

The proximal wrist joint (radiocarpal joint) is a typical condyloid joint. It is located between the radius and ulna on one side, and the wrist on the other (Figure 1.6). Wrist movements include flexion, extension, abduction, and adduction.

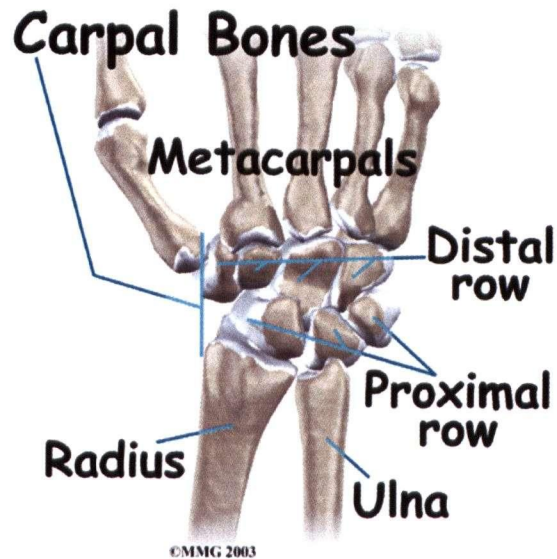


Figure 1.6 Back view of the right wrist joint (Image courtesy of medicalmultimedialogroup.com [14]).

1.4 Terminology

MWP is a stroke cycle whose Stroke Time (ST) is divided into two main phases: (a) propulsion phase, and (b) recovery phase. The propulsion phase or the Contact Time (CT) occurs when the hand of the user has contact with the handrim. The recovery phase, or Recovery Time (RT), occurs when the hand has no contact with the handrim. The sum of CT and RT is equal to ST. The Hand Contact and Hand Release are abbreviated as HC and HR, respectively. The propulsion phase consists of pull and push phases. The

recovery phase is divided into four parts: follow through, retrieval, preload and pre-impact. Figure 1.7 illustrates the complete six phases of standard manual wheelchair propulsion [12]; role of the push phase should not be confused with the propulsion phase. In some research reports, these two terms have been incorrectly used interchangeably.

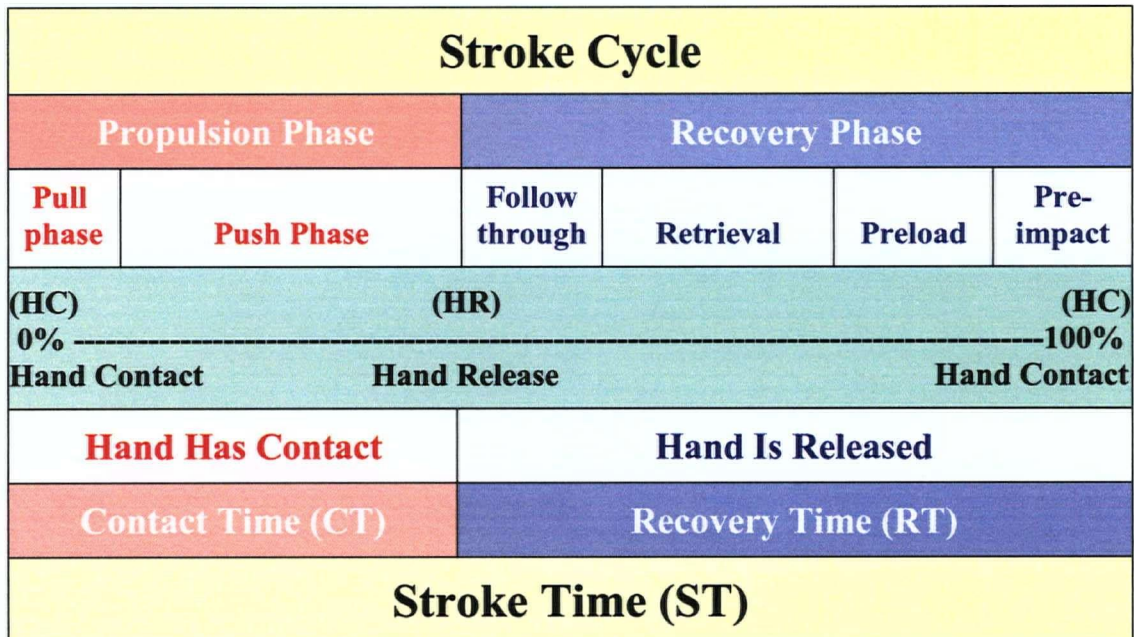


Figure 1.7 Different phases of a complete stroke cycle and the related terminology.

1.5 Previous Studies

There are many published studies related to MWP. Some of the previous research related to the present work is presented in this section. Due to the vast area of these studies, they are classified into four specific topics: Kinetics of MWP, Injuries Due to MWP, Effect of Seat Position on MWP, and Metabolic Energy Expenditure (MEE) during MWP.

1.5.1 Kinetics of MWP

Some of the previous studies focused on the kinetics of MWP [7–9,17–23]. In this Section, some of the key kinetic factors during MWP are reviewed. Figure 1.8 illustrates the most important forces and moments applied by the hand of the manual wheelchair user on the handrim and thus on the wheel center. $F_{h-x, y, z}$, $F_{c-x, y, z}$, $M_{h-x, y, z}$, $M_{c-x, y, z}$ are the force and moment components with respect to the hand and wheel center coordinate systems, respectively. F_c , M_{hy} and M_{cy} are not shown in Figure 1.8. The origin of the hand coordinate system is placed at the contact point between the hand and the handrim. The origin of the wheel coordinate system is placed at the center of the wheel. r_h is the mean radius of the handrim and φ is the angular position of the hand at the handrim contact point.

Total applied force (F_{total}) on the handrim is obtained by using the force components and either Equation 1.1a or 1.1b.

$$F_{total} = \sqrt{F_{hx}^2 + F_{hy}^2 + F_{hz}^2} \quad (1.1a)$$

$$F_{total} = \sqrt{F_{cx}^2 + F_{cy}^2 + F_{cz}^2} \quad (1.1b)$$

Total Effective Force (TEF), which is the virtual force required to produce propulsion, is obtained by using M_{cz} , the moment around the z-axis, and Equation 1.2 [8,9,17–19]:

$$TEF = M_{cz} \cdot r_h^{-1} \quad (1.2)$$

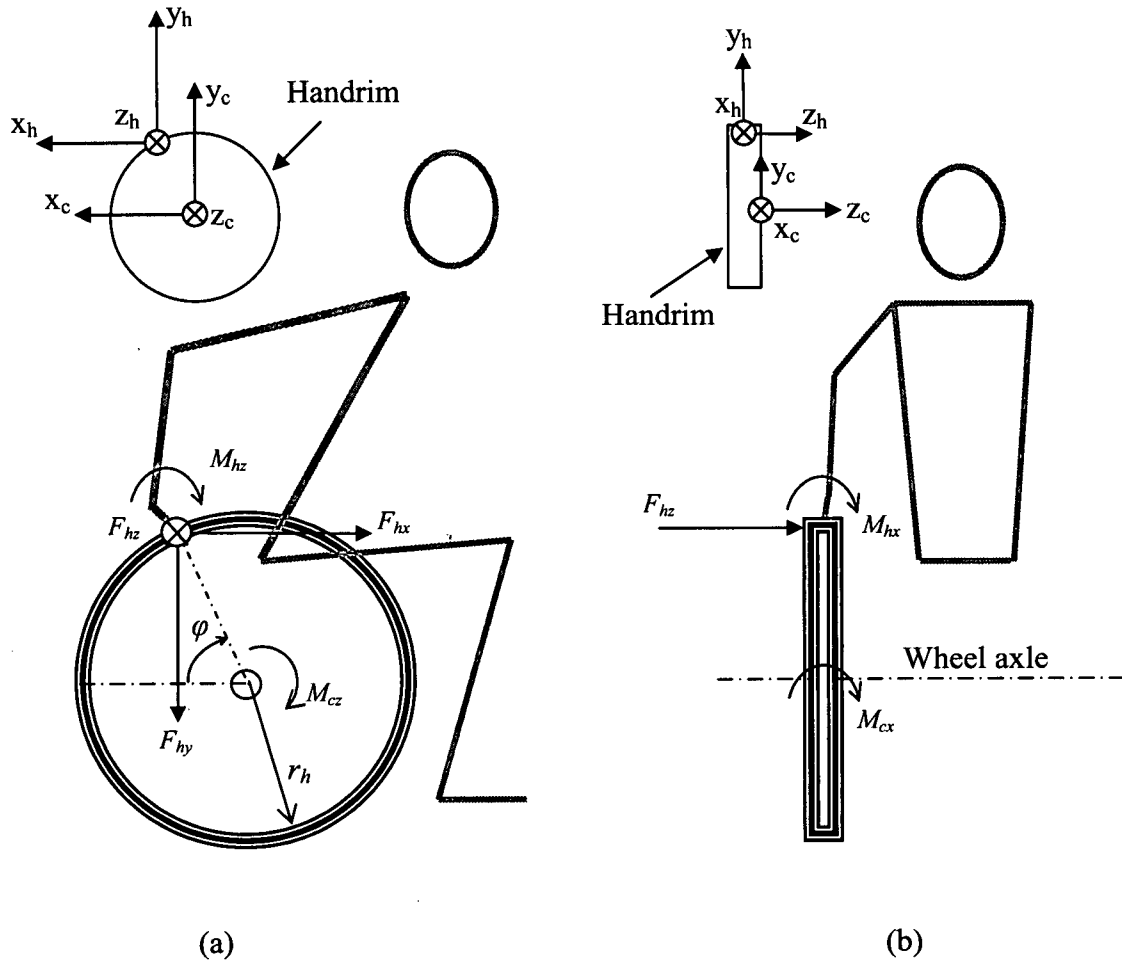


Figure 1.8 Illustration of forces and moments applied on the handrim during wheelchair propulsion: (a) side view; (b) front view.

Fractional Effective Force (FEF) is an important factor because it shows the ratio of the required force for propulsion to the force produced by the wheelchair user during the propulsion phase [8,9,20–22]. FEF is related to F_{total} and TEF as follows:

$$FEF = TEF \cdot F_{total}^{-1} \cdot 100 \quad (1.3)$$

Partial Effective Force (PEF) is the tangential part of the total force applied on the hand rim. PEF is related to F_{cx} , F_{cy} and φ as follows:

$$\text{PEF} = F_{cx} \cdot \sin \varphi - F_{cy} \cdot \cos \varphi \quad (1.4)$$

The torque around the wheel center (M_{cz}) is dependent on the torque around the hand (M_{hz}) and PEF as [9]

$$M_{cz} = M_{hz} + \text{PEF} \cdot r_h \quad (1.5)$$

M_{hz} can be obtained by using Equations 1.4 and 1.5, and is given by

$$M_{hz} = M_{cz} - (F_{cx} \cdot \sin \varphi - F_{cy} \cdot \cos \varphi) \cdot r_h \quad (1.6)$$

From the mechanical point of view, if we increase TEF, we should expect FEF and the mechanical efficiency to increase, but we still cannot say that GME will also increase.

de Groot et al. [9] found that using feedback-based learning, TEF increases, but GME decreases. This could be because of a conflict around the elbow that arises with the direction of application of the tangential force. Figure 1.9 illustrates that applying tangential force on the handrim could lead to a contradictory situation. The flexor muscles should act to mechanically balance the resultant moment around the elbow resulting from tangential force, whereas the extensor muscles must act to extend the elbow. This co-contraction may help the stability of the motion in some cases, but it will

produce negative power from the physiological point of view. To arrive at an optimum situation, one should avoid this conflict by redirecting the applied tangential force [9].

One should consider both mechanical and biological aspects of wheelchair propulsion to be able to analyze this motion properly before offering any suggestions for its improvement. However, there is no guarantee that the more efficient propulsion is the safer one for the user. A concurrent optimization of GME and probable injury prevention can lead to a breakthrough in this field.

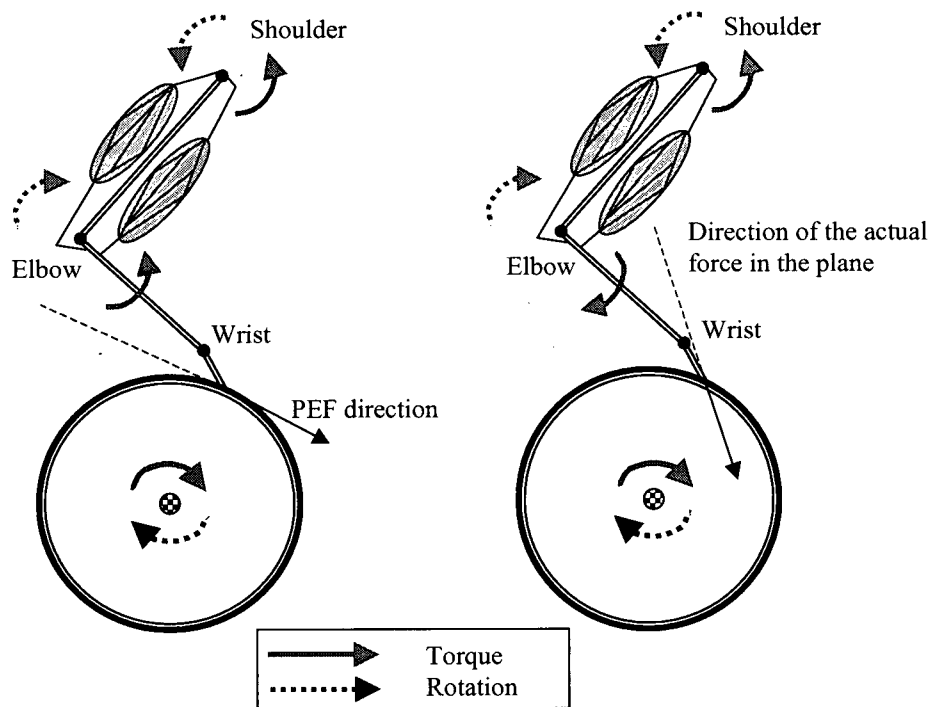


Figure 1.9 The relationships among the direction of the applied force, joint torques, and rotation around the shoulder and elbow (inspired by [9]).

1.5.2 Injuries Due to MWP

Statistics reported by researchers indicate that a considerable number of wheelchair users suffer from pain in their upper limb joints. In MWUs, the most commonly reported site of musculoskeletal injury is the shoulder (rotator cuff injuries, etc.), and the most common neurological cause of upper limb pain is Carpal Tunnel Syndrome (CTS), with prevalences of between 31 and 73% [2,7, 24–27] and between 49 and 73%, respectively [7,28–33]. Another common musculoskeletal injury is elbow tendonitis, being most prevalent in this site. Boninger et al. [4] reported that the prevalence of elbow pain in MWUs is about 16%. Prolonged use of a wheelchair could result in upper limb overuse injury [2], however, MWUs do benefit from the cardiovascular exercise associated with propulsion [34].

Efficient wheelchair propulsion with minimum injury pain is related to the manner and level of the loads that a user applies to the handrim during MWP [12]. Median nerve damage has been associated with high-force and high-repetition wrist motions. It has been found that weight loss of MWUs may prevent such nerve injury, which is the fundamental pathophysiology behind the development of CTS [23].

Su et al. [17] reported in 1999 that high upper limb joint loads may imply the risk of joint over-use injury. Boninger et al. suggested that reducing the forces during wheelchair propulsion may minimize developing shoulder injuries [18].

None of the previous studies on MWP introduced an injury index, which covers different factors that can cause injury during propulsion. An index that considers different aspects of the propulsion and anatomical specification of a user may help to estimate the probable injury due to MWP.

1.5.3 Effect of Seat Position on MWP

The wheelchair seat is one of the interfaces between the user's body and the wheelchair in the closed-loop linkage model of the human body and the wheelchair during MWP. Changing the wheelchair seat positions will alter the position and orientation of the upper limb segments of the user. This alteration affects the dynamics of MWP.

It has been reported that there is a relationship between wheelchair seat height, and both cardio-respiratory and kinematic parameters [19]. For example, differences in the kinematics and kinetics of the upper limbs appear at different seat positions, significantly affecting the Wheelchair Propulsion Strength Rate (WPSR) ($p < 0.05$). Su et al. [17] used WPSR in their study as an index, and concluded that optimal alignment of the wheelchair for the user could reduce joint loads and prevent injury. They used nine positions for the user during the tests, by considering three horizontal positions of the seat with respect to the wheel axle and three elbow angles when the hand is on the top of the handrim.

Boninger et al. [35] determined that the pushing angle was related to the horizontal and vertical distances of the subject's shoulder from the wheel axle. Their study showed that the frequency of propulsion and the rate of rise of the resultant force were significantly correlated to the horizontal distance of the subject's shoulder from the wheel axle— $p < 0.01$ and $p < 0.05$, respectively.

Richter [13] suggested that the seat position of the wheelchair affects the torques on the shoulder and elbow joints, the push angle, and the push frequency during MWP.

Richter considered the length of the position vector from the hub of the wheel to the user's shoulder as the variable for seat position.

Van der Woude et al. [19] evaluated the effect of seat height on the cardio-respiratory system and kinematics of nine non-wheelchair users. They concluded that seat height adjustment is critical, and is related to the anthropometric dimensions of the user. They considered elbow angle as a measure for seat height. This angle was measured when the user put his hand on the top of the handrim. They suggested that the seat height is optimum when the elbow angle is between 100° to 120°.

In another study, Wei et al. [36] reported that the seat position is a critical factor affecting the MWP movement and wrist kinematics. The wrist joint angle and range of motion varied according to seat height. However, they did not indicate the ideal seat position in their study.

Kotajarvi et al. [11] in a recent study investigated the effect of seat position on wheelchair propulsion biomechanics. They used thirteen experienced wheelchair users to propel an instrumented wheelchair over a smooth level floor at a self-selected speed. They changed the seat position horizontally and vertically and performed the tests at nine different positions. They reported that a shorter distance between the axle and shoulder (low seat height) improve the push time and push angle ($p < 0.0001$). They did not normalize the horizontal and vertical positions for the subjects.

The above studies indicated that there is a relationship between the seat position and the parameters of the dynamics of MWP. All of these studies referred to the effect of changing the seat position on different factors. Actually, most did not consider two-dimensional variations for the seat position, and those who used two-dimensional

changes for the seat position did not determine the optimal seat position for each individual.

1.5.4 Metabolic Energy Expenditure during MWP

Researchers and designers have made numerous attempts to improve the efficiency of MWP. They have tried to better understand this activity and improve its efficiency by using new propulsion techniques, new wheelchair designs, or both. One category of related research focuses solely on the mechanical energy and efficiency of MWP [10,37,38].

In fact, mechanical efficiency is not a good measure to verify the degree of suitability of a wheelchair's seat position. As MWP is produced by the combination of a human being and a mechanical device, one cannot determine the efficiency of MWP by using the mechanical efficiency equation only. To define the optimum seat position, GME must be used [9].

To determine GME, the physiological cost, or Metabolic Energy Expenditure (MEE) must be measured. MEE can be measured by indirect calorimetry, which assumes that all energy produced in the body depends on oxygen uptake. The most common method of measuring oxygen uptake is by spirometry, which analyzes exhaled air for its oxygen content [9].

Another method of measuring MEE is counting the heartbeats. It has been reported that there is a very good linear relationship between the heartbeat and the oxygen uptake profile for both steady and non-steady state situations [39,40]. Hood et al.

[39] studied both steady-state and non-steady-state human gait, and proposed a Total Heart-Beat Index (THBI) as

$$\text{THBI} = \text{Total heartbeats during exercise period} / \text{Total distance traveled (m)} \quad (1.7)$$

They used repeatability statistics and found the THBI is comparable to the oxygen cost, and that it is more reliable than the Physiological Cost Index (PCI) given by

$$\text{PCI} = (HR_{(ss)} - HR_{(R)}) / \text{velocity} \quad (1.8)$$

where $HR_{(ss)}$ is the average steady-state working heart rate, $HR_{(R)}$ is the average resting heart rate, and *velocity* is the average linear velocity of the wheelchair. Hood et al. also reported that THBI can be considered as a reflection of the metabolic energy expenditure and may be used in comparative studies, as long as the same subjects are involved.

Andrea Natali et al. [41] asked 12 young healthy individuals to use a cycloergometer. They reported a relationship close to linear for heartbeat and oxygen uptake during a cycling test after a bolus intravenous (IV) injection of either carnitine or saline was administered 10 min before the test. Their study consisted of 5 periods: (1) 30 min baseline period; (2) 40 min of cycling (aerobic exercise); (3) 2 min pause; (4) 2 min of intense (anaerobic) exercise; (5) 50 min of recovery.

Izerman et al. [42] reported that during paraplegic gait analysis, they observed a good correlation ($r = 0.86$) between the oxygen cost and the change of heartbeat (steady state minus rest). However, Schmid et al. [43] performed a study using different groups

of Spinal Cord Injury (SCI) and able-bodied subjects and reported that the slope of the line that represents the linear relationship between the oxygen consumption and the heart rate, changes for different groups of the subjects.

Bot et al. [40] investigated the validity of using heart rate response to estimate oxygen uptake during various non-steady-state activities. They studied interval tests on a cycloergometer by using 16 able-bodied subjects, and took simultaneous heart rate and $\dot{V}O_2$ measurements. Linear regression analysis revealed a high correlation between heart rate and $\dot{V}O_2$ ($r = 0.90 \pm 0.07$). In the second experiment they used 14 non-wheelchair-bound subjects and performed a wheelchair field test. A significant relationship was found for all subjects ($r = 0.86 \pm 0.09$). They suggested that $\dot{V}O_2$ may be estimated from individual Heart rate- $\dot{V}O_2$ regression lines during non-steady-state exercise.

Sawatzky et al. [44] reported in a recent study that heart rate has a very good correlation with oxygen consumption ($r = 0.82$) in SCI individuals with lesions below the fifth thoracic vertebrae (T5). For subjects with higher lesions, the correlation was weaker. They reported that this may be caused by the effect of the autonomic parasympathetic nerves on heart rate. They indicated that it is important to consider that heart rate does have its limitation and it should only be used to measure within-subject differences.

In another study, Tolfrey et al. [45] performed steady-state wheelchair propulsion of 16 paraplegic, elite male wheelchair racers with the classification of T3 and T4 lesions and reported that the group mean of the individual correlation coefficient for the $\dot{V}O_2$ -heart rate relationship was 0.99.

The above studies give enough confidence to assume a relationship close to linear between oxygen consumption and the heart rate of SCI subjects with lesions below T5.

Therefore, heart rate can be used as an alternative to oxygen consumption to estimate the variation of the GME in these subjects for within-subject analysis.

1.5.5 Instrumented Wheel

Knowing the forces and moments that a wheelchair user exerts on the handrim is necessary for an inverse dynamics approach to calculate the forces and moments in the upper limb joints. Collecting reliable 3D kinetic data, especially the forces and moments applied to the handrim of a manual wheelchair, is one of the most challenging aspects of gaining an in-depth understanding of the biomechanics of wheelchair propulsion.

A number of research groups have fabricated and instrumented wheels to measure the forces and moments applied on the handrim by the wheelchair user [46,47–51]. Although it is advantageous to develop and fabricate an in-house system, which allows greater flexibility in adding hardware and obtaining various signals, it is important to determine the specifications of such an instrument. Detailed specifications determine the system's level of reliability and usefulness. The collected data cannot be useful if they are unreliable.

Uncertainty analysis is a method that helps the researcher to calculate the level of uncertainty of the acquired data. This method can estimate the expected errors for different results obtained from the system. Cooper et al. [52] determined the uncertainties for the data acquired from their instrumented wheel (Smart^{wheel}). They determined the uncertainty for the forces and moments as 1.1–2.5 (N) and 0.03–0.19 (N.m) in the plane of the handrim, and 0.93 (N) and 2.24 (N.m) in the wheel axle direction, respectively. As uncertainty analysis is an analytical method, one will have greater confidence when an

experimental technique uses the actual output of the system to determine the specification of the respective instrumented device.

Wu et al. [48] performed static and dynamic analyses for their fabricated instrumented wheel and determined the degree of linearity and drift of their system. They determined part of the specification of their system by using the experimental method.

In this section, the previous studies have been presented to explain the motivations regarding the related topics. As this study consists of different aspects of MWP, such as fabrication of an instrumented wheel, clinical experiments, modeling of the upper limb, and analytical analysis, additional related published studies are presented in the corresponding chapters that follow.

1.6 Possible Solutions

Our review of the previous studies indicated that determining the optimum seat position for a user is still a challenge and warrants further investigation. One of the main purposes of the present study is to develop a method to increase efficiency and prevent or reduce probable injuries during MWP. In this research, three new indices for manual wheelchair propulsion analysis are proposed, as follows:

- Equivalent Biomedical Index (EBI) reflects the behavior of GME. The total heartbeats of the subject represents the pattern of MEE, and is one of the factors used in EBI equation. The above literature review indicates that there is a reliable relationship between the heart rate and the oxygen uptake. Heart rate can then be a good alternative to oxygen uptake for estimating GME.

- The Wheelchair User Joint Injury Index (WUJII) reflects a value that is representative of the MWU's joint injury, and uses the joint loads, pushing frequency, Body Mass Index (BMI), and total weight of the user and the wheelchair. If WUJII has a high value, the risk of injury is also high.
- The third index is WUJII', which is the same as WUJII except that Percentage of Body Fat (%BF) is used instead of the BMI in the relation. Comparing the results of the two injury indices will help to determine the role of BMI and %BF on the probable injury. The effects of changing the two seat-position parameters on the value of the proposed indices are investigated to find the optimum position.

In this study, an instrumented wheel is fabricated, and validated through a general uncertainty analysis method. The specifications of the instrumented wheel are determined by using both static and dynamic experiments. The loads that a user applies on the handrim during MWP are part of the data required to calculate propulsion efficiency and analyze the optimum seat position for wheelchair users, in order to improve performance and develop injury-prevention techniques.

The values of the proposed indices for six possible seat positions are calculated and the results are analyzed to derive some generic rules that can be used to estimate the optimum seat positions for all users.

Some of the data needed to determine WUJII or WUJII' at each of the upper limb joints are the values of the loads at these joints. To calculate the net joint forces and moments of the upper limb during MWP, an algorithm necessary for an inverse dynamics solution is developed. Considering probable priorities for injury prevention at specific

joint, corresponding injury index for the joint of interest will be used to determine the optimum position.

To make the testing procedure and post-processing of the acquired data more convenient, a new model for the dynamics of the upper limb is introduced that only needs the geometric positions of two anatomical sites to perform kinematic analysis. This model has some advantages and some limitations (see discussion in Section 6.4). However, it makes data acquisition noticeably more convenient compared with other models that use more anatomical sites [12,46].

1.7 Thesis Organization

The thesis is organized as follows. The current chapter has provided a general background and the motivation for this study, and outlined the research questions, hypothesis and objectives. It has also presented an overview of MWP kinetics to open the related discussions. Numerous studies have analyzed MWP. Some were reviewed in this chapter; additional related work will be referred to in subsequent chapters.

Chapter 2 describes the design, fabrication and validation of an instrumented wheel. Uncertainty analysis for the instrumented wheel is presented, and the required static and dynamic experiments for determining the specification of the instrumented wheel are described. One book chapter [53] and two journal papers [54,55] have been published based on the results presented in this chapter.

In Chapter 3, an assessment of the efficiency and injury potential during MWP is presented. Three new indices, EBI, WUII, and WUIII' are proposed and described for this purpose.

Chapter 4 outlines the proposed method for determining the optimum seat position of a manual wheelchair, involving experiments conducted on eight wheelchair user subjects. This is followed by an analysis of the results to extract generic rules to estimate the optimum seat position for all users. Also, the optimum positions are prescribed for two subjects. One conference paper has been prepared based on part of the results of this chapter and presented as poster [56].

In Chapter 5, a 3D rigid-body model for the dynamics of the upper limb is presented, and a method of calculating the upper limb joint forces and moments is described. This chapter also addresses the injury-assessment method for the upper limb joints during MWP.

Chapter 6 provides a new model for analysis of the dynamics of the upper limb. The reliability of the new model is investigated by determining the relative error for the calculated loads. The advantages and limitations of the new model instead of the method used in Chapter 5 are then presented.

In Chapter 7, a summary of the main conclusions drawn from the research, its limitations and contributions, and suggestions for future work are presented.

1.8 Concluding Remarks

Many of the studies cited in this chapter used able-bodied or non-wheelchair user individuals as subjects. The absence of actual manual wheelchair user subjects eliminates most of the external validity of the results [57]. Also, the repeatability of the tests for each individual is an important factor and is not considered in most of the studies. However, they do shed light on new trends and approaches, and some suggest innovative

ideas for analyzing MWP. In this thesis, a reliable instrumented wheel for measuring the loads applied by the user on the handrim is fabricated. A methodology is developed for prescribing the optimum seat position for each individual, using three new indices proposed to perform efficiency and injury assessments. A 3D rigid-body inverse dynamics method was used to calculate the loads at the upper limb joints as part of the data required to calculate the values of the proposed indices at each joint. The optimum seat positions were determined for two subjects to prevent injury at specific joints by using the joint injury indices. Finally, a new model for the analysis of the dynamics of the upper limb was developed and validated to simplify the experimental procedure and the required post-processing.

CHAPTER 2

The Instrumented Wheel

2.1 Introduction

In Chapter 1, the importance of the instrumented wheel for kinetic analysis of MWP was explained, and a review of the relevant literature was presented, to emphasize that this equipment is an essential device for kinetic analysis of MWP.

In the present work, an instrumented wheel system is fabricated and validated by using the general uncertainty analysis. Also, the specifications of the wheel system are determined using both static and dynamic experiments. This system enables the forces and moments applied by the wheelchair user on the handrim to be determined. It is important to understand how these forces and moments are generated and what factors influence them. The applied loads are part of the data required to calculate propulsion efficiency and analyze the optimum seat position for wheelchair users, in order to

improve performance, identify the probable causes of injuries, and develop injury prevention techniques.

This chapter also presents a procedure for calculating the essential dynamic variables used in the study of manual wheelchair propulsion. An important feature of the force/moment calculation procedure is that, together with encoder data analysis, it allows one to determine the angular position of the contact point between the hand and the handrim without the use of cameras. This angular position is a critical factor in determining moments and the effective tangential force acting on the wheelchair user's hands and upper limbs, which can result in discomfort or injury. The general uncertainty analysis was performed for different outputs of the instrumented wheel, and the system's level of reliability was determined. The results indicated that the uncertainty for the forces and the moments of interest were in the range of 1.4–1.7 N and 0.58–0.68 N.m in the plane of the handrim, and about 3.40 N and 0.25 N.m in the wheel axle direction, respectively. For the developed system, however, the uncertainty values for the important load components, namely the planar forces and axial moment, were low. The resulting uncertainties represent an estimation of the expected errors in future data gathering and analysis.

The static and dynamic test protocols were designed to cover all loading conditions. To determine the specifications of the system, the linearity, repeatability and mean error of the measurement system in both static and dynamic situations were calculated. These specifications allow one to determine the level of the system's reliability, and gain confidence in the results and future applications.

2.2 Instrumentation

To conduct an uncertainty analysis, as well as static and dynamic verification for manual wheelchair propulsion, stationary tests were performed to measure the forces and moments applied by the wheelchair user on the handrim, and the angular position of the wheel during propulsion. Currently, there is no sensor available that can measure the required forces and moments directly. Instrumented wheels are mechatronic systems (a combination of hardware and software) that process the data acquired by the sensors and calculate the desired values. In this research, an instrumented wheel assembly was designed and fabricated and the required setup for the tests was prepared to accurately determine uncertainties and system specifications. The setup for this part of the study consisted of a wheelchair, the instrumented wheel, a platform with two rollers to allow stationary tests (roller-rig), an AC motor, two Personal Computers (PCs), an Analog-to-Digital (A/D) data acquisition board, and four different static and dynamic loading setups.

2.2.1 Wheelchair

A Quickie (Sunrise Medical Inc.) 40-cm-wide wheelchair with standard spokes was used in this study. The wheelchair had solid gray rubber tires 58.25 cm in diameter and 3 cm in width. The handrim was 54 cm in diameter, and the positions of the backrest and axle of the wheels (thus the seat) were adjustable.

2.2.2 The Instrumented Wheel

The instrumented wheel system itself consisted of a standard-spoke wheel from Quickie wheelchair, a six-component load transducer (Model PY6-500, Bertec Inc., Measurement ExcellenceTM), an AM 6500 external amplifier, a signal conditioning circuit, a power supply, a handrim assembly, an encoder (S1 360 IB), a slip ring (AC 6373), two gears, and insulated shielded cables (Figure 2.1). As some of the data acquisition components had to be mounted within the wheelchair, counterweights were used to maintain the wheel's rotational balance.

The PY6 load transducer came with a digitally stored calibration matrix and used 16-bit digital signal acquisition and conditioning with a sampling rate of 1 kHz. The digital signal output could be plugged directly into the standard Universal Serial Bus (USB) port of a personal computer via the AM 6500 amplifier without requiring an additional PC board for A/D signal conversion.

The transducer had sensitivity levels of 2 mV/N and 2 mV/(N.m), an accuracy of 99.5%, $\pm 1.0\%$ cross-talk, a full mechanical load rating of 1250 N for in-plane forces F_x and F_y , 2500 N for the out-of-plane force F_z , 60 N.m for moments M_x and M_y , and 30 N.m for moment M_z with respect to the first local coordinate system (Figure 2.2). The load cell was mounted on the wheel with its z-axis aligned with the axle of the wheel. The origins of the global and first local coordinate systems were concentric.

The handrim assembly had three parts: a handrim, a 3-mm thick round aluminum face-plate, and six reinforced aluminum spokes. The encoder had three input-output channels, and its resolution was 1°. Gears were used to transfer the wheel rotation, and, with a gear ratio of 8 to 1, increase the resolution of the measured angular position (θ) to

0.125°. The first (large) gear was mounted on the wheel shaft and the second (small) gear was mounted on the encoder shaft (Figure 2.3). A slip ring aligned with the wheel axle allowed continuous transfer of the transducer signals to the computer during wheel rotation (Figure 2.1).

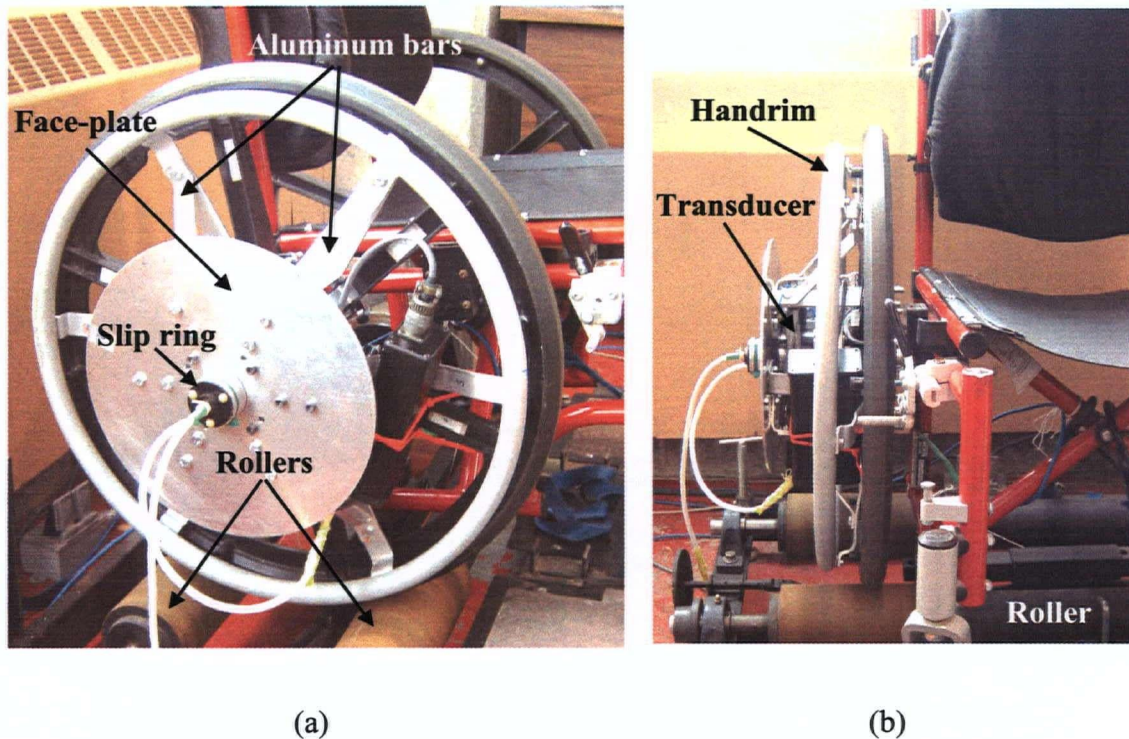


Figure 2.1 Instrumented wheel: (a) side view; (b) front view.

2.2.3 Roller-rig

The roller-rig was a platform with two parallel rollers to allow stationary tests. The entire wheelchair was placed on the roller-rig, which had adjustable legs to maintain a horizontal position (Figures 2.1 and 2.4).

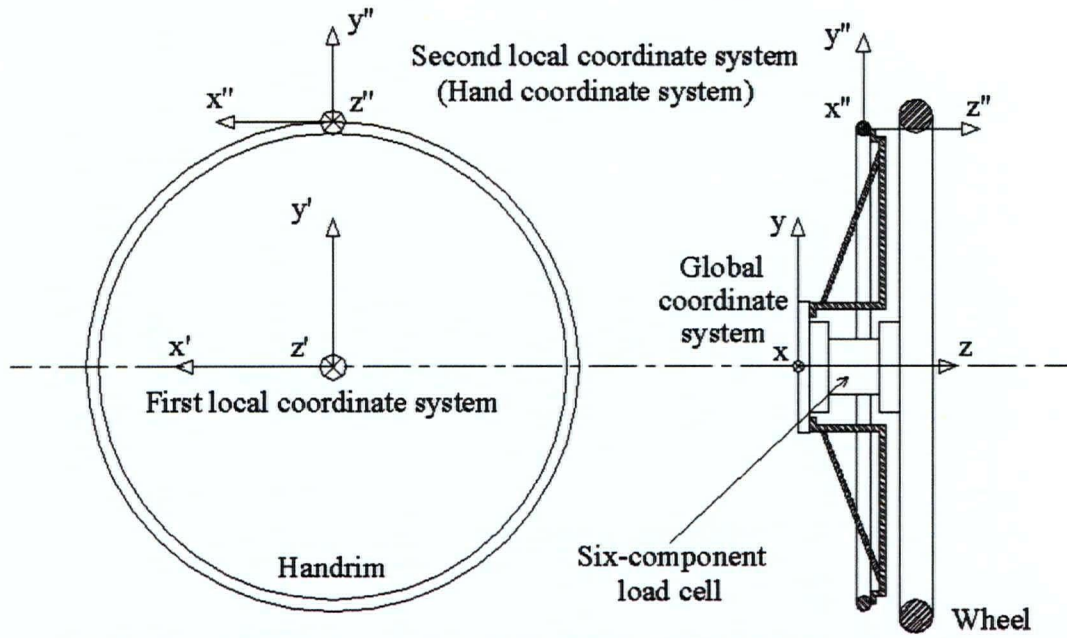


Figure 2.2 Initial position and orientation of global and two local coordinate systems on the instrumented wheel.

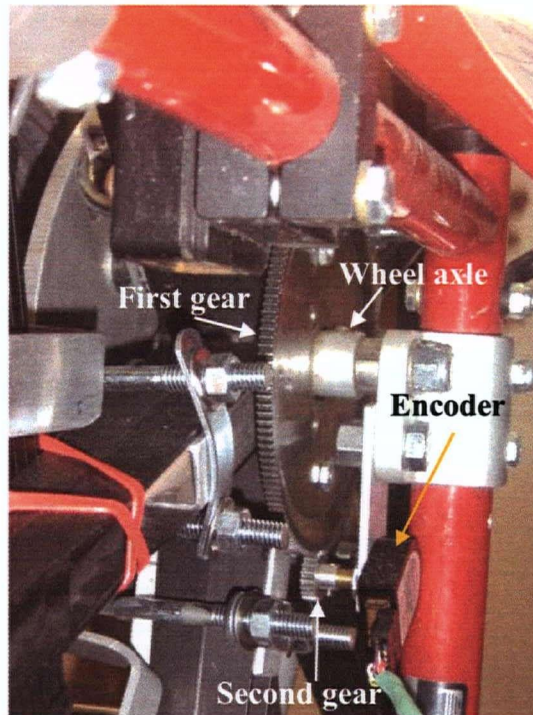


Figure 2.3 Encoder gear system.

2.2.4 AC Motor

The AC motor was connected to the shaft of one of the rollers to rotate the instrumented wheel during some of the tests. The motor speed was adjustable, and three different wheelchair angular velocities (3.0, 3.8 and 4.8 rad/s) close to required speeds for the subject tests, in this study, were used for the dynamic tests (Figure 2.4). The equivalent linear velocities were 3.15, 3.98 and 5.03 km/h, respectively.

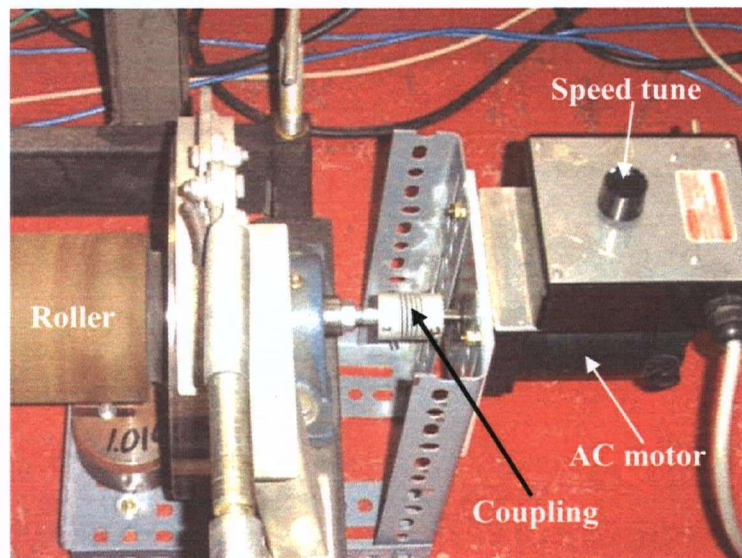


Figure 2.4 AC motor and its coupling to a shaft of the roller-rig.

2.2.5 Computers

The experimental setup included two personal computers. The transducer interface software, Digital Acquire™, used one computer to record the load exerted on the handrim by the user. The LabVIEW™ software on the second computer calculated the wheel's angular position as the load data was collected on the first computer. The

output of the encoder was analog voltage. Therefore, the angular position of the wheel was calculated using the LabVIEW™ software and its counting option, where the value of the output increased 360 counts per revolution of the shaft of the encoder. A single PC was not used for both measurements because running two different software programs at the same time on one PC caused the measured times to be incompatible and shifted.

2.2.6 Data Acquisition Board

A 12-bit A/D signal conversion board (PCI-6025E) transferred the encoder's analog output data to the computer (note: the encoder had built-in hardware that converted the encoder pulses into an analog output). For consistency, when tests were set up, a specially wired push-button was used to activate both PCs at the same instance.

Figures 2.5 and 2.6 give global views of the system as a schematic sketch and a block diagrams, respectively.

2.2.7 Static and Dynamic Loading Setups

To perform the tests, three different static loading setups and one dynamic loading setup were used. These setups are elaborated in Section 2.5.1.

In the next section, three coordinate systems for the instrumented wheel are introduced and the required dynamic equations are derived to determine the forces and moments applied by the user on the handrim.

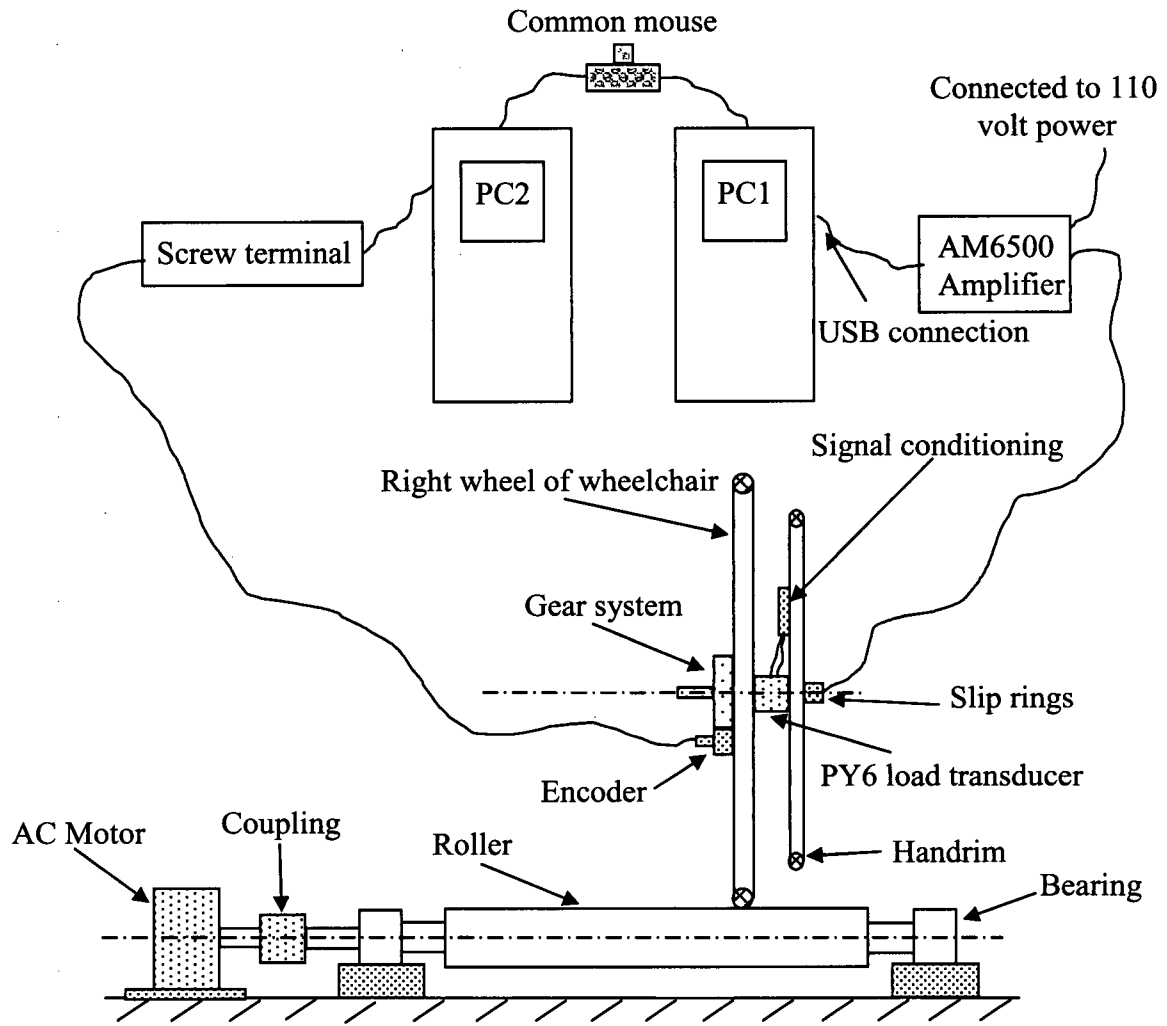


Figure 2.5 Global schematic rear view of the physical data acquisition system.

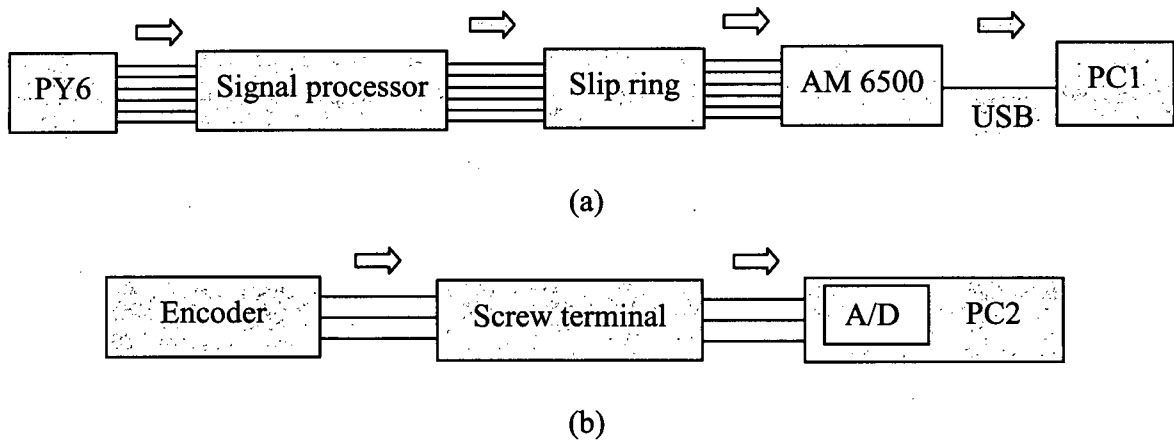


Figure 2.6 Measurement signal flow diagram for: (a) load; (b) angular position.

2.3 Preliminary Experimental Protocol

In this part of the study, one 27-year-old able-bodied male subject was used for the stationary tests because we were interested in testing the system rather than acquiring specific information related to the subject himself. The main idea was to propel the wheelchair, measure loads, and calculate uncertainties to verify the system. The subject had a daily training of 5 min for one week to become familiar with the experimental setup. For the main test, the subject propelled the wheelchair for 2 min, increasing his speed as much as conveniently possible and maintaining it steady for 1 min [49]. The data were then collected for the final minute of the test.

2.4 Derivation of Dynamic Equations

To characterize and measure the forces and moments applied by the user on the handrim, three different coordinate systems were used (Figure 2.2). The global and first local coordinate systems have the same origin at the center of the wheel and the same direction at the beginning of the propulsion, which is the direction of the transducer coordinate system. The first local coordinate rotates with the wheel. The origin of the second local coordinate system (hand-coordinate system) is at the contact point between the hand and the handrim and moves with the handrim, but its axes remain parallel to the global coordinate axes.

2.4.1 System Calibration

As indicated before, the PY6 load transducer came with the calibration matrix digitally stored within and interfaces to the PC through software (Digital Acquire™). Therefore, there was no need to determine this matrix, due to the automatic conversion of voltages to forces and moments, and the cross-coupling involved. Using this transducer, the digital signal output was plugged directly into the standard USB port of a personal computer without requiring an A/D signal conversion board. During the propulsion phase, in addition to the loads produced by the user, the system experienced dynamic preloads due to the rotating weight of the measurement system and the balancing weights, which should be taken into account to eliminate their effects.

2.4.2 Preload Equations

The instrumented wheel was mechanically turned by the AC motor on the rollers without applying any force on the handrim to measure the net preloads. As the preloads changed sinusoidally with the rotation of the wheel, their values were calculated and their equations were determined with respect to the global coordinate system.

All of the preloads can be described by the following generic periodic equation:

$$P = a \cdot \sin(\theta + \xi) + b \quad (2.1)$$

In this equation, P represents preload forces or moments, a and b are constants with dimensions [N] or [N.m], θ is the wheel's angular position [radian] (which is a function of time), and ξ is the phase difference [radian] for the output of the x, y, and z

channels. Table 2.1 shows the preload equation constants for various load components. They were obtained by using the measured preloads, $F_{P-x,y,z}$ and $M_{P-x,y,z}$, with respect to the first local coordinate system.

2.4.3 Local and Global Forces and Moments

Forces and moments measured by the data acquisition software are not the values directly required for the MWP analysis. The effects of preloads must be considered, and by using the following equations, one can calculate the net local forces and moments with respect to the first local coordinate system:

$$F_{Lx} = F_x - F_{Px} \quad (2.2a)$$

$$F_{Ly} = F_y - F_{Py} \quad (2.2b)$$

$$F_{Lz} = F_z - F_{Pz} \quad (2.2c)$$

$$M_{Lx} = M_x - M_{Px} \quad (2.2d)$$

$$M_{Ly} = M_y - M_{Py} \quad (2.2e)$$

$$M_{Lz} = M_z - M_{Pz} \quad (2.2f)$$

where $F_{L-x,y,z}$ and $M_{L-x,y,z}$ are the force and moment components applied by the wheelchair user, and $F_{x,y,z}$ and $M_{x,y,z}$ are the measured force and moment components. All values are with respect to the first local coordinate system at the center of the wheel.

Table 2.1 Constants for different preload equations.

P (preload)	a [N, N.m]	b [N, N.m]	ξ [radian]
F_{Px}	-26.5	2.5	0
F_{Py}	25.5	24.5	$-\pi/2$
F_{Pz}	1	~ 0	0
M_{Px}	1.05	-1.05	$\pi/2$
M_{Py}	-1.2	-0.2	0
M_{Pz}	-0.1	~ 0	0

The first local coordinate system is fixed to the wheel and rotates with it. The global coordinate system must therefore be used to calculate the forces and moments with respect to a fixed reference system. It should be emphasized that the origin of the global coordinate system coincides with that of the first local coordinate system, and that their z-axes are aligned. To calculate forces and moments in the global coordinate system, the following transformation relations, with reference to Figure 2.7, were used:

$$F_{gx} = \cos \theta \cdot F_{Lx} - \sin \theta \cdot F_{Ly} \quad (2.3a)$$

$$F_{gy} = \sin \theta \cdot F_{Lx} + \cos \theta \cdot F_{Ly} \quad (2.3b)$$

$$F_{gz} = F_{Lz} \quad (2.3c)$$

$$M_{gx} = \cos \theta \cdot M_{Lx} - \sin \theta \cdot M_{Ly} \quad (2.3d)$$

$$M_{gy} = \sin \theta \cdot M_{Lx} + \cos \theta \cdot M_{Ly} \quad (2.3e)$$

$$M_{gz} = M_{Lz} \quad (2.3f)$$

where, $F_{g-x,y,z}$ and $M_{g-x,y,z}$ are the applied force and moment components with respect to the global coordinate system.

These relations can be expressed in matrix form as

$$\begin{bmatrix} F_{gx} \\ F_{gy} \\ F_{gz} \\ M_{gx} \\ M_{gy} \\ M_{gz} \end{bmatrix} = \begin{bmatrix} \cos \theta & -\sin \theta & 0 & 0 & 0 & 0 \\ \sin \theta & \cos \theta & 0 & 0 & 0 & 0 \\ 0 & 0 & 1 & 0 & 0 & 0 \\ 0 & 0 & 0 & \cos \theta & -\sin \theta & 0 \\ 0 & 0 & 0 & \sin \theta & \cos \theta & 0 \\ 0 & 0 & 0 & 0 & 0 & 1 \end{bmatrix} \begin{bmatrix} F_{Lx} \\ F_{Ly} \\ F_{Lz} \\ M_{Lx} \\ M_{Ly} \\ M_{Lz} \end{bmatrix} \quad (2.4)$$

and in the compact form:

$$L_g = \lambda \cdot L_L \quad (2.5)$$

where λ is the transformation matrix for transforming the local into global values, L_g is the matrix of global force and moment components and L_L is the matrix of local force and moment components (Figures 2.8 and 2.9).

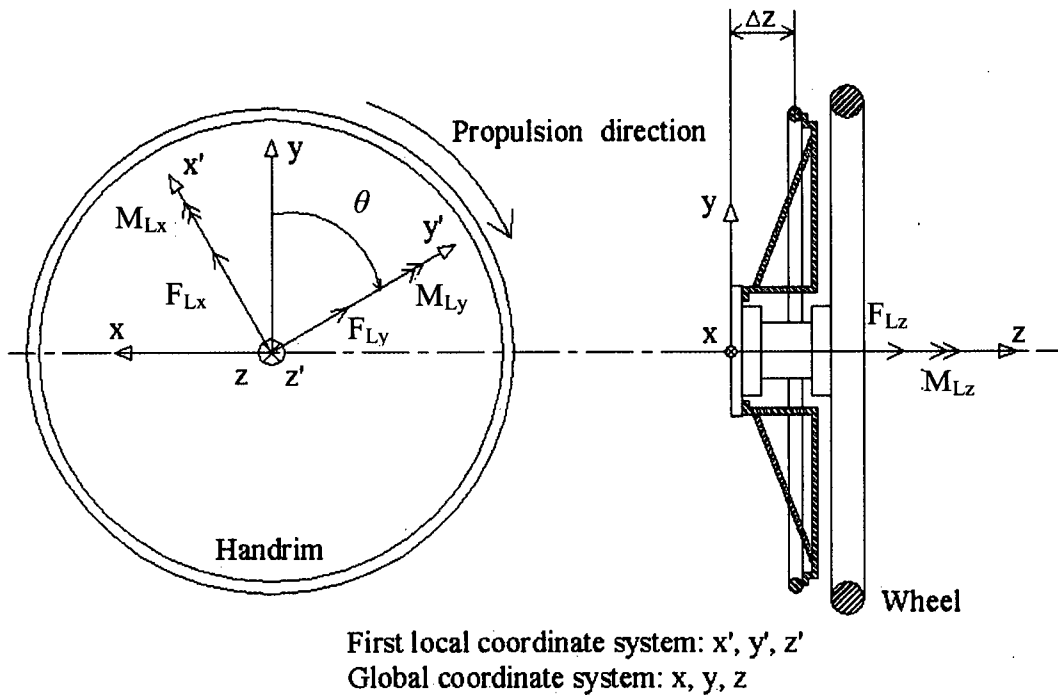


Figure 2.7 Illustration of local loads after θ degrees of wheel rotation.

Using Equations 2.1, 2.2 and 2.3, the global forces and moments during the propulsion phase were calculated. The global forces are the same as the local (hand-coordinate system) forces. Figure 2.8 shows the forces produced by the wheelchair user during the pushing phase on the handrim with respect to the global coordinate system. It is postulated that the dips on the curves for F_{gx} and F_{gy} and the spike on the curve for F_{gz} during the primary time of the propulsion phase are due to the contact impact between the hand and the handrim. These dips and spikes appeared in the results because an able-bodied subject (inexperienced wheelchair user) was used in this set of experiments. The presence or absence of the dip or spike has also been reported by other researchers who employed inexperienced or experienced wheelchair users in their investigations,

respectively [8, 49]. However, the spike or dip may happen for experienced users because of the bad propulsion technique or seating position, as well.

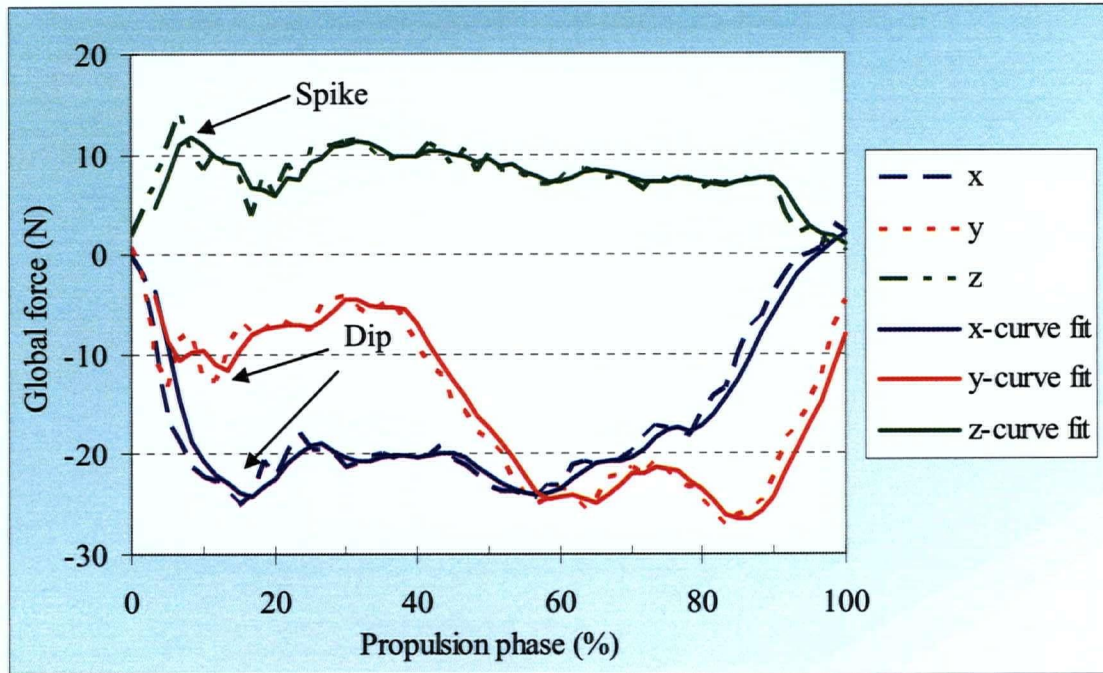


Figure 2.8 Propulsion force components with respect to global and hand local coordinate systems.

Figure 2.9 shows the moments produced by the wheelchair user with respect to the global coordinate system. These moments were calculated using Equations 2.1, 2.2 and 2.3. The curves of M_{gz} and M_{gx} (the moment about the global coordinate system's z and x-axis) show a spike, and the curve of M_{gy} shows a dip in the early phase of the propulsion. The only important moment for manual wheelchair propulsion is M_{gz} , which is the effective moment. The other two moments are undesirable and reduce the propulsion efficiency.

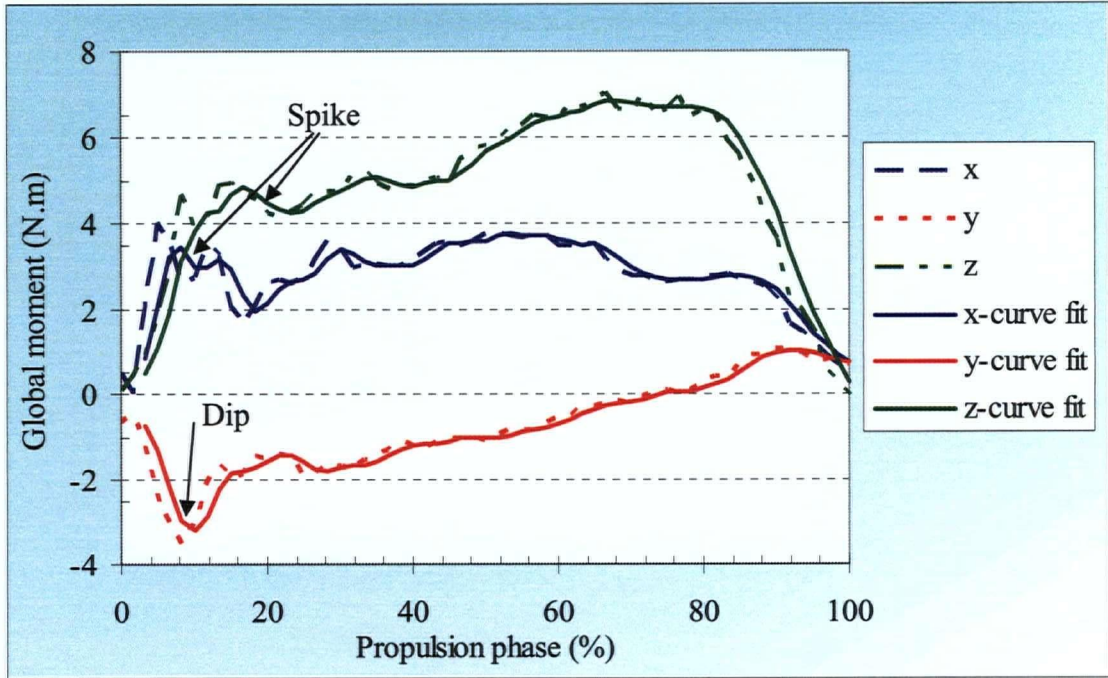


Figure 2.9 Propulsion moment components with respect to global coordinate system.

Since we need to determine the forces and moments at the contact point between the hand of the wheelchair user and the handrim during the pushing phase, another transformation from the global coordinate system to the parallel-moving local hand (second local) coordinate system is required. These forces and moments, with reference to Figures 1.8 and 2.7, are as follows:

$$F_{hx} = F_{gx} \quad (2.6a)$$

$$F_{hy} = F_{gy} \quad (2.6b)$$

$$F_{hz} = F_{gz} \quad (2.6c)$$

$$M_{hx} = M_{gx} - F_{gz} \times r_h \times \sin \varphi + F_{gy} \times \Delta z \quad (2.6d)$$

$$M_{hy} = M_{gy} + F_{gz} \times r_h \times \cos \varphi - F_{gx} \times \Delta z \quad (2.6e)$$

$$M_{hz} = M_{gz} + r_h \times (F_{gx} \times \sin \varphi - F_{gy} \times \cos \varphi) \quad (2.6f)$$

where r_h is the mean radius of the handrim, and Δz is the offset distance between the plane of the handrim and the origin of the global coordinate system in the z direction. Also, the angle φ is the instantaneous position of the hand on the handrim in the global coordinate system (x-y plane) measured clockwise with respect to the +x axis.

2.4.4 Important Kinetic Factors

In Section 1.5, some of the most important kinetic factors during MWP were introduced. In this section, the kinetic factors are elaborated by presenting the results of a sample test. Figure 2.10 illustrates F_{total} , Total effective force (TEF) and Fractional Effective Force (FEF), which were calculated using Equations 1.1, 1.2 and 1.3, and the data from the test. All calculations were made with respect to the global coordinate system.

The figure shows a spike on the curve for F_{total} during the early part of the propulsion phase. It is postulated that this spike has resulted from the contact impact between the hand of an able-bodied or inexperienced wheelchair user and the handrim. The hand of the wheelchair user is in contact with the handrim for the entire propulsion phase, but the nature of the grip changes and affects the level of the loads transmitted. At the beginning and end of the propulsion phase the grip is partial and soft, but during the rest of the propulsion phase the user has a firm grip. During part of the early period of the propulsion phase, the strength of the grip increases sharply for able-bodied or inexperienced wheelchair users, which produces the spike.

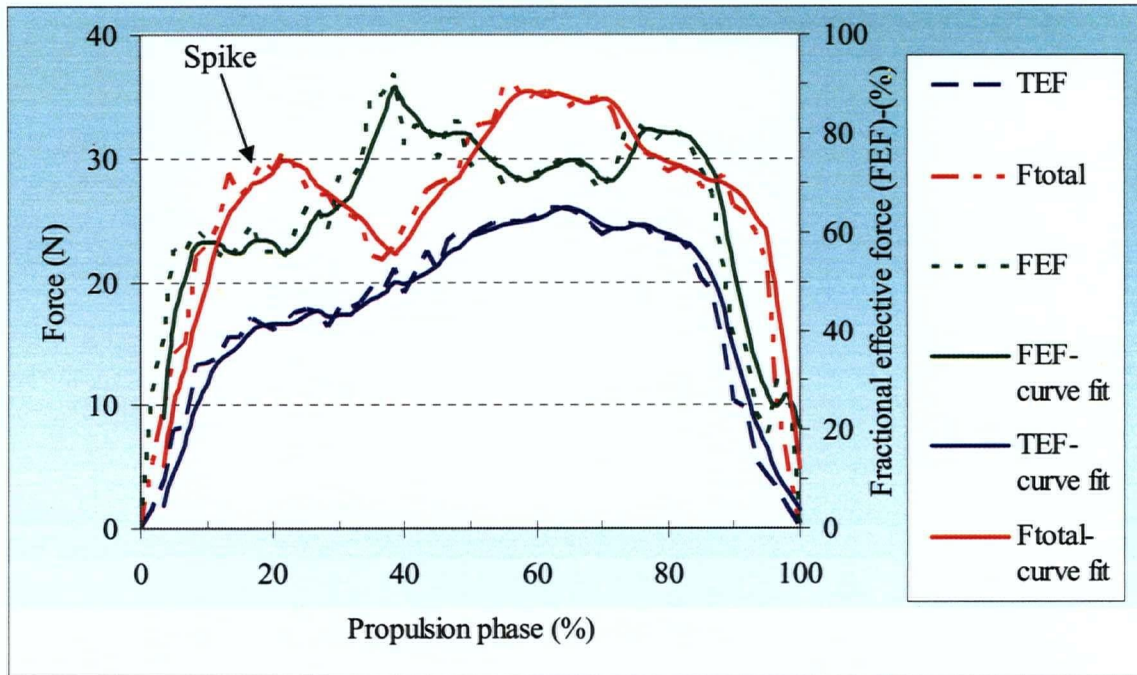


Figure 2.10 F_{total} and TEF with respect to the global coordinate system, and the FEF during the propulsion phase.

The location or the time of the spike is not exactly the same during different tests. The shape of the spike depends on the propulsion style of the wheelchair user. This spike represents a loss of energy that the user should learn to avoid.

TEF is a virtual force that produces the propulsive moment. Considering the generally low levels of efficiency for manual wheelchair propulsion, it is reasonable to expect a lower value for the total effective force compared with the total force produced during the propulsion phase. To improve manual wheelchair propulsion, one should attempt to reduce the total force as much as possible, closer to the total effective force, by choosing the proper seating position, and propulsion technique.

FEF is an important factor in determining the effectiveness of manual wheelchair propulsion and is used as an alternative to efficiency [49,58,59]. Figure 2.10 shows that FEF was less than 60% during approximately the first 25% and the last 10% of the propulsion phase. There is not high reliability in the early and late phases of the propulsion phase because of the vibrations due to the initial contact between the hand and the handrim, and releasing the handrim. So, except for the early and the late parts of the propulsion phase, FEF has its lowest value at the time the spike was produced, which verifies the moments stated earlier.

2.4.5 Determining the Position of the Hand on the Handrim

The angle φ can be obtained in a number of ways, but some assumptions must be made [49]. Equations 2.6d and 2.6e can be used to obtain Equation 2.7. First, if M_{hx} and M_{hy} are assumed to be zero (their values are small and have less importance compared with M_{hz}) Equation 2.8 is obtained. Although this is a viable approach, it was not used because Equation 2.8 is based on five parameters, of which only Δz is directly measurable. This poses a high risk of accumulation and propagation of error within the different equations that are needed to calculate φ .

$$\varphi = \tan^{-1} \left(\frac{M_{gx} - M_{hx} + F_{gy} \times \Delta z}{-M_{gy} + M_{hy} + F_{gx} \times \Delta z} \right) \quad (2.7)$$

With $M_{hx} \approx M_{hy} \approx 0$, one has

$$\varphi = \tan^{-1} \left(\frac{M_{gx} + F_{gy} \times \Delta z}{-M_{gy} + F_{gx} \times \Delta z} \right) \quad (2.8)$$

Instead, Equation 2.6e was used to obtain Equation 2.9. By assuming that only M_{hy} is zero, Equation 2.10 is derived for φ . This equation is also based on five parameters, but three are directly measurable (Δz , F_{gz} , r_h). Therefore, the risk of error accumulation and propagation is less.

$$\varphi = \cos^{-1} \left(\frac{M_{hy} - M_{gy} + F_{gx} \times \Delta z}{F_{gz} \times r_h} \right) \quad (2.9)$$

With $M_{hy} \approx 0$, which is a reasonable assumption (see later discussion on this assumption), φ_c is calculated as

$$\varphi_c = \cos^{-1} \left(\frac{-M_{gy} + F_{gx} \times \Delta z}{F_{gz} \times r_h} \right) \quad (2.10)$$

φ_c is the “calculated φ ,” but for simplicity we will continue to use the symbol φ in our derivations.

To evaluate the above procedure as a kinetic method, the VICON motion analysis system was used to acquire the kinematic data from the wheel center and a point on the handrim to calculate φ . The VICON system is described in Chapter 4.

Figure 2.11 shows the calculated φ by using kinetic and kinematic methods, and the exponential curve fit of the kinetic method. The results show that one does not have sufficient reliability at the beginning and end of the propulsion phase for the calculated φ ,

as similarly reported by Cooper et al. [52]. This is likely because of the lack of constant stability during the initial period of the propulsion phase (roughly the first 20%) when the hand impacts the handrim. During the later part of the propulsion phase (roughly the last 15%) the grip on the handrim becomes soft, and the propulsive moment begins to decrease. Therefore, it is reasonable to attribute these instabilities to the making and breaking of the hand contact with the handrim. During much of the propulsion phase, there is a reasonable relationship between the two calculated ϕ by using the kinetic and kinematic methods. To improve the reliability of the results, ϕ was estimated by using the exponential curve fit of the kinematic method. The equations in the Figure were automatically generated by the Excel[®] software. It gives the relation between ϕ and the propulsion phase.

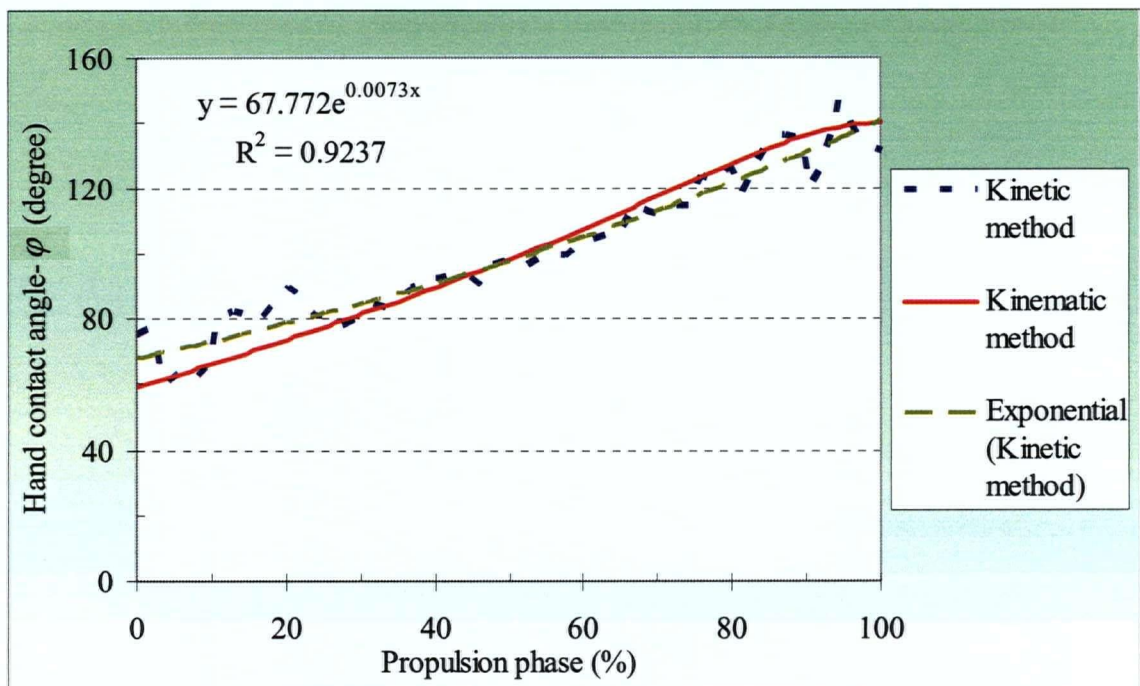


Figure 2.11 Calculated ϕ using kinetic and kinematic methods, and the exponential curve fit of the kinetic method.

The kinematic method was considered as a more reliable way to calculate φ . The other two methods were validated by comparing their calculated values for φ with those determined by using the kinematic method. Five consecutive propulsion cycles were used to determine the absolute error and its standard deviation (Std. Dev.) for calculated φ by using the kinetic method and the exponential curve fit of the kinetic method, respectively (Figures 2.12–13). The figures show an absolute error of about $\pm 3^\circ$ for φ , or ± 1.5 cm, for the hand-contact point during most of the propulsion phase.

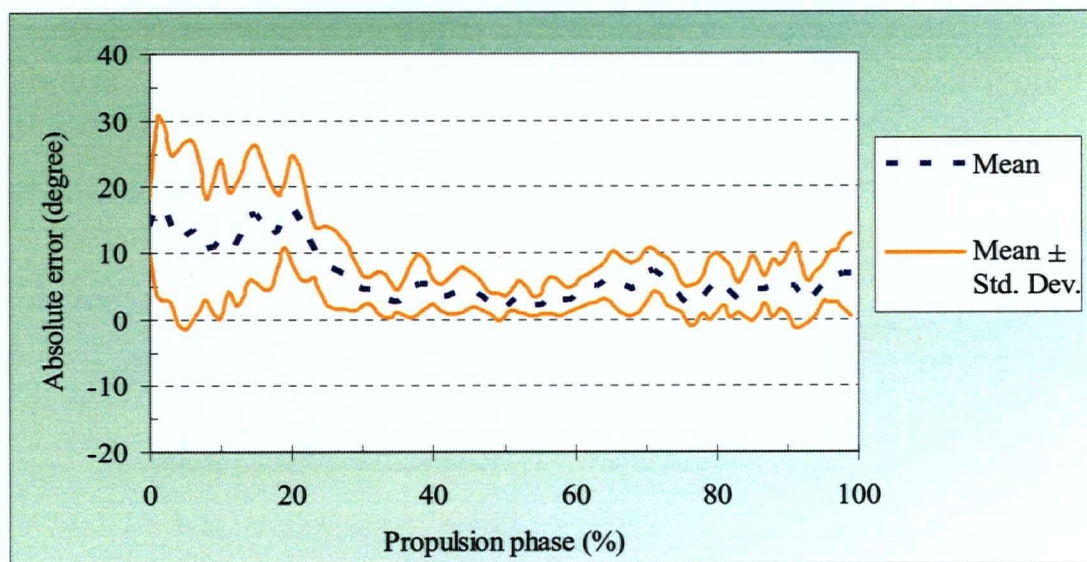


Figure 2.12 Mean absolute error and Std. Dev. for calculated φ using the kinetic method.

Now, using φ and Equation 2.6f one can calculate M_{hz} . Figure 2.14 illustrates the behavior of the global propulsive moment and the hand moment in the z direction during the propulsion phase. It can be seen that they act in opposite directions, meaning that M_{hz} reduces the propulsive moment. This situation is unavoidable and necessary for the natural stability of the propulsion.

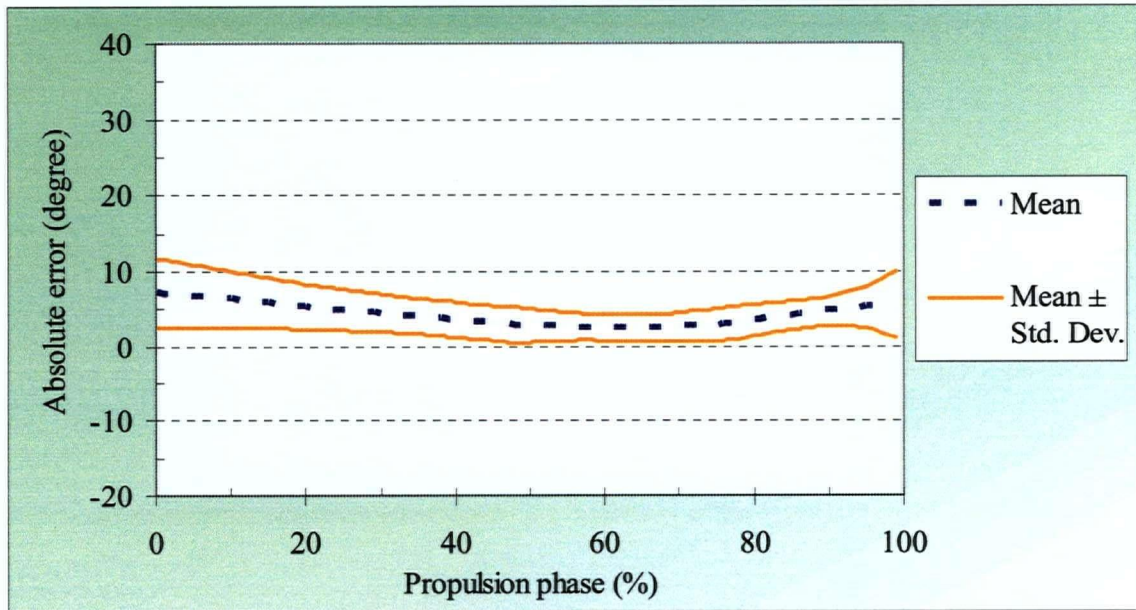


Figure 2.13 Mean absolute error and Std. Dev. for calculated ϕ using the exponential curve fit for the kinetic method.

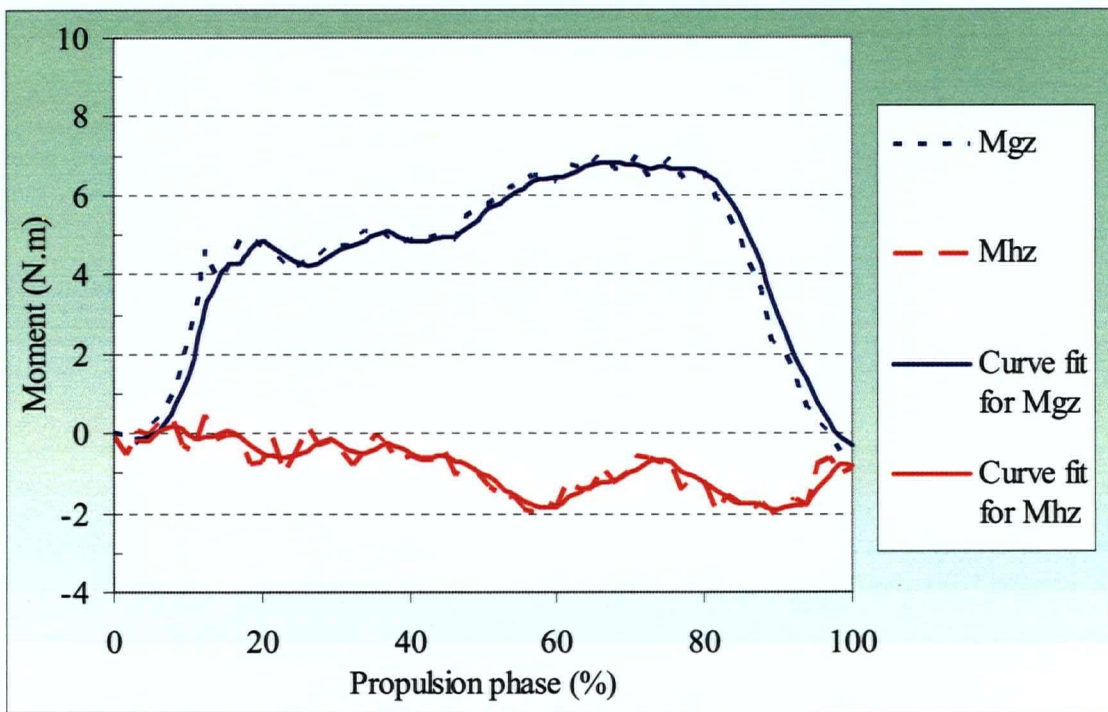


Figure 2.14 Global propulsive and hand moments in z direction.

Figure 2.15 shows the components of the user's hand moment, calculated by using the kinematic method to determine φ . The figure indicates that considering M_{hy} as zero in the kinetic method for calculating φ , is a reasonable assumption.

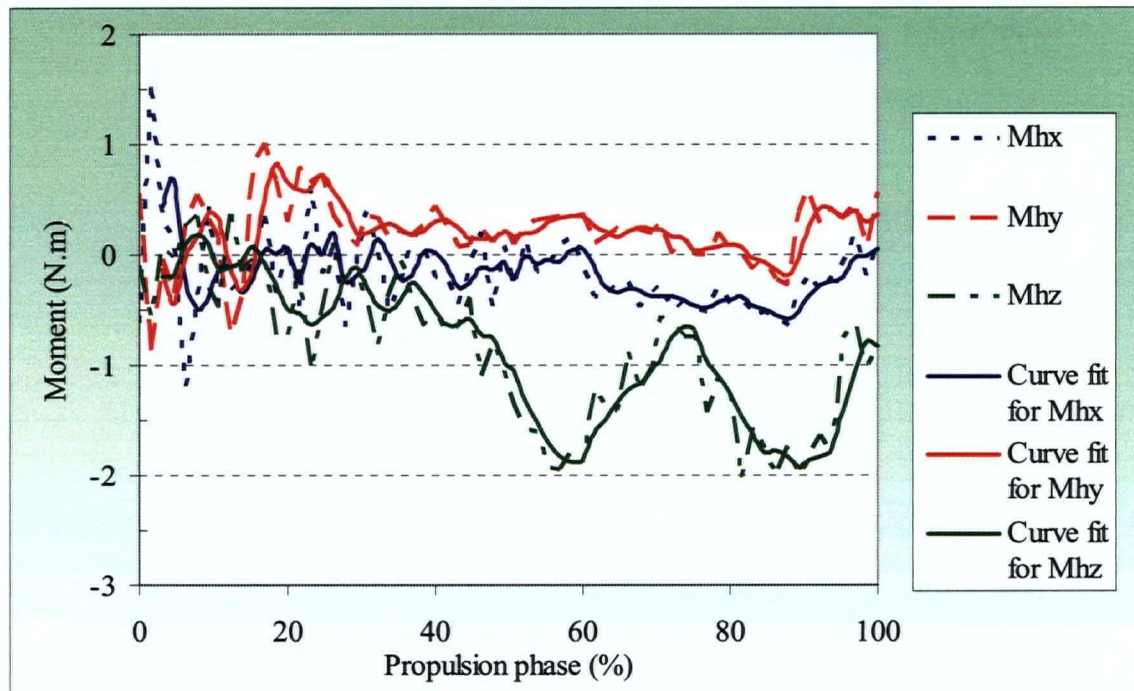


Figure 2.15 Components of the user's hand moment.

Microsoft Excel[®], MATLAB[®] and LabVIEW[™] software were used to calculate all forces, moments, and φ .

In this section, the transformation matrix between the local and global values was determined, and the applied forces and moments between the wheelchair user's hand and the handrim were calculated. The angular position of the hand on the handrim during the pushing phase was calculated by means of the kinetic parameters without using cameras or a motion analysis system. φ was validated and its mean absolute error and standard

deviation (Std. Dev.) were determined. Finally, the propulsion moment with respect to the hand coordinate system was calculated using the determined φ . The negative value of M_{hz} is significant and has been addressed by other researchers [9, 60]. This negative value shows that M_{hz} is against the propulsive moment. However, from another point of view it is believed to stabilize the transmission of loads to the handrim.

In the following section, the experimental errors of the system will be estimated using the general uncertainty method.

2.5 Uncertainty Analysis

The concept of uncertainty describes the degree of goodness of a measurement or an experimental result [61]. Kline defines uncertainty as “what we think the error would be if we could and did measure it by calibration” [62]. Uncertainty is thus an estimate of the experimental error.

Uncertainty analysis is a necessary and powerful tool, particularly when used in the planning and design of experiments. There are cases in which all of the measurements in an experiment can be made with 1% uncertainty, yet the uncertainty in the final experimental result could be greater than 50% [61]. Uncertainty analysis, used in an experiment’s initial planning phase, can identify such situations and save the researcher much time.

2.5.1 General Uncertainty Analysis

In the planning phase of an experimental program, one focuses on the general, or overall, uncertainties. Consider a general case in which an experimental result, f_0 , is a function of n measured variables Ψ_i [61]:

$$f_0 = f_0(\Psi_1, \Psi_2, \dots, \Psi_n) \quad (2.11)$$

Equation 2.11 is the data reduction equation and is used to determine f_0 from the measured values of the variables Ψ_i . The overall uncertainty in the result is then given by

$$U_{f_0}^2 = \left(\frac{\partial f_0}{\partial \Psi_1} \right)^2 U_{\Psi_1}^2 + \left(\frac{\partial f_0}{\partial \Psi_2} \right)^2 U_{\Psi_2}^2 + \dots + \left(\frac{\partial f_0}{\partial \Psi_n} \right)^2 U_{\Psi_n}^2 \quad (2.12)$$

where U_{Ψ_i} are the uncertainties in the measured variables Ψ_i .

It is assumed that the relationship given by Equation 2.11 is continuous and has continuous derivatives in the domain of interest, that the measured variables Ψ_i are independent of one another, and that the uncertainties in the measured variables are also independent of one another.

If the partial derivatives are interpreted as absolute sensitivity coefficients such that

$$\delta_i = \frac{\partial f_0}{\partial \Psi_i} \quad (2.13)$$

then Equation 2.12 can be written as

$$U_{f_0}^2 = \sum_{i=1}^n \delta_i^2 U_{\Psi_i}^2 \quad (2.14)$$

2.5.2 Uncertainty of Preloads

The general uncertainty equation for preloads is obtained by using Equations 2.12 and 2.1 as follows:

$$U_p = [(\sin(\theta + \xi))^2 U_a^2 + (a \cos(\theta + \xi))^2 U_\theta^2 + U_b^2]^{1/2} \quad (2.15)$$

where U_p represents the uncertainty for different preloads [N or N.m], U_a and U_b are the primary uncertainties for the constants a and b [N or N.m.], and U_θ is the uncertainty for the wheel angular position [radian]. Uncertainty equations for different preload components are then calculated by using Equation 2.15, as follows:

$$U_{F_{px}} = [(\sin(\theta + \xi_{F_x}))^2 U_{a_{F_x}}^2 + (a_{F_x} \cos(\theta + \xi_{F_x}))^2 U_\theta^2 + U_{b_{F_x}}^2]^{1/2} \quad (2.16a)$$

$$U_{F_{py}} = [(\sin(\theta + \xi_{F_y}))^2 U_{a_{F_y}}^2 + (a_{F_y} \cos(\theta + \xi_{F_y}))^2 U_\theta^2 + U_{b_{F_y}}^2]^{1/2} \quad (2.16b)$$

$$U_{F_{pz}} = [(\sin(\theta + \xi_{F_z}))^2 U_{a_{F_z}}^2 + (a_{F_z} \cos(\theta + \xi_{F_z}))^2 U_\theta^2 + U_{b_{F_z}}^2]^{1/2} \quad (2.16c)$$

$$U_{M_{px}} = [(\sin(\theta + \xi_{M_x}))^2 U_{a_{M_x}}^2 + (a_{M_x} \cos(\theta + \xi_{M_x}))^2 U_\theta^2 + U_{b_{M_x}}^2]^{1/2} \quad (2.16d)$$

$$U_{M_{py}} = [(\sin(\theta + \xi_{M_y}))^2 U_{a_{M_y}}^2 + (a_{M_y} \cos(\theta + \xi_{M_y}))^2 U_\theta^2 + U_{b_{M_y}}^2]^{1/2} \quad (2.16e)$$

$$U_{M_{pz}} = [(\sin(\theta + \xi_{M_z}))^2 U_{a_{M_z}}^2 + (a_{M_z} \cos(\theta + \xi_{M_z}))^2 U_\theta^2 + U_{b_{M_z}}^2]^{1/2} \quad (2.16f)$$

Tables 2.2, 2.3 and 2.4 show the values for primary uncertainties. These values were determined in static tests and on the basis of parameter resolution as reported by the manufacturer of the transducer.

Table 2.2 Primary uncertainties for measured variables.

Variable uncertainties	U_{θ} [radian]	U_{r_h} [m]	$U_{\Delta z}$ [m]
Value used	0.001745	0.001	0.001

Table 2.3 Primary uncertainties for measured loads.

Load uncertainties	$U_{F_{primx}}$ [N]	$U_{F_{primy}}$ [N]	$U_{F_{primz}}$ [N]	$U_{M_{primx}}$ [N.m]	$U_{M_{primy}}$ [N.m]	$U_{M_{primz}}$ [N.m]
Value used	1	1	2	0.4	0.4	0.2

Table 2.4 Primary uncertainties for constants.

Constant uncertainties	$U_{a_{F_x}}, U_{b_{F_x}}$ $U_{a_{F_y}}, U_{b_{F_y}}$ [N]	$U_{a_{F_z}} \& U_{b_{F_z}}$ [N]	$U_{a_{M_x}}, U_{b_{M_x}}$ $U_{a_{M_y}}, U_{b_{M_y}}$ [N.m]	$U_{a_{M_z}} \& U_{b_{M_z}}$ [N.m]
Value used	1	2	0.4	0.2

The values of $U_{F_{px}}, U_{F_{py}}, U_{F_{pz}}, U_{M_{px}}, U_{M_{py}}$ and $U_{M_{pz}}$ were calculated by using Equations 2.16 and Tables 2.2 and 2.4, when θ varies between 0° and 180° , the possible interval for the propulsion phase.

2.5.3 Uncertainty of Local Loads

The uncertainties of the local forces and moments were obtained by using Equations 2.2 and 2.16, and Table 2.3, as follows:

$$U_{F_{Lx}} = [U_{F_{px}}^2 + U_{F_{primx}}^2]^{1/2} \quad (2.17a)$$

$$U_{F_{Ly}} = [U_{F_{py}}^2 + U_{F_{primy}}^2]^{1/2} \quad (2.17b)$$

$$U_{F_{Lz}} = [U_{F_{pz}}^2 + U_{F_{primz}}^2]^{1/2} \quad (2.17c)$$

$$U_{M_{Lx}} = [U_{M_{px}}^2 + U_{M_{primx}}^2]^{1/2} \quad (2.17d)$$

$$U_{M_{Ly}} = [U_{M_{py}}^2 + U_{M_{primy}}^2]^{1/2} \quad (2.17e)$$

$$U_{M_{Lz}} = [U_{M_{pz}}^2 + U_{M_{primz}}^2]^{1/2} \quad (2.17f)$$

These uncertainties are shown in Figures 2.16 and 2.17.

The uncertainties for different outputs of the system were determined with respect to the local and global coordinate systems. The uncertainties for the preloads and local loads were calculated with the primary uncertainties for the measured variables and with Equations 2.15, 2.16 and 2.17, and the values are given in Tables 2.2, 2.3 and 2.4. The results show that there is not much difference between the uncertainties of the preloads and the local loads. Therefore, only the uncertainties of the local loads appear in the presented results.

Figure 2.16 shows the uncertainties for the local forces in the interval during which the propulsion phase can occur (from +x to -x direction of the global coordinate system). The figure indicates that F_{Lx} and F_{Lz} have their highest uncertainties (about 1.75 N for F_{Lx} and about 3.40 N for F_{Lz}) in the + y direction of the global coordinate system,

and that F_{Ly} has its highest uncertainty (about 1.75 N) in the +x and -x directions of the global coordinate system. F_{Lx} and F_{Ly} are the components of the applied force, which produces the propulsive moments. The above information indicates that the highest uncertainties for F_{Lx} and F_{Ly} are both low and acceptable.

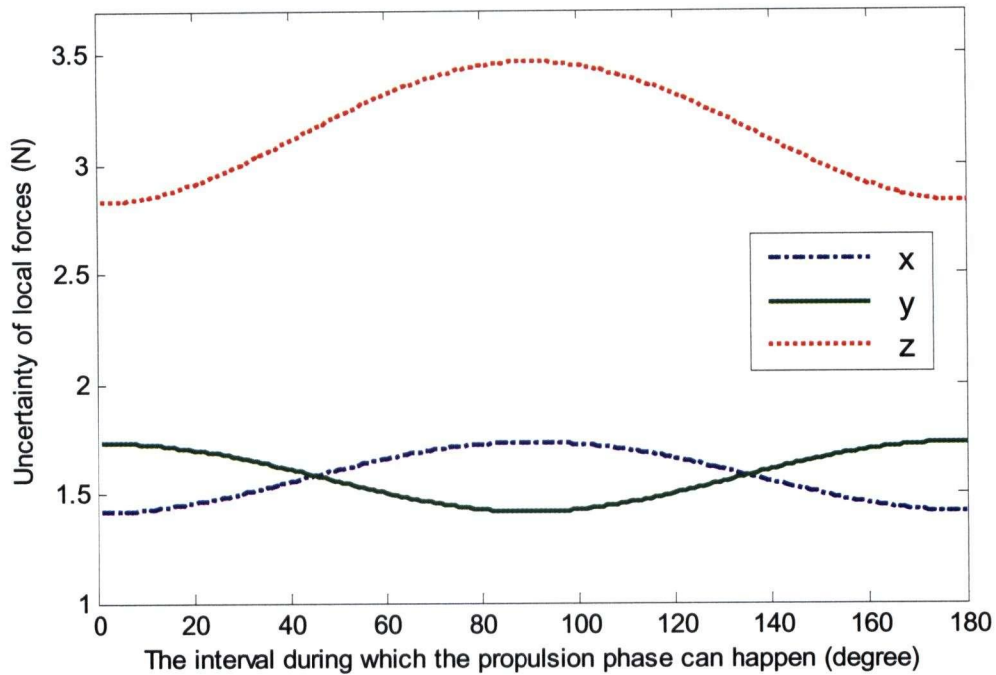


Figure 2.16 Uncertainties for local force components during possible range for propulsion phase.

Figure 2.17 shows the uncertainties for local moments in the interval during which the propulsion phase can take place (from +x to -x direction of the global coordinate system). The figure shows that M_{Ly} and M_{Lz} have their highest uncertainties (about 0.70 N.m for M_{Ly} and about 0.30 N.m for M_{Lz}) in the + y direction of the global coordinate system and that M_{Lx} has its highest uncertainty (about 0.70 N.m) in the + x

and $-x$ directions of the global coordinate system. M_{Lz} is the moment, which produces the propulsion; its highest uncertainty is comparatively very low.

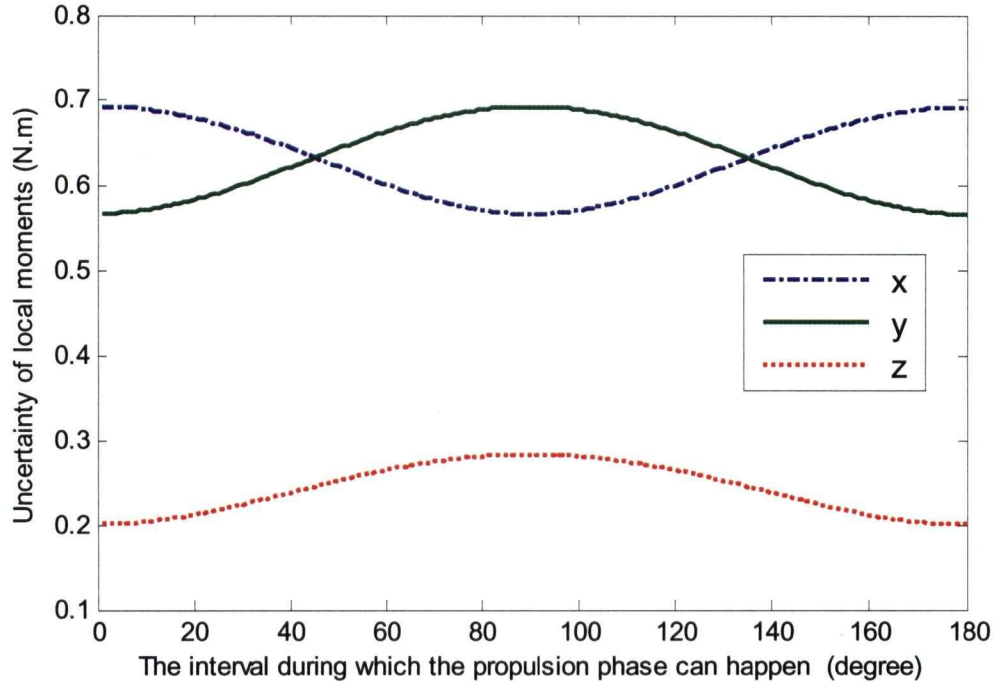


Figure 2.17 Uncertainties for local moment components during possible range for propulsion phase.

2.5.4 Uncertainty of Global Loads

The following relations were obtained by calculating F_{Lx} , F_{Ly} , F_{Lz} , M_{Lx} , M_{Ly} , M_{Lz} and $U_{F_{Lx}}$, $U_{F_{Ly}}$, $U_{F_{Lz}}$, $U_{M_{Lx}}$, $U_{M_{Ly}}$ and $U_{M_{Lz}}$ using Equations 2.2, 2.12 and 2.17, respectively, and employing Equations 2.3 and 2.12:

$$U_{F_{gx}} = [(-\sin \theta \times F_{Lx} - \cos \theta \times F_{Ly})^2 U_{\theta}^2 + \cos^2 \theta \times U_{F_{Lx}}^2 + \sin^2 \theta \times U_{F_{Ly}}^2]^{1/2} \quad (2.18a)$$

$$U_{F_{gy}} = [(\cos \theta \times F_{Lx} - \sin \theta \times F_{Ly})^2 U_{\theta}^2 + \sin^2 \theta \times U_{F_{Lx}}^2 + \cos^2 \theta \times U_{F_{Ly}}^2]^{1/2} \quad (2.18b)$$

$$U_{F_{gz}} = U_{F_{Lz}} \quad (2.18c)$$

$$U_{M_{gx}} = [(-\sin \theta \times M_{Lx} - \cos \theta \times M_{Ly})^2 U_{\theta}^2 + \cos^2 \theta \times U_{M_{Lx}}^2 + \sin^2 \theta \times U_{M_{Ly}}^2]^{1/2} \quad (2.18d)$$

$$U_{M_{gy}} = [(\cos \theta \times M_{Lx} - \sin \theta \times M_{Ly})^2 U_{\theta}^2 + \sin^2 \theta \times U_{M_{Lx}}^2 + \cos^2 \theta \times U_{M_{Ly}}^2]^{1/2} \quad (2.18e)$$

$$U_{M_{gz}} = U_{M_{Lz}} \quad (2.18f)$$

These uncertainties for the global forces and moments are shown in Figures 18 and 19. F_{Lx} , F_{Ly} , M_{Lx} , M_{Ly} and θ are the parameters calculated from the data measured in the tests.

Figure 2.18 shows the uncertainties for the local and global forces. These uncertainties were calculated for the normal propulsion phase of 80° , covering a range from 75 to 155° of the possible propulsion phase. The local uncertainties were compared with the global uncertainties in the same graph and for the same period. This figure shows that the global uncertainty of F_z is the same as its local uncertainty. The global uncertainty of F_x shows a small increase compared with the local one, but its highest value of about 1.60 N is not near the end of the propulsion phase; it reaches its highest point at about 60° into the propulsion phase. The global uncertainty for F_y shows a small decrease compared with the local value. Its highest value of about 1.70 N is around 10° after the beginning of the contact between the hand and the handrim. It decreases to a minimum at about 60° .

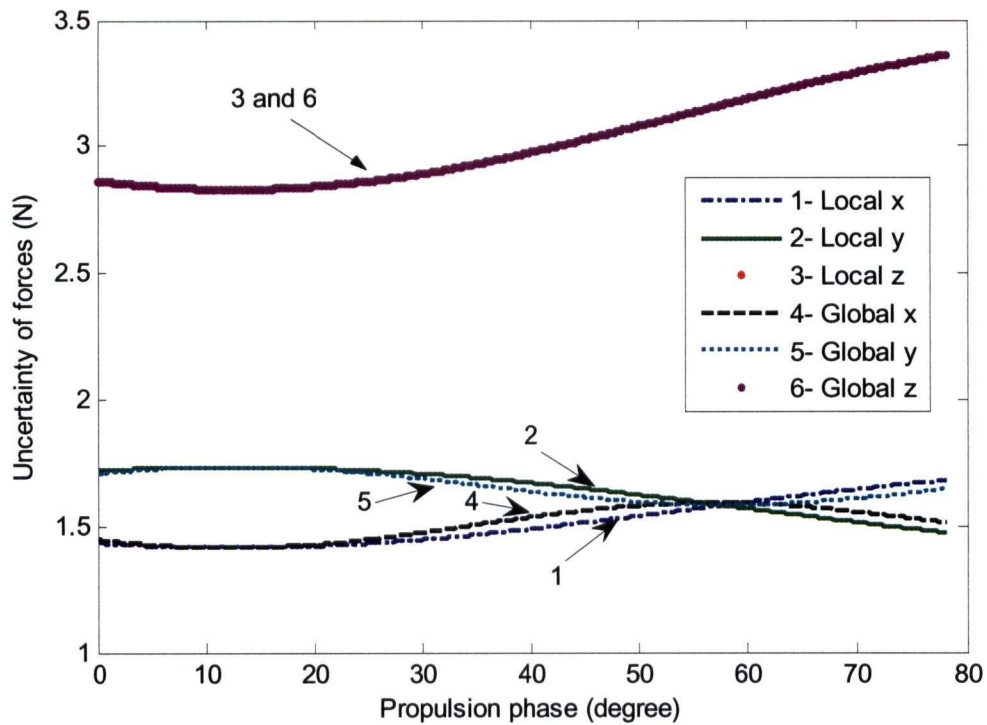


Figure 2.18 Uncertainties for local and global force components during propulsion phase.

Figure 2.19 shows the uncertainties for the local and global moments. These uncertainties were also calculated for the normal propulsion phase. This figure shows that the global uncertainty of M_z is the same as its local uncertainty. The global uncertainty of M_y shows a modest increase compared with the local values. It starts to decrease after its peak of about 0.63 N.m at around 60° after the beginning of the contact between the hand and the handrim. The global uncertainties for M_x decrease to some extent compared with the local value, whose peak value of about 0.70 N.m occurs near 10° after the beginning of the contact between the hand and the handrim. It drops to a minimum at about 60° .

Above results showed that the maximum uncertainties for the global loads appeared at early or late phases of the propulsion. In this study, the maximum applied

loads during the propulsion were calculated. These loads never occur at the early or late parts of the propulsion.

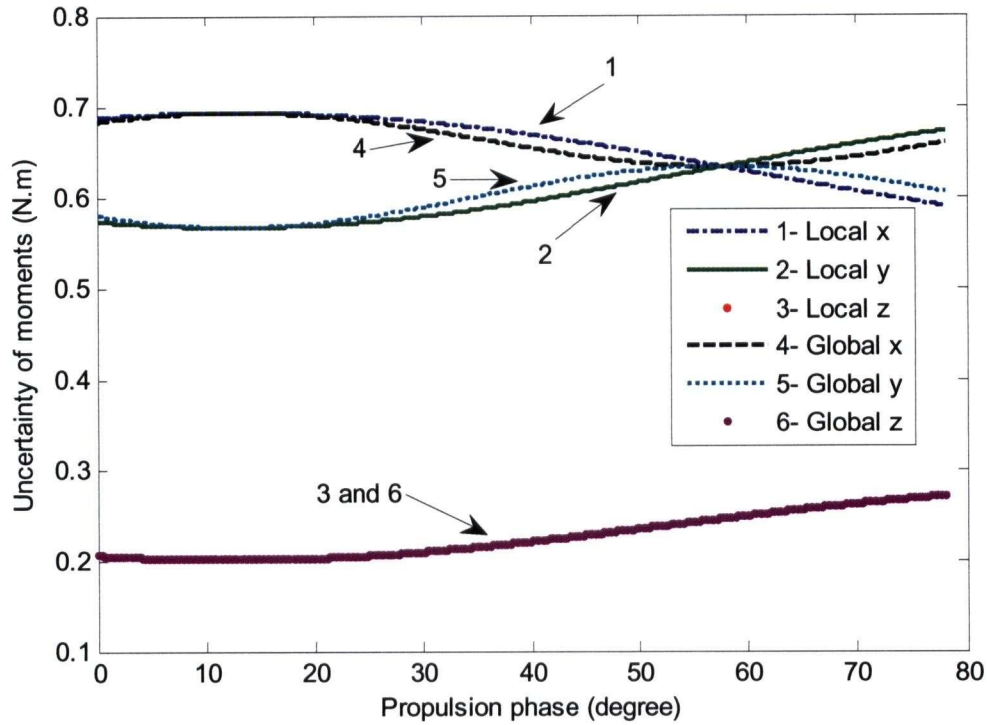


Figure 2.19 Uncertainties for local and global moment components during propulsion phase.

2.5.5 Uncertainty of φ

The uncertainty of φ is obtained using Equations 2.9 and 2.12, as

$$U_{\varphi} = \sqrt{(D_1 + D_2)} \quad (2.19a)$$

where

$$D_1 = (\partial\varphi/\partial M_{hy})^2 U_{M_{hy}}^2 + (\partial\varphi/\partial M_{gy})^2 U_{M_{gy}}^2 + (\partial\varphi/\partial F_{gx})^2 U_{F_{gx}}^2 \quad (2.19b)$$

$$D_2 = (\partial\varphi/\partial F_{gz})^2 U_{F_{gz}}^2 + (\partial\varphi/\partial \Delta z)^2 U_{\Delta z}^2 + (\partial\varphi/\partial r_h)^2 U_{r_h}^2 \quad (2.19c)$$

are lumped parameters to simplify the Equation 2.19a.

The derivatives of φ with respect to different variables are calculated as follows:

$$D_3 = \partial\varphi/\partial M_{hy} = -1/D \quad (2.20a)$$

$$D_4 = \partial\varphi/\partial M_{gy} = 1/D \quad (2.20b)$$

$$D_5 = \partial\varphi/\partial F_{gx} = -\Delta z/D \quad (2.20c)$$

$$D_6 = \partial\varphi/\partial F_{gz} = (M_{hy} - M_{gy} + F_{gx} \times \Delta z)/D \times F_{gz} \quad (2.20d)$$

$$D_7 = \partial\varphi/\partial \Delta z = -F_{gx}/D \quad (2.20e)$$

$$D_8 = \partial\varphi/\partial r_h = (M_{hy} - M_{gy} + F_{gx} \times \Delta z)/D \times r_h \quad (2.20f)$$

The lumped parameters D_{3-8} and D in Equations 2.20 are used to simplify some repetitive terms, and D is given by

$$D = \sqrt{(F_{gz} \times r_h)^2 - (M_{hy} - M_{gy} + F_{gx} \times \Delta z)^2} \quad (2.21)$$

U_φ is then determined as Equation 2.22 on the basis of Equations 2.19 and 2.20

as

$$U_\varphi = \sqrt{(D_3 \times U_{M_{hy}})^2 + (D_4 \times U_{M_{gy}})^2 + (D_5 \times U_{F_{gx}})^2 + (D_6 \times U_{F_{gz}})^2 + (D_7 \times U_{\Delta z})^2 + (D_8 \times U_{r_h})^2} \quad (2.22)$$

Using the above relations and data from measured tests, one can obtain the time-dependent uncertainty for φ . As the absolute error of the calculated φ was determined and presented in Section 2.4.5, the value of the uncertainty of φ was not calculated.

2.5.6 Uncertainty for Hand Contact Loads

Equations 2.6a–2.6f show that the forces are the same in both the second local and global coordinate systems for the hand contact with the handrim (Figure 2.18). Using Equation 2.12, the uncertainties for forces in the second local coordinate system are determined as

$$U_{F_{hx}} = U_{F_{gx}} \quad (2.23a)$$

$$U_{F_{hy}} = U_{F_{gy}} \quad (2.23b)$$

$$U_{F_{hz}} = U_{F_{gz}} \quad (2.23c)$$

Knowing the uncertainties for r_h and Δz , and calculating the other required uncertainties, one can obtain the uncertainties for the moments with respect to the local hand coordinate system as follows:

$$U_{M_{hx}} = [U_{M_{gx}}^2 + (r_h \sin \varphi)^2 U_{F_{gz}}^2 + (F_{gz} \sin \varphi)^2 U_{r_h}^2 + (F_{gz} r_h \cos \varphi)^2 U_{\varphi}^2 + \Delta z^2 U_{F_{gy}}^2 + F_{gy}^2 U_{\Delta z}^2]^{1/2} \quad (2.24a)$$

$$U_{M_{hy}} = [U_{M_{gy}}^2 + (r_h \cos \varphi)^2 U_{F_{gz}}^2 + (F_{gz} \cos \varphi)^2 U_{r_h}^2 + (F_{gz} r_h \sin \varphi)^2 U_{\varphi}^2 + \Delta z^2 U_{F_{gx}}^2 + F_{gx}^2 U_{\Delta z}^2]^{1/2} \quad (2.24b)$$

$$D_9 = U_{M_{gx}}^2 + (r_h \sin \varphi)^2 U_{F_{gz}}^2 + (F_{gz} \sin \varphi)^2 U_{r_h}^2 + (F_{gz} r_h \cos \varphi)^2 U_{\varphi}^2 \quad (2.24c)$$

$$D_{10} = (r_h \cos \varphi)^2 U_{F_{gz}}^2 + (F_{gz} \cos \varphi)^2 U_{r_h}^2 + (F_{gz} r_h \sin \varphi)^2 U_{\varphi}^2 \quad (2.24d)$$

$$U_{M_{hz}} = [D_9 + D_{10}]^{1/2} \quad (2.24f)$$

As the results of the tests presented low values for hand moments (Figure 2.15), their uncertainties were not calculated.

In the next section, the instrumented wheel system is verified by using an experimental technique, and system specifications are determined by applying statistical methods.

2.6 System Verification

To obtain the degree of reliability of the results obtained from the designed and fabricated instrumented wheel, an experimental technique was used to determine the system specifications by performing static and dynamic tests. Four different setups were used for these tests, and both qualitative and quantitative analyses were conducted. Pearson correlation and coefficient of variation techniques were used to determine linearity and repeatability, respectively, as key system specifications. Also, the error for quantitative analysis was estimated. Three different angular velocities were used in the dynamic tests. The static and dynamic tests were performed at different levels of loading on the handrim at four different loading positions.

2.6.1 Experimental Setup

The following four different loading setups were used: a first vertical loading for static tests, a second vertical loading for static tests, a horizontal loading for static tests, and a dynamic loading.

2.6.1.1 First Vertical Loading Setup

The first vertical loading setup for static tests was used to apply the selected vertical loads at four loading points (one at a time) when they were placed in turn at the loading position of point 1 (Figures 2.20 and 2.21) on the handrim. Points 1 and 2 were at the intersections of a horizontal line passing through the handrim and its center. A loading disk was connected via a wire cable to the handrim with a clamp. Six different weights (22.27, 44.48, 66.76, 89.04, 111.50 and 133.30 N) were used in this setup. The level of resolution for the weights depends on the resolution of the sensor—in our case, 0.01 N. The range of weights covers the typical loads applied on the handrim during the propulsion. The first local coordinate system, which is attached to the load transducer, turned in unison with points 2, 3 or 4, when they turned into the position of point 1. Rotation of the wheels during the static loading was prevented by locking the shaft of one of the rollers.

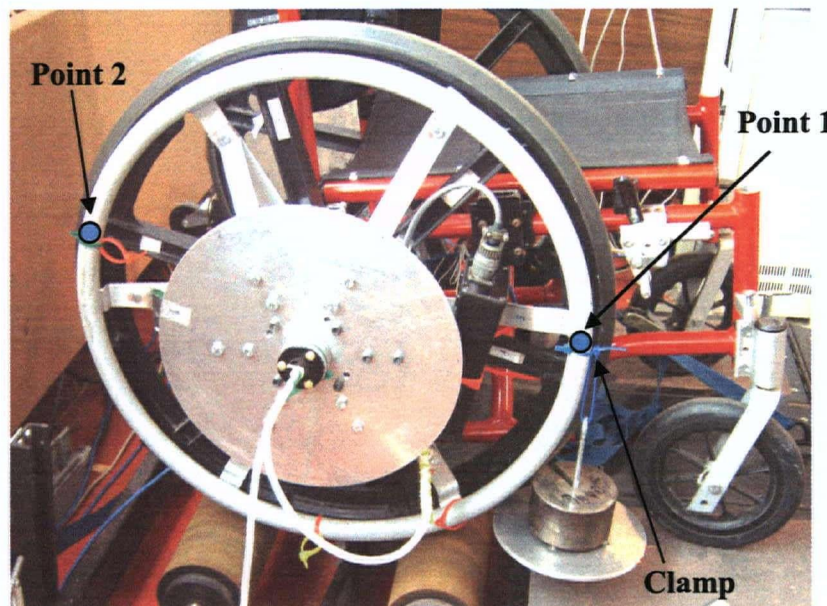


Figure 2.20 First vertical loading setup for static tests.

2.6.1.2 Second Vertical Loading Setup

The second vertical loading setup for static tests applied the selected vertical loads at the four points when they were placed at the position of point 3 (Figure 2.21) on the handrim. Points 3 and 4 were at the intersections of the handrim and a vertical line passing through its center. A load-holding disk was hung from a horizontal bar 2 m in length and 1.5 cm in diameter. One side of the bar was hung from the handrim using a rope so that only a normal load was transmitted. The other side of the bar rested perpendicularly on a bar 2 cm in length and 0.5 cm in diameter, which itself rested on a smooth horizontal surface. This combination provided a rolling effect and eliminated horizontal frictional loads on the long bar due to deformation and shortening of its span after loading. The set of six weights used in this setup was the same as the set used in the initial vertical loading setup.

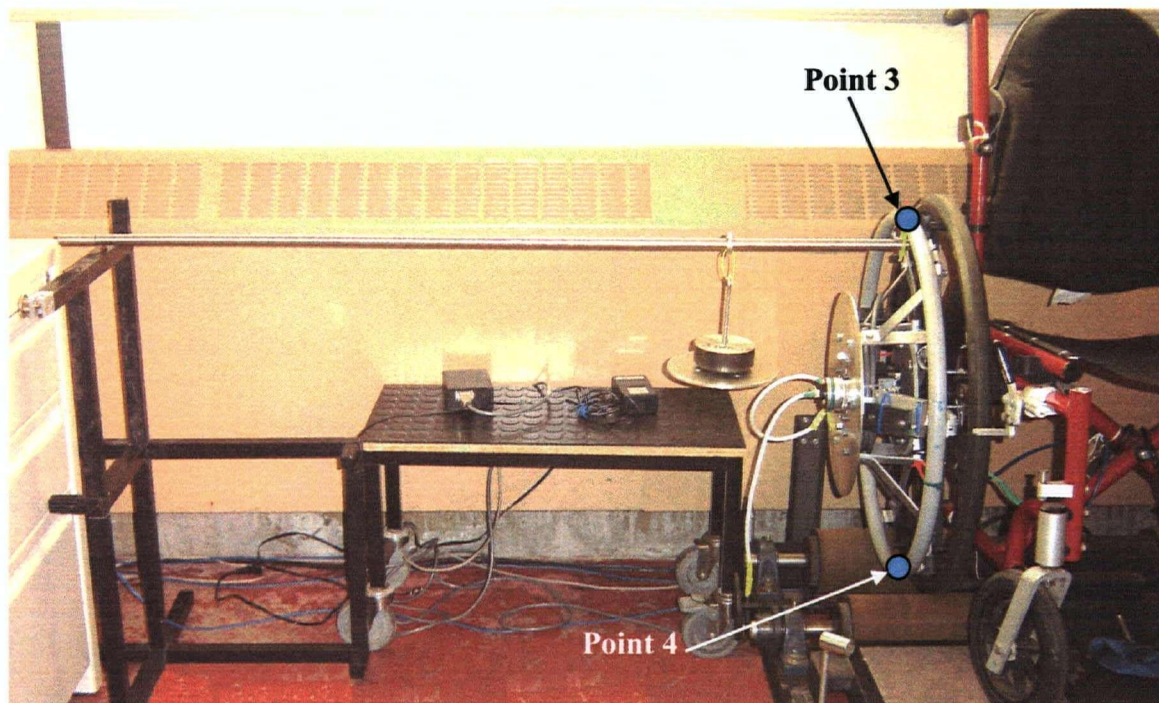


Figure 2.21 Second vertical loading setup for static tests.

2.6.1.3 Horizontal Loading Setup

The horizontal loading setup was used to apply horizontal static test loads at four different points located 90° apart from each other on the handrim's outer circumference. In fact, these were the same four points used in the previous tests. Four loading points were used to cover the entire circumference of the handrim. These points were at the intersections of the x and y axes of the first local coordinate system and the handrim, and were used to apply pure axial loads. A loading disk was connected to the loading point on the handrim through a pulley using a 2 mm wire cable (Figure 2.22). Six different weights (4.50, 9.02, 13.49, 16.41, 19.31 and 22.23 N) were used in this setup for each point. During manual wheelchair propulsion, the subject applied a lower load in the direction of the axle of the wheel compared with the loads in the plane of the wheel. Therefore, we used a new set of the loads in the horizontal static tests.

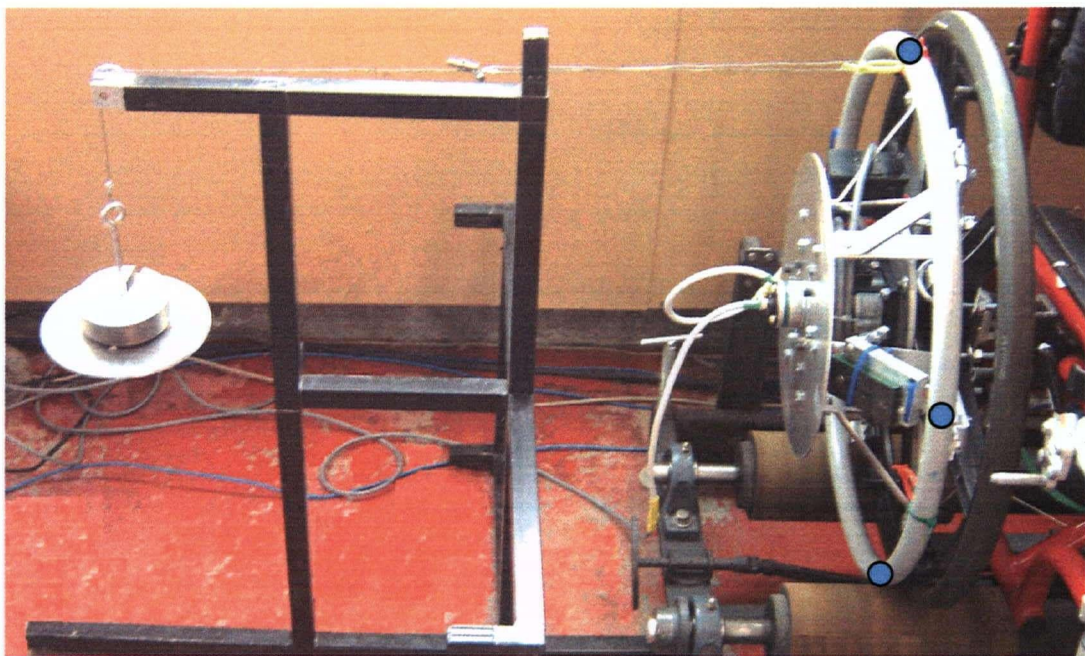


Figure 2.22 The horizontal loading setup for static tests.

2.6.1.4 Dynamic Loading Setup

The dynamic loading setup applied centrifugal test forces at four loading points, which were also the same as the loading points in the static setups. Three different weights (4.50, 8.95 and 13.39 N) were used as loads. The loads were attached individually to the handrim's lateral surface with a very powerful magnet (Figure 2.23). The AC motor was used to mechanically turn the wheel at three different speeds.

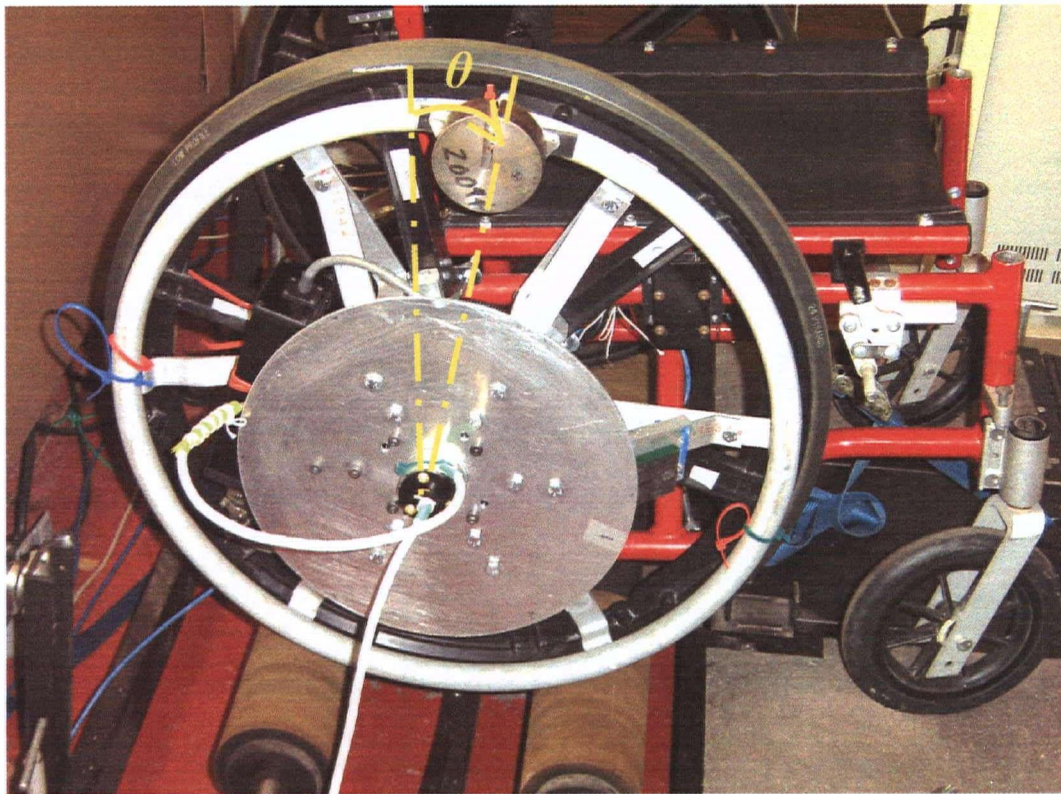


Figure 2.23 The dynamic loading setup.

Increasing the number of weights, loading points and tests can yield more data for different parts of the system, but it also increases the calculation time. Therefore, the

number of weights, loading points and tests were chosen such that proper statistical analysis could be performed within a reasonable time and with sufficient accuracy. The test loads were not meant to reproduce the level of the loads applied by the wheelchair user.

2.6.2 Verification Tests Protocol

After the design and fabrication of the instrumented wheel and determining the transformation equations for the applied forces and moments [56], the system had to be verified. For this purpose, both qualitative and quantitative analyses were performed for the output of the experiments. Two of the most important system specifications for qualitative analysis—linearity and repeatability— were determined using Pearson correlation and descriptive analysis, respectively. The error for the quantitative analysis was also estimated. Given the dynamic nature of the real situations, both static and dynamic conditions had to be considered to verify the system.

2.6.2.1 Static Verification

To verify the system under static conditions, the wheelchair was placed on and securely strapped to the roller-rig. Three different test setups, described in Section 2.6.1, were used to apply loads in three different directions (x , y and z) of the first local coordinate system (Figure 2.2). For vertical loading in the static tests, six different weights (22.27, 44.48, 66.76, 89.04, 111.50 and 133.30 N) were suspended independently from points 1,2,3 and 4 on the handrim circumference using two vertical loading setups (Figures 2.20 and 2.21). The loading positions were 90° apart in the $-x'$, $-y'$, x' , and y'

directions of the first local coordinate system (Figure 2.2). The baseline of the load holding disk's own weight was measured by performing a no-load test, and the results subtracted from the measured loads accordingly. Measurements were repeated three times at four different loading points with respect to the first local coordinate system.

To determine the specifications for qualitative analysis, the Pearson correlation coefficient (r) was used, which is defined as

$$r = b_0 \times (s_x / s_y) \quad (2.25)$$

where s_x and s_y are the standard deviations of the independent and dependent variables and the value b_0 is determined as

$$b_0 = \sum_{i=1}^N \left(\frac{(x_i - \bar{x})(y_i - \bar{y})}{(N-1)s_x^2} \right) \quad (2.26)$$

where x_i is the case value for the independent variable, \bar{x} is the mean of the independent variable, y_i is the case value for the dependent variable, \bar{y} is the mean of the dependent variable, N is the number of cases and s_x^2 is the variance of the independent variable [63]. In this study, dependent variables are the measured forces and moments and independent variables are the applied loads at different loading points.

The Pearson correlation coefficient method was used to obtain the linearity of the system. The coefficient of variation was used for all different tests to determine system repeatability, and to compare the variability of different parameters with different units.

The coefficient of variation expresses the standard deviation as a percentage of the mean. This allows one to compare the variability of different parameters. The coefficient of variation is given by

$$\text{Coefficient of variation} = \left(\frac{\text{standard deviation}}{\text{mean}} \right) \times 100 \quad (2.27)$$

where *mean* is the mean of the variable of interest.

To determine the specifications of the instrumented wheel from the quantitative analysis, the actual values were compared with the measured values. SPSS[®] 11.0 and Microsoft Excel[®] software were used to analyze the data and calculate the system specifications. All *r* values were calculated by using the results of the first series of tests.

Table 2.5 shows *r* due to static verification. The “Position” column gives the different load application points, and the “Channel” row gives different measurements. The values of *r* show high linearity (above 0.9) at different loading points and for different measuring channels in the static situation.

Table 2.5 Pearson correlation coefficient *r* (static verification).

Channel \ Position	F_x	F_y	F_z	M_x	M_y	M_z
1	1.000	1.000	0.999	1.000	1.000	1.000
2	1.000	0.994	0.998	0.993	1.000	0.985
3	1.000	1.000	0.997	1.000	1.000	1.000
4	1.000	1.000	0.999	1.000	1.000	1.000

Table 2.6 shows the mean of the percentages of the coefficient of variation for different measured loads at the four loading points. The “Load” column gives the different loading forces used during the tests. The loads differ for channel F_z because they did not reach high values during propulsion. These values indicate low coefficients of variation (less than 2%), and were calculated using the measured values of the three different tests. The entries in Tables 2.6 show high repeatability of the instrumented wheel. Tables 2.5 and 2.6 present the results for the qualitative analysis and collectively show reliable values for system specification. The average of the results from three series of the repeated tests has been used to calculate the mean errors.

Table 2.6 Mean coefficient of variation of measured loads (%; static verification).

Channel Load (N)	F_x	F_y	M_x	M_y	M_z	Channel Load (N)	F_z
22.273	0.110	0.166	1.547	1.784	0.133	4.50	1.736
44.482	0.045	0.147	1.545	0.398	0.166	9.02	1.293
66.755	0.059	0.174	1.401	0.289	0.082	13.49	0.863
89.043	0.070	0.053	1.314	0.355	0.067	16.41	0.747
111.504	0.102	0.117	1.192	0.381	0.563	19.31	0.895
133.299	0.096	0.106	0.234	0.485	0.117	22.23	1.325

Table 2.7 presents the results of the quantitative analysis and lists the mean errors of the measured forces and moments as percentages of the loads. The values indicate low mean error (mostly less than 5%) for different loads on all channels. Some errors were

expected because of the effect of other sources of errors, such as human or experimental errors. The low levels of the errors indicate that the parameters measured by the instrumented wheel are reliable.

Table 2.7 Mean errors as percentage of loads (static verification).

Channel Load (N)	F_x	F_y	M_x	M_y	M_z	Channel Load (N)	F_z
22.273	0.857	0.070	1.608	2.969	0.344	4.504	3.572
44.482	0.583	0.291	8.422	4.556	0.113	9.015	1.374
66.755	0.640	0.144	2.586	1.088	0.179	13.489	2.037
89.043	0.576	0.170	1.922	1.420	0.081	16.406	2.680
111.504	0.726	0.074	3.187	0.881	0.259	19.308	3.718
133.299	0.666	0.097	3.383	0.614	0.128	22.225	7.401

The results of qualitative and quantitative analyses for the instrumented wheel in the static situation show a reliable range of the values for all system specifications.

2.6.2.2 Dynamic Verification

Dynamic verification was more challenging than static verification. The local coordinate system of the transducer spun with the wheel and the loadings were weights, so the loads (in the global coordinate system) could not be measured directly. An encoder was used to determine the position of the load attached to the wheel with respect to the global coordinate system. The wheelchair was placed on the roller-rig, and the AC motor

rotated the driving roller. Three different angular velocities (3.0, 3.8, and 4.8 [rad/s]) were used for the dynamic tests to cover the wheeling speeds of the user. Three different weights (4.50, 8.95 and 13.39 N) and one powerful magnet were used for loading at points 1 to 4 (Figures 2.20, 2.21 and 2.22) on the handrim lateral surface. The loading positions were the same as for the static verification tests. The measured forces and moments of three successive cycles were used to verify the system repeatability. The baseline of the attachment's own weight was set to zero by using the method described in the static verification tests. The actual values were compared with the measured values to obtain the specifications for quantitative analysis. The actual values were determined using the inverse dynamics method. The angular motion of the loaded wheel was considered in the vertical plane, where the centripetal force, F_s was determined as

$$F_s = m_w r_h \dot{\theta}^2 + m_w g \quad (2.28)$$

Here, m_w is the mass of the weight that was attached to the wheel, r_h is the moment arm (handrim radius), $\dot{\theta}$ is the wheel angular velocity and g is the acceleration of gravity. There was no force component in the z direction because the object had a planar motion (x-y) and the wheel camber angle was zero with respect to the global coordinate system. The x and y planar components are as follows:

$$F_{sx} = m_w r_h \dot{\theta}^2 \sin \theta \quad (2.29a)$$

$$F_{sy} = m_w r_h \dot{\theta}^2 \cos \theta - m_w g \quad (2.29b)$$

where θ is the angular position of the wheel (or load for these tests), and $F_{s-x,y}$ are the components of the centripetal force.

Equations 2.25, 2.26 and 2.29 were used to determine the specifications for qualitative analysis in the dynamic tests with three different angular velocities.

As the nature of the manual wheelchair propulsion is dynamic, qualitative and quantitative analyses were performed for the instrumented wheel under dynamic situations. These analyses were carried out for three different angular velocities (3, 3.8 and 4.8 rad/s).

Table 2.8 shows the Pearson correlation coefficient for the tests conducted. These values mostly show high correlation (r above 0.9) between different angular velocities and loadings implying very good linearity. Channel F_z was not considered for dynamic verification because there was no appreciable load on this channel, due to the nature of dynamic loading.

The values in Tables 2.9 show a low mean coefficient of variation for different measured loads (less than 4%) at four loading points, and high repeatability of the instrumented wheel. Tables 2.8 and 2.9 show the results of the qualitative analysis. They indicate reliable values for system specification in the dynamic verification tests.

The mean errors produced by the instrumented wheel as a percentage of loads are presented in Table 2.10 (quantitative analysis). The low mean error values (mostly less than 6%) indicate that, the parameters measured by the instrumented wheel are equally reliable for the dynamic situations.

Table 2.8 Pearson correlation coefficient r (dynamic verification).

Channel Position	F_x	F_y	M_x	M_y	M_z
$\dot{\theta}=3$ rad/s					
1	1.000	1.000	0.999	1.000	1.000
2	1.000	1.000	1.000	1.000	0.992
3	1.000	1.000	1.000	0.997	0.998
4	1.000	1.000	0.993	1.000	0.987
$\dot{\theta}=3.8$ rad/s					
1	1.000	1.000	0.999	1.000	1.000
2	0.999	1.000	0.999	0.996	0.982
3	1.000	1.000	0.994	1.000	0.995
4	1.000	1.000	0.996	1.000	0.989
$\dot{\theta}=4.8$ rad/s					
1	1.000	1.000	0.993	0.985	1.000
2	0.998	1.000	0.993	0.989	0.991
3	1.000	1.000	0.998	1.000	0.989
4	0.997	1.000	0.999	0.999	0.991

Table 2.9 Mean coefficient of variation of measured loads (%; dynamic verification).

Channel Load (N)	F_x	F_y	M_x	M_y	M_z
$\dot{\theta}=3$ rad/s					
4.50	2.170	1.467	1.547	0.967	0.842
8.95	1.871	1.752	1.236	1.226	0.144
13.39	1.230	0.954	0.638	0.761	0.115
$\dot{\theta}=3.8$ rad/s					
4.50	2.511	3.196	2.892	1.475	0.445
8.95	2.144	1.498	2.781	1.915	0.300
13.39	1.054	0.968	0.896	0.937	0.078
$\dot{\theta}=4.8$ rad/s					
4.50	3.986	3.404	2.191	3.051	0.844
8.95	2.529	1.604	2.247	3.695	0.456
13.39	1.691	0.856	3.380	1.721	1.347

Table 2.10 Mean errors as percentage of loads (dynamic verification).

Channel Load (N)	F_x	F_y	M_x	M_y	M_z
$\dot{\theta}=3$ rad/s					
4.50	5.675	7.724	3.276	4.514	4.395
8.95	6.532	6.820	1.924	5.227	6.005
13.39	6.723	7.038	2.944	6.878	5.638
$\dot{\theta}=3.8$ rad/s					
4.50	4.115	4.833	3.762	4.116	3.134
8.95	5.581	6.636	4.798	2.867	5.530
13.39	7.430	6.909	5.579	3.259	5.640
$\dot{\theta}=4.8$ rad/s					
4.50	5.837	6.200	3.079	6.189	4.643
8.95	5.675	7.211	5.794	4.329	4.300
13.39	5.590	8.079	2.281	3.467	4.639

Given the actual performance for the instrumented wheel and its measurements, Figures 2.24 and 2.25 show the measured and predicted values for F_x , F_y , M_x , M_y and M_z with respect to the global coordinate system. As mentioned previously, F_z was not considered in the dynamic measurements because there was no significant load on this channel due to the nature of loadings for dynamic tests. These figures show that the patterns of the measured and predicted curves of the data for forces and moments are highly compatible with typical results measured by other researchers [49].

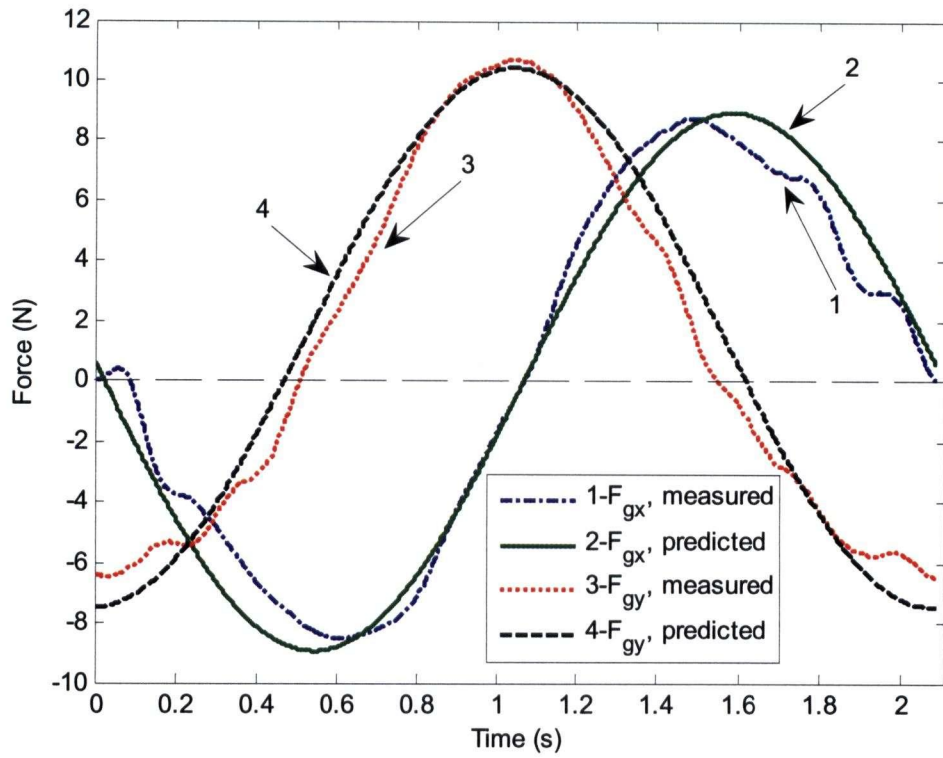


Figure 2.24 Measured and predicted global sample force components.

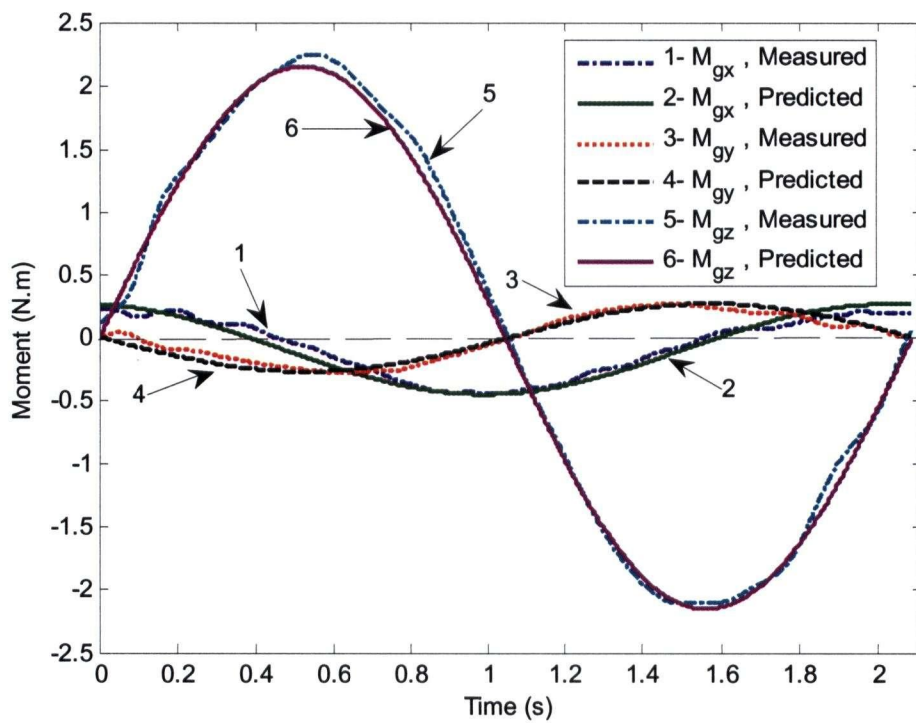


Figure 2.25 Measured and predicted global sample moment components.

2.7 Conclusions

In this chapter, a general uncertainty analysis was performed to determine the uncertainty equations for the local and global forces and moments, the local hand forces and moments, and the hand-contact angular position in MWP. The uncertainty values for the local and global forces and moments and the hand-contact forces were then calculated. The results provided an estimation of the errors and uncertainty in the output of the instrumented wheel. The uncertainties were found to vary from 1.40 to 3.40 N for the local forces and from 0.20 to 0.70 N.m for the local moments. The maximum and minimum of the uncertainties for global values were about the same as the uncertainties for the local values, but the patterns of variation were different. Uncertainties determined by Cooper et al. [52] for the forces and moments are in the range of 1.1–2.5 N and 0.03–0.19 N.m in the plane of the handrim, and 0.93 N and 2.24 N.m in the wheel axle direction, respectively. Our results show uncertainty for the forces and moments in the range of 1.40–1.70 N and 0.58–0.68 N.m in the plane of the handrim, and about 3.40 N and 0.25 N.m in the wheel axle direction, respectively. For our system, however, the uncertainty values for the important load components, namely the planar forces and the axial moment, are low. The absolute error for hand-contact position was determined as $\pm 3^\circ$ or ± 1 cm for most of the propulsion phase. Cooper et al. reported uncertainties between 1.8° and 16° for the hand-contact position using their Smart^{Wheel} [52].

A complete experimental technique was designed and performed under different static and dynamic conditions to determine the specification of the instrumented wheel. The verification techniques, which were highlighted and demonstrated step-by-step, can be implemented in similar wheelchair instrumentation setups. The results of the static and

dynamic tests were used for both qualitative and quantitative analyses to determine the system specifications. The static tests showed high linearity (r above 0.9), very low standard deviation (mostly close to zero) and a low mean coefficient of variation for measured loads (less than 2%). These results indicate high repeatability and low mean error (mostly less than 5%) due to the different loading for all load channels. Two cells of Table 2.6 show mean errors above 5%, with one at the maximum horizontal load. Usually, the horizontally applied loads are not so high during manual wheelchair propulsion, and the main idea is that the users try to apply planar loads. Therefore, the system is not proportionally responsive to higher horizontal loading due to its structure, but it had mean errors less than 5% for all other lower horizontal loadings. The other mean error above 5% corresponded to M_x . All of the mean errors for this column were close to 2% or more. Generally, higher values of the mean error (%) were obtained for M_x compared with the mean errors (%) for the other channels. Dynamic tests were performed at three angular velocities and at four loading positions for all measuring channels. The results also showed high linearity (r above 0.9). The low mean coefficient of variation for measured loads (less than 4%) confirmed high repeatability (reliability) of the instrumented wheel. The results showed that most of the mean errors were around 5%. The resultant specifications showed high linearity, repeatability and a low percentage for errors.

The results presented in this chapter collectively show that it is possible to reliably obtain the essential information required for manual wheelchair propulsion analysis, including the applied forces and moments, using the designed and fabricated instrumented wheel. The tests with one able-bodied subject reproduced patterns and

overall behavior comparable to the available data, ensuring that the system can be used for the designed experiments. It is worth emphasizing that a system developed in-house allows flexibility in enhancing the experimental scope.

The instrumented and verified wheel can now be used to determine the kinetic aspects of wheelchair propulsion. Varying the seat position with respect to the wheel axle affects all the forces and moments, as well as the mechanics, of propulsion. Determining and prescribing optimum positions is expected to reduce pain and help prevent injury of manual wheelchair users, and may improve the gross mechanical efficiency of propulsion.

In the next chapter, the proposed indices for efficiency and injury assessment of MWP are described. These indices are used as criteria to determine the optimum wheelchair variables.

CHAPTER 3

Efficiency and Injury Assessment

3.1 Introduction

Previous studies have reported a low value of about 10% for the efficiency of Manual Wheelchair Propulsion (MWP) [22]. The Gross Mechanical Efficiency (GME) for human movement is defined as the ratio of the work accomplished to the amount of the corresponding Metabolic Energy Expenditure (MEE) [23]. However, few studies have focused on the mechanical factors only and have not considered the physiological aspects of the MWP in calculating the efficiency [64].

Although the reasons for this low efficiency have not been sufficiently addressed in many studies [8, 65,66], Veeger, et al. [8] reported that it can be partially attributed to nonoptimal tuning of the wheelchair to the functional abilities of the user. Braking torques at the start and end of the propulsion phase [21], and suboptimal direction of the propulsion force [8] are reported as the other possible causes for the low efficiency of

MWP. Whereas, de Groot et al. [9] reported that even the applied tangential force acting in the optimal direction tends to decrease GME because of the conflict that was explained in Section 1.5.1.

Injuries due to MWP are usually consistent with pain. It has been determined that the pain is a limiting factor in the daily activities for MWUs [67]. Roach et al. [68] developed the Shoulder Pain and Disability Index (SPADI) to quantify shoulder pain and difficulties during the functional activities in an ambulatory population. Curtis et al. [67] developed the Wheelchair User's Shoulder Pain Index (WUSPI) to measure the severity of the shoulder pain associated with functional activity in the individuals who use wheelchairs. SPADI and WUSPI are in fact 38-item and 15-item questionnaires, respectively. A score is given for the response to each item. The higher the total score, the greater pain interference of activities. These indices do not measure pain intensity, but pain interference.

Wheelchair Propulsion Strength Rate (WPSR) is a reported injury index and is the ratio of the joint moment generated during propulsion and during the maximum isometric strength test in different directions [17]. It has been hypothesized that larger values of this ratio indicates a high risk of injury.

In this chapter, a new index for efficiency assessment during MWP is proposed. This index uses the heart rate of the subject as a factor to estimate the variation of the MEE. This is followed by developing two new injury indices to estimate the level of the probable injury due to MWP.

3.2 Efficiency Assessment

Wheelchair-user system is a combination of a mechanical device and a human body. A major requirement for reliability of the efficiency assessment for MWP is to consider both physiological and mechanical aspects of the motion. Measuring the oxygen uptake is one way of estimating MEE, but some of the subjects may feel uncomfortable to have the device on their face during the tests, which may affect their natural performance. Finding an alternative method could be helpful for some of the studies that have above consideration for the subjects or do not have access to the respective equipment. However, one should consider that the calculated results using the heart rate can be used for within-subject analysis.

In Section 1.5.4, we reviewed some studies, which reported that the physiological cost of the body can be predicted by measuring heart rate. Figure 3.1 shows the variation of heart rate versus time, during the start, performance and finishing a steady-state exercise [39]. Area 2 represents the total number of the subject's heartbeats above the resting level during the steady-state phase of the test. The area 2 is determined by subtracting the numbers of heartbeats during the exercise from the resting level, multiplied by the seconds of the test period. In this study, the area 2 will be determined for the tests. While the areas 1 and 2 represent the total heartbeats during the exercise above the resting level, the areas 1, 2 and 4 show the total number of the heartbeats during the exercise, including the resting level. Area 3 represents the extra heartbeats during the recovery phase. Areas 3 and 5 together represent the total heartbeats during the recovery. The resting heartbeats during the exercise and recovery are defined by areas 4 and 5, respectively.

Gross Mechanical Efficiency (GME) considers the biological aspects of the manual wheelchair propulsion [9], and is defined as

$$\text{Gross Mechanical Efficiency} = \text{Useful Energy Out} / \text{Metabolic Energy Expenditure}$$

or:

$$\text{GME} = \bar{M}_z \cdot \Delta\theta / \text{MEE} \quad (3.1)$$

where \bar{M}_z is the average propulsive moment applied on the hub of the wheel, and $\Delta\theta$ is the angular displacement of the wheel; both during the test period.

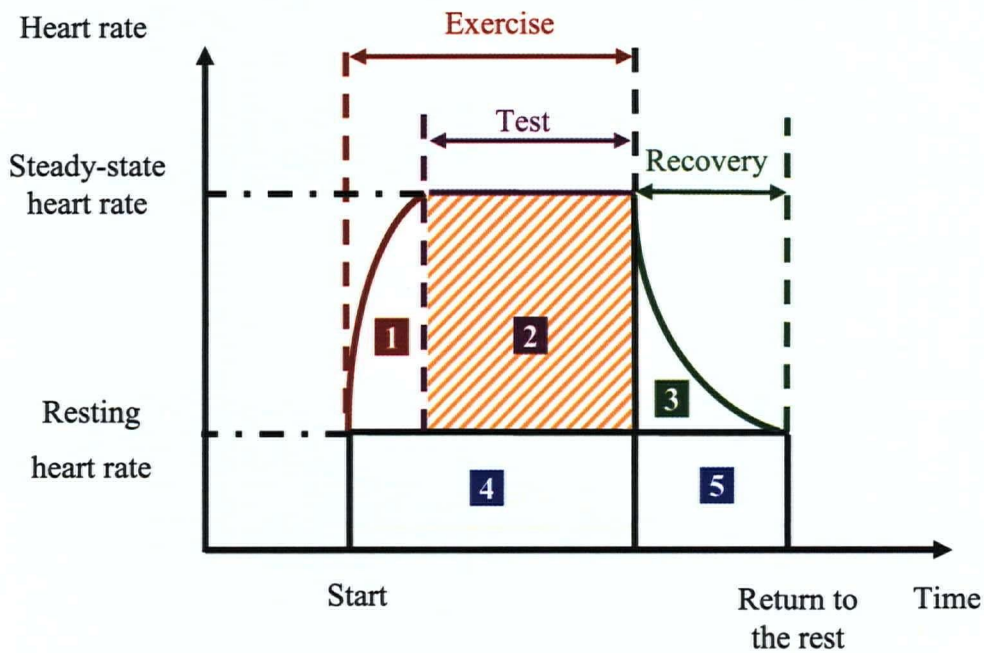


Figure 3.1 Variation of heart rate versus time, from start to completion of a steady-state exercise and back to rest (inspired by [39]).

Methodology— The linear relationship between the heartbeats and the oxygen uptake profile for steady state and non-steady state situations allows us to use an alternative and convenient method for measuring MEE. We prefer the heart rate measurement over oxygen uptake measurement because it is more comfortable, cheaper and the equipment is lighter. Continuous heart rate monitoring is now possible with the development of portable heart rate monitors.

We have proposed Equivalent Biomedical Index (EBI) for efficiency assessment, which reflects the behavior of GME and is given by

$$\text{Equivalent Biomedical Index} = \text{Useful Energy Out} / \text{Total Heartbeats}$$

or:

$$\text{EBI} = \bar{M}_z \cdot \Delta\theta / \text{THB} \quad (3.2)$$

where THB is the area 2 in Figure 3.1.

A comparison of the Equations 3.1 and 3.2 shows that their numerators are the same and their denominator have linear relationship with one another. Therefore, EBI can reflect the behavior of GME.

3.3 Injury Assessment

The referenced studies in Chapter 1 indicated that MWP is associated with injuries. To predict probable injuries during MWP, two injury indices were proposed. These indices consist of the important factors that may lead to injury.

As reported by other researchers, higher applied forces and moments on the handrim may increase the risk of RSI or over-use injury [17,69]. Therefore, the applied forces and moments can be considered as key factors that can cause the injury.

It has been reported that the subject's weight is related to pushrim forces and the median nerve function [23]. Also, previous studies have shown that the Body Mass Index (BMI) is significantly related to the shoulder injury [70,71]. BMI is based on the anthropometric data of the subject and can be considered as another factor in injury assessment.

As it is assumed that repetitive motion puts a person at the risk of RSI, therefore the pushing frequency of the MWU has direct influence on the wheelchair user's joint injury. Boninger et al. [35] suggested that decreasing the frequency of propulsion may help to prevent median nerve injury and thus CTS.

Methodology—Wheelchair User Joint Injury Index (WUJII) is our first proposed injury index and reflects a value that is representative of the level of possible MWU joint injury. A general idea for linking WUJII to the above factors can be expressed as

$$WUJII \equiv F_m \cdot M_m \cdot BMI \cdot f_p \quad (3.3)$$

Variables F_m and M_m are the maximum total force and moment applied on the hub of the wheel during the propulsion phase, respectively, and f_p is the pushing frequency.

BMI is defined as

$$\text{BMI} = m_s / h_s^2 \quad (3.4)$$

where m_s and h_s are the mass and the height of the subject, respectively.

Substituting Equation 3.4 in Equation 3.3, WUJII is related to individual parameters as follows:

$$\text{WUJII} \equiv F_m \cdot M_m \cdot f_p \cdot m_s / h_s^2 \quad (3.5)$$

To be able to compare this index between different subjects, the index is normalized with respect to the subject arm length (anthropometric parameter), and the total weight of the subject and the wheelchair, which affect the applied moment and force on the upper limb's joints:

$$\text{WUJII} = \frac{\frac{F_m}{W_t} \cdot \frac{M_m}{W_t \cdot L_a} \cdot f_p \cdot m_s}{h_s^2} \times 100 \quad (3.6a)$$

$$\text{or} \quad \text{WUJII} = \frac{F_m \cdot M_m \cdot f_p \cdot m_s}{W_t^2 \cdot h_s^2 \cdot L_a} \times 100 \quad (3.6b)$$

where L_a is the arm length, and W_t is the weight of the user and wheelchair combined. The index was multiplied by 100 to avoid presenting the values as a percentage. A pre-test showed small numerical value of the index without using a hundred as a coefficient.

WUJII can be used for estimating the injury at the shoulder, elbow or wrist joints by using the joint loads instead of the applied loads in Equation 3.6b. The modified form is presented as

$$\text{WUJII}_i = \frac{100 \cdot m_s \cdot f_p \cdot F_{mi} \cdot M_{mi}}{W_i^2 \cdot h_s^2 \cdot L_{ai}} \quad (3.7)$$

$i = 1,2,3$

Variable i represents the corresponding joint as follows: 1-shoulder, 2-elbow, and 3-wrist. F_{mi} and M_{mi} are the maximum total force and moment applied on the joint i during the propulsion, and L_{ai} is the length of the upper limb segments connected to the distal part of the joint i , such that L_{a1} is the total length of the arm and hand, L_{a2} is the total length of the forearm and the hand, and L_{a3} is the length of the hand.

As BMI is not a perfect index for all cases (compare BMI between two persons, who have the same height and weight but one has more fat, and the other has stronger muscles), WUJII' is proposed by using calculated %BF as equations 3.8a and 3.8b for general form and the joints injury analysis, respectively.

$$\text{WUJII}' = \frac{100 \cdot \%BF \cdot f_p \cdot F_m \cdot M_m}{W_i^2 \cdot L_a} \quad (3.8a)$$

$$\text{WUJII}'_i = \frac{100 \cdot \%BF \cdot f_p \cdot F_{mi} \cdot M_{mi}}{W_i^2 \cdot L_{ai}} \quad (3.8b)$$

$i = 1,2,3$

Percentage of Body Fat is the ratio of the fat to the total body mass, and therefore is unitless. A variety of techniques have been developed to measure this parameter such

as using calipers (skinfold measurements - anthropometry), bioelectrical impedance analysis, hydrodensitometry weighting, near-infrared interactance, magnetic resonance imaging, computed tomography, total body electrical conductivity, and Dual Energy X-ray Absorptiometry (DEXA)[72–80].

The hand-held caliper that exerts a standard pressure was used in the previous studies for SCI subjects, and the skinfold thickness was measured at following body locations: Triceps, Biceps, Subscapula and Supraspinale [72–74]. In this study, the same method and measuring sites were used.

Linear regression equation for the estimation of body density (kg/m^3) has been reported by Durnin et al. [75] as follows:

$$\text{Density} = A_0 - B_0 \times \log S_{total} \quad (3.9)$$

where A_0 and B_0 are the constants and their values differ for different genders and ages, and S_{total} is the sum of the skinfold measurements at four sites. In the same report, %BF has been determined as

$$\%BF_{(\text{skinfold})} = \left(\frac{4.95}{\text{Density}} - 4.50 \right) \cdot 100 \quad (3.10)$$

where $\%BF_{(\text{skinfold})}$ is the value of %BF that is measured by using the skinfold method.

Maggioni et al. [73] reported that measured %BF for people with spinal cord injury using the skinfold method is under-estimated. They introduced Equation 3.11 that shows the relationship between %BF calculated by the skinfold and DEXA methods.

DEXA is known as the best method to determine %BF. In this study, the values of %BF were modified by using the following equation as

$$\%BF_{(DEXA)} = 1.45 \cdot \%BF_{(Skinfold)} + 2.58 \quad (3.11)$$

where %BF_(DEXA) is the value of %BF that is measured by using the DEXA method.

Wheelchair velocity has also been reported as a factor that can affect the efficiency of MWP [4]. Veeger et al. [8] performed manual wheelchair exercise tests on a stationary ergometer for nine able-bodied subjects and determined that GME increases with lower tangential velocities of the handrim, whereas another study reported that propulsion speed slightly lower than the freely chosen speed is energy efficient [38].

In this study, to verify the effect of velocity on the indices, several tests were performed, which are described in the next chapter. It was found that the injury indices increase by raising the Average Linear Wheelchair Velocity (would be referred as velocity) during the propulsion phase. Considering the dependency of the injury indices on the velocity, the relations of the injury indices were modified to include the velocity as one of their parameters. This allows the injury indices to be stand alone measures for the level of possible joint injury due to MWP. The modified injury indices for general evaluation are then stated as

$$WUJII = \frac{100 \cdot F_m \cdot M_m \cdot f_p \cdot \bar{V}_l \cdot m_s}{W_t^2 \cdot h_s^2 \cdot L_a} \quad (3.12)$$

$$WUJII' = \frac{100 \cdot \%BF \cdot f_p \cdot \bar{V}_l \cdot F_m \cdot M_m}{W_t^2 \cdot L_a} \quad (3.13)$$

where \bar{V}_l is the symbol that represents the velocity.

To determine the level of the possible injury at the joints, the modified injury indices are given by

$$WUJII_i = \frac{100 \cdot m_s \cdot f_p \cdot \bar{V}_l \cdot F_{mi} \cdot M_{mi}}{W_t^2 \cdot h_s^2 \cdot L_{ai}} \quad (3.14)$$

$$i = 1,2,3$$

$$WUJII'_i = \frac{100 \cdot \%BF \cdot f_p \cdot \bar{V}_l \cdot F_{mi} \cdot M_{mi}}{W_t^2 \cdot L_{ai}} \quad (3.15)$$

$$i = 1,2,3$$

The units of WUJII and WUJII' are kg/(m.s²) and m/s², respectively.

The risk of the injury may increase with higher values of WUJII or WUJII'. The effects of changing the seat position on the proposed indices were investigated in this research. The minimum value for each injury index corresponds to the optimum seat position. We think that WUJII' can be a more realistic index and will discuss it more in Chapter 5.

3.4 Chapter Summary

Most of the previous research on the efficiency assessment has been conducted for sport wheelchairs, and some did not consider the physiological aspects of MWP. All

of the previous studies about MWP that we found have used oxygen uptake to determine MEE for efficiency assessment.

Two reported indices in the previous studies measure the interference of the pain, and they are based on questionnaires. Previous reported injury index was based only on the joint moments during MWP and the maximum isometric strength of the muscles. This injury index does not consider the other factors like the applied force, the frequency of the propulsion, and the weight of the subject that have effects on the injury during MWP.

In this chapter, a new index was presented for efficiency assessment of MWP. The use of the subject's heart rate in the proposed index represents the biological factors. EBI was considered as a good alternative to estimate the efficiency of MWP because it uses the heartbeats of the user to estimate the variation of the MEE. Measuring the heartbeats by using the newly developed heart rate monitors is cheaper, more comfortable and the required equipment is lighter.

To measure the level of the possible injuries, two indices were proposed. The general forms of the indices determine the level of the probable injury totally at the upper limb of the subject. The indices were modified to be used for injury assessment at each joint of the upper body of the user. Also, there is a choice of using BMI or %BF to calculate the injury indices.

In the next chapter, the test procedures are explained and the calculated values of the proposed indices are given. The sensitivities of the indices are verified, and the optimum seat positions for two users are determined by presenting the values of the indices in 3D graphs.

CHAPTER 4

Optimum Seat Position

4.1 Introduction

The wheelchair-user interface, based on the design and settings of the wheelchair and the physical and habitual characteristics of the user, will affect the pattern of the applied loads, cardio-respiratory factors, kinetic and kinematic parameters, pushing angle, pushing frequency, and joint loads during MWP [13,17,19,35,36,81]. Inappropriate settings can lead to RSI [82]. Furthermore, the results from at least one study have confirmed the possibility of reducing, or even eliminating, back pain and discomfort related to wheelchair seating by individually adjusting the settings of the subjects' wheelchair ($p < 0.001$) [83]. Actually they did not explain their adjustment procedure. Also, another study presented a significant relationship between the wheelchair seat's tilt angle and the biomechanical efficiency [84].

Determining the optimal seating positions for MWUs is a major challenge for researchers. Masee et al. [85] found a low position to be optimal for smoother upper limb motion, less electromyogram (EMG) activity and lower pushing frequency, while another study reported greater upper limb motion in a low position [86], and Kotajarvi et al. [11] did not find lower pushing frequency at the low seat height positions. These contradictions imply that more work is required in this area.

In this chapter, a new method for determining the optimum seat position for a user is described, followed by explaining the experimental setup and a subject model. Also, the optimum seat position is determined using an analytical method, and the reliability of the indices are investigated by sensitivity analysis. Four research questions concerning the optimum seat position and the relationship between linear wheelchair velocity and the proposed indices are addressed.

4.2 Modeling and Analysis Approach

The data acquired from this study covers the kinetic, kinematic, and part of the anthropometric and physiological information for the subject group of the manual wheelchair users. The above parameters were measured and/or monitored using several devices and instruments that we provided in the Human Measurement Studio at the Institute for Computing, Information and Cognitive System (ICICS), the University of British Columbia (UBC). All measurements were taken at the same time to acquire synchronized data. A medical student assisted in the measurement of the heart rate, blood pressure and the %BF of the subjects.

The following method was devised and applied to determine the optimum seat position for each user by analyzing the calculated values of the indices at different seat positions. The subsequent sections of this chapter describe in details the study population, study design, test protocol, setup and modeling.

4.2.1 An Overview

In this research, new injury and efficiency indices were proposed as criteria to determine the optimum wheelchair variables for each manual wheelchair user. To accomplish these, the parameters that are measurable and have significant effect on the factors in the proposed indices were investigated. Possible wheelchair parameters are the horizontal and vertical positions of the seat with respect to the wheel axle, the backrest position or angle, the seat angle, the footrest position and the camber angle of the wheels. Choosing the proper parameters depends on the situations and characteristics of different wheelchairs. If the specifications of the wheelchair are flexible enough for setting and measuring these variables, and the subjects can handle the requirements of the tests, one can use the new method with different combinations of the parameters listed above to determine the optimum position.

In this study, the vertical and horizontal positions of the seat with respect to the wheel axle were considered as the adjustable variables of the seat position, which have significant effects on the factors in the proposed indices. The lower and upper bound values of the seat position can be different for various manual wheelchairs.

4.2.2 Study Population

This study was approved by the Clinical Research Ethics Board at UBC (Appendix). Subjects were recruited through a database provided by Dr. Bonita Sawatzky and the Spinal Cord Injury Research Registry at the GF Strong Rehabilitation Center (Vancouver, BC). All of the subjects were of legal age (> 18 years) and they signed a consent form. Subjects were provided with a \$50 honorarium upon completion of the protocol to primarily cover transportation related expenses.

All of the subjects met the inclusion and exclusion criteria for the study. The inclusion criteria for the subjects in this study were as follows:

- Males with a spinal cord injury for longer than one year.
- Age between 19 and 59 years.
- Height ideally between 160 and 190 cm.
- Dominant right hand side.
- Fit into a 16" wide wheelchair or use the same size wheelchair.
- Can independently use a manual wheelchair for 50% of the day.

Potential subjects were excluded from this study if they:

- had been previously diagnosed with any kind of heart or lung disease.
- had lesion level higher than the sixth thoracic vertebrae (T6; see Section 1.5.4).
- had significant shoulder pain during wheeling.
- have had surgery within three months prior to the tests.
- were unable to transfer themselves independently from their wheelchair to the test wheelchair.

In Chapters 1 and 3, the linear relationship between the heart rate and MEE was explained. Also, it was discussed that among SCI subjects, this linear relationship only works for the individuals with lesions at T6 or lower.

Eight adult male MWUs (n= 8) participated in this study. Demographic data are given in Table 4.1.

Table 4.1 Demographic data for the manual wheelchair user subjects.

Subject code	Gender	Age (years)	Diagnosis	Level of lesion
1	M	52	Paraplegia	T11-12
2	M	27	Paraplegia	T10
3	M	20	Spina Bifida	Lumbar
4	M	48	Paraplegia	T10
5	M	59	Paraplegia	T11-12
6	M	49	Paraplegia	T6-7
7	M	24	Paraplegia	T6
8	M	34	Paraplegia	T10

M = Male; T_n = The nth thoracic vertebrae.

4.2.3 Study Design

In this research, the relationship between the proposed indices and the seat position for eight MWUs were analyzed and their sensitivity was evaluated. To do this, experiments were designed and implemented in two categories: 1- Fixed seat position; 2- Constant wheelchair velocity.

In the fixed seat position tests, the experiments were performed at three different velocities for all subjects in search of a meaningful relationship between the indices and the velocity for MWUs.

In the constant velocity tests, the experiments were performed at two vertical and three horizontal positions of the seat (six tests) for all subjects, to conduct sensitivity analysis and to verify the possibility of establishing some generic rules to estimate the optimum seat positions for all users. Performing at least nine tests enables one to acquire the required data for a response surface, which relates the indices to the seat position. To determine the response surface, two subjects participated in nine tests. The methodology is elaborated in Section 4.3.

4.2.4 Test Protocol

First, the study procedure was explained in detailed and an easy to follow format to the subjects, and they were asked to sign the ethical consent form. Some individuals with spinal cord injury have a condition known as “Autonomic Dysreflexia (AD)”, which affects their heart rate if the bladder is full [87,88]. Although, we chose subjects with lesion levels below T5, which is the cut off level for a possibility of AD, we still asked the subjects to void their bladders before the tests. This was considered as a matter of convenience for testing, as well as to prevent its probable effects on the blood pressure, and to avoid distraction during the tests. The subjects’ anthropometric data (height, arm length, joint circumference, and hand width) were measured. They were asked to stretch their arms straight to the sides such that the distance from the tip of their left middle finger to the tip of right middle finger can be measured. This measurement is a good

representative of the height of a subject, which is normally hard to measure in seated individuals. Previous studies have reported a high correlation (0.73–0.89) between the arm-span and height for different genders and ethnicities [89,90]. The subjects' %BFs were determined using a caliper for skinfolds test at Triceps, Biceps, Subscapula and Supraspinale. The measurements were taken three times and the average values were used. Then using a custom made scale the weights of the wheelchair users were obtained. Ten semi-spherical passive markers were attached to the upper limb and trunk landmarks, and two markers were attached to the instrumented wheel (Figure 4.1). The markers reflected the infrared waves emitted from the six surrounding cameras of an advanced Motion Analysis System (VICON). The joint positions and the motion of the upper limb of the subjects were determined by tracking the markers through the VICON system and a digital camcorder. All measurements were non-invasive.

The subjects wore sleeveless shirts (tank top) during the tests. They transferred themselves onto the stationary instrumented test wheelchair. As part of subject calibration for the motion analysis system, they were asked to take a "T" pose (stretch arms horizontally) for a few seconds; and turn their upper limb segments starting from their hand, forearm, and upper arm around their joints for about a minute in front of the cameras.

The base line of the heart rate and the blood pressure of the subjects were measured just prior to the tests (Figure 4.1). The wheelchair seat could be positioned at three vertical positions (Y1, Y2 and Y3) and three horizontal positions (X1, X2 and X3) (Figure 4.2). There were two different sets of the tests. In the first set, three velocities of 0.9, 1.1 and 1.3 m/s were used, at a fixed position (X2 and Y2) for eight subjects. The

selected velocities are typical wheeling velocities for MWUs. In the second set, the tests were performed at a fixed velocity of 0.9 m/s. In this category, the tests were conducted at six different combinations resulting from two incremental vertical seat positions (Y1 and Y2) and three incremental horizontal seat positions (X1, X2 and X3) for all eight subjects. Two subjects had three more tests at three different combinations of the seat position (X1, X2, and X3; all at Y3). A speedometer measured the speed of the wheelchair. The order of the tests was selected randomly for each subject. The magnitude of X1, X2, and X3 were 11, 14, and 17cm, and Y1, Y2, and Y3 were 15, 18, and 20cm with respect to wheel axle, respectively. X values were negative. Figure 4.2 illustrate these positions with respect to the wheel axle.



Figure 4.1 A subject on the instrumented wheelchair and roller-rig during blood pressure measurement. The marker on the left hip is not shown.

To change the seat position, it was necessary for the subjects to transfer themselves in and out of the wheelchair a number of times. Each test took 3 minutes and the data was collected during the final minute of the test. The subjects rested between the tests, and prior to each test their heart rate and blood pressure were measured to ensure they had returned to the baseline levels.

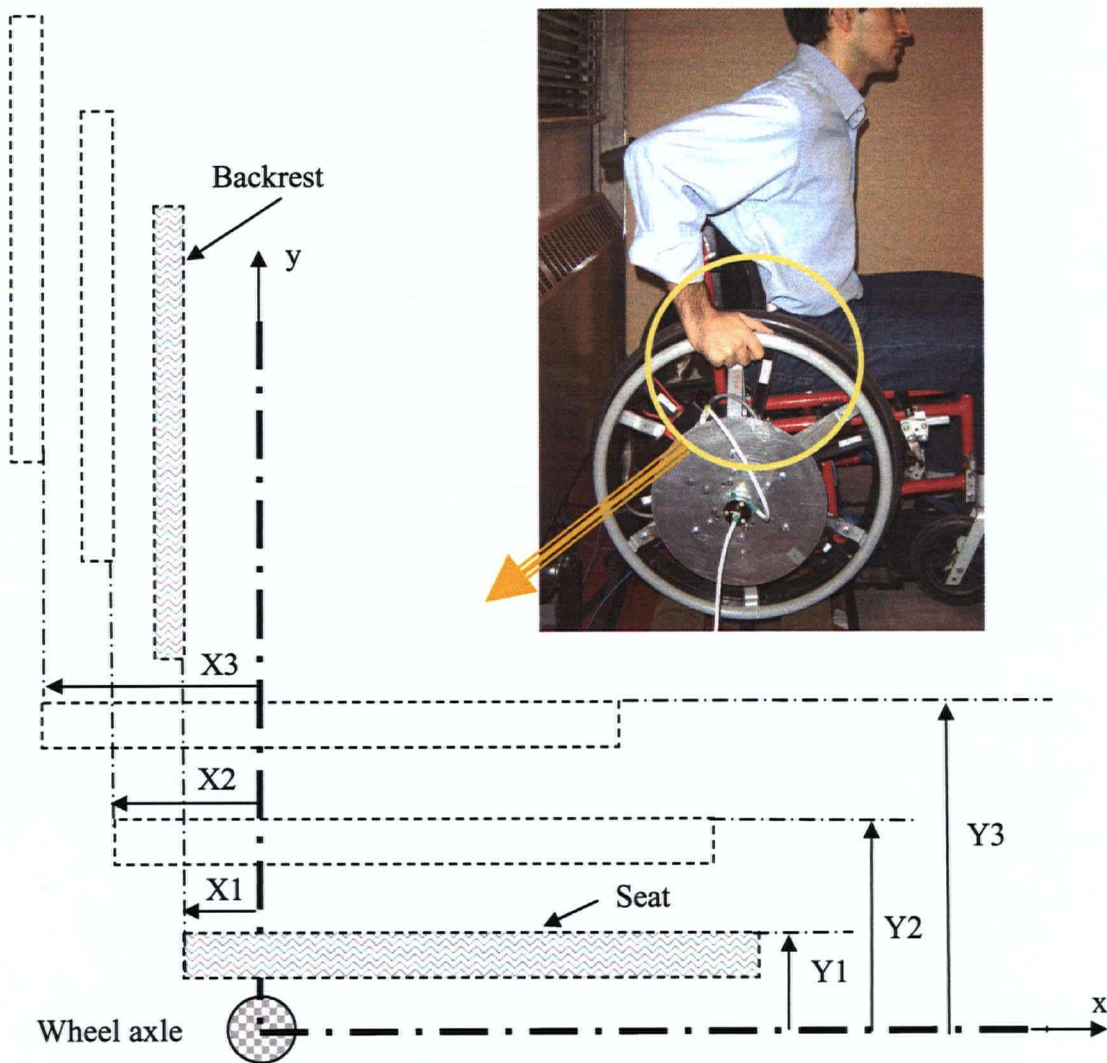


Figure 4.2 Possible seat and backrest positions. The seat position is set at X_1 and Y_1 in this figure. Dimensions are not to scale.

The forces and moments that the subjects apply during propulsion are needed for the analysis, and were measured with the instrumented wheel. During the tests, the heart rate, and the kinetic and kinematic data of the subjects were recorded, simultaneously.

4.2.5 Anthropometric Data

The anthropometric dimensions of the upper limb were obtained using a tape measure. A platform was designed for this study to determine the weight of the subjects as well as the weight of the instrumented wheel, separately (see Section 4.2.6.6). BMI and %BF were calculated using the Equations 3.4 and 3.11, respectively.

4.2.6 Experimental Setup

In this study, it was necessary to measure a number of physical and biological parameters; therefore several devices were used to acquire such data. The wheelchair, the instrumented wheel, the roller-rig and the two computers for kinetic data acquisition were described in Chapter 2. This section outlines the rest of the equipment used.

4.2.6.1 Motion Analysis System

©VICON Motion Analysis System was used to acquire the kinematic data. VICON is equipped with infrared cameras, which are more accurate compared with the conventional video cameras (Figure 4.3).

To conduct a 3D kinematic study of the upper body during MWP, at least four cameras are necessary for a good all around coverage of the subject for data acquisition, with less possibility of any marker being missed. Figure 4.4 illustrates a schematic view

of the multi-camera setup. We used six cameras in our tests to have more confidence in covering all landmarks and to ensure redundancy in data acquisition.

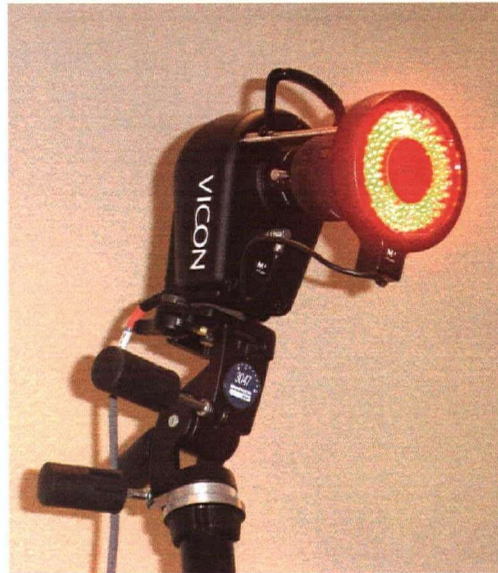


Figure 4.3 VICON infrared camera.

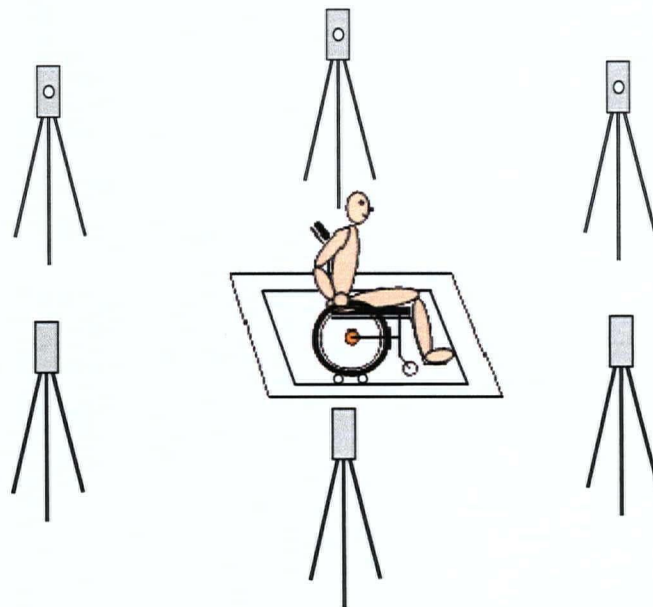


Figure 4.4 Positions of six infrared cameras, a subject, the wheelchair and the roller-rig for stationary MWP.

4.2.6.2 Heart Rate Monitor

A heart rate monitor (HR-Polar S610TM) was used to measure the heart rate of the subjects. This was one of the data required to determine EBI for the subjects (Figure 4.5).



Figure 4.5 HR-polar heart rate monitor: (a) Heart rate sensor and transmitter; (b) recorder.

4.2.6.3 Blood Pressure Monitor

An automatic blood pressure monitor (© 2005 A&D Medical) was used to determine the blood pressure of the subjects at rest and prior to each test (Figure 4.6).



Figure 4.6 Blood pressure monitor.

4.2.6.4 Fat Caliper

Skinfold tests were performed using a Slim Guide fat caliper (SLIMGUIDE®) to determine %BF for each subject (Figure 4.7).



Figure 4.7 Fat caliper.

4.2.6.5 Speedometer

A speedometer (FilZER dB4L) was used to measure the linear propulsion speed of the wheelchair during the tests (Figure 4.8). The subjects were able to see the speed on the digital display of the speedometer. This online feedback helped them to adjust their propulsion and maintain the desired constant speed during the tests.

4.2.6.6 Weighting Scale

A special scale was designed and fabricated to determine the combined weight of the wheelchair and the sitting subject (Figure 4.9). We then subtracted the weight of the wheelchair from the total weight to obtain the net weight of the subject.



(a)

(b)

(c)

Figure 4.8 Speedometer: (a) Cycling computer; (b) Holding magnet; (c) Wiring kit and sensor.

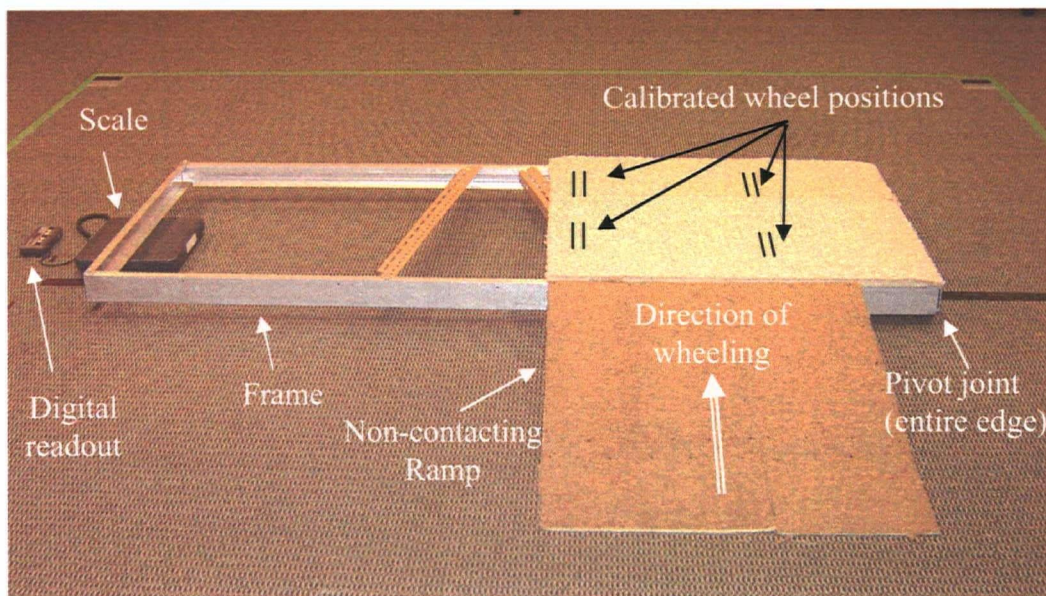


Figure 4.9 The setup for measuring the wheelchair user weight.

4.2.7 Modeling

Although, there may be some differences between the left and right side of the subjects, but since we had a right-side instrumented wheel, we studied subjects with dominant right hand side. The right upper limb was emulated as a linkage system with three links (upper arm, forearm, and hand) and three joints (shoulder, elbow, and wrist) (Figure 4.11).

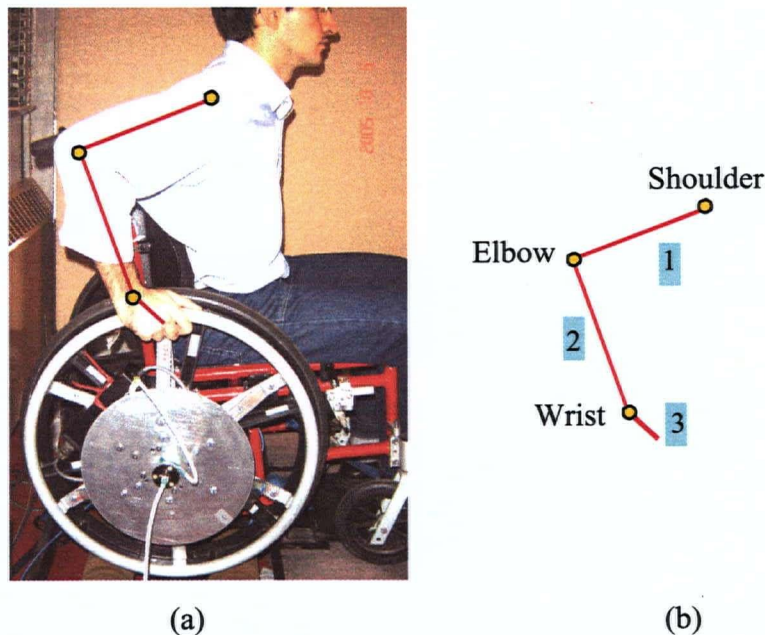


Figure 4.11 The Model of the upper limbs: (a) Sagittal view of the half body; (b) the linkage model. Numbers 1–3 represent upper arm, forearm, and hand, respectively.

Twelve semi-spherical passive camera markers were used to determine the positions of 10 anatomical landmarks (cervical 7, acromion, medial and lateral epicondyle, radial and ulnar styloid, second and fifth metacarp, left and right greater trochanter), and 2 points on the wheel (wheel axle and wheel angular position) (Figure

4.12). The neck and hip information were used to construct the “prismatic-box model” in the VICON software system, and the wheel markers were used to determine the angular position of the wheel. All of the markers were attached on the skin of the subject. The prismatic-box model was designed using the subjects’ anthropometric dimensions. The VICON system resizes the designed model using the acquired data through a subject calibration test as explained in Section 4.2.4.

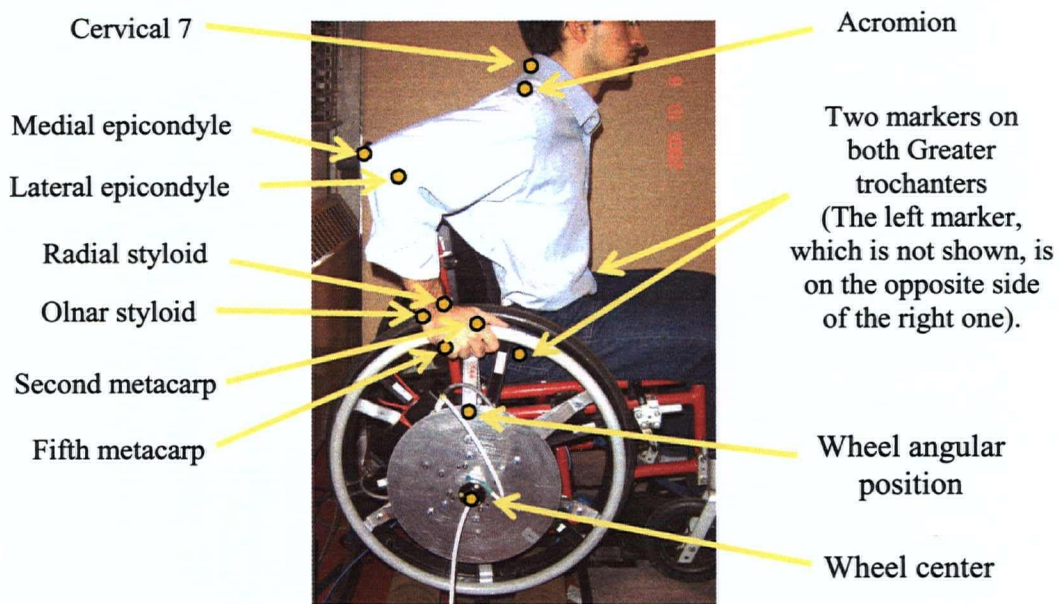


Figure 4.12 Landmark positions on the upper limbs and trunk of the subject, and the wheel.

Figure 4.13 shows the designed 3D model of the upper body of the subject, which was used for kinematic data acquisition. VICON IQ2 software was used to construct this model and re-play animations of the tests. During the re-play mode, it was possible to turn the viewing camera around the prismatic-box model to see the details of the wheelchair propulsion.

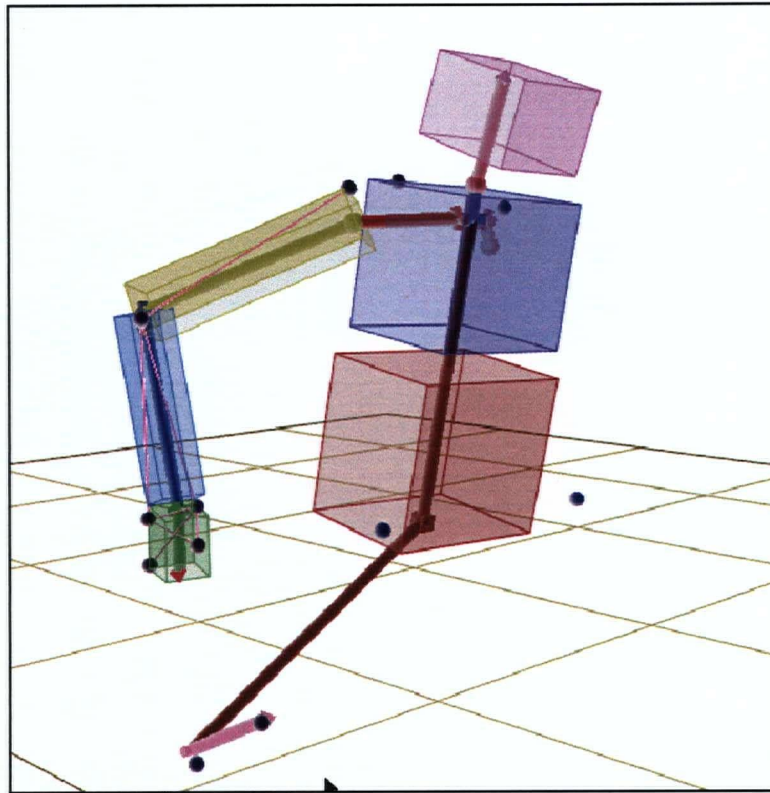


Figure 4.13 A 3D model of the upper body and wheel, developed by using the VICON system.

4.3 Analytical Methodology

To determine the optimum seat position for each user, focusing on the efficiency aspect, it is necessary to obtain an equation, which relates seat position (X and Y) to EBI. It has been reported that heart rate and propulsive moment are related to seat position [19]. Considering Equation 3.2, it is assumed that THB and \bar{M}_z are related to X and Y , whereas $\Delta\theta$ is a constant, because the experiments are conducted for a pre-determined period of time and velocity. THB and \bar{M}_z are related to X and Y as follows:

$$\text{THB} = g_1(X, Y) \quad (4.1a)$$

$$\bar{M}_z = g_2(X, Y) \quad (4.1b)$$

where g_i stands for function i . EBI is related to THB and \bar{M}_z as

$$\text{EBI} = g_3(\text{THB}, \bar{M}_z) \quad (4.2)$$

EBI is now obtained using Equations 4.1 and 4.2:

$$\text{EBI} = g_4(X, Y) \quad (4.3)$$

To determine the optimum seat position for each user considering the injury aspect, it is also necessary to obtain an equation that relates X and Y to WUJII or WUJII'.

In Equations 3.12–3.15, m_s , W_t , h_s , L_a , \bar{V}_l , and %BF are constant. Also, F_m , M_m , and f_p are related to X and Y . F_m , M_m and f_p are related to X and Y as follow:

$$F_m = g_5(X, Y) \quad (4.4a)$$

$$M_m = g_6(X, Y) \quad (4.4b)$$

$$f_p = g_7(X, Y) \quad (4.4c)$$

Equation 4.5 shows the relationship amongst WUJII, F_m , M_m and f_p .

$$\text{WUJII} = g_8(F_m, M_m, f_p) \quad (4.5)$$

Using Equations 4.4 and 4.5, WUJII is re-stated as

$$\text{WUJII} = g_9(X, Y) \quad (4.6)$$

In a similar fashion, WUJII' is determined as

$$\text{WUJII}' = g_{10}(X, Y) \quad (4.7)$$

Human responses are not exactly the same in repeated tests. Therefore, determining the Std. Dev. (σ) can provide a measure of the variability of the results. We defined z as a general function of X and Y , which represents EBI, WUJII, or WUJII'. The test were repeated five times at each position with the same velocity to determine the average value for each index (\bar{z}) and its standard deviations (σ_z). \bar{z} and σ_z are functions of X and Y (Equations 4.8), and we called them the response model. One needs these equations to determine the optimum position for a wheelchair user.

$$\bar{z} = g(X, Y) \quad (4.8a)$$

$$\sigma_z = u(X, Y) \quad (4.8b)$$

4.3.1 Design of Experiments

Clearly, a large number of physical experiments requires long time and costs more. Also, because of the physiological and/or anatomical limitations of the subjects, it is not always possible to perform many experiments. Specially, the number of the experiments has to be reduced to a practical one. In statistical analysis, the problem of choosing a suitable sample of design variables is referred to as Experimental Design or Design of Experiments (DOE) [91,92].

When a required parameter is related to two variables the resulting function is called the response surface. To have a more reliable response surface, one has to increase the number of tests and have the variables reasonably distributed over the possible range. In this study, the subject fatigue, total test time, and the possible range for X and Y were the factors that constrained the number of the experiments. Therefore, a DOE method was used to build the response model that related the biomedical indices to the seat position. DOE methods reduce the number of the experiments required. Using a DOE method, one can generate a set of representative input parameters that uniformly cover the entire design surface. The response model is used as a surrogate model to substitute the actual response.

4.3.1.1 Grid-base Design

In this study, three levels for the vertical and horizontal positions of the seat were considered. As the number of the experiments was limited, four sub-areas were defined with four data points (P_i) on the corners of each sub-area. The grid for this experimental design is shown in Figure 4.14. The values of the variables have been normalized.

This model presents nine data points for the experiments. Two more tests with different velocities at position X2 and Y2 were needed that increased the total number of the tests to eleven. It was not possible for all subjects to follow all eleven tests continuously, due to considerations given to possible fatigue. Therefore, the above model was used for two subjects, who could complete the eleven tests, and another design was used with two vertical seat positions (Y1 and Y2) and three horizontal seat positions (X1, X2 and X3) for the rest. The other design required eight tests consisting of six experiments at six different positions and two additional tests at the position X2 and Y2 for different velocities.

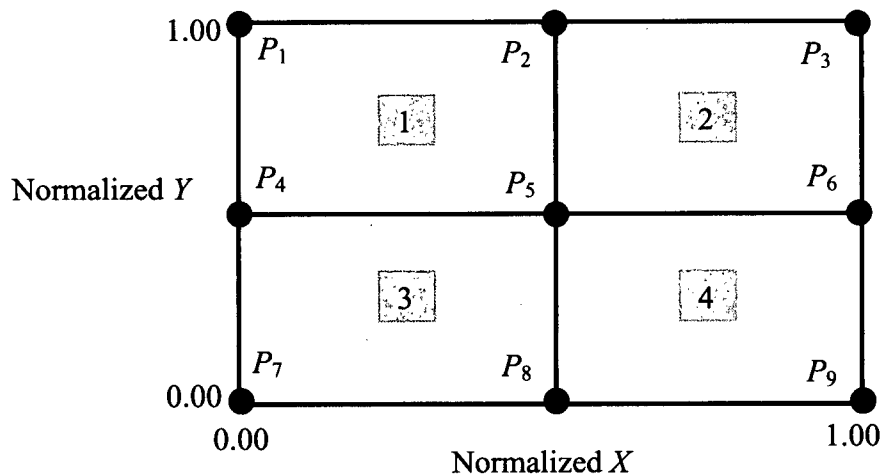


Figure 4.14 Grid-base design for two variables with four sub-areas and nine data points.

Dimensions are not to scale.

4.3.2 Response Equation

Using the results of the experiments, the responses were calculated at the designed data points. The response equations can be determined using one of the following three approximation methods:

- Artificial Neural Network (ANN)
- Local interpolation of the discrete database [93]
- Bivariate Quadratic Function (BQF)

4.3.2.1 Artificial Neural Network

ANN method is very versatile approach and there are many applications of it in areas such as signal processing, controls, pattern recognition, medicine, business, speech recognition and production. ANN is an information-processing system, and is a generalization of mathematical models of human cognition or neural biology [94].

In this research, ANN was not used because there was insufficient data to train and check the network.

4.3.2.2 Local Interpolation

In this method the response at a query point (P_0) is calculated as follows.

First the closest pair of data points of the database (P_1, P_2) are identified and the distances d_{12} between them, and d_1 and d_2 from the points P_1 and P_2 to the query point P_0 are determined. The weights h_1 and h_2 are calculated as

$$\begin{aligned} h_1 &= d_2/d_{12} \\ h_2 &= d_1/d_{12} \end{aligned} \tag{4.9}$$

Normalized weights are shown by w_1 and w_2 and given as

$$\begin{aligned}w_1 &= h_1 / (h_1 + h_2) \\w_2 &= h_2 / (h_1 + h_2)\end{aligned}\tag{4.10}$$

The response is obtained as

$$R(P_0) = w_1 R(P_1) + w_2 R(P_2)\tag{4.11}$$

where $R(P_0)$ is the response at the query point P_0 , and $R(P_1)$ and $R(P_2)$ are the known responses at data points P_1 and P_2 , respectively [93].

In this method, if the database is sufficiently dense and if the query point P_0 is located such that the distance d_1 or d_2 are less than d_{12} , the calculated response is a good approximation of the real case. Again, since the database was not sufficiently dense, this method was not used.

4.3.2.3 Bivariate Quadratic Function (BQF)

In this study, each of the response equations was estimated by using a BQF [95] as follows:

$$\bar{z} = g(X, Y) = b_1 X^2 + b_2 Y^2 + b_3 X + b_4 Y + b_5 XY + b_6\tag{4.12}$$

where b_1, b_2, b_3, b_4, b_5 and b_6 are unknown constants and were determined by having the values of X, Y , and \bar{z} for n' data points or tests and m' unknown, and using the m' -equation- n' -variable method. \bar{z} represents the response surface and gives the value of the corresponding index at different seat positions. BQF is a practical method that can be

used for the cases with a small number of the data points. However, increasing the number of the tests will increase the reliability of the results. Although, this method can be used with equal number of the equations and the variables, in case the data points are at the border of the sampling region there is no solution and more data points are needed. This conflict is because of the singularity that may occur in the solution.

4.3.3 The Big Picture

The big picture of the entire test process is given as a flowchart in Figure 4.15. It shows the steps, which are followed to determine the optimum seat position of a manual wheelchair for a user. This method determines the procedure, which can be used to prescribe a more suitable manual wheelchair considering the injury priorities, conditions and concerns, of the subject.

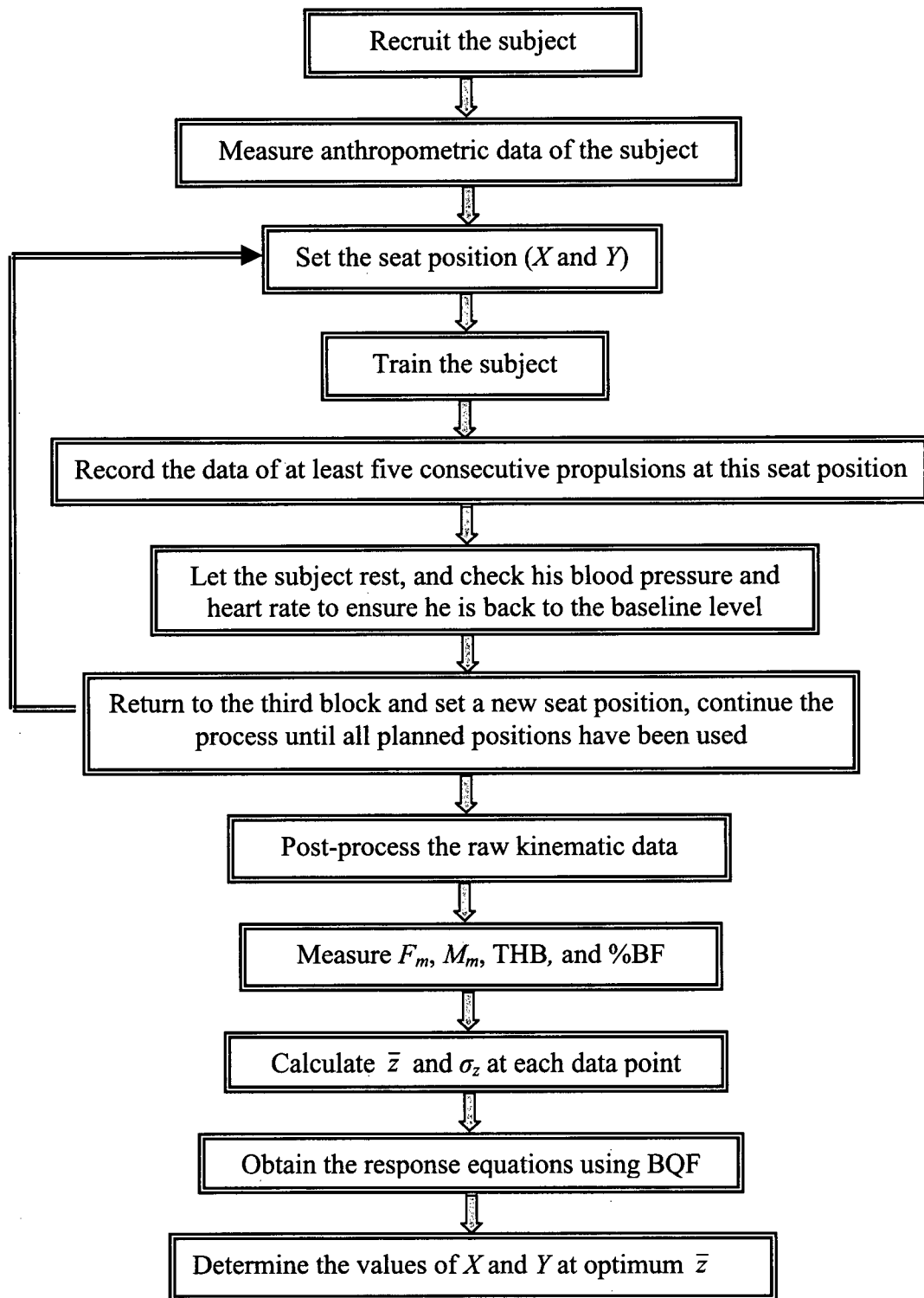


Figure 4.15 Flowchart for the entire test process to determine the optimum positions of a wheelchair for a MWU.

4.4 Results and Discussion

In the sections that follow, different categories of the results are presented. First, the heart rate, blood pressure and the anthropometric data of the subjects are given. Then, four research questions are explained and answered by addressing the following issues:

- Relationship between the biomedical indices and the propulsion velocity.
- Sensitivity of the biomedical indices to the seat position.
- Generic rules for estimating the optimum seat position for all users.
- Optimum seat position for a particular user.

4.4.1 Heart Rate, Blood Pressure and Anthropometric Data

The measured and calculated resting level of heart rate and blood pressure, and anthropometric data for the subjects are presented in Tables 4.2a and 4.2b, respectively. These data were used in the kinetic and kinematic analysis. Also, the subject's limb segment lengths were required to design the prismatic-box model (see Sections 4.2.5 and 4.2.7).

Table 4.2a. Heart rate and blood pressure for the subjects.

Subject	Heart rate (Beats/min)	Systolic blood pressure (mmHg)	Diastolic blood pressure (mmHg)
1	72	129	76
2	94	141	85
3	45	130	82
4	71	122	78
5	100	173	91
6	87	94	66
7	80	112	64
8	76	118	62

Table 4.2b Anthropometric data for the subjects.

Subject code	Height (m)	Upper arm length (m)	Forearm length (m)	Hand length (m)	Hand width (m)	Shoulder joint circumference (m)	Elbow joint circumference (m)	Wrist joint circumference (m)	Mass (kg)	BMI (kg/m ²)	%BF
1	1.85	0.32	0.29	0.11	0.10	0.45	0.26	0.16	88	25.71	28.9
2	1.62	0.28	0.25	0.08	0.09	0.38	0.26	0.15	58	22.10	27.1
3	1.65	0.27	0.26	0.08	0.09	0.40	0.25	0.17	53	19.47	21.5
4	1.93	0.29	0.30	0.10	0.09	0.42	0.28	0.17	100	26.85	24.0
5	1.80	0.30	0.26	0.10	0.09	0.44	0.29	0.19	94	29.01	32.2
6	1.80	0.28	0.28	0.09	0.09	0.42	0.29	0.18	80	24.69	29.5
7	1.77	0.29	0.27	0.09	0.08	0.36	0.25	0.16	58	18.51	8.8
8	1.91	0.31	0.30	0.10	0.10	0.43	0.30	0.19	87	23.84	22.8

4.4.2 Fixed Seat Position

In this category, the fixed positions at X2 and Y2, and the velocities of 0.9, 1.1 and 1.3 m/s for eight subjects were used to determine the relationship between the biomedical indices and the speed. The mean and Std. Dev. of five consecutive pushing phases were analyzed for each test. In this study, because of the small sample size of the subjects we performed the statistical analysis for estimating the Type I or Alfa error.

The results from statistical analysis using repeated-measures Analysis of Variance (ANOVA) showed that velocity alter the injury indices significantly ($p < 0.01$). Figures 4.16 and 4.17 illustrate the variation of the mean values of WUJII and WUJII' (\overline{WUJII} and $\overline{WUJII'}$) with respect to the velocity using Equations 3.6b and 3.8a, respectively. The figures show that these two indices increase by increasing the velocity for all subjects. Tables 4.3 and 4.4 present the mean and Std. Dev. of WUJII and WUJII', which confirm the above finding. So, the relations of the injury indices were modified to include the velocity as one of their parameters.

The results from repeated-measures ANOVA did not show significant relationship between the velocity and the mean value of EBI (\overline{EBI}). Figure 4.18 presents the variation of \overline{EBI} with respect to the velocity. The figure shows that EBI increases for five subjects by increasing the velocity up to about 1.1 m/s. Three subjects have their maximum \overline{EBI} at the middle speed. As this seems case dependent, we cannot determine a specific rule for variation of \overline{EBI} with respect to the velocity. This result confirm the findings of Mukherjee et al. [38] that efficient propulsion velocity is case dependent and is not related to lower or higher speeds. The mean and Std. Dev. of EBI are shown in Table 4.5.

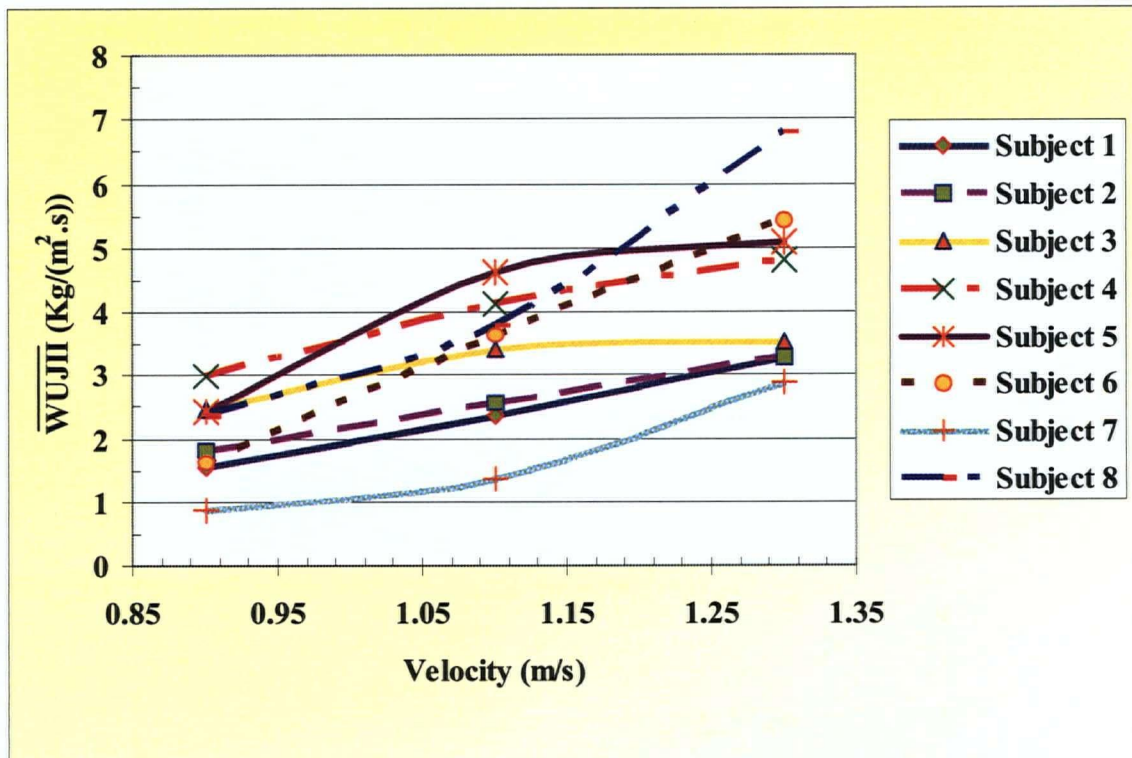


Figure 4.16 Variation of \overline{WUJII} versus velocity.

Table 4.3 Mean and Std. Dev. of \overline{WUJII} for the subjects for three velocities.

Subject code \ Velocity (m/s)	1	2	3	4	5	6	7	8
0.9	1.553 ±0.195	1.809 ±0.396	2.453 ±0.576	2.970 ±0.220	2.416 ±0.249	1.608 ±0.255	0.869 ±0.108	2.369 ±0.171
1.1	2.343 ±0.232	2.552 ±0.335	3.399 ±0.513	4.126 ±0.425	4.632 ±0.660	3.622 ±0.618	1.356 ±0.131	3.797 ±0.429
1.3	3.272 ±0.658	3.274 ±0.158	3.543 ±0.563	4.813 ±0.801	5.087 ±0.974	5.441 ±0.594	2.87 ±0.553	6.800 ±1.047

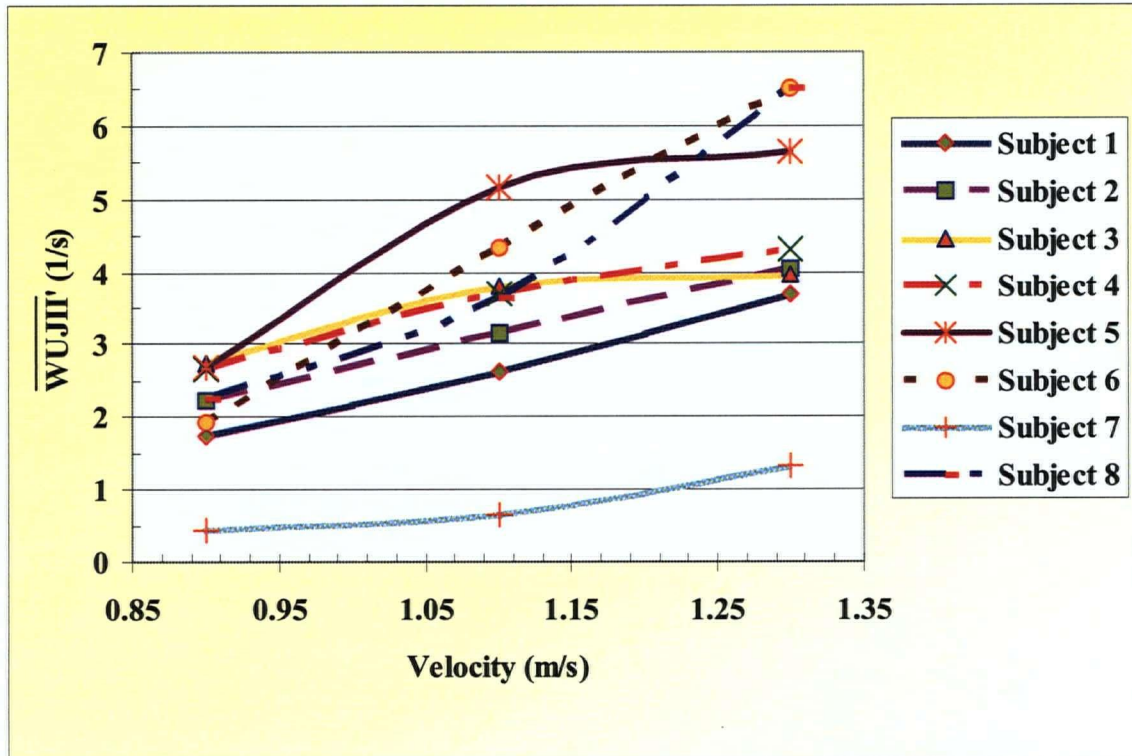


Figure 4.17 Variation of $\overline{WUJII'}$ versus velocity.

Table 4.4 Mean and Std. Dev. of WUJII' for the subjects for three velocities.

Subject code \ Velocity (m/s)	1	2	3	4	5	6	7	8
0.9	1.748 ±0.219	2.233 ±0.488	2.741 ±0.643	2.660 ±0.197	2.684 ±0.277	1.923 ±0.304	0.429 ±0.050	2.265 ±0.164
1.1	2.637 ±0.261	3.151 ±0.414	3.798 ±0.574	3.696 ±0.381	5.145 ±0.732	4.331 ±0.740	0.645 ±0.062	3.629 ±0.410
1.3	3.682 ±0.740	4.042 ±0.195	3.959 ±0.630	4.311 ±0.717	5.650 ±1.082	6.506 ±0.710	1.326 ±0.191	6.500 ±1.001

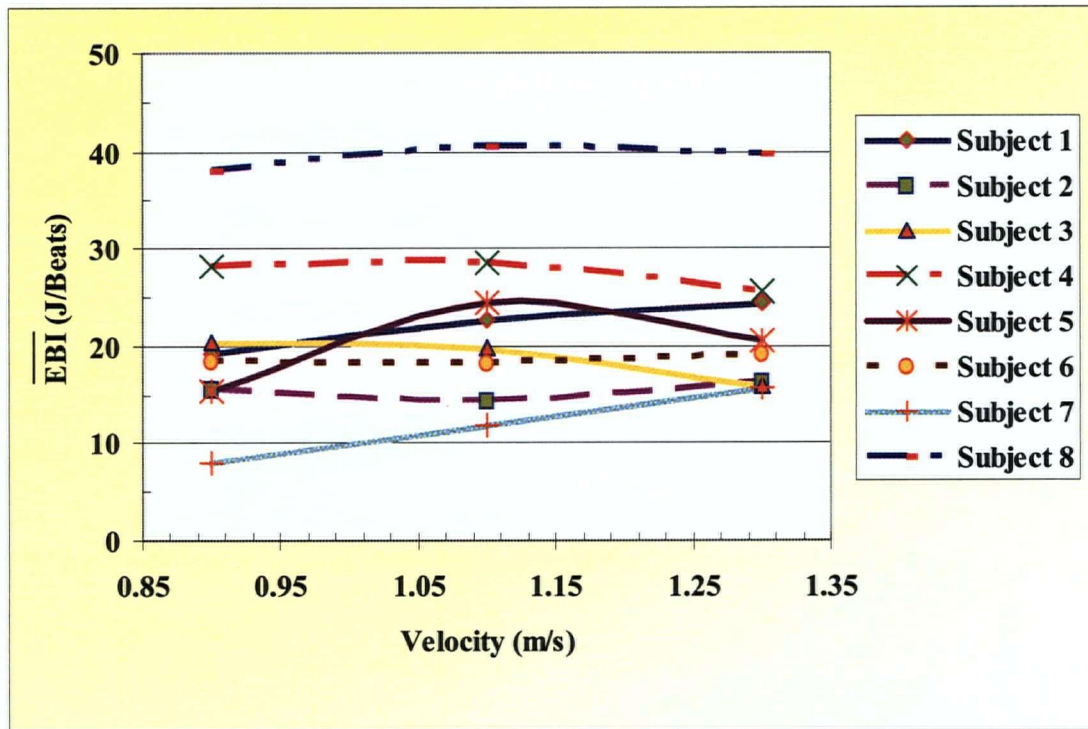


Figure 4.18 Variation of $\overline{\text{EBI}}$ versus velocity.

Table 4.5 Mean and Std. Dev. of EBI for the subjects for three velocities

Subject code \ Velocity (m/s)	1	2	3	4	5	6	7	8
0.9	19.152 ±1.933	15.428 ±1.647	20.308 ±3.429	28.194 ±1.333	15.378 ±1.962	18.443 ±0.896	8.016 ±0.455	38.019 ±2.217
1.1	22.641 ±1.320	14.327 ±2.298	19.731 ±2.177	28.520 ±2.840	24.374 ±2.019	18.157 ±4.328	11.868 ±0.780	40.522 ±0.643
1.3	24.328 ±3.688	16.318 ±1.251	15.967 ±3.921	25.539 ±1.933	20.582 ±2.284	19.176 ±1.287	15.670 ±0.758	39.785 ±1.407

4.4.3 Constant Wheelchair Velocity

In the second category of the experiments, the tests were performed at three X and two Y settings, and the velocity of 0.9 m/s for all subjects. Five consecutive pushing phases were analyzed for each test.

4.4.3.1 Seat Height Y1

Using repeated-measures ANOVA the results showed that the horizontal position of the seat was significantly related to the indices at low seat position Y1 ($p < 0.05$). Figures 4.19, 4.20 and 4.21 show the variations of \overline{WUJII} , \overline{WUJII}' , and \overline{EBI} against the ratio of X to the arm length (X -ratio) at Y1, respectively. X -ratio was used to normalize the horizontal seat position amongst the subjects. It is seen that \overline{WUJII} and \overline{WUJII}' increase by moving the seat forward, except for the subjects 1, 4 and 7 in Figure 4.19 and subjects 1, 4, 6 and 7 in Figure 4.20. Figure 4.21 shows that, except subjects 1 and 4, the other subjects had their minimum values of \overline{EBI} at most backward seat position, and six subjects had their maximum value of \overline{EBI} at most forward seat position.

Tables 4.6, 4.7 and 4.8 present the mean and Std. Dev. of \overline{WUJII} , \overline{WUJII}' and \overline{EBI} for the subjects at three X -ratios at seat height Y1, respectively. The Std. Dev. of \overline{WUJII} and \overline{WUJII}' vary between 0.053–0.783, and 0.025–0.967, respectively, but are predominantly under 0.400. The Std. Dev. of \overline{EBI} varies between 0.75–3.06 and is mostly below 2.00.

The results indicated that the average values of the injury indices and \overline{EBI} at low seat height Y1, can vary between 5–27.5% and between 3.1–21.1%, respectively.

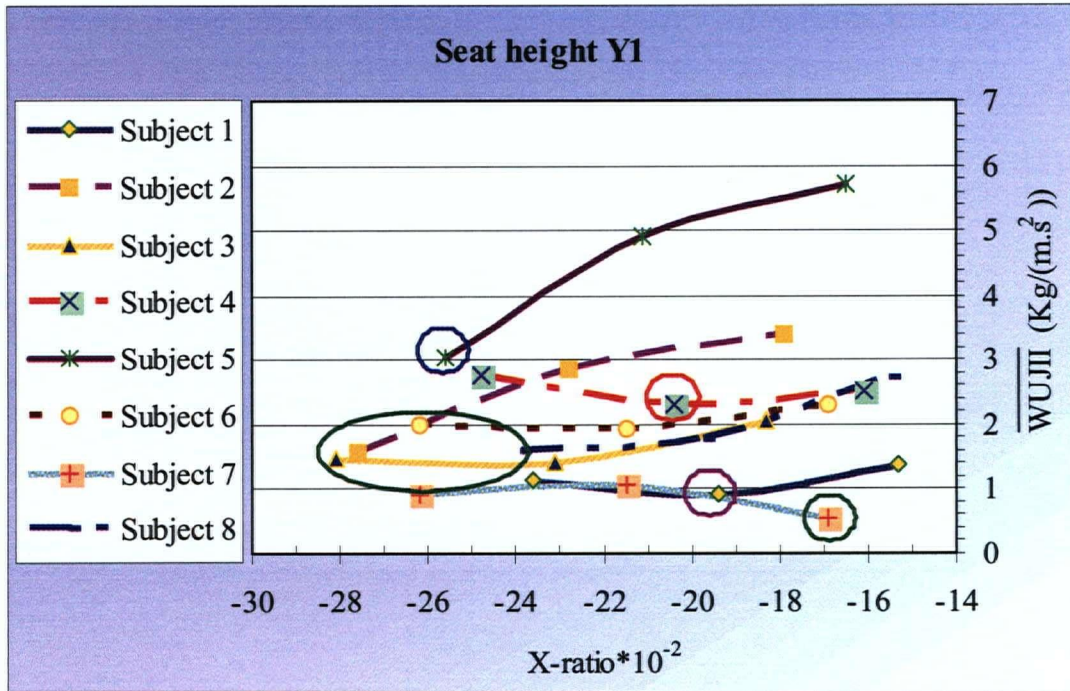


Figure 4.19 Variation of \overline{WUJII} against X-ratio at Y1. Minimum values encircled.

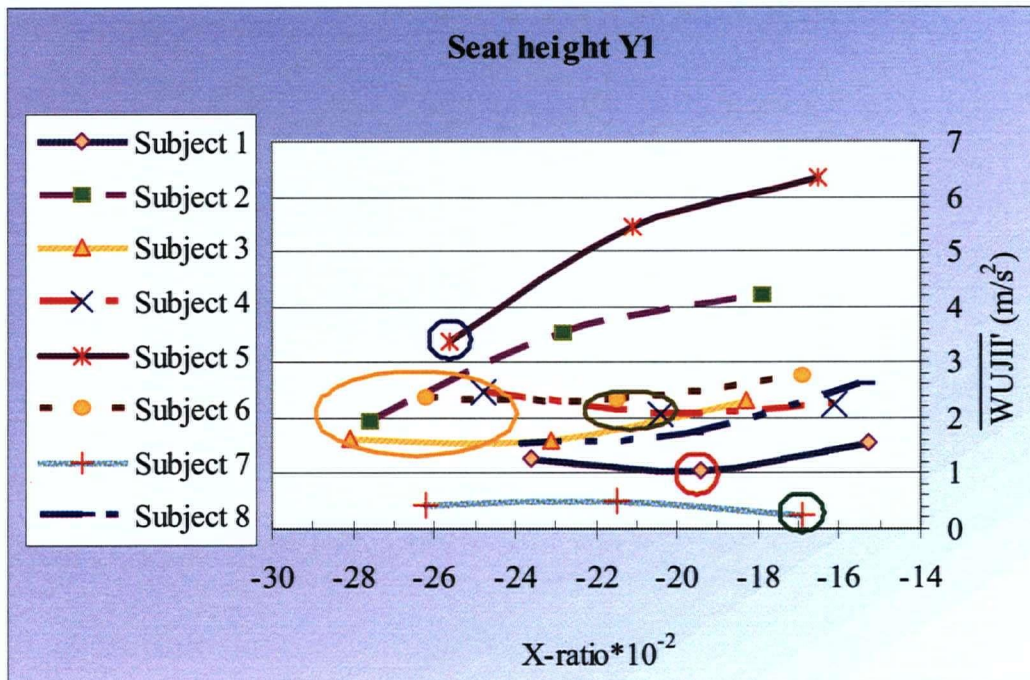


Figure 4.20 Variation of $\overline{WUJII'}$ against X-ratio at Y1. Minimum values encircled.

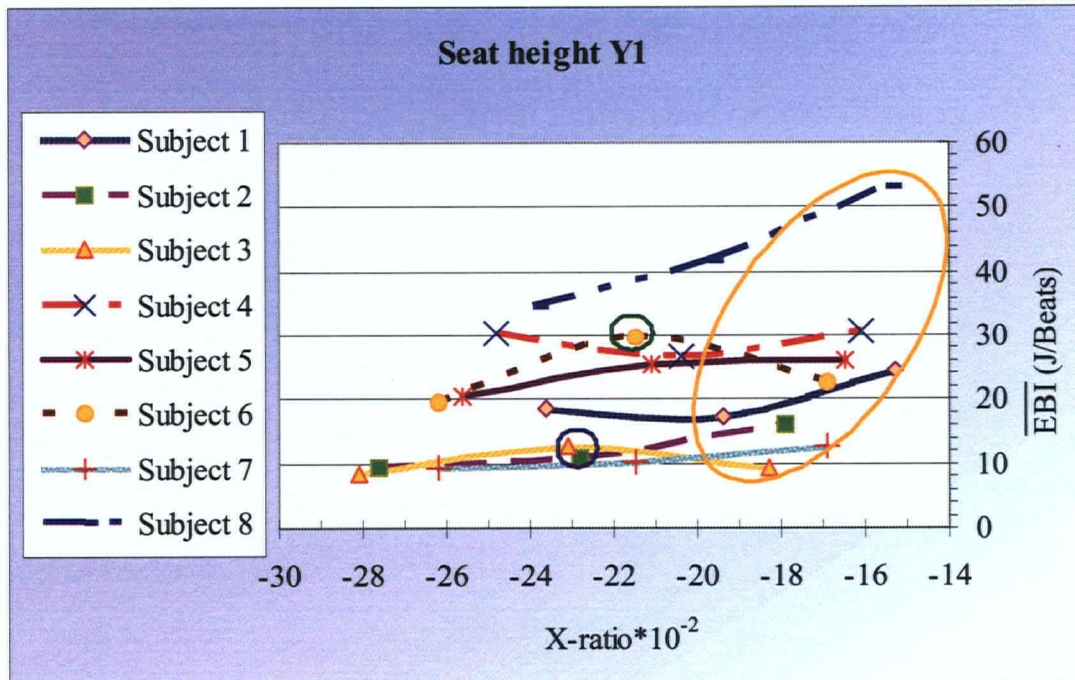


Figure 4.21 $\overline{\text{EBI}}$ with respect to the X-ratio at Y1. Maximum values encircled.

Table 4.6 Mean and Std. Dev. of WUJII for the subjects at three X-ratios and seat height Y1.

Subject code	1	2	3	4	5	6	7	8
X1	1.370 ±0.099	3.414 ±0.738	2.068 ±0.361	2.529 ±0.612	5.708 ±0.568	2.315 ±0.154	0.551 ±0.053	2.734 ±0.245
X2	0.934 ±0.093	2.849 ±0.783	1.415 ±0.355	2.317 ±0.167	4.905 ±0.576	1.941 ±0.500	1.085 ±0.152	1.790 ±0.201
X3	1.134 ±0.114	1.566 ±0.308	1.472 ±0.074	2.766 ±0.383	3.034 ±0.261	1.981 ±0.346	0.929 ±0.110	1.589 ±0.114

Table 4.7 Mean and Std. Dev. of WUJII' for the subjects at three X-ratios and seat height Y1.

Seat X-position \ Subject code	1	2	3	4	5	6	7	8
X1	1.542 ±0.112	4.214 ±0.911	2.311 ±0.403	2.265 ±0.548	6.339 ±0.631	2.768 ±0.184	0.262 ±0.025	2.614 ±0.234
X2	1.051 ±0.104	3.517 ±0.967	1.582 ±0.397	2.075 ±0.149	5.448 ±0.640	2.321 ±0.598	0.516 ±0.072	1.711 ±0.192
X3	1.275 ±0.128	1.933 ±0.380	1.644 ±0.083	2.477 ±0.343	3.369 ±0.290	2.368 ±0.413	0.442 ±0.053	1.519 ±0.109

Table 4.8 Mean and Std. Dev. of EBI for the subjects at three X-ratios and seat height Y1.

Seat X-position \ Subject code	1	2	3	4	5	6	7	8
X1	24.526 ±0.752	15.953 ±1.518	9.193 ±0.881	30.519 ±2.251	25.884 ±1.461	22.470 ±2.375	12.610 ±0.796	53.123 ±1.430
X2	17.211 ±1.114	10.851 ±1.830	12.539 ±2.661	26.653 ±1.123	25.323 ±1.403	29.675 ±3.057	10.289 ±0.933	41.715 ±2.219
X3	18.511 ±1.166	9.325 ±1.075	8.475 ±0.708	30.333 ±2.424	20.303 ±0.690	19.556 ±1.569	9.235 ±0.706	34.602 ±1.314

To have a better understanding of the variation of the average values of the indices, Figures 4.22, 4.23 and 4.24 show the maximum and minimum values of \overline{WUJII} , $\overline{WUJII'}$, \overline{EBI} and their Std. Dev. among the subjects with respect to the X-ratio at Y1.

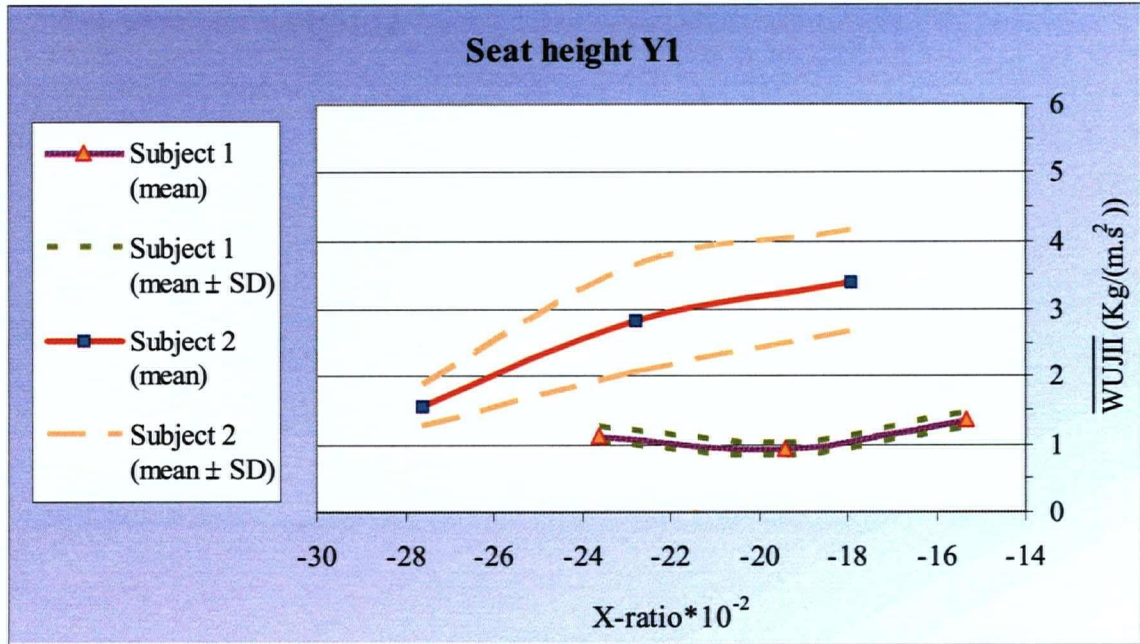


Figure 4.22 Maximum and minimum values of \overline{WUJII} and its Std. Dev. against X-ratio at Y1, among the subjects.

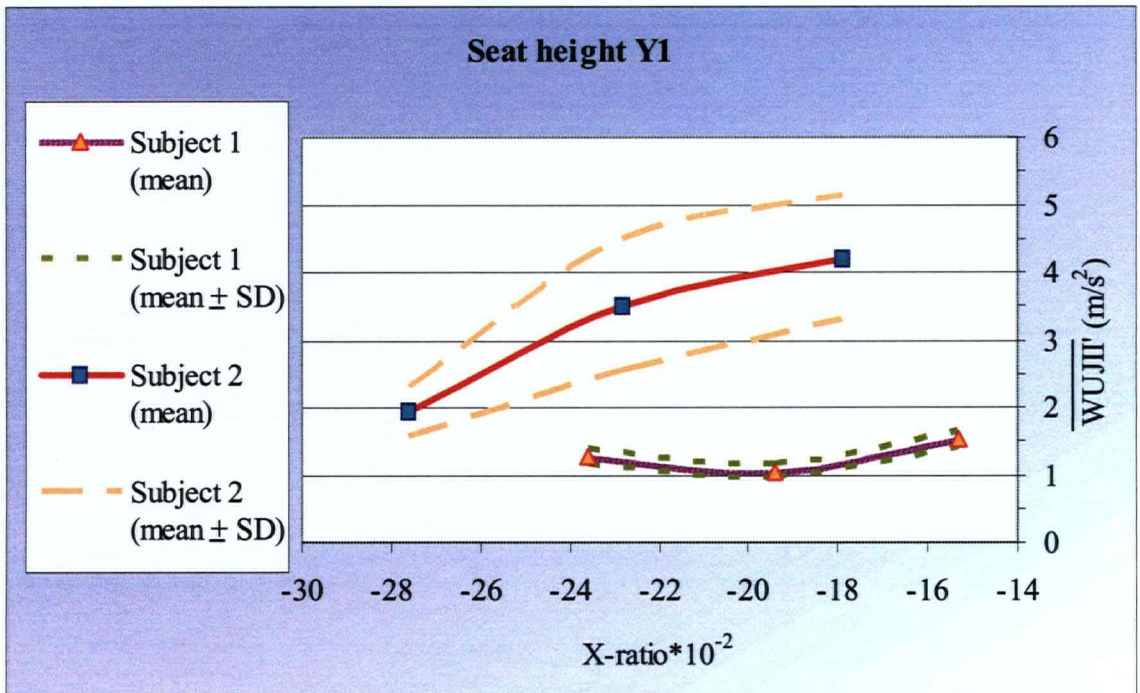


Figure 4.23 Maximum and minimum values of $\overline{WUJII'}$ and its Std. Dev. against X-ratio at Y1, among the subjects.

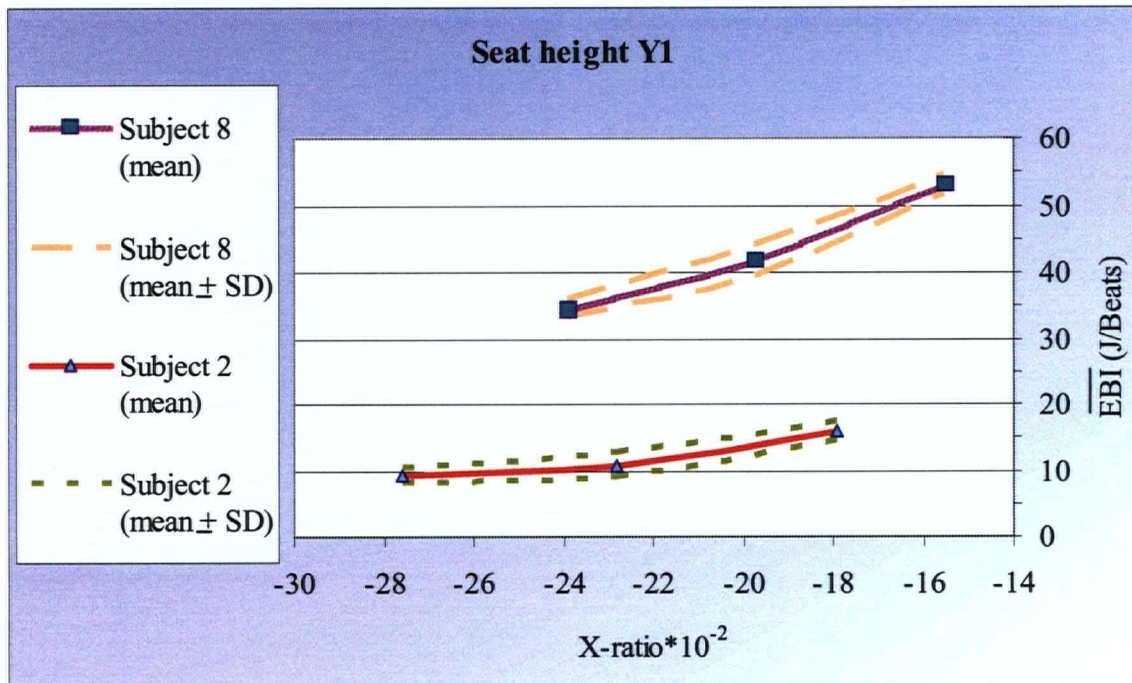


Figure 4.24 Maximum and minimum values of $\overline{\text{EBI}}$ and its Std. Dev. against X-ratio at Y1, among the subjects.

The above results show that by decreasing the magnitude of X-ratio or moving the seat forward at low seat height Y1, both the average value of the injury indices and $\overline{\text{EBI}}$ may increase. Overall, the results show that the indices are sensitive to horizontal seat position at seat height Y1.

4.4.3.2 Seat Height Y2

Using repeated-measures ANOVA the results showed that horizontal position of the seat was significantly related to the indices at high seat position Y2 ($p < 0.05$). Figures 4.25, 4.26 and 4.27 show the variation of $\overline{\text{WUJII}}$, $\overline{\text{WUJII}'}$ and $\overline{\text{EBI}}$ with respect to X-ratio at seat height Y2, respectively. Five subjects showed their highest values of the

injury indices at the most forward seat position or highest X-ratio, whereas, subject 4 showed the minimum value at this position and the other two subjects did not show significant change. Five subjects showed that their \overline{EBI} decreases by increasing X-ratio or moving the seat backward, whereas two subjects had their maximum \overline{EBI} at X2. \overline{EBI} had insignificant change with respect to the X-ratio for subjects 3.

Tables 4.9, 4.10 and 4.11 present the mean and Std. Dev. of \overline{WUJII} , \overline{WUJII}' and \overline{EBI} for the subjects at three X-ratios and seat height Y2, respectively. The Std. Dev. of \overline{WUJII} and \overline{WUJII}' vary between 0.098–0.629, and are mostly under 0.40. The Std. Dev. of \overline{EBI} varies between 0.46–3.62, and is mostly under 2.00. The results indicated that the average values of the injury indices vary between 5.6–29.9% and the average value of \overline{EBI} varies between 3.7–26.0%.

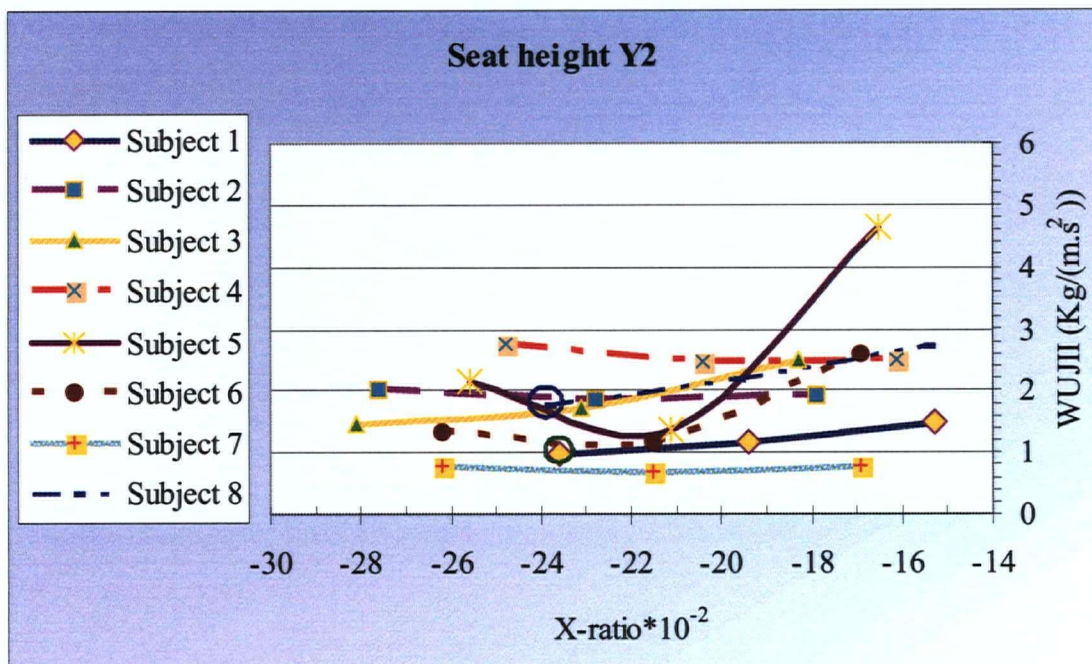


Figure 4.25 Variation of \overline{WUJII} against X-ratio at Y2. Minimum values encircled.

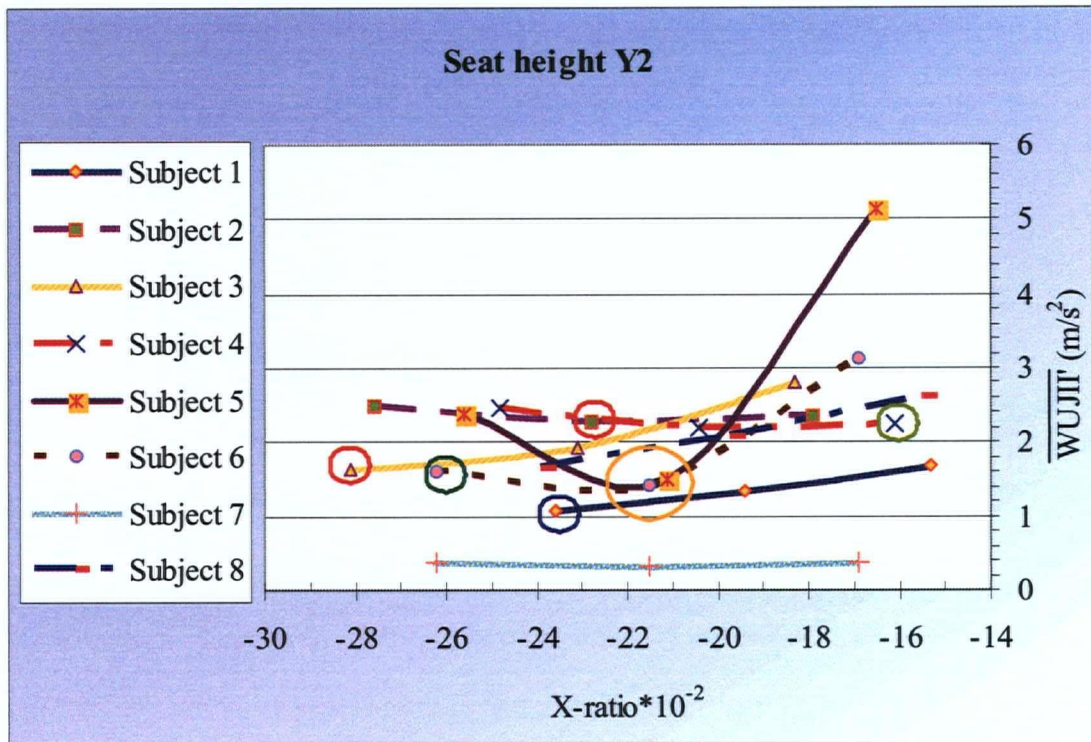


Figure 4.26 Variation of \overline{WUJII}' against X-ratio at Y2. Minimum values encircled.

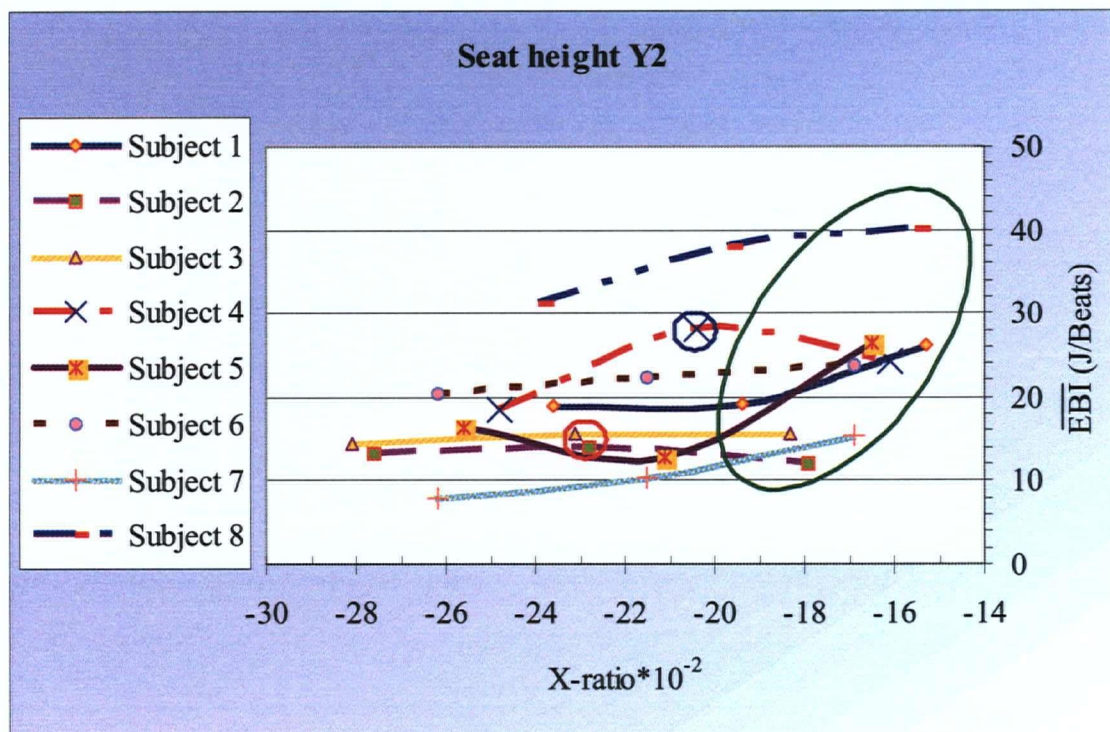


Figure 4.27 Variation of \overline{EBI} against X-ratio at Y2. Maximum values encircled.

Table 4.9 Mean and Std. Dev. of WUJII for the subjects at three X-ratios and seat height Y2.

Seat X-position \ Subject code	1	2	3	4	5	6	7	8
X1	1.495 ±0.102	1.917 ±0.573	2.508 ±0.139	2.503 ±0.364	4.642 ±0.629	2.610 ±0.144	0.782 ±0.098	2.736 ±0.322
X2	1.182 ±0.134	1.836 ±0.392	1.176 ±0.144	2.450 ±0.273	1.352 ±0.231	1.180 ±0.184	0.693 ±0.180	2.188 ±0.194
X3	0.957 ±0.179	2.012 ±0.262	1.468 ±0.273	2.762 ±0.337	2.136 ±0.283	1.338 ±0.254	0.794 ±0.112	1.748 ±0.223

Table 4.10 Mean and Std. Dev. of WUJII' for the subjects at three X-ratios and seat height Y2.

Seat X-position \ Subject code	1	2	3	4	5	6	7	8
X1	1.682 ±0.115	2.366 ±0.707	2.802 ±0.156	2.242 ±0.326	5.156 ±0.699	3.121 ±0.172	0.372 ±0.046	2.615 ±0.308
X2	1.330 ±0.151	2.266 ±0.484	1.918 ±0.161	2.194 ±0.245	1.502 ±0.257	1.411 ±0.220	0.330 ±0.086	2.092 ±0.186
X3	1.077 ±0.202	2.484 ±0.324	1.640 ±0.305	2.474 ±0.302	2.372 ±0.314	1.600 ±0.304	0.378 ±0.053	1.671 ±0.213

Figures 4.28, 4.29 and 4.30 illustrate the maximum and minimum values of \overline{WUJII} , $\overline{WUJII'}$ and \overline{EBI} and their Std. Devs. among the subjects with respect to the X-ratio at Y2, respectively.

Table 4.11 Mean and Std. Dev. of EBI for the subjects at three X-ratios and seat height Y2.

Seat X-position \ Subject code	1	2	3	4	5	6	7	8
1	26.317 ±2.311	11.931 ±2.104	15.548 ±1.019	24.331 ±1.778	26.337 ±2.200	23.813 ±1.427	15.376 ±0.570	40.157 ±0.907
2	19.175 ±1.038	13.902 ±3.621	15.737 ±1.040	28.015 ±1.347	12.634 ±1.699	22.433 ±0.976	10.293 ±1.117	38.019 ±2.217
3	18.894 ±1.048	13.243 ±1.468	14.359 ±2.950	18.463 ±0.977	16.231 ±0.534	20.358 ±0.531	8.016 ±0.455	31.319 ±1.985

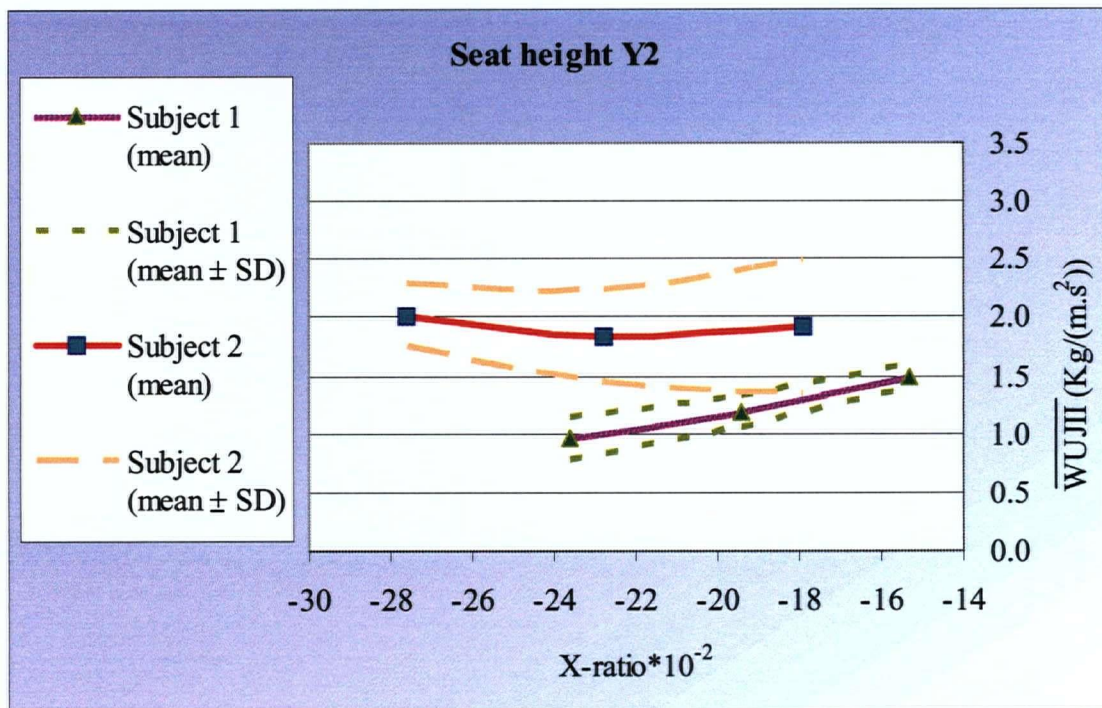


Figure 4.28 Maximum and minimum values of \overline{WUJII} and its Std. Dev. against X-ratio at Y2, among the subjects.

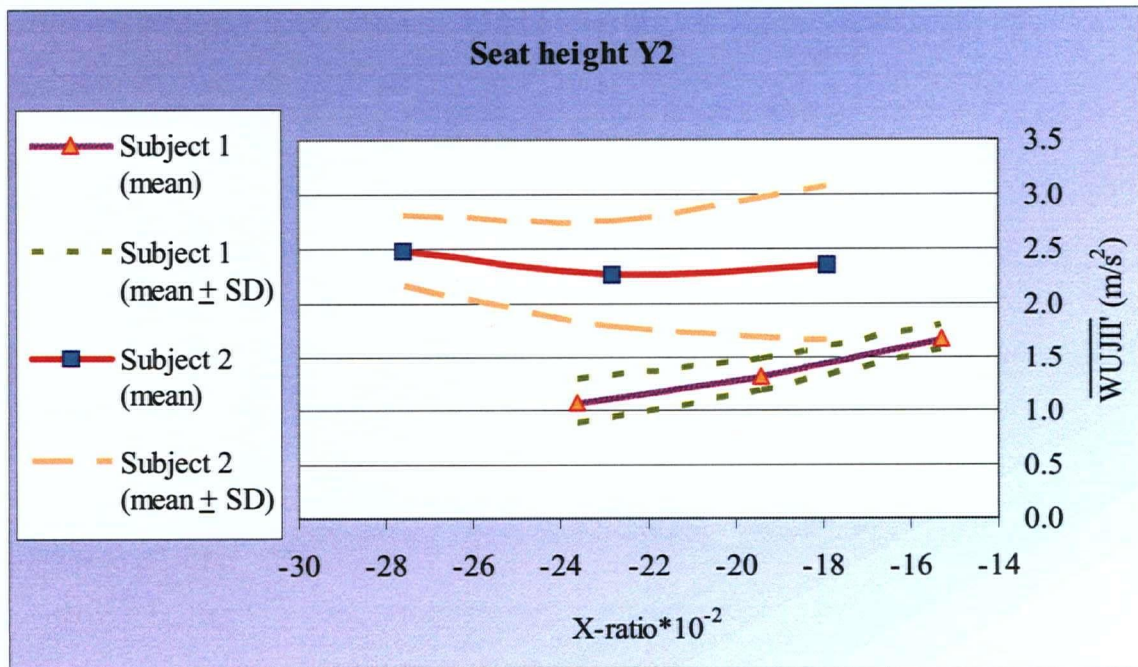


Figure 4.29 Maximum and minimum values of $\overline{WUJII'}$ and its Std. Dev. against X-ratio at Y2, among the subjects.

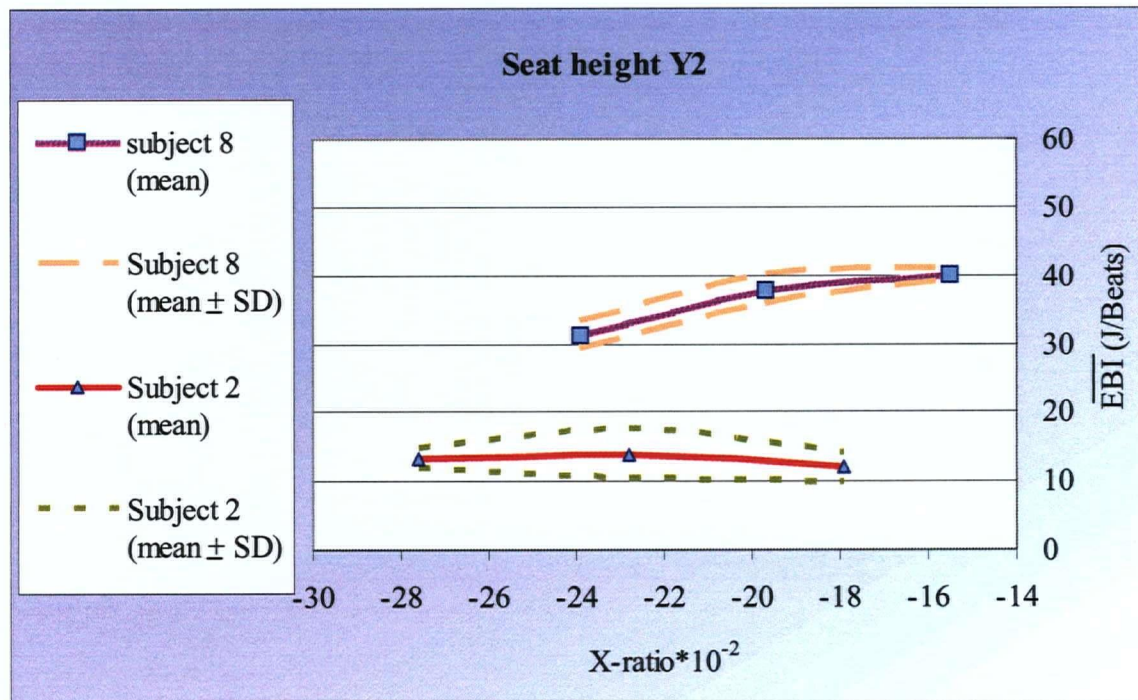


Figure 4.30 Maximum and minimum values of \overline{EBI} and its Std. Dev. against X-ratio at Y2, among the subjects.

The above results show that the average values of the injury indices may increase at the most forward seat position at seat height Y2. Also, it can be possible that \overline{EBI} increase by moving the seat forward. The results show that indices are sensitive to horizontal seat position at seat height Y2.

4.4.3.3 Horizontal Seat Position X1

Two tests were performed for all subjects at horizontal seat position X1 with two possible vertical seat positions Y1 and Y2. To normalize the seat height for the subjects, the ratio of Y to the arm length was defined as Y-ratio.

Figures 4.31 and 4.32 show that \overline{WUJII} and \overline{WUJII}' decrease by increasing the Y-ratio (or seat height) for four subjects at position X1, whereas they increase for subjects 2 and 8. The average values of the injury indices do not show considerable variation for subjects 3 and 4.

Figure 4.33 shows that four subjects have their maximum values of \overline{EBI} at Y1. Three subjects have their maximum values of \overline{EBI} at Y2. Subject 1 did not show considerable variation by changing the seat height.

Performing repeated-measures ANOVA the results did not show significant relationship between that vertical position of the seat and the indices at horizontal seat position X1.

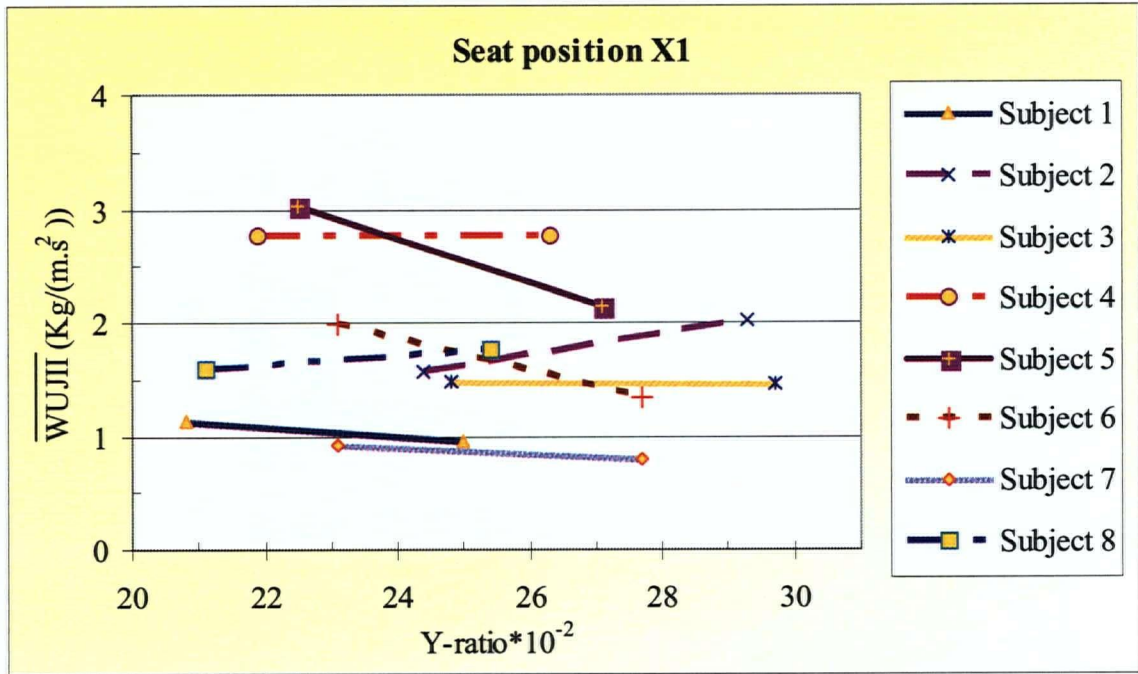


Figure 4.31 Variation of \overline{WUJII} against Y-ratio at X1.

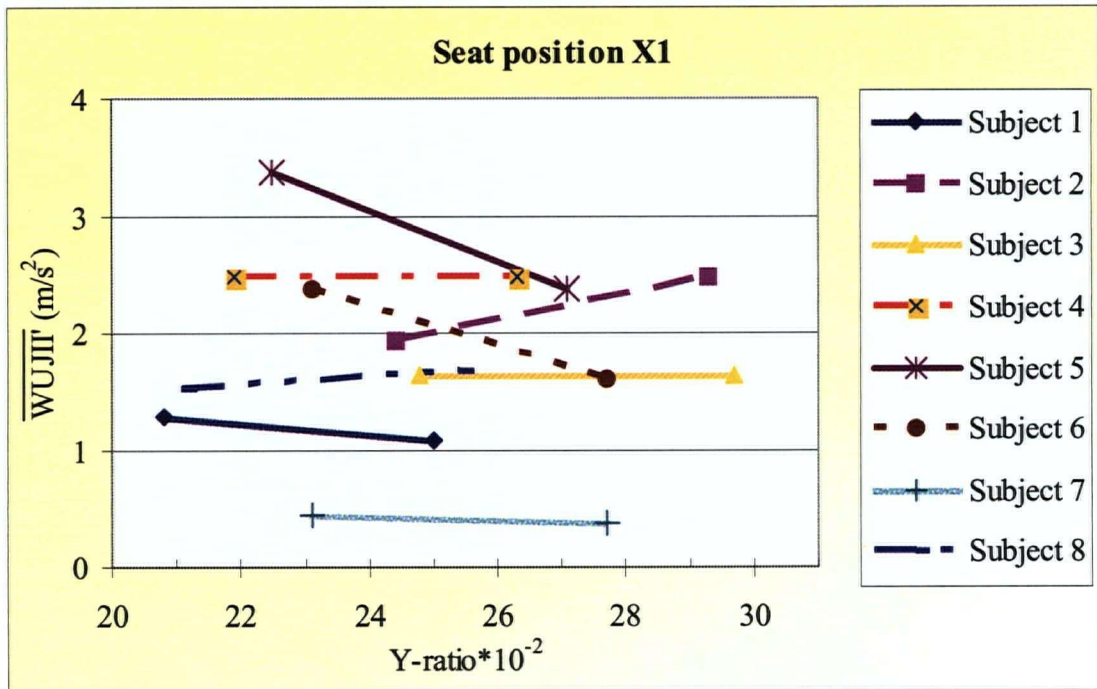


Figure 4.32 Variation of \overline{WUJII}' against Y-ratio at X1.

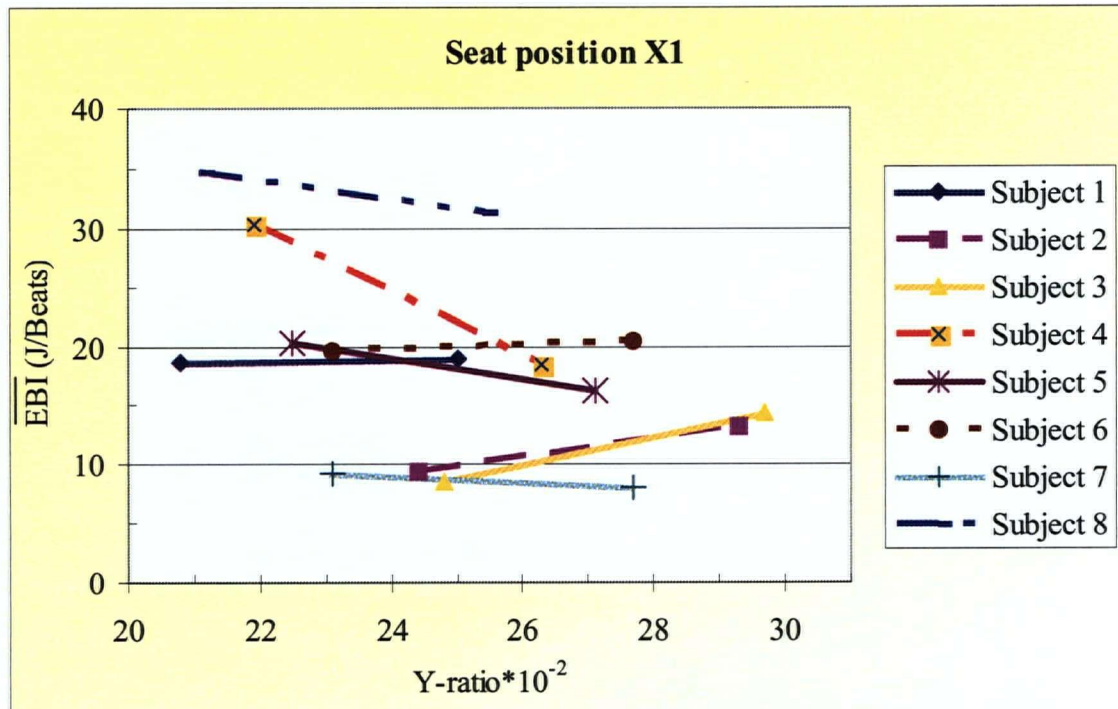


Figure 4.33 Variation of \overline{EBI} against Y-position at X1.

4.4.3.4 Horizontal Seat Position X2

At position X2, two tests were performed for all subjects with seat heights Y1 and Y2. Figures 4.34 and 4.35 show \overline{WUJII} and \overline{WUJII}' versus Y-ratio. For half of the subjects no specific relationship is observed.

Figure 4.36 illustrates that \overline{EBI} increases for four subjects and decreases for three by increasing Y-ratio. Subject 7 does not show considerable change for \overline{EBI} against Y-ratio.

Overall, using repeated-measures ANOVA the results did not show significant relationships between the average values of the indices and the seat height at position X2.

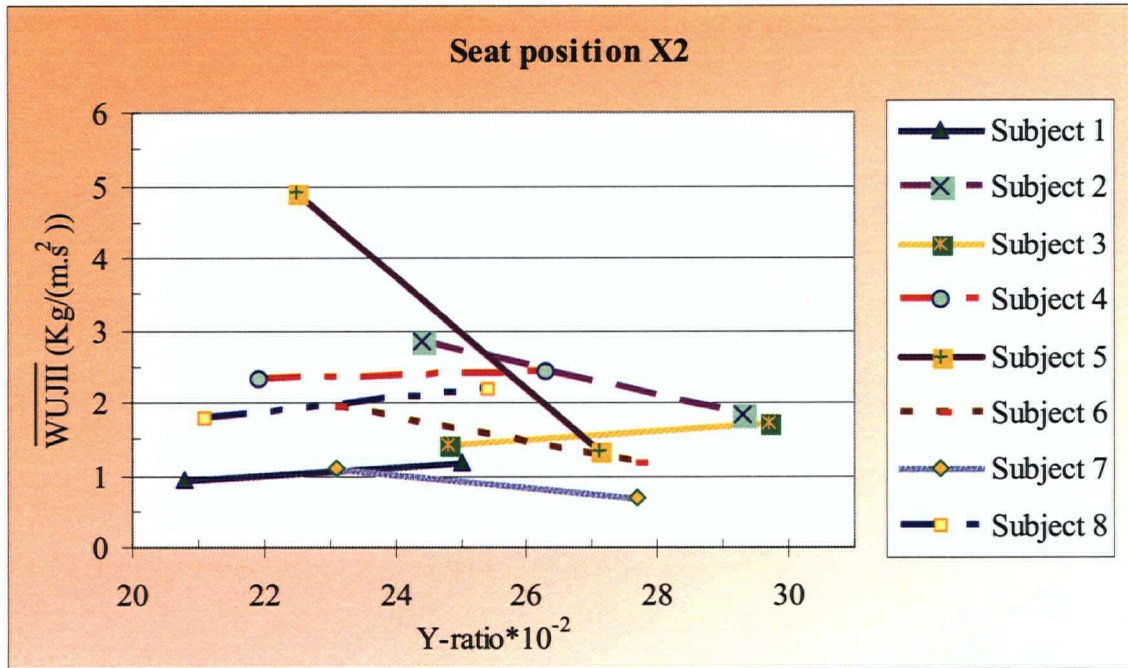


Figure 4.34 Variation of \overline{WUJII} against Y-ratio at X2.

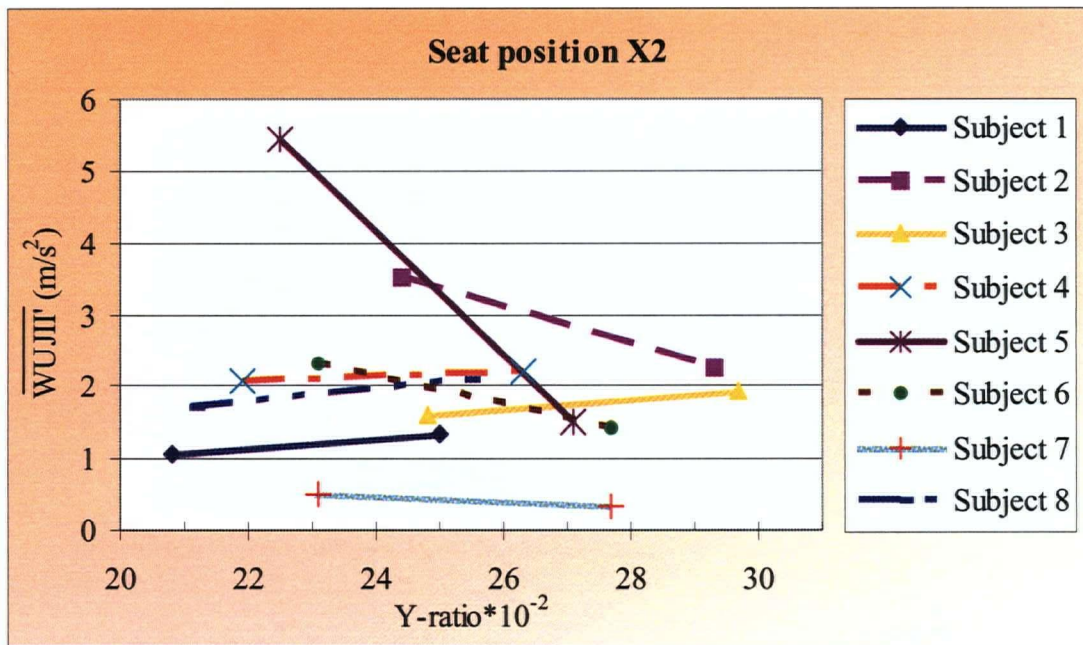


Figure 4.35 Variation of \overline{WUJII}' against Y-ratio at X2.

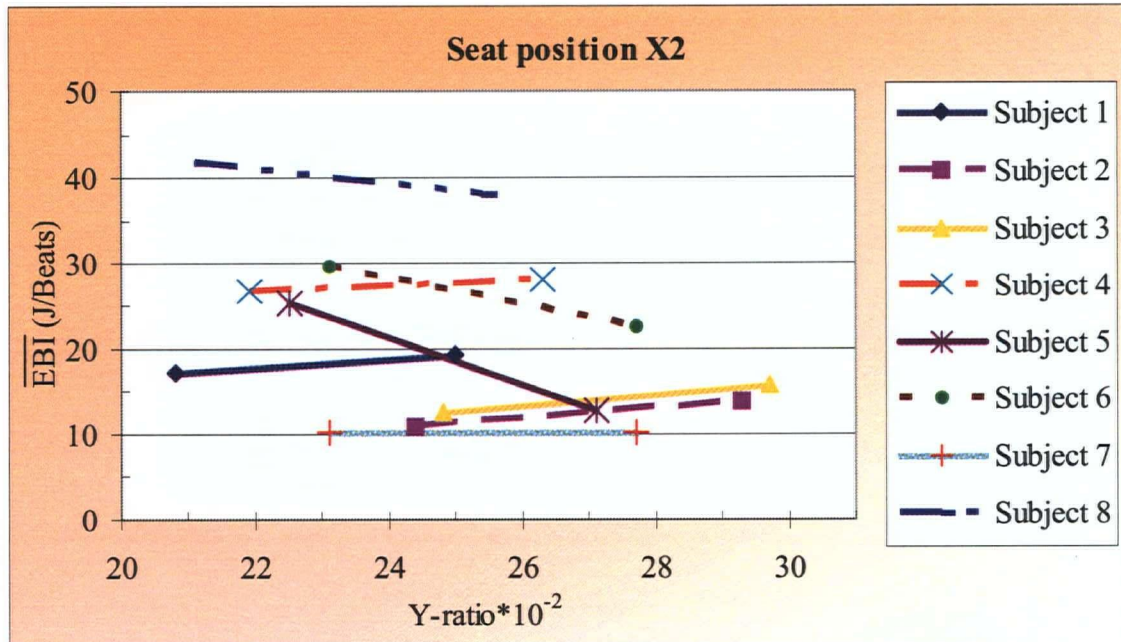


Figure 4.36 Variation of \overline{EBI} against Y-ratio at X2.

4.4.3.5 Horizontal Seat Position X3

Figures 4.37 and 4.38 show that both \overline{WUJII} and \overline{WUJII}' increase by increasing Y-ratio for six subjects. An increasing trend for the average values of injury indices against Y-ratio at X3 can be seen.

Figure 4.39 shows that \overline{EBI} increases by increasing Y-ratio for four subjects. \overline{EBI} decreases for three other subjects. Subject 5 did not show considerable variation for \overline{EBI} against Y-ratio.

Using repeated-measures ANOVA the results did not show significant relationship between the indices and the seat height at horizontal seat position X3.

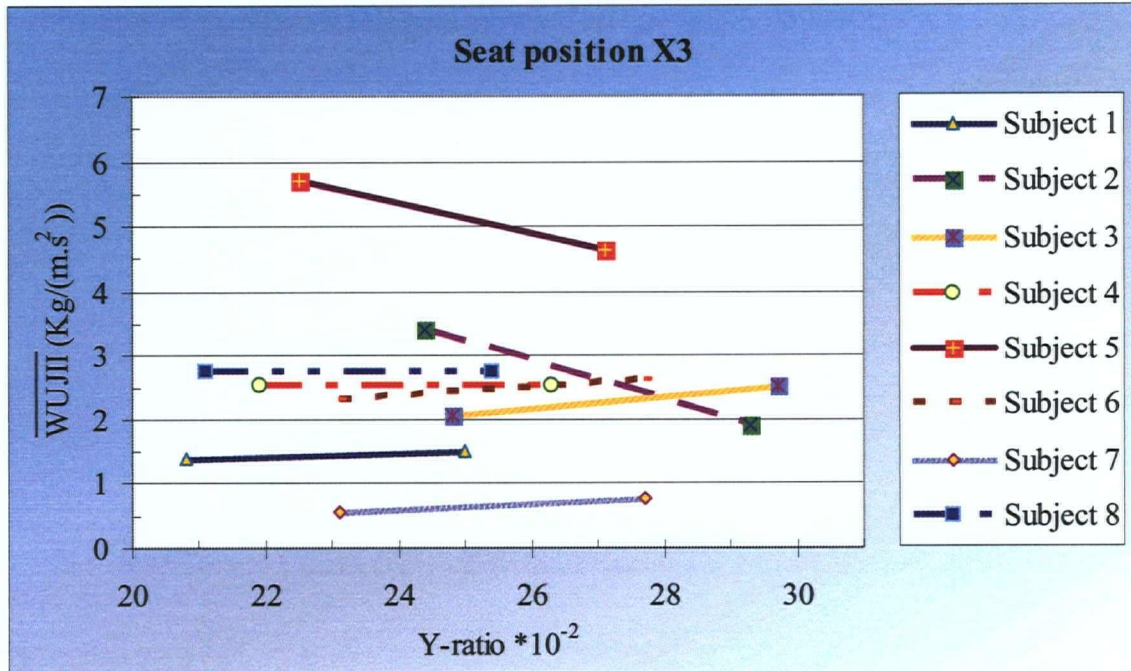


Figure 4.37 Variation of \overline{WUJII} against Y-ratio at X3.

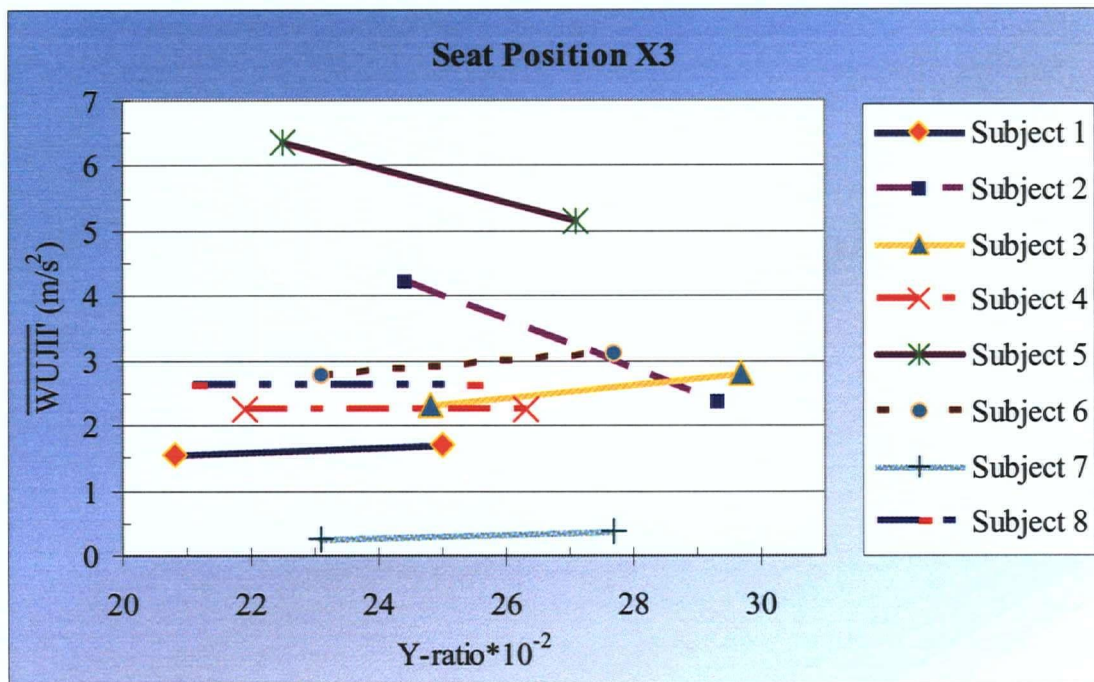


Figure 4.38 Variation of $\overline{WUJII'}$ against Y-ratio at X3.

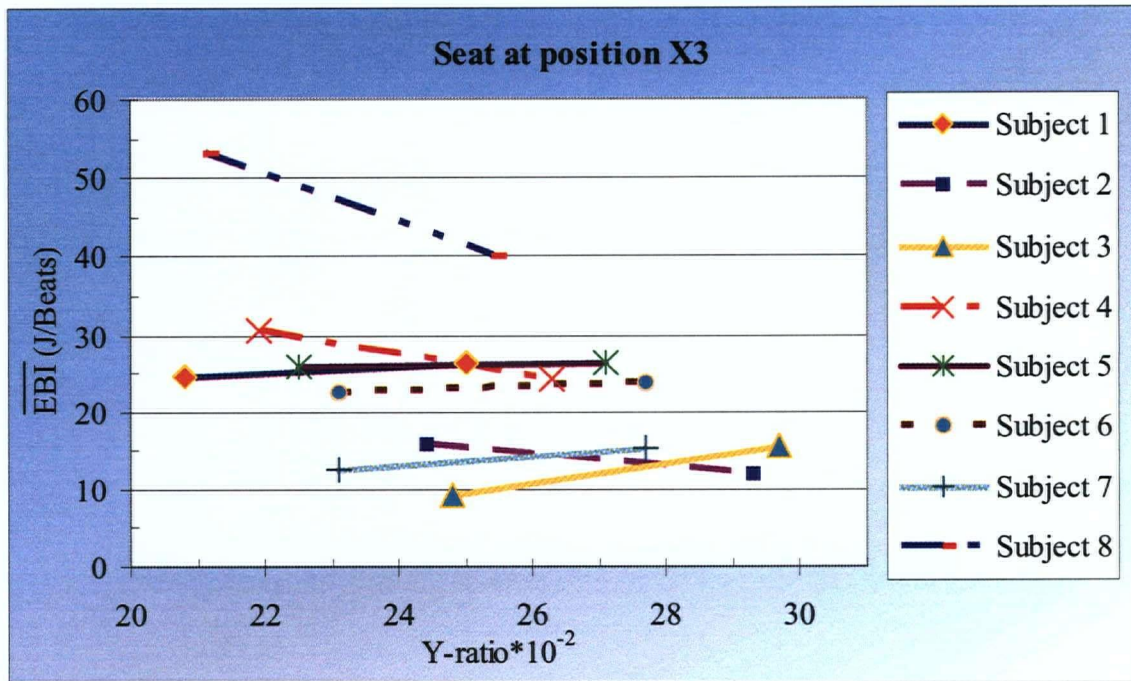


Figure 4.39 Variation of \overline{EBI} against Y-ratio at X3.

4.4.3.6 Optimum Seat Position

To determine the optimum seat position for a user at a propulsion velocity the Bivariate Quadratic Function (BQF) was used. BQF method requires at least nine tests. This method was performed for subjects 7 and 8 that were able to perform nine tests at nine seat positions. The approximate locations of X1 to X3 and Y1 to Y3 are shown in the X-ratio - Y-ratio plane of the following figures for ease of reference.

Figure 4.40 presents a saddle surface and illustrates the lowest \overline{WUJII} , between Y1 and Y2, and close to X1 for subject 7. The lowest value of \overline{WUJII}' is seen in Figure 4.41 almost at the same location as the lowest \overline{WUJII} . Figure 4.42 shows the response surface for \overline{EBI} against X and Y-ratios for subject 7. It shows that the maximum \overline{EBI} appears close to Y2 and X1.

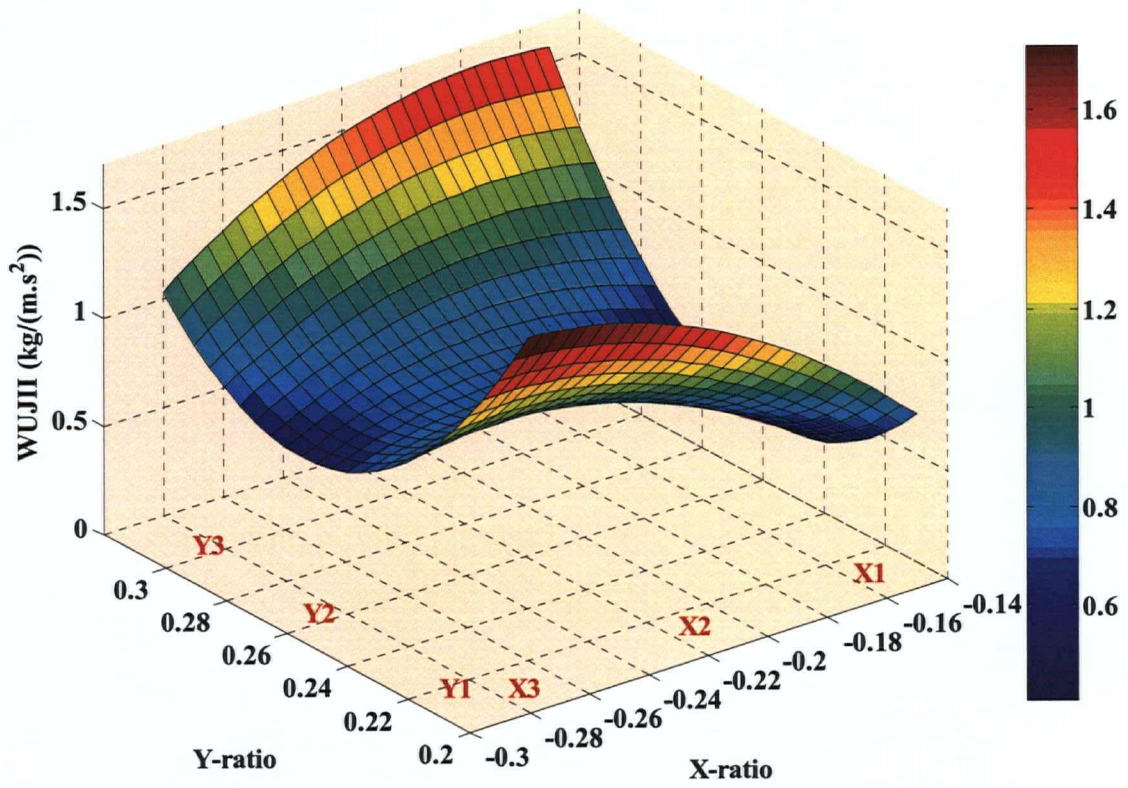


Figure 4.40 Variation of \overline{WUJII} versus seat position, for subject 7.

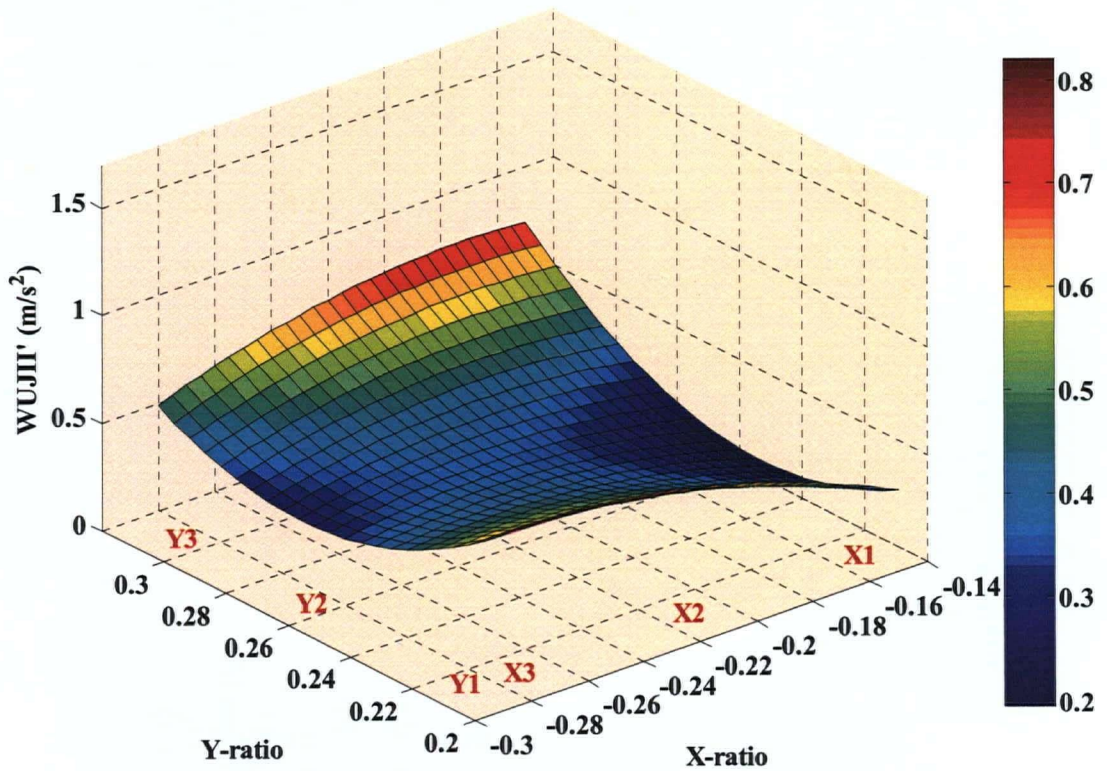


Figure 4.41 Variation of \overline{WUJII}' versus seat position, for subject 7.

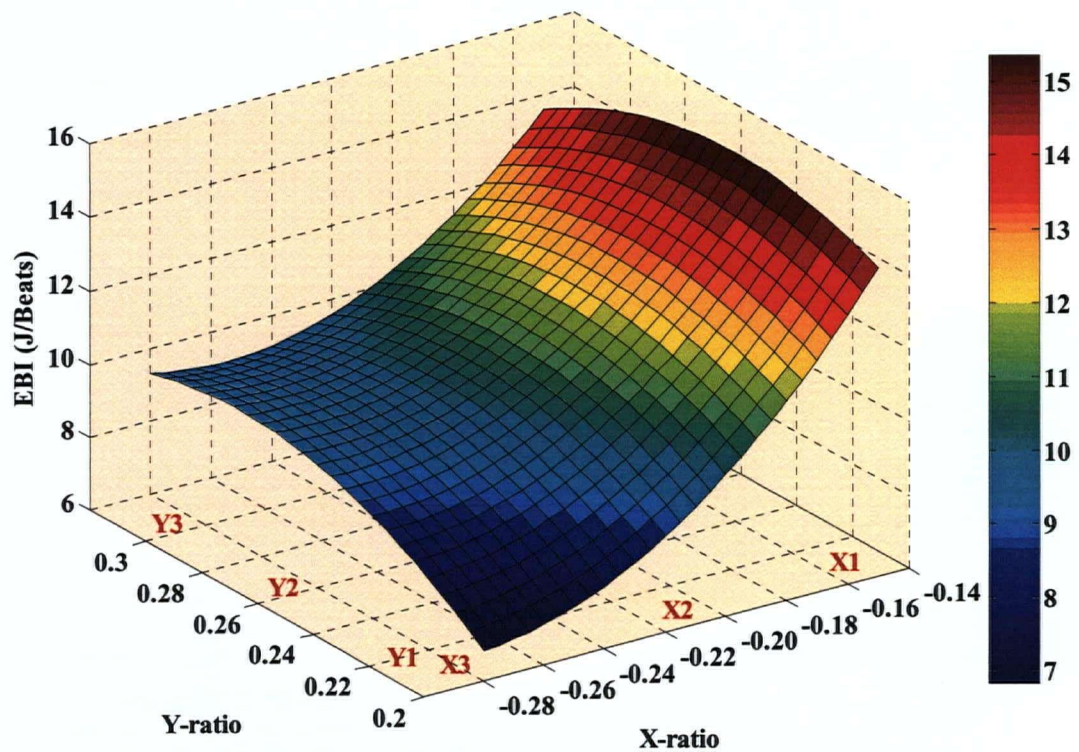


Figure 4.42 Variation of $\overline{\text{EBI}}$ versus seat position, for subject 7.

Considering the general form of BQF as in Equation 4.12 and by using the MATLAB[®] software, the coefficients and constants of the response equations for subject 7 were determined (Table 4.12).

Table 4.12 The coefficients and constants for the response equations that determine the indices at different seat positions for subject 7.

Coefficients & Constant Index	b_1	b_2	b_3	b_4	b_5	b_6
EBI	401.785	-365.205	273.914	150.773	-213.573	24.520
WUJII	-48.251	200.876	-46.751	-83.883	94.303	6.447
WUJII'	-22.929	95.426	-22.234	-39.828	44.870	3.055

The same procedure was performed for subject 8 and the results are presented in Figures 4.43–4.45. Figure 4.43 shows that the maximum value of \overline{WUJII} occurs close to Y2 and X1. The maximum value of \overline{WUJII}' is shown in Figure 4.44 at the same location as the maximum \overline{WUJII} . Figure 4.45 shows that the maximum value of \overline{EBI} is at X1 and Y1 for subject 8. The minimum value appears in the opposite side of the maximum value.

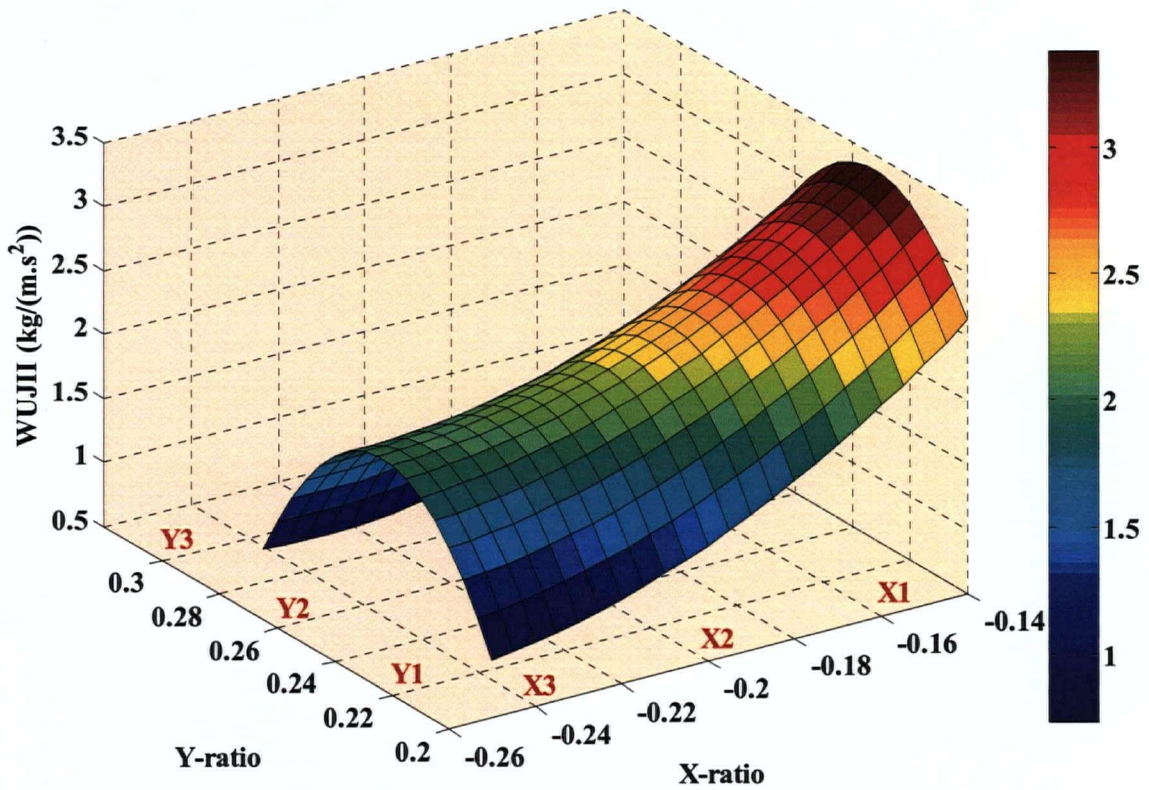


Figure 4.43 Variation of \overline{WUJII} versus seat position, for subject 8.

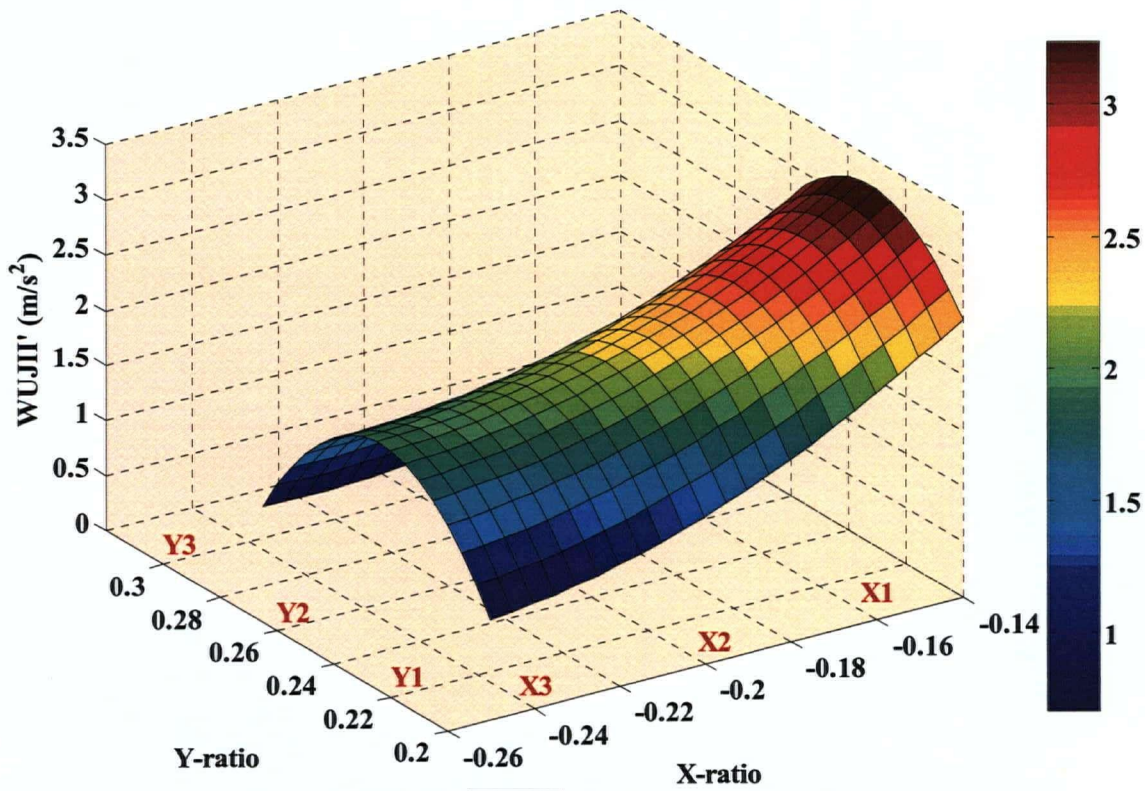


Figure 4.44 Variation of $\overline{WUJII'}$ versus seat position, for subject 8.

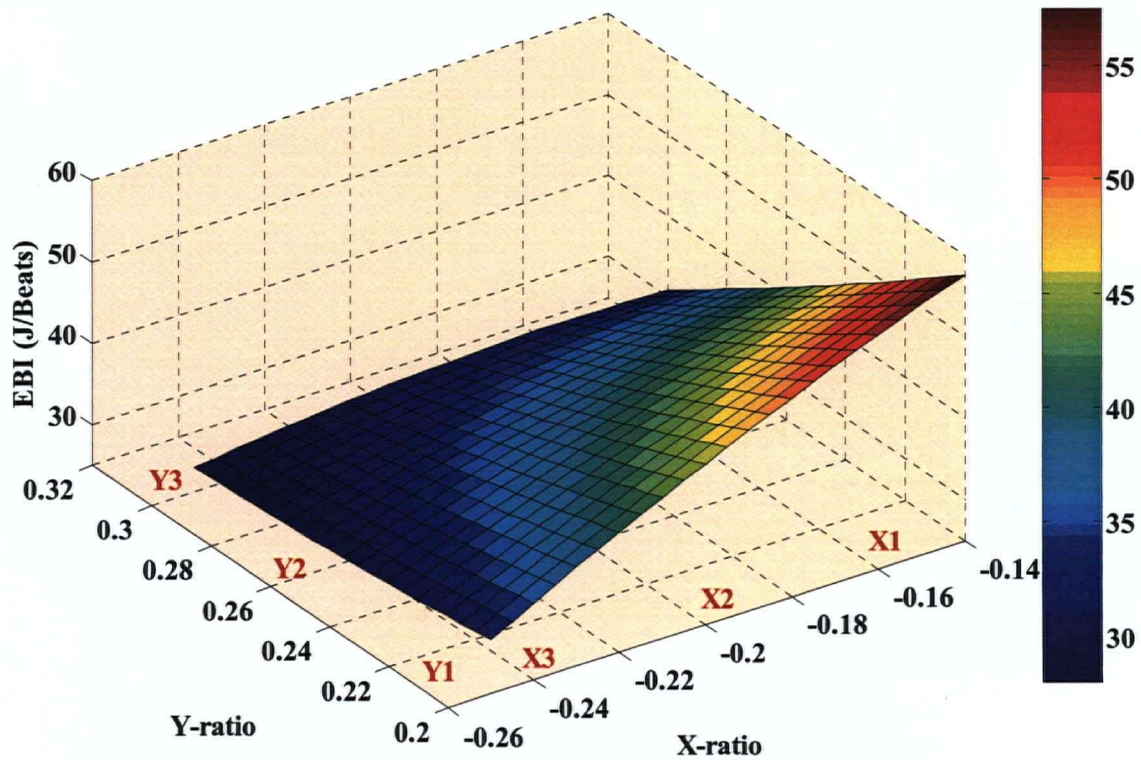


Figure 4.45 Variation of \overline{EBI} versus seat position for subject 8.

The coefficients and constants of the related response equations for subject 8 have been determined and presented in Table 4.13:

Table 4.13 The coefficients and constants for the response equations that determine the indices at different seat positions for subject 8.

Coefficients & Constant Index	b_1	b_2	b_3	b_4	b_5	b_6
EBI	-414.777	189.879	488.559	652.596	2079.642	198.779
WUJII	106.198	-718.477	72.073	323.304	-76.75	-27.430
WUJII'	101.662	-686.740	68.995	300.985	-73.546	-26.203

4.5 Conclusions

In this chapter, a new method for determining the optimum seat position for the MWU was introduced. Description of the study population, the demographic and anthropometric data were given. The test protocol and experimental setup were explained. The kinematic and kinetic parameters and values of the proposed indices were calculated for each subject at different seat positions. The optimum positions for the users were determined by using the values of indices at different settings. The results of the experiments answered four research questions.

In this study, because of the small sample size of the subjects we performed the statistical analysis for estimating the Type I or Alfa error. We can decrease the Type II or Beta error by increasing the sample size of the subjects.

The results showed that the average values of the injury indices for all subjects increase considerably by increasing the linear wheelchair velocity ($p < 0.01$). This result verifies the direct effect of velocity on the injury indices. Therefore, one may conclude that higher propulsion velocity will increase the risk of injury. Boninger et al. [4,69] reported that the flexion/extension and rotation angles for the shoulder and elbow joint of MWUs, as well as applied radial force, increase with increasing propulsion speeds confirming our results.

However, a significant relationship was not observed between the values of $\overline{\text{EBI}}$ and velocity. Efficient propulsion velocity is therefore case dependent, and relates to the physiological, anatomical and technical characteristics of the subjects. Efficient propulsion velocity for one subject would not necessarily be the same for the others, and should be determined individually. This result corroborates the report of Mukherjee et al. [38] that there is no specific relationship between the propulsion speed and efficiency, and that the energy-efficient propulsion speed is related to the user's freely chosen speed as a characteristic of the subjects.

Considering the results for the constant speed and fixed seat height experiments, one may say it is possible that the values of $\overline{\text{EBI}}$ increase by moving the seat forward related to the wheel axle ($p < 0.05$). Whereas, the average values of the injury indices may decrease by moving the seat backward ($p < 0.05$). We know of no other research that investigated the variation of the GME with respect to the horizontal seat position with constant speed of propulsion. However, the report of Cooper [12, page 271] confirms our results for the injury indices. He explained that if the seat is too far forward, the shoulder will be excessively extended and internally rotated, which may lead to rotator cuff injury.

Also, the results of Boninger et al. [35] report that more forward seat position can increase median nerve injury that compliment above results.

Our results indicated that the average values of the injury indices and $\overline{\text{EBI}}$ can be 5.6–29.9% and 5–27.5%, respectively. Lower seat height showed lower variation for the results. The higher variations mostly are related to the subjects whose index values changed significantly with respect to the X and Y-positions. Therefore, the indices appear to be sensitive to the seat position.

The response equations were determined for subjects 7 and 8 by using the BQF method. These equations can be used to determine the optimum seat position. The presented 3D-graphs for these two subjects show the optimum seat positions and indicate that the positions determined by using $\overline{\text{EBI}}$ and the average values of injury indices are not necessarily the same. These graphs illustrate the probable average values and variations of the indices at different positions by using the BQF method.

Subject 5 had the highest BMI and %BF, and subject 7 had the lowest, at the time of the experiments. They presented the highest and lowest average values of the injury indices for most of the test situations, respectively. This supports the work of Boninger et al. [23] and other researches [70,71] that BMI affects CTS and shoulder injuries. Also, the above figures showed that subjects 2, 3, and 4, who were younger and had less wheelchair experience, had lower $\overline{\text{EBI}}$ s.

In the next chapter, a method is introduced to determine the values of the injury indices at the upper limb joints of a wheelchair user. This method helps to determine the optimum wheelchair variables by considering the regarding concerns and priorities.

CHAPTER 5

Injury Assessment for the Upper Limb Joints

5.1 Introduction

In Chapter 1, the prevalence of pain in the upper limb joints of MWUs was discussed. Previous studies presented methods for measuring pain or injury were explained in Chapter 3. There are very few studies that determine the pain or injury at the upper limb joints. The previous methods have shortcomings as they use questionnaires rather than direct measurements, or focus only on measuring a specific factor.

In this chapter, the values of the proposed injury indices are calculated for different joints of the upper body for subjects 7 and 8. To do this, a 3D rigid-body dynamic model for the upper limb is presented, and a method (Method I) for calculating the upper limb joint forces and moments is described. Cooper [12] introduced the

structure of this method in 1995, and Vrongistinos [46] presented it with some differences in 2001. This method is reproduced here with some changes to the load calculations. The joint loads are calculated using the new method and are used as part of the required data for determining the values of the injury indices.

5.2 Method I

In Chapter 4, the test setup, the model, and the methods were explained. The upper limb segments were assumed as rigid-bodies to be able to use the dynamics of the rigid body.

In this chapter, the focus is on determining the optimum wheelchair variables for each user considering the risk of the injury for the upper limb joints. Subjects 7 and 8 participated in this part of the experiments. To define the optimum position, nine tests at different combinations of three X-positions and three Y-positions for each user were performed at a constant propulsion speed.

WUJII and WUJII' using Equations 3.14 and 3.15 were used as criteria to determine the optimum position. The values of the injury indices were determined at shoulder, elbow and wrist joints for each subject. The kinematic data acquired by VICON motion analysis system, the kinetic data measured by the instrumented wheel, and the subject's anthropometric data were used in the model to determine the joint loads as part of the required data to calculate the injury indices. The optimum positions determined minimize the probable injuries at different joints for each subject.

Considering the general form of Bivariate Quadratic Function (BQF) and using the MATLAB[®] software, the coefficients and constants of the related equations were obtained for the subjects.

5.2.1 The Kinematics of the Upper Limb

To determine the orientation of each body segment with respect to a fixed coordinate system in a 3D analysis, a frame is attached to the Center Of Mass (COM) of the segment, and then a description of this frame is given relative to the reference system. Figure 5.1 shows local frame B ($\{B\}$) attached to COM of a segment. A description of $\{B\}$ relative to global frame A ($\{A\}$) gives the orientation of the segment. To describe the orientation of $\{B\}$, the unit vectors of its three principal axes with respect to $\{A\}$ are determined. ${}^A P_{BORG}$ is the vector that determines the position of the origin of $\{B\}$ with respect to $\{A\}$.

\hat{X}_B , \hat{Y}_B , and \hat{Z}_B are the unit vectors giving the principal directions of $\{B\}$. When written in terms of $\{A\}$, they are shown as ${}^A \hat{X}_B$, ${}^A \hat{Y}_B$, and ${}^A \hat{Z}_B$. If one stacks these three unit vectors together as columns of a 3×3 matrix, a new matrix ${}^A R_B$ is obtained, which is referred to as the rotation matrix (Equation 5.1) [96].

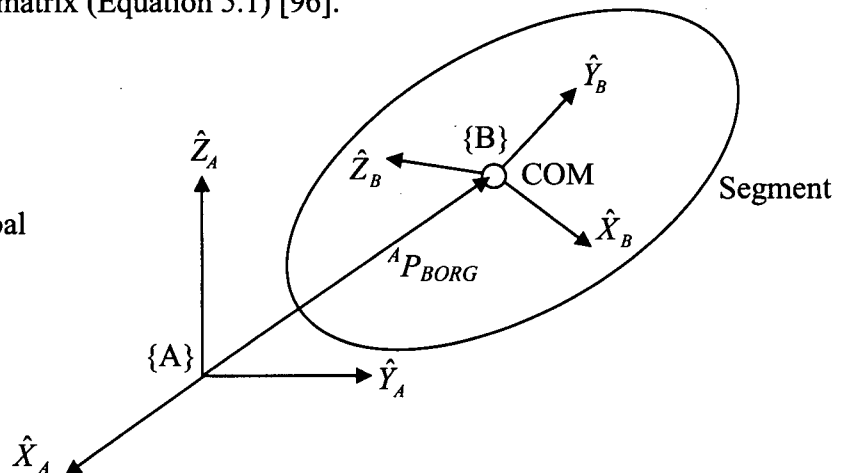


Figure 5.1 Local and global frames for a rigid body.

$${}^A R_B = \begin{bmatrix} {}^A \hat{X}_B & {}^A \hat{Y}_B & {}^A \hat{Z}_B \end{bmatrix} = \begin{bmatrix} r_{11} & r_{12} & r_{13} \\ r_{21} & r_{22} & r_{23} \\ r_{31} & r_{32} & r_{33} \end{bmatrix} \quad (5.1)$$

where, r_{11-33} are the components of ${}^A \hat{X}_B$, ${}^A \hat{Y}_B$, and ${}^A \hat{Z}_B$.

Figure 5.2 shows a randomly selected point E in {B} and its relationship to {A}. ${}^A P_E$ represents the position vector of point E with respect to {A}, and ${}^B P_E$ is the vector that shows the position of point E with respect to {B}.

$${}^A P_E = {}^A R_B {}^B P_E + {}^A P_{BORG} \quad (5.2)$$

In the case where the local and global coordinate systems are concentric and one needs the information with respect to the global coordinate system, the following equation is used:

$${}^A P_E = {}^A R_B {}^B P_E \quad (5.3)$$

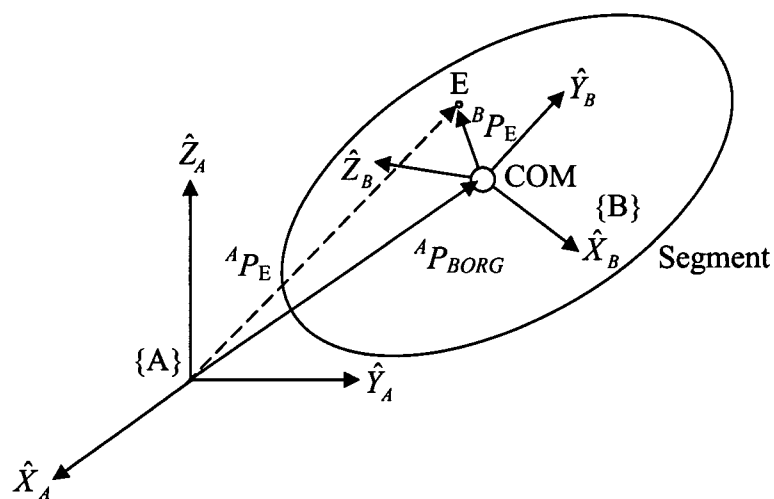


Figure 5.2 General transformation of a vector.

5.2.1.1 Velocity of the Segment

The linear velocity of a point with respect to {A} is obtained at any instant by using the position vectors as

$${}^A V_E = \frac{d}{dt} {}^A P_E = \lim_{\Delta t \rightarrow 0} \frac{{}^A P_E(t + \Delta t) - {}^A P_E(t)}{\Delta t} \quad (5.4)$$

where E is a point in {B}, A represent {A}, and P is its position vector, and ${}^A V_E$ is the linear velocity of point E with respect to {A} [96].

Euler angles, Bryant angles, and Euler parameter are different methods, which are commonly used to derive the rotation matrix. In this study, three non-collinear markers on each segment, and the Euler angles were used to define the segments in the local coordinate system [12,46].

5.2.1.2 Z-Y-X Euler Angles

One method of describing the orientation of {B} with respect to {A} is as follows. Start with the frame coinciding with known {A}, first rotate {B} about \hat{Z}_B by an angle α to obtain {A'}, then rotate about the new \hat{Y}_B by an angle β to find {A''}, and finally rotate about the last \hat{X}_B by an angle γ [96,97]. Frames A' and A'' are the intermediate frames for transforming {A} to {B}.

These rotations give us ${}^B R_A$ as

$${}^B R_A = ROT({}^B \hat{X}, \gamma) ROT({}^B \hat{Y}, \beta) ROT({}^B \hat{Z}, \alpha) \quad (5.5)$$

Because ${}^B R^{-1} = {}^A R$, we can compute ${}^A R$ as

$${}^A R = ROT({}^B \hat{Z}, \alpha) \quad ROT({}^B \hat{Y}, \beta) \quad ROT({}^B \hat{X}, \gamma) \quad (5.6a)$$

$${}^A R = \begin{bmatrix} c\alpha & -s\alpha & 0 \\ s\alpha & c\alpha & 0 \\ 0 & 0 & 1 \end{bmatrix} \begin{bmatrix} c\beta & 0 & s\beta \\ 0 & 1 & 0 \\ -s\beta & 0 & c\beta \end{bmatrix} \begin{bmatrix} 1 & 0 & 0 \\ 0 & c\gamma & -s\gamma \\ 0 & s\gamma & c\gamma \end{bmatrix} \quad (5.6b)$$

$${}^A R = \begin{bmatrix} c\alpha.c\beta & c\alpha.s\beta.s\gamma - s\alpha.c\gamma & c\alpha.s\beta.c\gamma + s\alpha.s\gamma \\ s\alpha.c\beta & s\alpha.s\beta.s\gamma + c\alpha.c\gamma & s\alpha.s\beta.c\gamma - c\alpha.s\gamma \\ -s\beta & c\beta.s\gamma & c\beta.c\gamma \end{bmatrix} \quad (5.6c)$$

where $c\alpha = \cos(\alpha)$ and $s\alpha = \sin(\alpha)$, etc. ${}^A R$ is determined by using Equations 5.1 and 5.6c as

$${}^A R = \begin{bmatrix} r_{11} & r_{12} & r_{13} \\ r_{21} & r_{22} & r_{23} \\ r_{31} & r_{32} & r_{33} \end{bmatrix} = \begin{bmatrix} c\alpha.c\beta & c\alpha.s\beta.s\gamma - s\alpha.c\gamma & c\alpha.s\beta.c\gamma + s\alpha.s\gamma \\ s\alpha.c\beta & s\alpha.s\beta.s\gamma + c\alpha.c\gamma & s\alpha.s\beta.c\gamma - c\alpha.s\gamma \\ -s\beta & c\beta.s\gamma & c\beta.c\gamma \end{bmatrix} \quad (5.7)$$

The results for Z-Y-X Euler angles from a known rotation matrix are as follows:

$$\alpha = \text{Atan2}(r_{21}, r_{11}) \quad (5.8a)$$

$$\beta = \text{Atan2}(-r_{31}, \pm \sqrt{r_{11}^2 + r_{21}^2}) \quad (5.8b)$$

$$\gamma = \text{Atan2}(r_{32}, r_{33}) \quad (5.8c)$$

Considering the positive square root in the formula for β , a single solution was computed. The range for β was $-90 \leq \beta \leq 90$.

5.2.1.3 Determining the Directional Cosines

In this study, three markers were placed on three non-collinear landmarks to determine the position and orientation of each segment of the upper body of the MWU. The positions of the markers were tracked during the tests using the VICON Motion Analysis System with a sampling frequency of 100 Hz. Points 1, 2, and 3 represent the three markers on a typical segment, and E_1 , E_2 are the position vectors between points 3 and 1, and between points 3 and 2, respectively. Directional cosines (r_{ij}) were determined for the rotation matrix, which transforms the coordinates from the local frame to another, with the origin of the local and the orientation of the global coordinate system. $\{B\}$ is transformed to the center of mass of the segment. $\{A\}$ and $\{B\}$ are concentric. Figure 5.3 shows the directional cosines of the x-axis of $\{B\}$ with respect to the three axes of $\{A\}$.

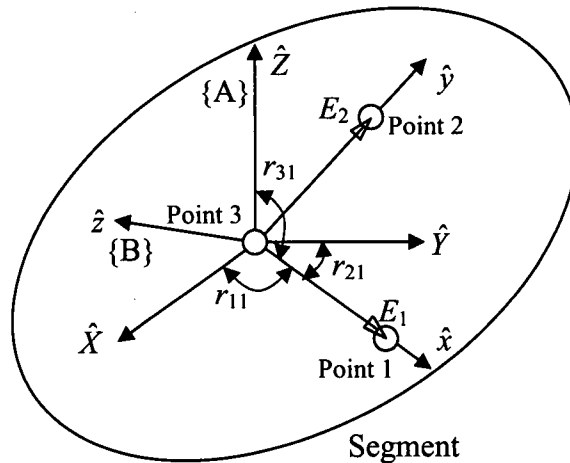


Figure 5.3 Directional cosines of rotation matrix for the axes of $\{B\}$ with respect to $\{A\}$.

To determine r_{ij} , the unit vectors of the axes of frames $\{A\}$ and $\{B\}$ are calculated. The unit vectors of the axes of the global coordinate system $\{A\}$ are

$$\hat{I} = \begin{bmatrix} 1 \\ 0 \\ 0 \end{bmatrix}, \quad \hat{J} = \begin{bmatrix} 0 \\ 1 \\ 0 \end{bmatrix}, \quad \hat{K} = \begin{bmatrix} 0 \\ 0 \\ 1 \end{bmatrix} \quad (5.9)$$

To determine the unit vectors of the axes of frame {B}, the vectors E_1 and E_2 are calculated as

$$E_1 = \begin{bmatrix} x_1 - x_3 \\ y_1 - y_3 \\ z_1 - z_3 \end{bmatrix}, \quad E_2 = \begin{bmatrix} x_2 - x_3 \\ y_2 - y_3 \\ z_2 - z_3 \end{bmatrix} \quad (5.10)$$

where $x_{1,2,3}$, $y_{1,2,3}$ and $z_{1,2,3}$ are the position components of the points 1, 2 and 3 with respect to the global coordinate system.

The unit vectors are now determined as

$$\hat{E}_1 = \frac{E_1}{|E_1|}, \quad \hat{E}_2 = \frac{E_2}{|E_2|}, \quad \hat{E}_3 = E_1 \times E_2 \quad (5.11)$$

The directional cosines are calculated using Equations 5.9 and 5.11 as

$$\begin{aligned} r_{11} &= \hat{I} \cdot \hat{E}_1, & r_{12} &= \hat{I} \cdot \hat{E}_2, & r_{13} &= \hat{I} \cdot \hat{E}_3 \\ r_{21} &= \hat{J} \cdot \hat{E}_1, & r_{22} &= \hat{J} \cdot \hat{E}_2, & r_{23} &= \hat{J} \cdot \hat{E}_3 \\ r_{31} &= \hat{K} \cdot \hat{E}_1, & r_{32} &= \hat{K} \cdot \hat{E}_2, & r_{33} &= \hat{K} \cdot \hat{E}_3 \end{aligned} \quad (5.12)$$

Linear velocity of a point on a segment is determined as

$${}^B V_E = \frac{d}{dt} {}^B P_E = \lim_{\Delta t \rightarrow 0} \frac{{}^B P_E(t + \Delta t) - {}^B P_E(t)}{\Delta t} \quad (5.13)$$

where ${}^B V_E$ and ${}^B P_E$ are the velocity and position vector of a selected point E on the segment with respect to frame B.

Angular velocity of the segment with respect to the global coordinate system, ${}^A \Omega_B$, can be determined at any instant by using the time derivatives of α , β and γ as

$${}^A \Omega_B = \dot{\alpha} {}^A \hat{k} + \dot{\beta} {}^A \hat{j}_{A'} + \dot{\gamma} {}^A \hat{i}_{A'} \quad (5.14)$$

where ${}^A \hat{k}$, ${}^A \hat{j}_{A'}$ and ${}^A \hat{i}_{A'}$ are the unit vectors for the z, y and x-axes of the frames {A}, {A'} and {A''} with respect to the frame {A}, respectively [96,97]. The time derivatives of α , β and γ are determined as

$$\dot{\alpha} = \frac{d}{dt} \alpha = \lim_{\Delta t \rightarrow 0} \frac{\alpha(t + \Delta t) - \alpha(t)}{\Delta t} \quad (5.15a)$$

$$\dot{\beta} = \frac{d}{dt} \beta = \lim_{\Delta t \rightarrow 0} \frac{\beta(t + \Delta t) - \beta(t)}{\Delta t} \quad (5.15b)$$

$$\dot{\gamma} = \frac{d}{dt} \gamma = \lim_{\Delta t \rightarrow 0} \frac{\gamma(t + \Delta t) - \gamma(t)}{\Delta t} \quad (5.15c)$$

${}^A \hat{k}$, ${}^A \hat{j}_{A'}$ and ${}^A \hat{i}_{A'}$ are calculated by using the following equations:

$${}^A \hat{k} = \begin{bmatrix} 0 \\ 0 \\ 1 \end{bmatrix} \quad (5.16a)$$

$${}^A j_{A'} = \begin{bmatrix} c\alpha & -s\alpha & 0 \\ s\alpha & c\alpha & 0 \\ 0 & 0 & 1 \end{bmatrix} \begin{bmatrix} 0 \\ 1 \\ 0 \end{bmatrix} = \begin{bmatrix} -s\alpha \\ c\alpha \\ 0 \end{bmatrix} \quad (5.16b)$$

$${}^A i_{A'} = \begin{bmatrix} c\alpha & -s\alpha & 0 \\ s\alpha & c\alpha & 0 \\ 0 & 0 & 1 \end{bmatrix} \begin{bmatrix} c\beta & 0 & s\beta \\ 0 & 1 & 0 \\ -s\beta & 0 & c\beta \end{bmatrix} \begin{bmatrix} 1 \\ 0 \\ 0 \end{bmatrix} = \begin{bmatrix} c\alpha \cdot c\beta \\ s\alpha \cdot c\beta \\ -s\beta \end{bmatrix} \quad (5.16c)$$

Substituting Equations 5.16 into Equation 5.14, the relation for ${}^A \Omega_B$ is determined as

$${}^A \Omega_B = \begin{bmatrix} 0 & -s\alpha & c\alpha \cdot c\beta \\ 0 & c\alpha & s\alpha \cdot c\beta \\ 1 & 0 & -s\beta \end{bmatrix} \begin{bmatrix} \dot{\alpha} \\ \dot{\beta} \\ \dot{\gamma} \end{bmatrix} \quad (5.17)$$

5.2.1.4 Acceleration of a Segment

Linear and angular acceleration of body segment can be determined at any instant by using the linear and angular velocity vectors as

$${}^B \dot{V}_E = \frac{d}{dt} {}^B V_E = \lim_{\Delta t \rightarrow 0} \frac{{}^B V_E(t + \Delta t) - {}^B V_E(t)}{\Delta t} \quad (5.18a)$$

$${}^A \dot{\Omega}_B = \frac{d}{dt} {}^A \Omega_B = \lim_{\Delta t \rightarrow 0} \frac{{}^A \Omega_B(t + \Delta t) - {}^A \Omega_B(t)}{\Delta t} \quad (5.18b)$$

where ${}^B V_E$ is the linear velocity of point E in the frame B [96].

Linear acceleration— The linear velocity of the vector ${}^B P_E$ with respect to frame {A} is given as

$${}^A V_E = {}^A V_{BORG} + {}^A R^B V_E + {}^A \Omega_B \times {}^A R^B P_E \quad (5.19)$$

The linear acceleration of the vector ${}^A P_E$ is determined by calculating the derivative of Equation 5.19 as

$${}^A \dot{V}_E = {}^A \dot{V}_{BORG} + {}^A R^B \dot{V}_E + 2{}^A \Omega_B \times {}^A R^B V_E + {}^A \dot{\Omega}_B \times {}^A R^B P_E + {}^A \Omega_B \times ({}^A \Omega_B \times {}^A R^B P_E) \quad (5.20)$$

In case ${}^B P_E$ is constant, Equation 5.20 simplifies to

$${}^A \dot{V}_E = {}^A \dot{V}_{BORG} + {}^A \dot{\Omega}_B \times {}^A R^B P_E + {}^A \Omega_B \times ({}^A \Omega_B \times {}^A R^B P_E) \quad (5.21)$$

Angular acceleration— Considering three frames {A}, {B} and {C}, if frame {B} rotates relative to {A} with angular velocity ${}^A \Omega_B$, and {C} rotates relative to frame {B} with ${}^B \Omega_C$, then ${}^A \Omega_C$ is determined as

$${}^A \Omega_C = {}^A \Omega_B + {}^A R^B \Omega_C \quad (5.22)$$

and by differentiating, we obtain

$${}^A \dot{\Omega}_C = {}^A \dot{\Omega}_B + {}^A R^B \dot{\Omega}_C + {}^A \Omega_B \times {}^A R^B \Omega_C \quad (5.23)$$

When ${}^B \Omega_C$ is zero, Equation 5.23 simplifies to

$${}^A\dot{\Omega}_C = {}^A\dot{\Omega}_B \quad (5.24)$$

5.2.2 Kinetics of the Upper Limbs

MWP produces repetitive stress on the user's joints. Determining the loads that cause this stress can help researchers to better understand the biomechanics of MWP. It is possible to directly measure moments and forces in the joints by surgically implanting transducers! However, this method is used in special circumstances. One case is with the implantable prostheses. Indirect estimation of joints loads can be made from the measured external loads, kinematic data (trajectory points of the upper limb), and anthropometric data. Knowledge of the time profiles of the joint loads is necessary for an understanding of the cause and implications for any movement [12].

In this research, rigid linkage system model was used to calculate net joint action/reaction forces and net muscle moments using inverse solution with the Newton-Euler method. The lengths of the segments are assumed to remain constant during the motion. The free body diagrams for all segments are similar.

5.2.3 Mass Distribution

Each segment is assumed as a rigid body, which can move in three dimensions. Inertia tensor is required to describe the moment of the segment. The inertia tensor with respect to $\{A\}$ is expressed as the 3×3 matrix:

$${}^A I = \begin{bmatrix} I_{xx} & -I_{xy} & -I_{xz} \\ -I_{xy} & I_{yy} & -I_{yz} \\ -I_{xz} & -I_{yz} & I_{zz} \end{bmatrix} \quad (5.25)$$

The elements I_{xx} , I_{yy} and I_{zz} are called the mass moments of inertia. The elements with mixed indices are called mass products of inertia. These six independent quantities depend on the position and orientation of the frame in which they are defined. If we consider the axes of calculating the moment of inertia to coincide with the principal axes, the products of inertia will be zero, and the corresponding mass moments will be the principal moments of inertia.

To determine the change of inertia tensor under translation of the reference coordinate system, the parallel axes theorem is used, which relates the inertia tensor in a frame with origin at COM to the inertia tensor with respect to another reference frame. Following equations present this theorem [96]:

$${}^A I_{zz} = {}^C I_{zz} + m(x_c^2 + y_c^2) \quad (5.26a)$$

$${}^A I_{xy} = {}^C I_{xy} + mx_c y_c \quad (5.26b)$$

where x_c , y_c , and z_c are the coordinates of the center of mass with respect to {A}. The remaining moments and products of inertia are computed from permutation of x , y , and z in Equations 5.26.

In this study, the shape of the upper arm and forearm were assumed as a frustum of cone, and that of the hand as a rectangular prism. The local frame of each segment is

placed at its own center of mass. Figure 5.4 shows a frustum of conic segment and its local frame $\{C\}$. H and h are the height of the frustum and its center of mass in the x direction.

The inertia tensors with respect to the local frame at the center of mass, which is the principal frame, is determined as

$${}^c I = \begin{bmatrix} I_{xx} & 0 & 0 \\ 0 & I_{yy} & 0 \\ 0 & 0 & I_{zz} \end{bmatrix} \quad (5.27)$$

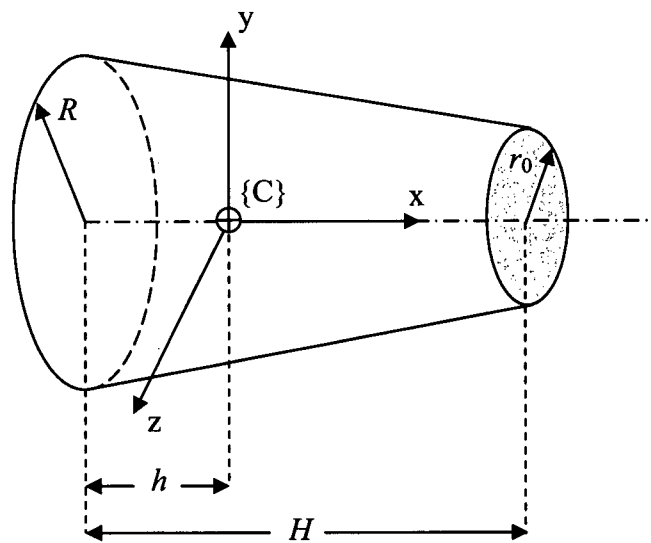


Figure 5.4 Frustum of conic rigid body with local frame on its center of mass.

where R and r_0 are the radius of the proximal (larger) and distal (smaller) ends of the frustum, respectively. The position of COM for the frustum is given by

$$h = \frac{H(R^2 + 2Rr_0 + 3r_0^2)}{4(R^2 + Rr_0 + r_0^2)} \quad (5.28)$$

The inertia tensor for the frustum is determined using Equations 5.29 as

$${}^c I_{yy} = {}^c I_{zz} = \frac{m}{20} \left[\frac{H^2(2R^2 + 6Rr_0 + 12r_0^2) - 3r_0^2 R^2}{R^2 + Rr_0 + r_0^2} - \frac{5H^2(R^2 + 2Rr_0 + 3r_0^2)^2}{4(R^2 + Rr_0 + r_0^2)^2} + 3(R^2 + r_0^2) \right] \quad (5.29a)$$

$${}^c I_{xx} = \frac{3m(R^5 - r_0^5)}{10(R^3 - r_0^3)} \quad (5.29b)$$

where m is the mass of the segment [98].

Figure 5.5 shows a rectangular prism segment, which represent the rigid body model for the hand. The local frame $\{C\}$ is located at COM. H_h , W_h and L_h are the parameters corresponding to the thickness, width and the length of the hand.

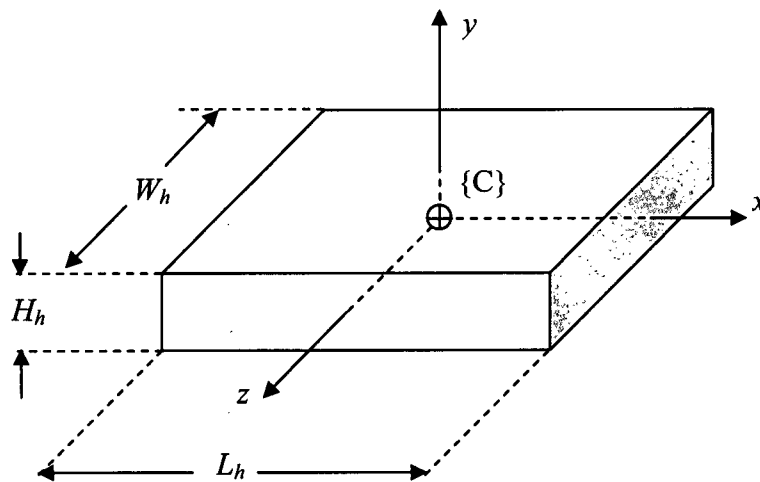


Figure 5.5 Rectangular prism rigid body with local frame at its center of mass.

The components of the inertia tensor for the rectangular prism are determined using Equations 5.30 as

$${}^c I_{xx} = \frac{m}{12}(W_h^2 + H_h^2), \quad {}^c I_{yy} = \frac{m}{12}(W_h^2 + L_h^2), \quad {}^c I_{zz} = \frac{m}{12}(H_h^2 + L_h^2) \quad (5.30)$$

5.2.4 Modeling

In linkage system model, four basic groups of loads act: 1- Gravitational forces (weights), 2- External forces and moments (reactions on the hand of the user), 3- Muscle and ligament forces (net muscle moments and joint forces), 4- Inertial loads. To calculate the net muscle moments and joint forces, three free body diagrams in sagittal (Figure 5.6), frontal (Figure 5.7), and transverse (Figure 5.8) planes, and the following force and moment balance equations are used.

$$\sum F_x = ma_x, \quad \sum F_y = ma_y, \quad \sum F_z = ma_z \quad (5.31a)$$

$$\sum M_x = \frac{d(I\omega_x)}{dt}, \quad \sum M_y = \frac{d(I\omega_y)}{dt}, \quad \sum M_z = \frac{d(I\omega_z)}{dt} \quad (5.31b)$$

where $a_{x,y,z}$ are the linear acceleration, and $\omega_{x,y,z}$ are the angular velocity components of the segment. All parameters are with respect to the global frame {A}[12,46].

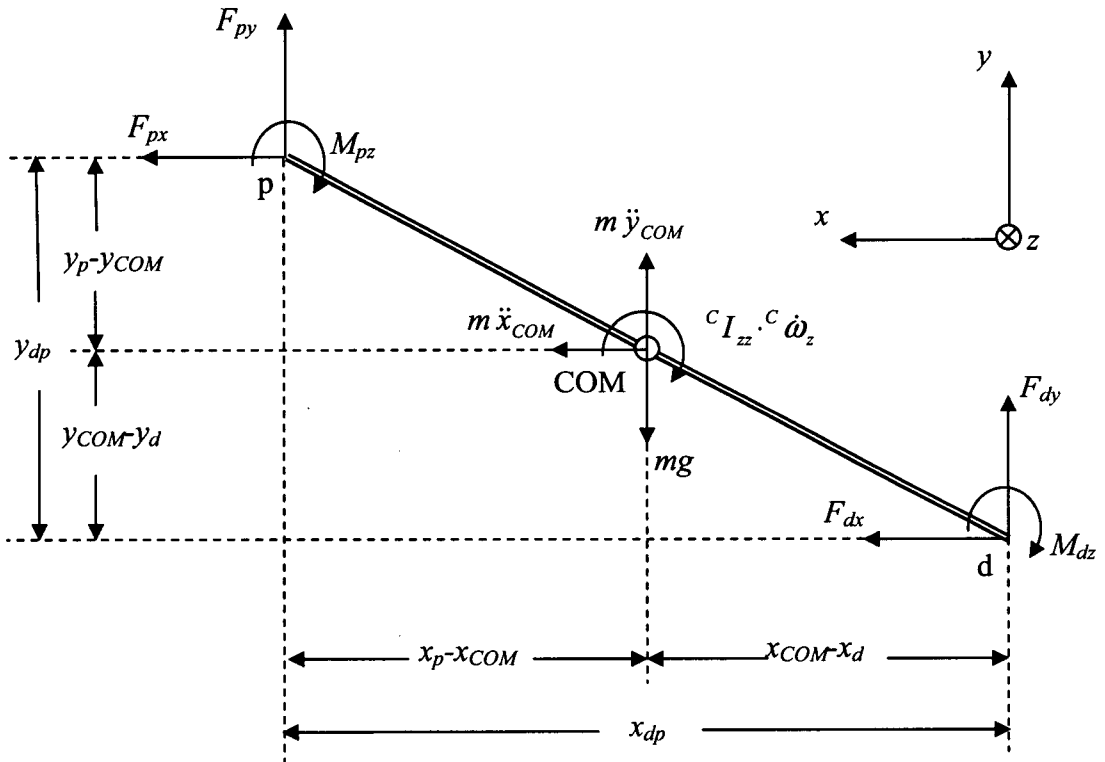


Figure 5.6 Free body diagram of a segment in sagittal plane.

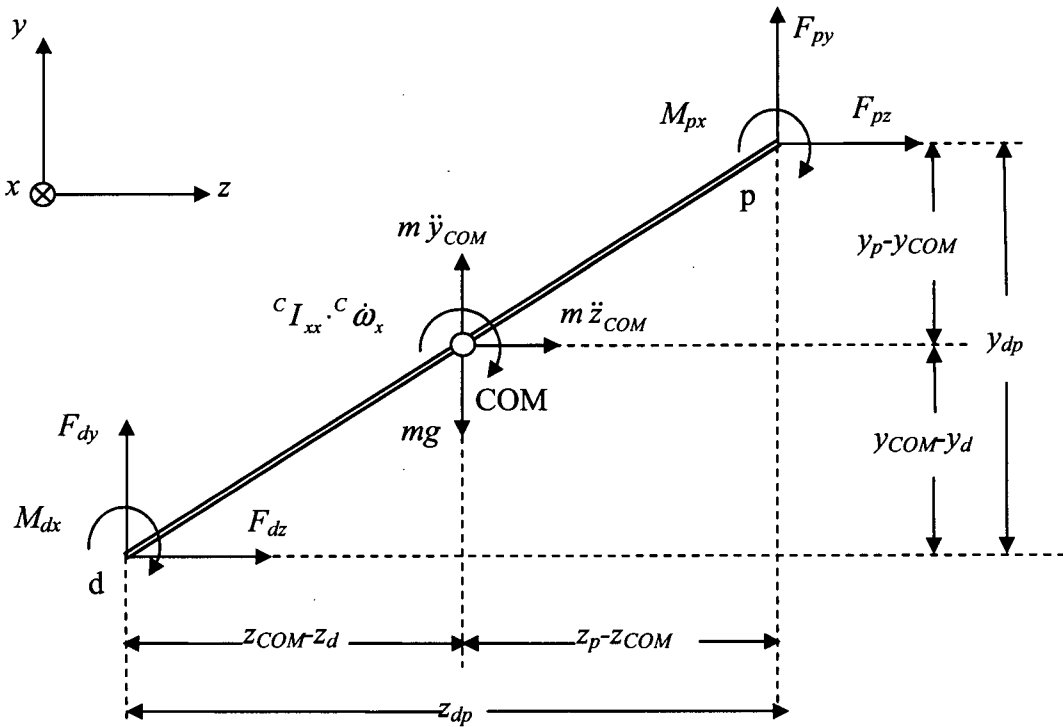


Figure 5.7 Free body diagram of a segment in frontal plane.

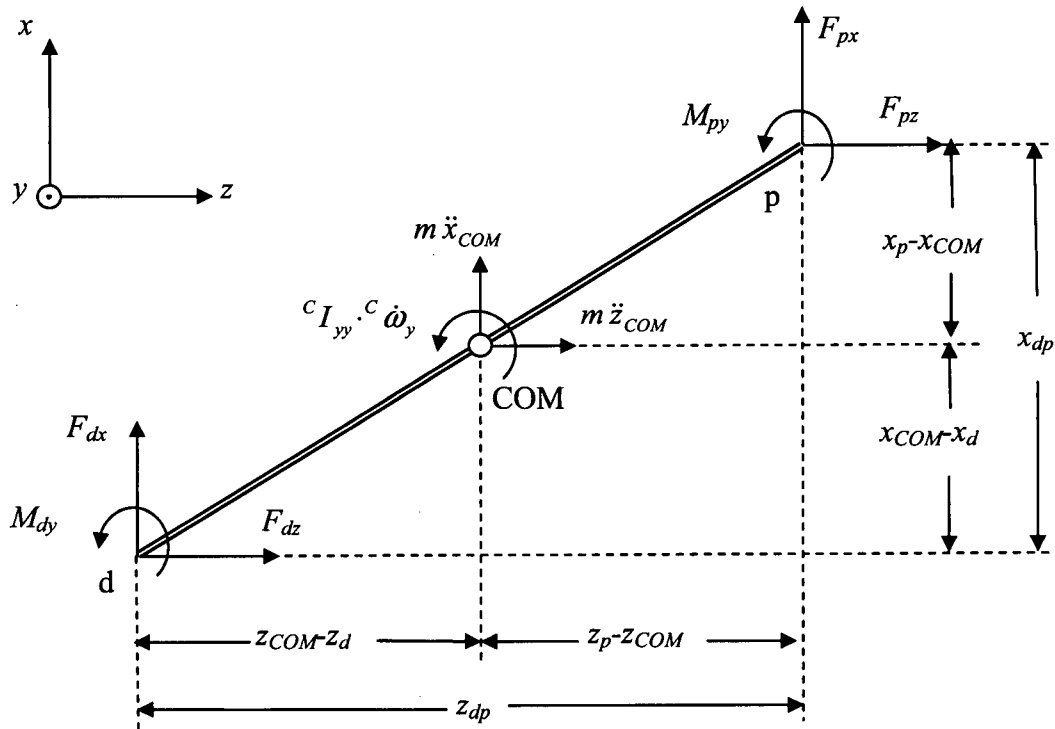


Figure 5.8 Free body diagram of a segment in transverse plane.

The force balance in Equation 5.31a is expressed in the vector notation as

$$\begin{bmatrix} \sum F_x \\ \sum F_y \\ \sum F_z \end{bmatrix} = m \begin{bmatrix} \ddot{x}_{com} \\ \ddot{y}_{com} \\ \ddot{z}_{com} \end{bmatrix} \Rightarrow \begin{bmatrix} F_{px} + F_{dx} \\ F_{py} + F_{dy} \\ F_{pz} + F_{dz} \end{bmatrix} - m \begin{bmatrix} 0 \\ g \\ 0 \end{bmatrix} = m \begin{bmatrix} \ddot{x}_{com} \\ \ddot{y}_{com} \\ \ddot{z}_{com} \end{bmatrix} \quad (5.32)$$

Having the external force (F_d), mass of the segment (m), gravitational acceleration (g), and linear acceleration of COM (a_{COM}), one can calculate the unknown force on the proximal end of the segment (F_p).

$$\begin{bmatrix} F_{px} \\ F_{py} \\ F_{pz} \end{bmatrix} = m \begin{bmatrix} \ddot{x}_{COM} \\ \ddot{y}_{COM} + g \\ \ddot{z}_{COM} \end{bmatrix} - \begin{bmatrix} F_{dx} \\ F_{dy} \\ F_{dz} \end{bmatrix} \quad (5.33)$$

Also, the moment balance in Equation 5.31b, is expressed in the vector notation as

$$\begin{bmatrix} \sum M_x \\ \sum M_y \\ \sum M_z \end{bmatrix} = {}^A I \begin{bmatrix} \dot{\omega}_x \\ \dot{\omega}_y \\ \dot{\omega}_z \end{bmatrix} + \frac{d({}^A I)}{dt} \begin{bmatrix} \omega_x \\ \omega_y \\ \omega_z \end{bmatrix} \quad (5.34)$$

Using Equations 5.12, and 5.29–30, one can determine ${}^A I$ as

$${}^A I = {}^A R {}^C I {}^A R^{-1} = {}^A R {}^C I {}^A R^T \quad (5.35)$$

where ${}^A R$ is the rotation matrix, which describes {C} in COM of the segment with respect to the global frame A , ${}^A R^{-1}$ is inverse of ${}^A R$, ${}^A R^T$ is transpose of ${}^A R$, and ${}^C I$ is the inertia tensor with respect to {C}.

Equation 5.34 then becomes

$$\sum M = {}^A I \cdot \dot{\omega} + \omega \times {}^A I \cdot \omega \quad (5.36)$$

where all of the parameters are with respect to {A}. A cross product between any two vectors (q and e) in 3D space can be written in terms of pure matrix multiplication as the product of a Skew-symmetric matrix and a vector as follows:

$$q \times e = Q \times e = \begin{bmatrix} 0 & -q_3 & q_2 \\ q_3 & 0 & -q_1 \\ -q_2 & q_1 & 0 \end{bmatrix} \begin{bmatrix} e_1 \\ e_2 \\ e_3 \end{bmatrix} = \begin{bmatrix} q_2 e_3 - q_3 e_2 \\ q_3 e_1 - q_1 e_3 \\ q_1 e_2 - q_2 e_1 \end{bmatrix} \quad (5.37)$$

where Q is the Skew-symmetric matrix of q .

In the matrix form, Equation 5.36 is expressed as

$$\begin{bmatrix} \sum M_x \\ \sum M_y \\ \sum M_z \end{bmatrix} = \begin{bmatrix} {}^A I_{xx} & -{}^A I_{xy} & -{}^A I_{xz} \\ -{}^A I_{yx} & {}^A I_{yy} & -{}^A I_{yz} \\ -{}^A I_{zx} & -{}^A I_{zy} & {}^A I_{zz} \end{bmatrix} \begin{bmatrix} \dot{\omega}_x \\ \dot{\omega}_y \\ \dot{\omega}_z \end{bmatrix} + \begin{bmatrix} 0 & -\omega_z & \omega_y \\ \omega_z & 0 & -\omega_x \\ -\omega_y & \omega_x & 0 \end{bmatrix} \begin{bmatrix} {}^A I_{xx} & -{}^A I_{xy} & -{}^A I_{xz} \\ -{}^A I_{yx} & {}^A I_{yy} & -{}^A I_{yz} \\ -{}^A I_{zx} & -{}^A I_{zy} & {}^A I_{zz} \end{bmatrix} \begin{bmatrix} \omega_x \\ \omega_y \\ \omega_z \end{bmatrix} \quad (5.38)$$

Using the free body diagrams (Figures 5.6, 5.7 and 5.8) the equation of the moment balance for a segment is determined:

$$\sum M = \tau_d + \tau_p + M_d + M_p = (r_d - r_{COM}) \times F_d + (r_p - r_{COM}) \times F_p + M_d + M_p \quad (5.39)$$

where τ_d and τ_p are the produced moments due to the external forces at the segment's ends points d and p, respectively.

Using Equations 5.36 and 5.39 the unknown moment M_p is determined as

$$M_p = {}^A I \cdot \dot{\omega} + \omega \times {}^A I \cdot \omega - M_d - (r_p - r_{COM}) \times F_p - (r_d - r_{COM}) \times F_d \quad (5.40)$$

The quantities r_{COM} , r_p , r_d , and r_{pd} ($r_d - r_p$) are related together [12,46]. Figure 5.9 shows these position vectors.

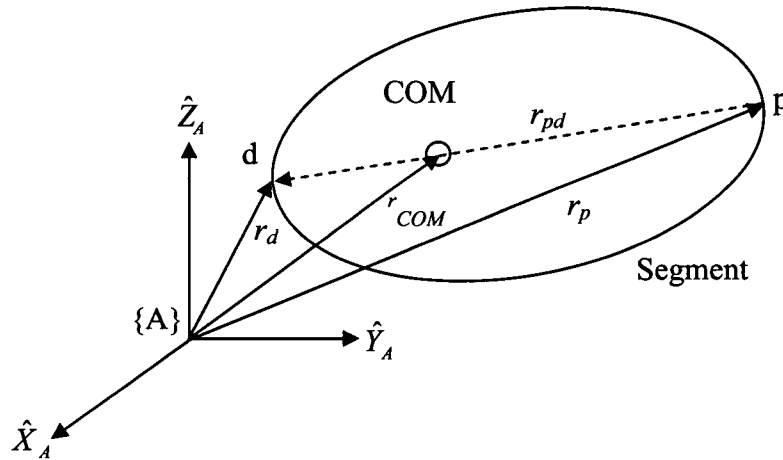


Figure 5.9 Position vectors for r_{pd} , proximal end (p), distal end (d), and COM of the segment.

r_{com} can be expressed in the following forms:

$$r_{COM} = r_p + r_{pd} \cdot k \quad (5.41a)$$

$$r_{COM} = r_d - r_{pd} \cdot (1 - k) \quad (5.41b)$$

where k is defined as

$$k = \left| \frac{\text{The distance from COM up to the proximal end}}{\text{Segments length}} \right| \quad (5.42)$$

Equation 5.40 is simplified using Equation 5.41 as

$$M_p = {}^A I \cdot \dot{\omega} + \omega \times {}^A I \cdot \omega - M_d + k \cdot r_{pd} \times F_p + (k-1) \cdot r_{pd} \times F_d \quad (5.43)$$

The matrix form of Equation 5.40 is

$$\begin{aligned} \begin{bmatrix} M_{px} \\ M_{py} \\ M_{pz} \end{bmatrix} &= \begin{bmatrix} {}^A I_{xx} & -{}^A I_{xy} & -{}^A I_{xz} \\ -{}^A I_{yx} & {}^A I_{yy} & -{}^A I_{yz} \\ -{}^A I_{zx} & -{}^A I_{zy} & {}^A I_{zz} \end{bmatrix} \begin{bmatrix} \dot{\omega}_x \\ \dot{\omega}_y \\ \dot{\omega}_z \end{bmatrix} + \begin{bmatrix} 0 & -\omega_z & \omega_y \\ \omega_z & 0 & -\omega_x \\ -\omega_y & \omega_x & 0 \end{bmatrix} \begin{bmatrix} {}^A I_{xx} & -{}^A I_{xy} & -{}^A I_{xz} \\ -{}^A I_{yx} & {}^A I_{yy} & -{}^A I_{yz} \\ -{}^A I_{zx} & -{}^A I_{zy} & {}^A I_{zz} \end{bmatrix} \begin{bmatrix} \omega_x \\ \omega_y \\ \omega_z \end{bmatrix} \\ &- \begin{bmatrix} M_{dx} \\ M_{dy} \\ M_{dz} \end{bmatrix} + k \begin{bmatrix} 0 & -z_{pd} & y_{pd} \\ z_{pd} & 0 & -x_{pd} \\ -y_{pd} & x_{pd} & 0 \end{bmatrix} \begin{bmatrix} F_{px} \\ F_{py} \\ F_{pz} \end{bmatrix} + (k-1) \begin{bmatrix} 0 & -z_{pd} & y_{pd} \\ z_{pd} & 0 & -x_{pd} \\ -y_{pd} & x_{pd} & 0 \end{bmatrix} \begin{bmatrix} F_{dx} \\ F_{dy} \\ F_{dz} \end{bmatrix} \end{aligned} \quad (5.44)$$

and with some manipulation

$$\begin{aligned} \begin{bmatrix} M_{px} \\ M_{py} \\ M_{pz} \end{bmatrix} &= \begin{bmatrix} {}^A I_{xx} & -{}^A I_{xy} & -{}^A I_{xz} \\ -{}^A I_{yx} & {}^A I_{yy} & -{}^A I_{yz} \\ -{}^A I_{zx} & -{}^A I_{zy} & {}^A I_{zz} \end{bmatrix} \begin{bmatrix} \dot{\omega}_x \\ \dot{\omega}_y \\ \dot{\omega}_z \end{bmatrix} + \begin{bmatrix} 0 & -\omega_z & \omega_y \\ \omega_z & 0 & -\omega_x \\ -\omega_y & \omega_x & 0 \end{bmatrix} \begin{bmatrix} {}^A I_{xx} & -{}^A I_{xy} & -{}^A I_{xz} \\ -{}^A I_{yx} & {}^A I_{yy} & -{}^A I_{yz} \\ -{}^A I_{zx} & -{}^A I_{zy} & {}^A I_{zz} \end{bmatrix} \begin{bmatrix} \omega_x \\ \omega_y \\ \omega_z \end{bmatrix} \\ &- \begin{bmatrix} M_{dx} \\ M_{dy} \\ M_{dz} \end{bmatrix} - \begin{bmatrix} 0 & -z_{pd} & y_{pd} \\ z_{pd} & 0 & -x_{pd} \\ -y_{pd} & x_{pd} & 0 \end{bmatrix} \begin{bmatrix} F_{dx} \\ F_{dy} \\ F_{dz} \end{bmatrix} + k \begin{bmatrix} 0 & -z_{pd} & y_{pd} \\ z_{pd} & 0 & -x_{pd} \\ -y_{pd} & x_{pd} & 0 \end{bmatrix} \begin{bmatrix} F_{px} + F_{dx} \\ F_{py} + F_{dy} \\ F_{pz} + F_{dz} \end{bmatrix} \end{aligned} \quad (5.45)$$

Using Equation 5.32 an alternative form for expressing Equation 5.45 is

$$\begin{aligned}
\begin{bmatrix} M_{px} \\ M_{py} \\ M_{pz} \end{bmatrix} &= \begin{bmatrix} {}^A I_{xx} & -{}^A I_{xy} & -{}^A I_{xz} \\ -{}^A I_{yx} & {}^A I_{yy} & -{}^A I_{yz} \\ -{}^A I_{zx} & -{}^A I_{zy} & {}^A I_{zz} \end{bmatrix} \begin{bmatrix} \dot{\omega}_x \\ \dot{\omega}_y \\ \dot{\omega}_z \end{bmatrix} + \begin{bmatrix} 0 & -\omega_z & \omega_y \\ \omega_z & 0 & -\omega_x \\ -\omega_y & \omega_x & 0 \end{bmatrix} \begin{bmatrix} {}^A I_{xx} & -{}^A I_{xy} & -{}^A I_{xz} \\ -{}^A I_{yx} & {}^A I_{yy} & -{}^A I_{yz} \\ -{}^A I_{zx} & -{}^A I_{zy} & {}^A I_{zz} \end{bmatrix} \begin{bmatrix} \omega_x \\ \omega_y \\ \omega_z \end{bmatrix} \\
&- \begin{bmatrix} M_{dx} \\ M_{dy} \\ M_{dz} \end{bmatrix} - \begin{bmatrix} 0 & -z_{pd} & y_{pd} \\ z_{pd} & 0 & -x_{pd} \\ -y_{pd} & x_{pd} & 0 \end{bmatrix} \begin{bmatrix} F_{dx} \\ F_{dy} \\ F_{dz} \end{bmatrix} + mk \begin{bmatrix} 0 & -z_{pd} & y_{pd} \\ z_{pd} & 0 & -x_{pd} \\ -y_{pd} & x_{pd} & 0 \end{bmatrix} \begin{bmatrix} \ddot{x}_{com} \\ \ddot{y}_{com} + g \\ \ddot{z}_{com} \end{bmatrix}
\end{aligned} \tag{5.46}$$

The combined form of the load balance equations is

$$L_p = I_T \cdot a_T + \Omega_T \cdot I_T \cdot \omega_T + \Phi \cdot L_d \tag{5.47}$$

where the parameters in the above equation are obtained from the following relations and using a recursive matrix back-propagation algorithm the loads at the joints of the other segments are obtained [12].

$$L_p = \begin{bmatrix} F_{px} \\ F_{py} \\ F_{pz} \\ M_{px} \\ M_{py} \\ M_{pz} \end{bmatrix} \tag{5.48a}, \quad I_T = \begin{bmatrix} m & 0 & 0 & 0 & 0 & 0 \\ 0 & m & 0 & 0 & 0 & 0 \\ 0 & 0 & m & 0 & 0 & 0 \\ 0 & -mkz_{pd} & mky_{pd} & {}^A I_{xx} & -{}^A I_{xy} & -{}^A I_{xz} \\ mkz_{pd} & 0 & -mkx_{pd} & -{}^A I_{yx} & {}^A I_{yy} & -{}^A I_{yz} \\ -mky_{pd} & mkx_{pd} & 0 & -{}^A I_{zx} & -{}^A I_{zy} & {}^A I_{zz} \end{bmatrix} \tag{5.48b}$$

$$a_T = \begin{bmatrix} \ddot{x}_{com} \\ \ddot{y}_{com} + g \\ \ddot{z}_{com} \\ \dot{\omega}_x \\ \dot{\omega}_y \\ \dot{\omega}_z \end{bmatrix} \tag{5.48c}, \quad \Omega_T = \begin{bmatrix} 0 & 0 & 0 & 0 & 0 & 0 \\ 0 & 0 & 0 & 0 & 0 & 0 \\ 0 & 0 & 0 & 0 & 0 & 0 \\ 0 & 0 & 0 & 0 & -\omega_z & \omega_y \\ 0 & 0 & 0 & \omega_z & 0 & -\omega_x \\ 0 & 0 & 0 & -\omega_y & \omega_x & 0 \end{bmatrix} \tag{5.48d}$$

$$\omega_r = \begin{bmatrix} 0 \\ 0 \\ 0 \\ \omega_x \\ \omega_y \\ \omega_z \end{bmatrix} \quad (5.48e), \quad \Phi = \begin{bmatrix} -1 & 0 & 0 & 0 & 0 & 0 \\ 0 & -1 & 0 & 0 & 0 & 0 \\ 0 & 0 & -1 & 0 & 0 & 0 \\ 0 & z_{pd} & -y_{pd} & -1 & 0 & 0 \\ -z_{pd} & 0 & x_{pd} & 0 & -1 & 0 \\ y_{pd} & -x_{pd} & 0 & 0 & 0 & -1 \end{bmatrix} \quad (5.48f)$$

$$L_d = \begin{bmatrix} F_{dx} \\ F_{dy} \\ F_{dz} \\ M_{dx} \\ M_{dy} \\ M_{dz} \end{bmatrix} \quad (5.48g)$$

5.3 Results

The optimum seat position for each user can be determined by considering the joint injury prevention priorities for subject. In this study, analyses have been performed for all upper limb joints. The approximate locations of X1 to X3 and Y1 to Y3 are shown in the X-ratio - Y-ratio plane of the next figures for ease of reference.

Figure 5.10 shows that the minimum \overline{WUJII} for the wrist joint is close to Y1 and X1 for subject 7. The highest value is close to the high seat position Y3 and X1.

Another method to determine the optimum seat position is by using \overline{WUJII}' . Figure 5.11 indicates that the minimum \overline{WUJII}' appears around the same location as the minimum \overline{WUJII} , but the maximum values of the injury indices are not co-incidental.

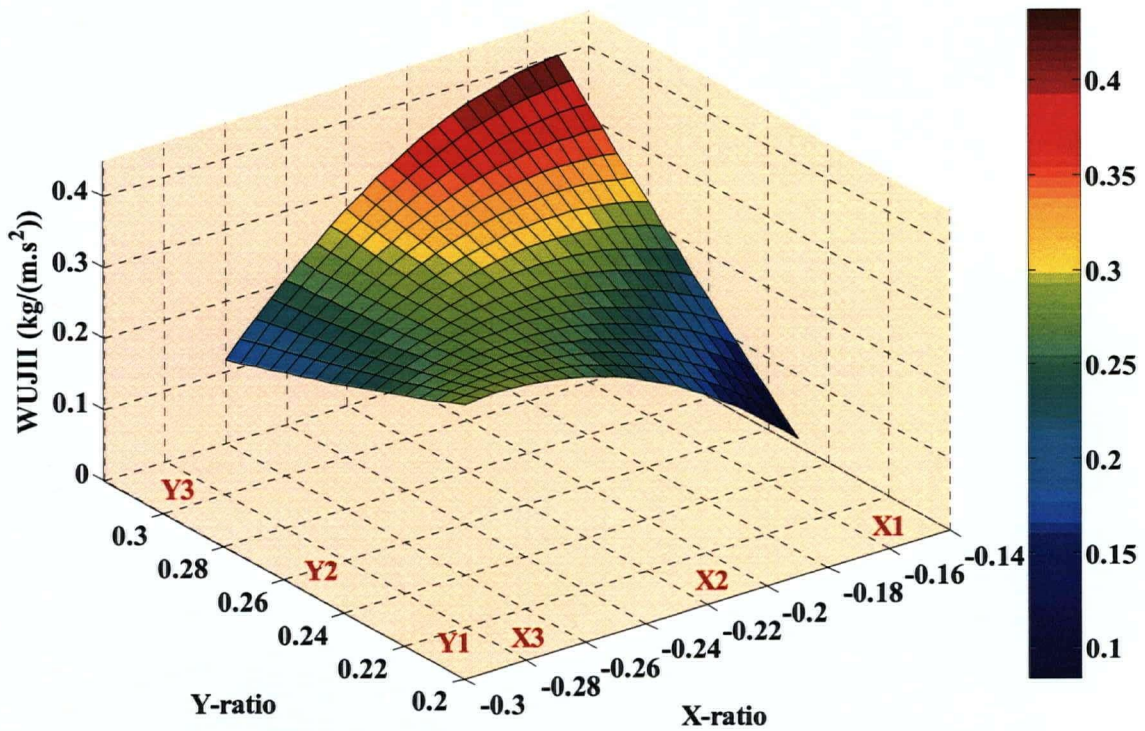


Figure 5.10 Variation of \overline{WUJII} versus X and Y-ratios for subject 7 at wrist joint.

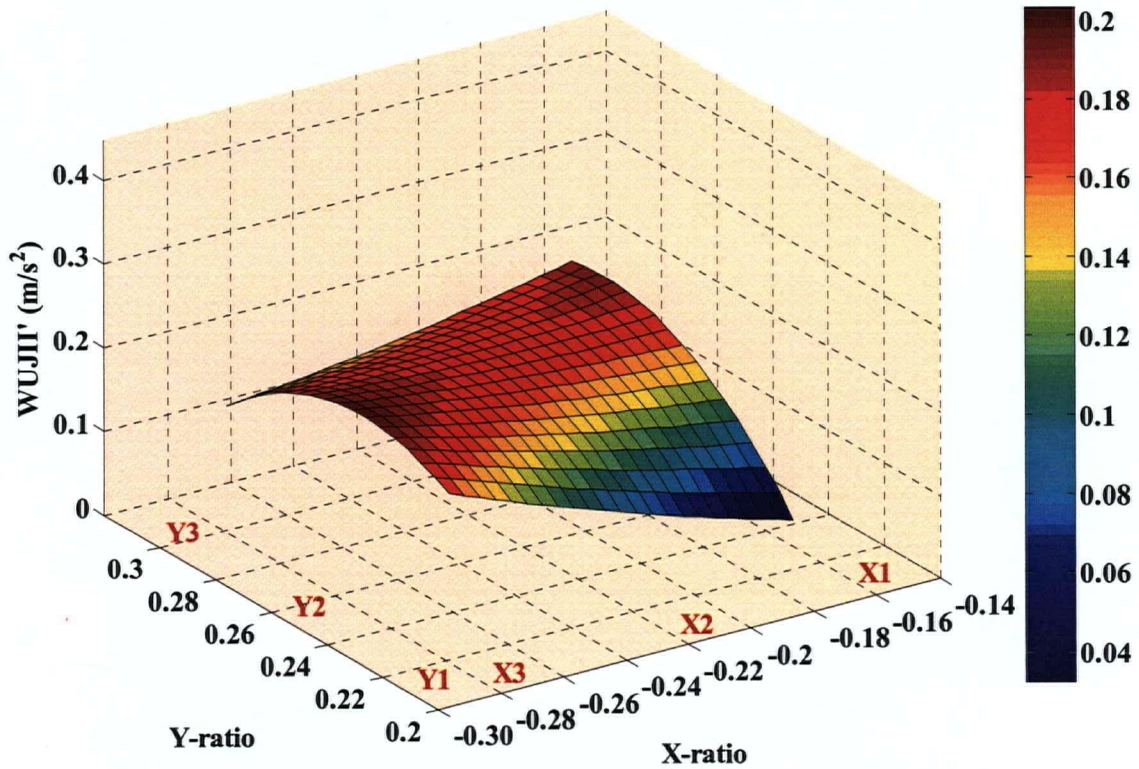


Figure 5.11 Variation of $\overline{WUJII'}$ versus X and Y-ratios for subject 7 at wrist joint.

Figure 5.12 illustrates the variation of \overline{WUJII} for elbow joint at different seat positions. The minimum \overline{WUJII} appears close to X2 and either of the low seat height Y1 or high seat Y3 for subject 7.

The optimum \overline{WUJII}' is determined in Figure 5.13 in the same position for \overline{WUJII} .

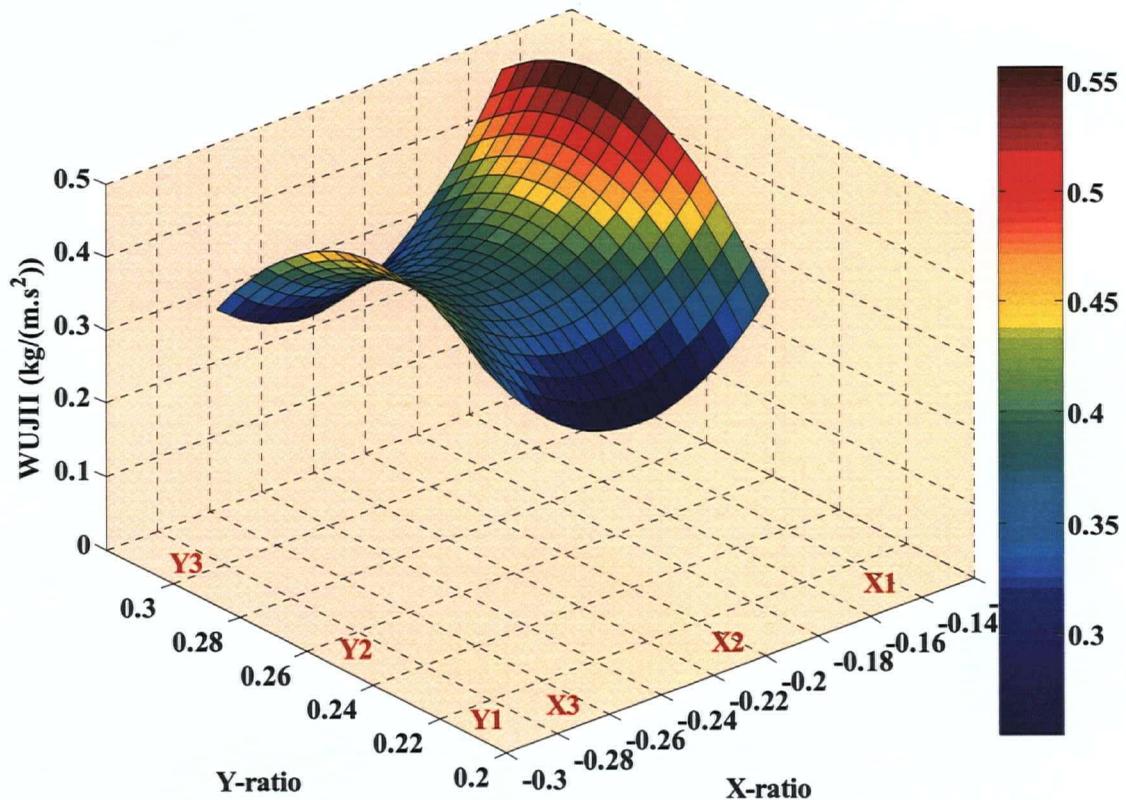


Figure 5.12 Variation of \overline{WUJII} versus X and Y-ratios for subject 7 at elbow joint.

Figure 5.14 and 5.15 show the variation of \overline{WUJII} and \overline{WUJII}' against seat position for shoulder joint of subject 7, respectively. The minimum injury indices have been appeared close to the high seat height Y3 and backward seat position X3 with respect to the wheel axle.

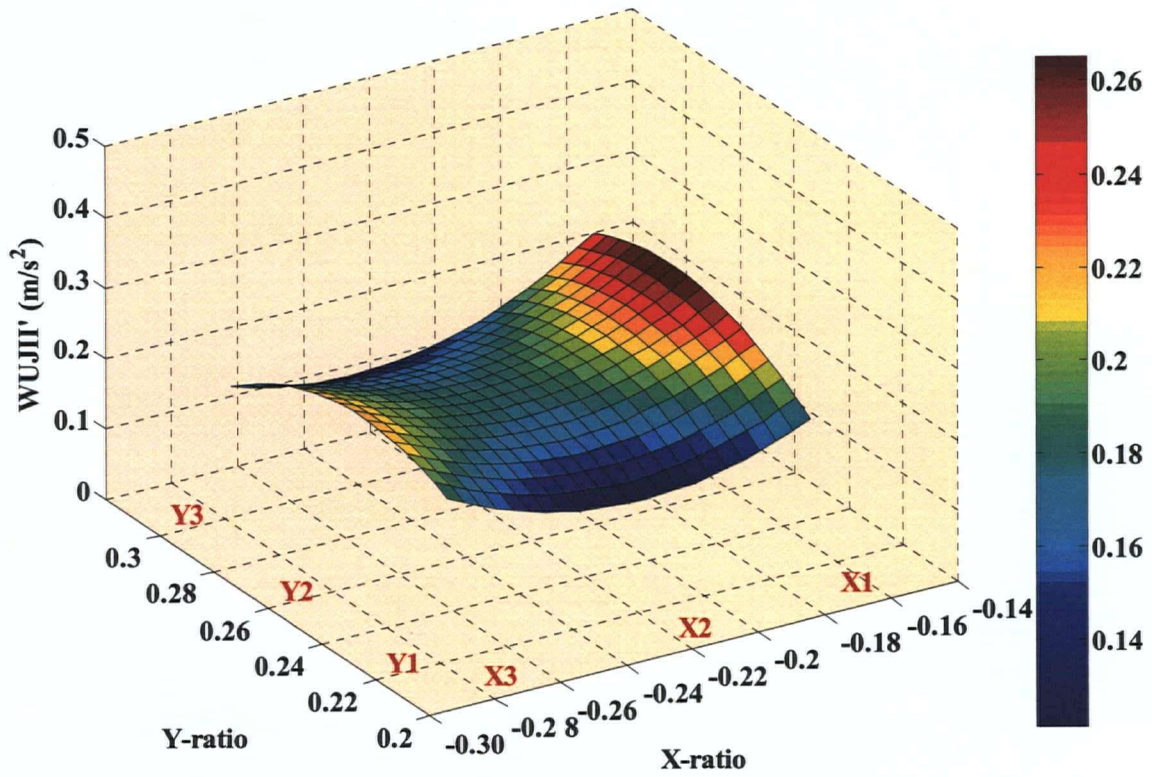


Figure 5.13 Variation of $\overline{WUJII'}$ versus X and Y-ratios for subject 7 at elbow joint.

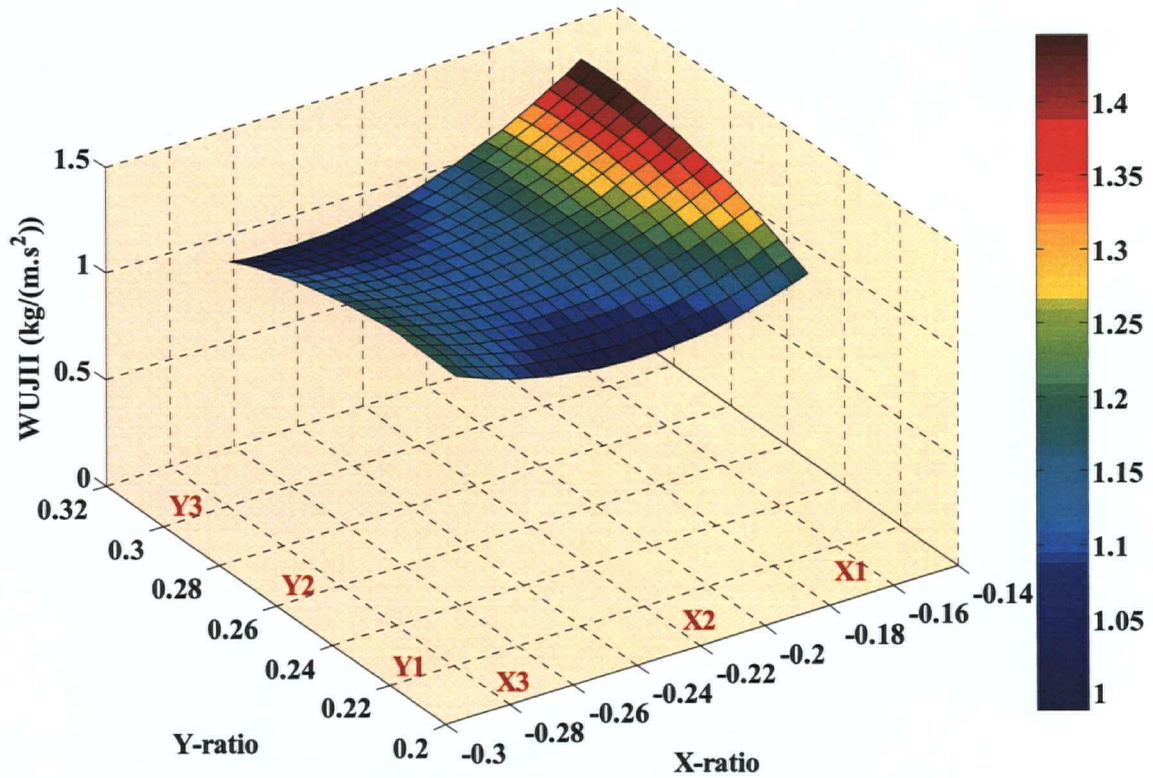


Figure 5.14 Variation of \overline{WUJII} versus X and Y-ratios for subject 7 at shoulder joint.

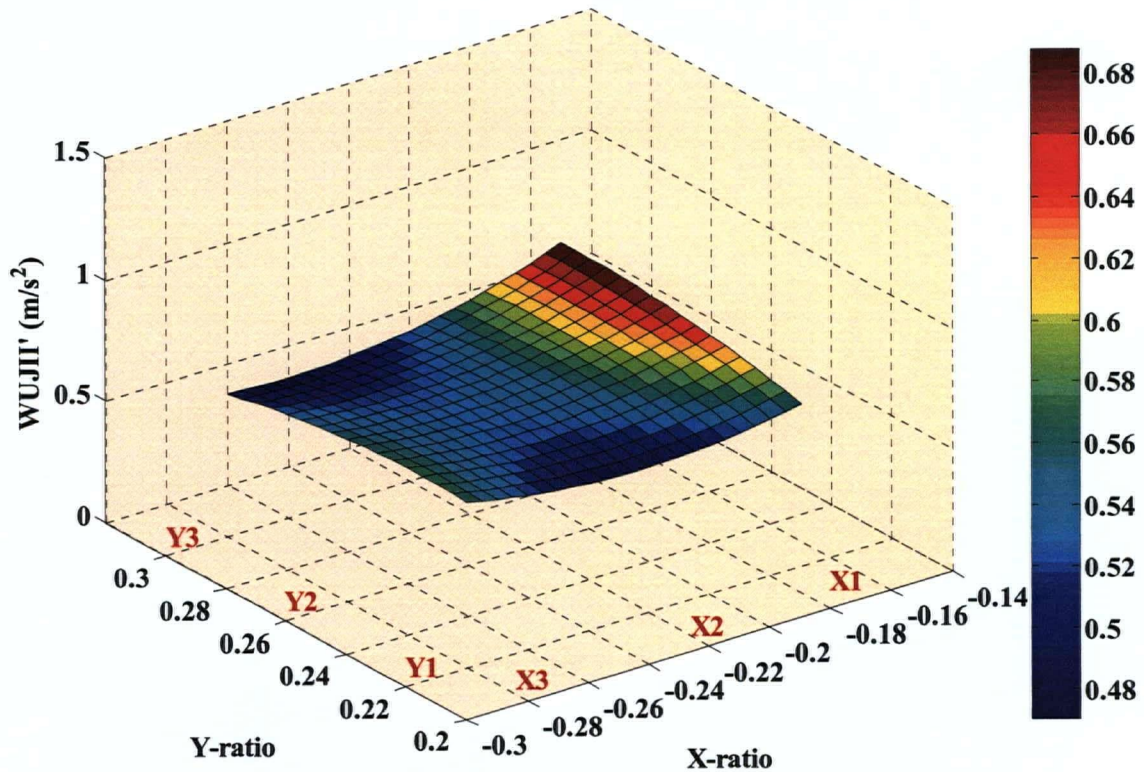


Figure 5.15 Variation of $\overline{WUJII'}$ versus X and Y-ratios for subject 7 at shoulder joint.

The above results showed that almost the same optimum positions were determined by using the injury indices at each joint of subject 7.

The response equations have the general form of Equation 4.12. Tables 5.1 and 5.2 show the coefficients and constants of \overline{WUJII} and $\overline{WUJII'}$ response equations, for the upper limb joints of the subject 7, respectively.

Figures 5.16–5.21 show the variations of injury indices for upper limb joints of subject 8. All of the Figures indicate that the minimum values for injury indices have been appeared close to Y3 and X3.

The coefficients and constants of \overline{WUJII} and \overline{WUJII}' response equations for the upper limb joints of the subject 8 have been determined and presented in Tables 5.3 and 5.4, respectively.

Table 5.1 The coefficients and constants for the response equations that determine \overline{WUJII} for the upper limb joints at different seat positions for subject 7.

Coefficients & Constant Joint	b_1	b_2	b_3	b_4	b_5	b_6
Wrist	-20.227	2.468	-22.948	11.763	54.293	-3.908
Elbow	43.625	-72.585	12.435	44.869	25.760	-4.289
Shoulder	53.785	-50.357	10.482	39.081	53.671	-2.869

Table 5.2 The coefficients and constants for the response equations that determine \overline{WUJII}' for the upper limb joints at different seat positions for subject 7.

Coefficients & Constant Joint	b_1	b_2	b_3	b_4	b_5	b_6
Wrist	2.014	-34.362	-5.712	24.167	23.127	-3.823
Elbow	20.885	-34.562	6.009	21.337	-12.133	-2.029
Shoulder	25.570	-23.682	5.016	18.417	25.385	-1.340

Analyzing the results for these two subjects, at each joint one can see that the magnitude of the calculated values of the injury indices are different for subject 7,

whereas they are very close together for subject 8. Actually, subject 7 had the lowest %BF. Therefore, if two people show the same value for \overline{WUJII} , the one who has less fat will show lower \overline{WUJII}' , which is reasonable. This may suggest \overline{WUJII}' as a better index to estimate the injury.

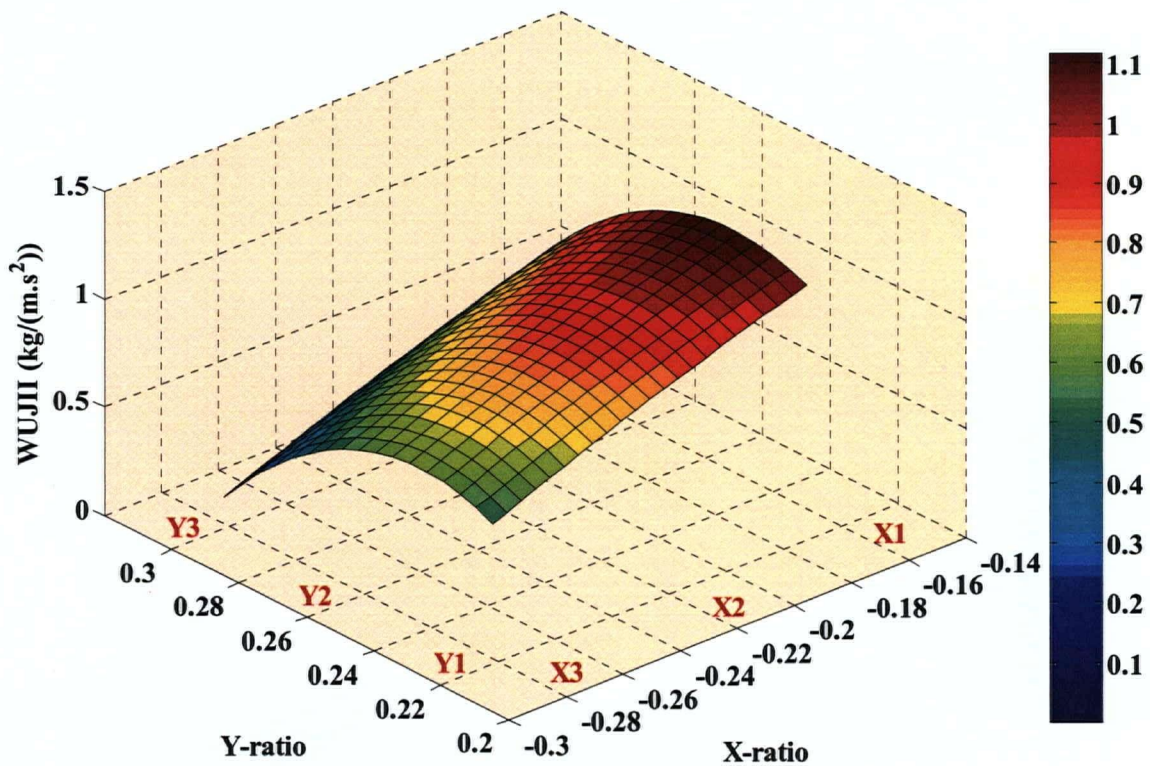


Figure 5.16 Variation of \overline{WUJII} versus X and Y-ratios for subject 8 at wrist joint.

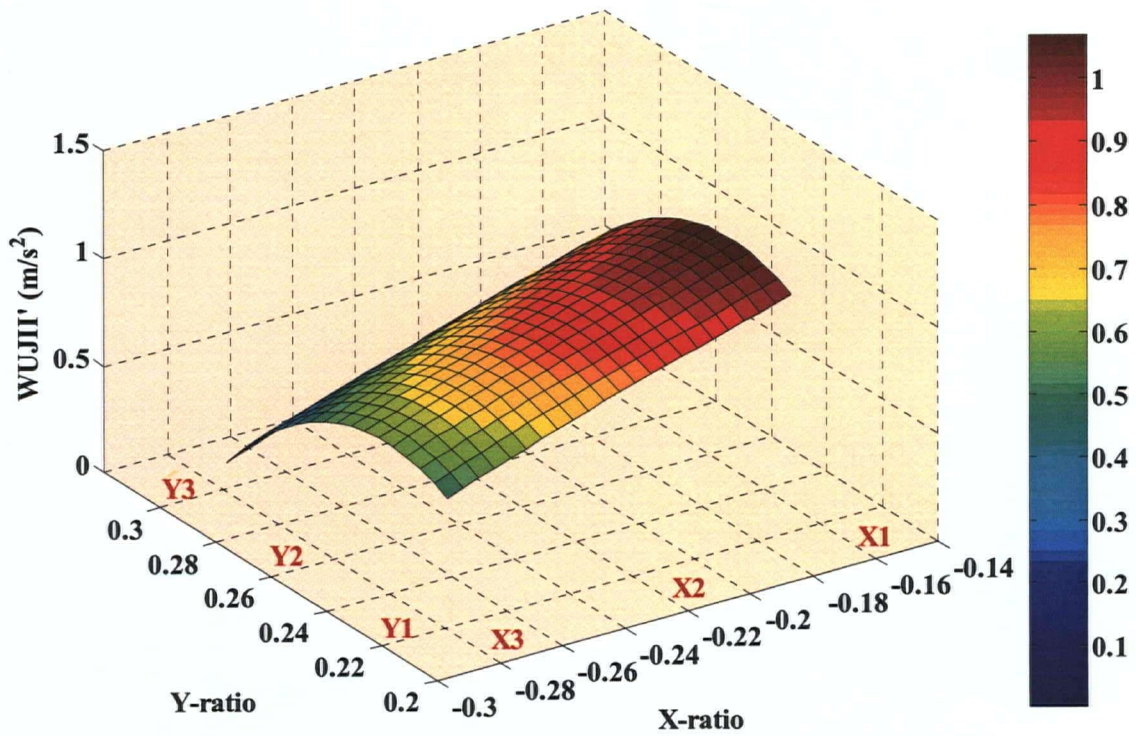


Figure 5.17 Variation of $\overline{WUJII'}$ versus X and Y-ratios for subject 8 at wrist joint.

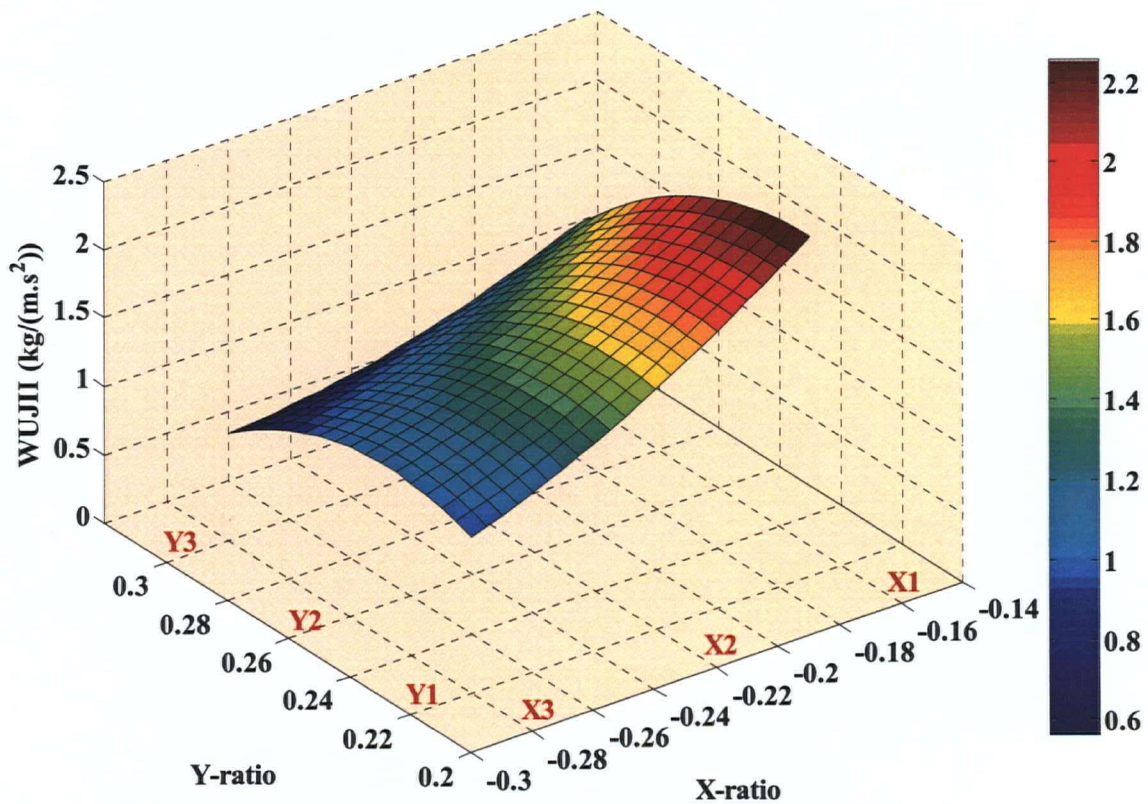


Figure 5.18 Variation of \overline{WUJII} versus X and Y-ratios for subject 8 at elbow joint.

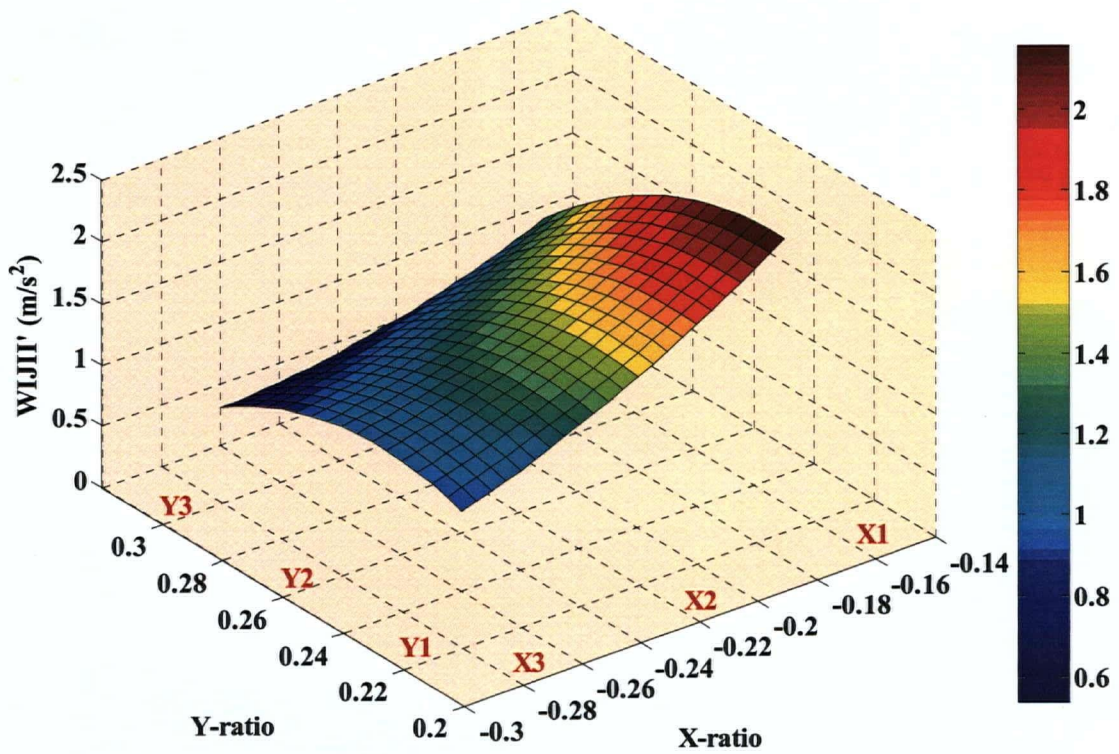


Figure 5.19 Variation of $\overline{WUJII'}$ versus X and Y-ratios for subject 8 at elbow joint.

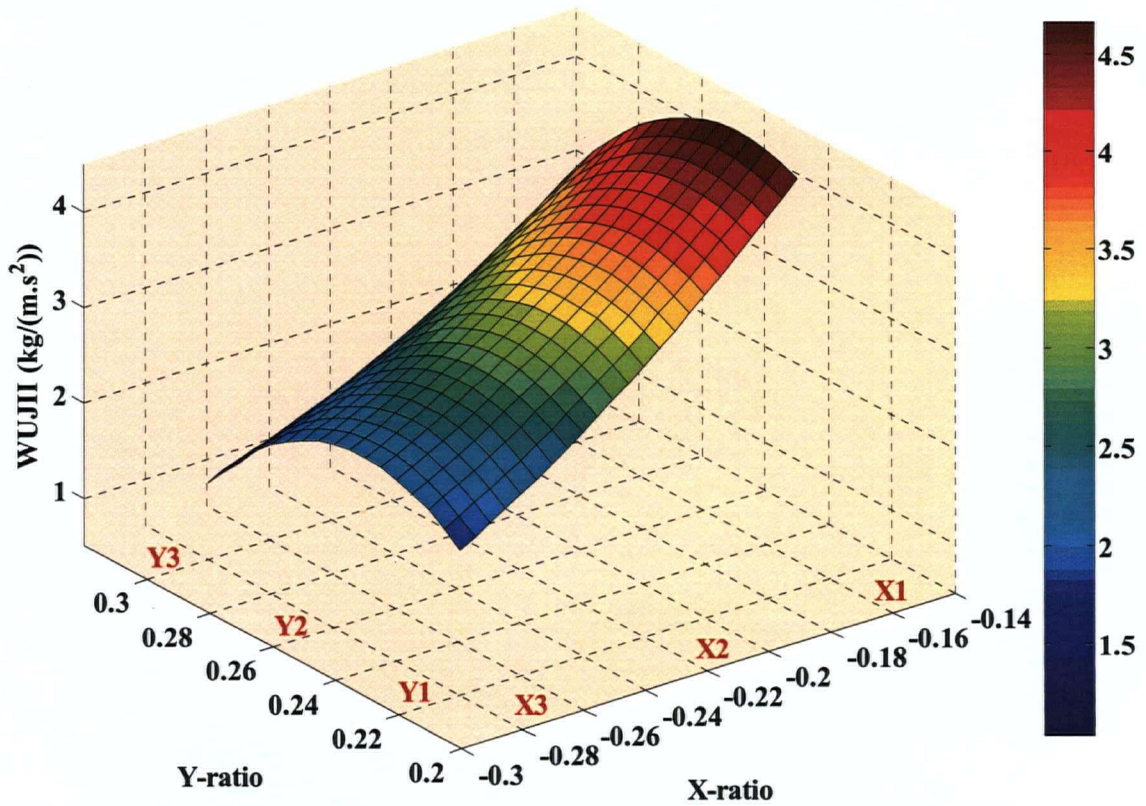


Figure 5.20 Variation of \overline{WUJII} versus X and Y-ratios for subject 8 at shoulder joint.

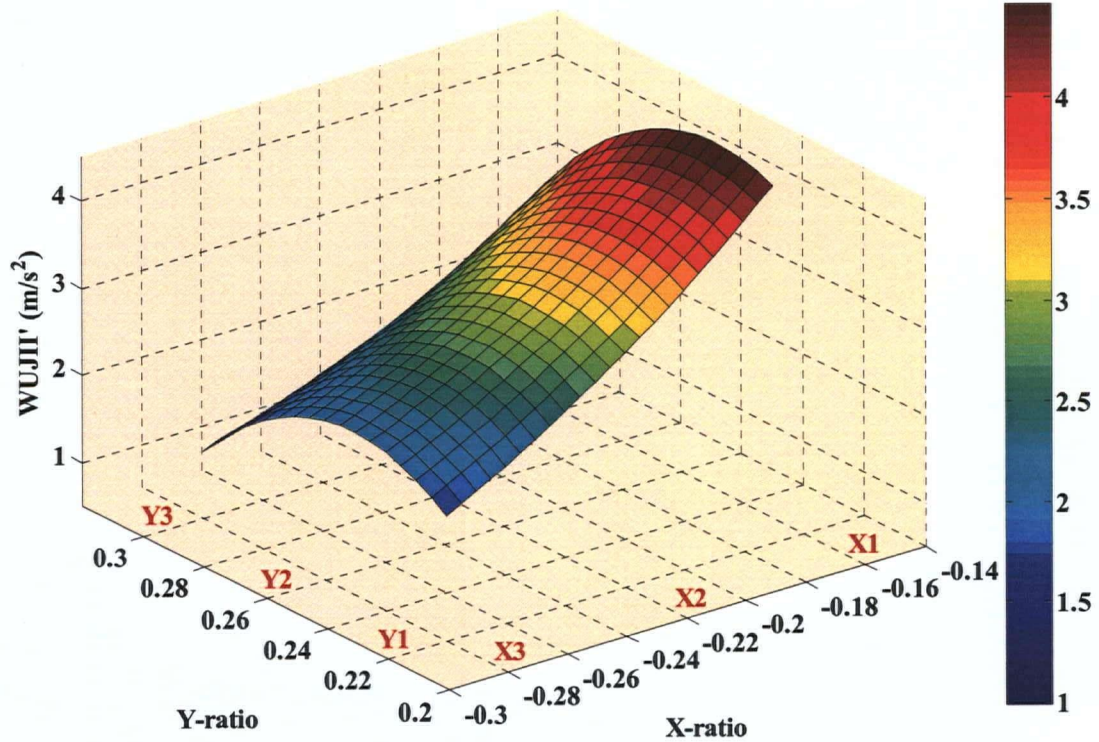


Figure 5.21 Variation of $\overline{WUJII'}$ versus X and Y-ratios for subject 8 at shoulder joint.

Table 5.3 The coefficients and constants for the response equations that determine \overline{WUJII} for the upper limb joints at different seat positions for subject 8.

Coefficients & Constant Joint	b_1	b_2	b_3	b_4	b_5	b_6
	Wrist	-6.518	-173.804	1.789	87.738	0.790
Elbow	39.541	-173.145	47.775	67.026	-81.220	-0.357
Shoulder	67.664	-471.257	78.949	216.618	-107.372	-13.429

Table 5.4 The coefficients and constants for the response equations that determine $\overline{WUJII'}$ for the upper limb joints at different seat positions for subject 8.

Coefficients & Constant Joint	b_1	b_2	b_3	b_4	b_5	b_6
Wrist	-6.184	-166.175	1.689	83.918	0.883	-9.061
Elbow	37.757	-165.625	45.676	64.111	-77.724	-0.346
Shoulder	64.833	-450.541	75.501	207.123	-102.528	-12.841

5.4 Conclusions

The joint loads during MWP are generated by muscle action and the interaction of MWU with the environment. These loads are repetitive and can cause RSI. It is necessary to determine the kinetic profile of the MWUs for calculating the injury indices to determine the optimum seat position to prevent injury. In this chapter, a model for the dynamic analysis of the upper limb was introduced. This model is generic and can be used for other parts of the body such as lower limbs. The joint loads of subjects 7 and 8 during the experiments were calculated by using this model, followed by calculation of the injury indices for the upper limb joints of the subjects. The results showed that both injury indices for each joint determine the same optimum position for the users, except the injury indices for the wrist joint of subject 7.

Subject 7, who had the lowest %BF showed that his response surfaces for \overline{WUJII} and $\overline{WUJII'}$ differ in magnitude and pattern, whereas the response surfaces were almost the same for subject 8, who had a higher %BF. Considering two persons with different

%BF, they may have the same value of \overline{WUJII} but the one with less %BF will appear to have a lower \overline{WUJII}' . Therefore, one may consider \overline{WUJII}' as a more suitable index to estimate probable injury, as it can evaluate the injuries more realistically.

The coefficients and constants of the BQF response equations of the injury indices were determined for subjects 7 and 8. The optimum seat position for subject 7 was different for various joints, but for subject 8 all of the experiments determined a unique optimum position.

Comparing these results with the results in Chapter 4 reveals that the optimum seat position can vary depending on the general injury indices or the specific joint used to calculate the injury indices.

In the next chapter, a new model is introduced to analyze the dynamics of the upper limb based on the concepts of robotics. This model requires less post-processing, as it uses the data of only two landmarks of the upper body for kinematic analysis.

CHAPTER 6

A New method for Dynamic Analysis of the Upper Limb

6.1 Introduction

A number of models for the dynamic analysis of the upper limbs have been developed in previous studies but shortcomings and/or oversimplifications of important aspects of MWP are evident in some. Models presented by Cooper [12] and Vrongistinos [46] are among the best and most widely referenced examples.

In Chapter 5, a 3D rigid-body model for the dynamic analysis of the upper limbs, similar to those of Cooper and Vrongistinos, but with some difference in the manner in which the loads are calculated was presented. This model needs at least three markers to determine the position and orientation of each segment. For a three-link model and assuming common markers at the two joints, at least seven markers are needed for the

dynamic analysis of the upper limb. To determine the orientation of the segments in a 3D analysis, the above requirement must be met. Hence, we refer to this as “Method I”.

In this chapter, a new method is introduced, which we refer to as “Method II”. It uses a model that needs data from two markers only for kinetic analysis of the upper limb. Using this method, the orientation of the segments cannot be determined, but the kinetic results can be readily calculated. The post-processing of the experimental data becomes much faster and easier when fewer markers are used for the tests.

The merits of using Method II are presented in this chapter, followed by a comparison of the results calculated by this method with those calculated using the method introduced in chapter 5. The results consist of the load profiles, over estimation rates of the calculated loads, and the relative errors and Std. Devs. of the calculated maximum loads for each joint of the subjects.

6.2 Method II

In Chapters 4 and 5 the specifications of the model were explained. In Method II the same model was used with two markers. The movement of the shoulder as origin of the linkage system, and the motion of the hand were tracked using these markers, and the VICON Motion Analysis System. The recorded data were used to determine the positions and orientations of the upper limb. The inverse kinematics method, and robotics concepts and relations were employed to calculate the local angles, angular velocities and accelerations of the users’ upper limb joints.

6.2.1 Link Parameters

A robot can be kinematically described in terms of four parameters for each link. Two of them describe the link itself and the other two describe the connection of one end of the link to its neighboring link. These parameters are referred to as the Denavit-Hartenberg notation [96].

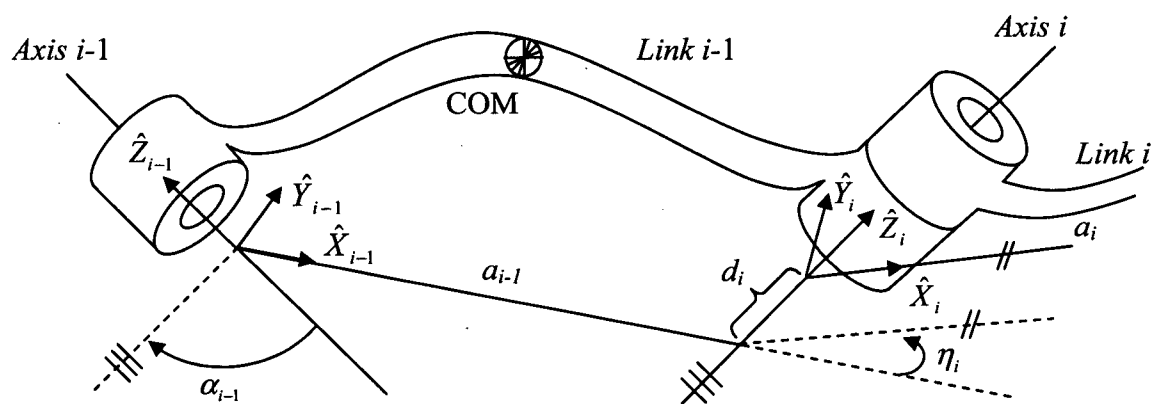


Figure 6.1 Link frames and link parameters.

Referring to Figure 6.1 these parameters are described as follows:

a_i : Distance from Z_i to Z_{i+1} measured along X_i

α_i : Angle between Z_i and Z_{i+1} measured about X_i

d_i : Distance from X_{i-1} to X_i measured along Z_i

η_i : Angle between X_{i-1} and X_i measured about Z_i

The coordinate systems are fixed at the joints.

Transforming matrix for each link is defined as [96,99,100]:

$${}^{i-1}T_i = \begin{bmatrix} \cos \eta_i & -\sin \eta_i & 0 & a_{i-1} \\ \sin \eta_i \cdot \cos \alpha_{i-1} & \cos \eta_i \cdot \cos \alpha_{i-1} & -\sin \alpha_{i-1} & -\sin \alpha_{i-1} \cdot d_i \\ \sin \eta_i \cdot \sin \alpha_{i-1} & \cos \eta_i \cdot \sin \alpha_{i-1} & \cos \alpha_{i-1} & \cos \alpha_{i-1} \cdot d_i \\ 0 & 0 & 0 & 1 \end{bmatrix} \quad (6.1)$$

This is referred to as the Denavit-Hartenberg matrix.

6.2.2 Link Parameters of the Model

Figure 6.2 shows the model and its local (1 to 8) and global (0 and 9) coordinate systems.

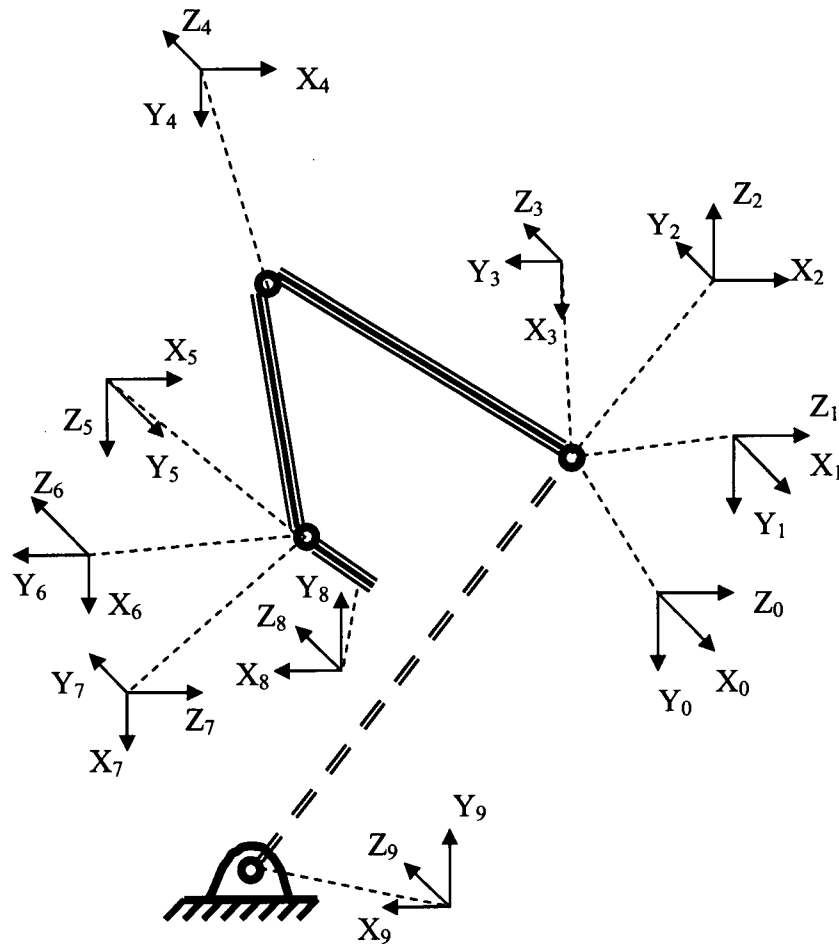


Figure 6.2 Half-body Linkage model for the upper limb with all coordinate reference systems.

Link parameters of the model are given in Table 6.1. The lengths of the upper arm, forearm, and hand are shown by L_a , L_f , and L_h , respectively.

Table 6.1 Link parameters of the model.

i	α_{i-1}	a_{i-1}	d_i	η_i
1	0°	0	0	η_1
2	90°	0	0	η_2
3	-90°	0	0	η_3
4	0°	L_a	0	η_4
5	-90°	0	L_f	η_5
6	90°	0	0	η_6
7	90°	0	0	η_7

There is no joint at the origin of frame 8, but this frame is needed to transform the reaction loads of the handrim from the contact point to frame 7. The transformation matrices for each reference frame are determined by using Equation 6.1 and Table 6.1 as follows:

$${}^0_1T = \begin{bmatrix} \cos \eta_1 & -\sin \eta_1 & 0 & 0 \\ \sin \eta_1 & \cos \eta_1 & 0 & 0 \\ 0 & 0 & 1 & 0 \\ 0 & 0 & 0 & 1 \end{bmatrix} \quad (6.2a), \quad {}^1_2T = \begin{bmatrix} \cos \eta_2 & -\sin \eta_2 & 0 & 0 \\ 0 & 0 & -1 & 0 \\ \sin \eta_2 & \cos \eta_2 & 0 & 0 \\ 0 & 0 & 0 & 1 \end{bmatrix} \quad (6.2b)$$

$${}^2_3T = \begin{bmatrix} \cos \eta_3 & -\sin \eta_3 & 0 & 0 \\ 0 & 0 & 1 & 0 \\ -\sin \eta_3 & -\cos \eta_3 & 0 & 0 \\ 0 & 0 & 0 & 1 \end{bmatrix} \quad (6.2c), \quad {}^3_4T = \begin{bmatrix} \cos \eta_4 & -\sin \eta_4 & 0 & L_a \\ \sin \eta_4 & \cos \eta_4 & 0 & 0 \\ 0 & 0 & 1 & 0 \\ 0 & 0 & 0 & 1 \end{bmatrix} \quad (6.2d)$$

$${}^4_5T = \begin{bmatrix} \cos \eta_5 & -\sin \eta_5 & 0 & 0 \\ 0 & 0 & 1 & L_f \\ -\sin \eta_5 & -\cos \eta_5 & 0 & 0 \\ 0 & 0 & 0 & 1 \end{bmatrix} \quad (6.2e), \quad {}^5_6T = \begin{bmatrix} \cos \eta_6 & -\sin \eta_6 & 0 & 0 \\ 0 & 0 & -1 & 0 \\ \sin \eta_6 & \cos \eta_6 & 0 & 0 \\ 0 & 0 & 0 & 1 \end{bmatrix} \quad (6.2f)$$

$${}^6_7T = \begin{bmatrix} \cos \eta_7 & -\sin \eta_7 & 0 & 0 \\ 0 & 0 & -1 & 0 \\ \sin \eta_7 & \cos \eta_7 & 0 & 0 \\ 0 & 0 & 0 & 1 \end{bmatrix} \quad (6.2g), \quad {}^7_8T = \begin{bmatrix} 0 & -1 & 0 & L_h \\ 0 & 0 & 1 & 0 \\ -1 & 0 & 0 & 0 \\ 0 & 0 & 0 & 1 \end{bmatrix} \quad (6.2h)$$

6.2.3 Calculating the Joints Angles

The joints angles were calculated by using the inverse kinematics method, and the positions of two markers on the shoulder and wrist. Considering the limitation of this method because of using minimal dynamic data and the general motion of the propulsion two assumptions were made. An abduction angle of 20° was considered at shoulder joint for η_1 . Also, the orientation of the hand was considered to remain vertical during the propulsion and while in grabbing contact with the handrim. However, these assumptions can be modified. Thus, the position and orientation of frame 7 are known as components of the following matrix.

$${}^0_7T = \begin{bmatrix} r_{11} & r_{12} & r_{13} & P_{wx} \\ r_{21} & r_{22} & r_{23} & P_{wy} \\ r_{31} & r_{32} & r_{33} & P_{wz} \\ 0 & 0 & 0 & 1 \end{bmatrix} = \begin{bmatrix} 0 & -1 & 0 & P_{wx} \\ 1 & 0 & 0 & P_{wy} \\ 0 & 0 & 1 & P_{wz} \\ 0 & 0 & 0 & 1 \end{bmatrix} \quad (6.3)$$

where $P_{wx,wy,wz}$ and r_{11-33} are the components of the wrist position and frame 7 orientation, respectively.

Considering Figure 6.2 and the fact that the orientation of frame 7 was assumed to remain fixed during the propulsion, one can determine 0R_7 as

$${}^0R_7 = \begin{bmatrix} {}^0\hat{X}_7 & {}^0\hat{Y}_7 & {}^0\hat{Z}_7 \end{bmatrix} = \begin{bmatrix} 0 & -1 & 0 \\ 1 & 0 & 0 \\ 0 & 0 & 1 \end{bmatrix} \quad (6.4)$$

Sequential transformation matrices are related as follows:

$${}^0T_7 = {}^0T_1 \cdot {}^1T_2 \cdot {}^2T_3 \cdot {}^3T_4 \cdot {}^4T_5 \cdot {}^5T_6 \cdot {}^6T_7 \quad (6.5)$$

Pre-multiplying both sides of Equation 6.5 by 2T_0 , one obtains:

$${}^2T_0 \cdot {}^0T_7 = {}^2T_3 \cdot {}^3T_4 \cdot {}^4T_5 \cdot {}^5T_6 \cdot {}^6T_7 \quad (6.6a)$$

$$\begin{bmatrix} c_1 c_2 & s_1 c_2 & s_2 & 0 \\ -c_1 s_2 & -s_1 s_2 & c_2 & 0 \\ s_1 & -c_1 & 0 & 0 \\ 0 & 0 & 0 & 1 \end{bmatrix} \begin{bmatrix} 0 & -1 & 0 & P_{wx} \\ 1 & 0 & 0 & P_{wy} \\ 0 & 0 & 1 & P_{wz} \\ 0 & 0 & 0 & 1 \end{bmatrix} = {}^2T_7 \quad (6.6b)$$

where c_i is $\cos(\eta_i)$ and s_i is $\sin(\eta_i)$, and $i=1$ to 7 is the reference frame number.

Since robot mechanisms are uniquely defined by the transformation matrices, there is a one-to-one equivalency between the matrix elements on the left and the right side of the equations derived here. We use this property to determine certain unknowns through the following calculations.

Multiplying the matrices in Equation 6.6b one has:

$$\begin{bmatrix} s_1 c_2 & -c_1 c_2 & s_2 & c_1 c_2 P_{wx} + s_1 c_2 P_{wy} + s_2 P_{wz} \\ -s_1 s_2 & c_1 s_2 & c_2 & -c_1 c_2 P_{wx} - s_1 s_2 P_{wy} + c_2 P_z \\ -c_1 & -s_1 & 0 & s_1 P_{wx} - c_1 P_{wy} \\ 0 & 0 & 0 & 1 \end{bmatrix} = \begin{bmatrix} L_{11} & L_{12} & L_{13} & L_{14} \\ L_{21} & L_{22} & L_{23} & L_{24} \\ L_{31} & L_{32} & L_{33} & L_{34} \\ L_{41} & L_{42} & L_{43} & L_{44} \end{bmatrix} \quad (6.7a)$$

$$\begin{aligned} L_{11} &= c_{34}(c_5 c_6 c_7 + s_5 s_7) - s_{34} s_6 c_7 ; & L_{12} &= c_{34}(-c_5 c_6 s_7 + s_5 c_7) + s_{34} s_6 s_7 \\ L_{13} &= c_{34} c_5 c_6 + s_{34} c_6 ; & L_{14} &= -s_{34} L_f + c_3 L_a \\ L_{21} &= -s_5 c_6 c_7 + c_5 s_7 ; & L_{22} &= s_5 c_6 s_7 + c_5 c_7 ; & L_{23} &= -s_5 s_6 ; & L_{24} &= 0 \\ L_{31} &= -s_{34}(c_5 c_6 c_7 + s_5 s_7) - c_{34} s_6 c_7 ; & L_{32} &= -s_{34}(-c_5 c_6 s_7 + s_5 c_7) + c_{34} s_6 s_7 \\ L_{33} &= -s_{34} c_5 c_6 + c_{34} c_6 ; & L_{34} &= -c_{34} L_f - s_3 L_a \\ L_{41} &= 0 ; & L_{42} &= 0 ; & L_{43} &= 0 ; & L_{44} &= 1 \end{aligned} \quad (6.7b)$$

where $s_{34} = \sin(\eta_3 + \eta_4)$, $c_{34} = \cos(\eta_3 + \eta_4)$, and L_{11-44} are lumped parameters.

Now, by equating the element (2,4) of both sides of the Equation 6.7a we obtain

$$-c_1 s_2 P_{wx} - s_1 s_2 P_{wy} + c_2 P_{wz} = 0 \quad (6.8a)$$

$$c_2 P_{wz} - s_2 (c_1 P_{wx} + s_1 P_{wy}) = 0 \quad (6.8b)$$

Converting to polar coordinate system the following relations can be written

$$P_{wz} = \rho \cdot s \varphi_0 \quad (6.9a)$$

$$c_1 P_{wx} + s_1 P_{wy} = \rho \cdot c \varphi_0 \quad (6.9b)$$

$$\rho = (P_{wz}^2 + (c_1 P_{wx} + s_1 P_{wy})^2)^{-1/2} \quad (6.9c)$$

$$\varphi_0 = \text{Atan2}(P_{wz}, c_1 P_{wx} + s_1 P_{wy}) \quad (6.9d)$$

where φ_0 and ρ are the polar coordinate angle and radius, respectively.

Substituting these in Equation 6.8b, η_2 is determined as

$$c_2 \cdot s\varphi_0 - s_2 \cdot c\varphi_0 = 0 \quad (6.10a)$$

$$\sin(\varphi_0 - \eta_2) = 0 \quad \Rightarrow \quad \cos(\varphi_0 - \eta_2) = \pm 1 \quad (6.10b)$$

$$\varphi_0 - \eta_2 = \text{Atan2}(0, \pm 1) \quad \Rightarrow \quad \eta_2 = \varphi_0 - \text{Atan2}(0, \pm 1) \quad (6.10c)$$

$$\eta_2 = \text{Atan2}(P_{wz}, c_1 P_{wx} + s_1 P_{wy}) - \text{Atan2}(0, \pm 1) \quad (6.10d)$$

Therefore, there are two answers for η_2 .

Equating elements (1,4) and (3,4) from both sides of Equation 6.7a and using Equation 6.7b, one obtains Equations 6.11a and 6.11b, respectively, and using Equations 6.11 η_4 is calculated.

$$c_1 c_2 P_{wx} + s_1 c_2 P_{wy} + s_2 P_{wz} = -s_{34} L_f + c_3 L_a \quad (6.11a)$$

$$s_1 P_{wx} - c_1 P_{wy} = -c_{34} L_2 - s_3 L_a \quad (6.11b)$$

$$K_1 = (c_1 c_2 P_{wx} + s_1 c_2 P_{wy} + s_2 P_{wz})^2 \quad (6.11c)$$

$$K_2 = (s_1 P_{wx} - c_1 P_{wy})^2 \quad (6.11d)$$

$$K_1 + K_2 = L_f^2 + L_a^2 - 2L_a L_f s_4 \quad (6.11e)$$

$$s_4 = \frac{h_f^2 + h_a^2 - (K_1 + K_2)}{2h_f h_a} \quad (6.11f)$$

$$c_4 = \pm \sqrt{1 - s_4} \quad (6.11g)$$

$$\eta_4 = \text{Atan2}(s_4, c_4) \quad (6.11h)$$

where K_1 and K_2 are lumped parameters.

To find the other angles, 4T is pre-multiplied to both sides of the Equation 6.5 as

$${}^4T_0 \quad {}^0T_7 = {}^4T_5 \quad {}^5T_6 \quad {}^6T_7 \quad (6.12a)$$

$$\begin{bmatrix} c_1c_2c_{34} - s_1s_{34} & s_1c_2c_{34} + c_1s_{34} & s_2c_{34} & -L_a c_4 \\ -c_1c_2s_{34} - s_1c_{34} & -s_1c_2s_{34} + c_1c_{34} & -s_2s_{34} & L_a s_4 \\ -c_1s_2 & -s_1s_2 & c_2 & 0 \\ 0 & 0 & 0 & 1 \end{bmatrix} {}^0T_7 = {}^4T_7 \quad (6.12b)$$

With some manipulation another form of Equation 6.12b is given by

$$\begin{bmatrix} K_{11} & K_{12} & K_{13} & K_{14} \\ K_{21} & K_{22} & K_{23} & K_{24} \\ K_{31} & K_{32} & K_{33} & K_{34} \\ K_{41} & K_{42} & K_{43} & K_{44} \end{bmatrix} = \begin{bmatrix} c_5c_6c_7 + s_5s_7 & -c_5c_6s_7 + s_5c_7 & c_5s_6 & 0 \\ s_6c_7 & -s_6s_7 & -c_6 & L_f \\ -s_5c_6c_7 + c_5s_7 & s_5c_6s_7 + c_5c_7 & -s_5s_6 & 0 \\ 0 & 0 & 0 & 1 \end{bmatrix} \quad (6.13a)$$

$$\begin{aligned} K_{11} &= s_1c_2c_{34} + c_1s_{34} \quad ; \quad K_{12} = -c_1c_2c_{34} + s_1s_{34} \\ K_{13} &= s_2c_{34} \quad ; \quad K_{14} = (c_1c_2c_{34} - s_1s_{34})P_{wx} + (s_1c_2c_{34} + c_1s_{34})P_{wy} + s_2c_{34}P_{wz} - L_a c_4 \\ K_{21} &= -s_1c_2s_{34} + c_1c_{34} \quad ; \quad K_{22} = c_1c_2s_{34} + s_1c_{34} \\ K_{23} &= -s_2s_{34} \quad ; \quad K_{24} = (-c_1c_2s_{34} - s_1c_{34})P_{wx} + (s_1c_2s_{34} + c_1c_{34})P_{wy} - s_2s_{34}P_{wz} + L_a s_4 \\ K_{31} &= -s_1s_2 \quad ; \quad K_{32} = c_1s_2 \quad ; \quad K_{33} = c_2 \quad ; \quad K_{34} = -c_1s_2P_{wx} - s_1s_2P_{wy} + c_2P_{wz} \\ K_{41} &= 0 \quad ; \quad ; \quad K_{42} = 0 \quad ; \quad K_{43} = 0 \quad ; \quad K_{44} = 1 \end{aligned} \quad (6.13b)$$

where K_{11-44} are lumped parameters.

Equating elements (1,4) and (2,4) from both sides of the Equation 6.13a and using Equations 6.13b, one obtains Equations 6.14a and 6.14b, respectively.

$$c_1 c_2 c_{34} P_{wx} - s_1 s_{34} P_{wx} + s_1 c_2 c_{34} P_{wy} + c_1 s_{34} P_{wy} + s_2 c_{34} P_{wz} - L_a c_4 = 0 \quad (6.14a)$$

$$-c_1 c_2 s_{34} P_{wx} - s_1 c_{34} P_{wx} - s_1 c_2 s_{34} P_{wy} + c_1 c_{34} P_{wy} - s_2 s_{34} P_{wz} + L_a s_4 = L_f \quad (6.14b)$$

First, solve for s_{34} and c_{34} :

$$s_{34} = \frac{(L_a s_4 - L_f)(c_1 c_2 P_{wx} + s_1 c_2 P_{wy} + s_2 P_{wz}) - L_a c_4 (s_1 P_{wx} - c_1 P_{wy})}{(s_1 P_{wx} - c_1 P_{wy})^2 + (c_1 c_2 P_{wx} + s_1 c_2 P_{wy} + s_2 P_{wz})^2} \quad (6.15a)$$

$$c_{34} = \frac{(L_a s_4 - L_f)(s_1 P_{wx} - c_1 P_{wy}) + L_a c_4 (c_1 c_2 P_{wx} + s_1 c_2 P_{wy} + s_2 P_{wz})}{(s_1 P_{wx} - c_1 P_{wy})^2 + (c_1 c_2 P_{wx} + s_1 c_2 P_{wy} + s_2 P_{wz})^2} \quad (6.15b)$$

Then, η_3 is calculated as

$$\eta_{34} = \text{Atan2}(s_{34}, c_{34}) \quad (6.15c)$$

$$\eta_3 = \eta_{34} - \eta_4 \quad (6.15d)$$

Now, elements (1,3) and (3,3) of both sides of Equation 6.13a and Equations 6.13b are equated to determine η_5 as

$$r_{13} c_1 c_2 c_{34} - r_{13} s_1 s_{34} + r_{23} s_1 c_2 c_{34} + r_{23} c_1 s_{34} + r_{33} s_2 c_{34} = s_5 c_6 \quad (6.16a)$$

$$-r_{13} c_1 s_2 - r_{23} s_1 s_2 + r_{33} c_2 = -s_5 s_6 \quad (6.16b)$$

$$K_3 = r_{13} s_1 s_2 + r_{23} s_1 s_2 - r_{33} c_2 \quad (6.16c)$$

$$K_4 = c_{34} (r_{13} c_1 c_2 + r_{23} s_1 c_2 + r_{33} s_2) + s_{34} (r_{33} c_1 - r_{13} s_1) \quad (6.16d)$$

$$s_6 \neq 0 \Rightarrow \eta_5 = \text{Atan2}(K_3, K_4) \quad (6.16e)$$

where K_3 and K_4 are lumped parameters.

Then, both sides of the Equation 6.5 are pre-multiplied by 5_0T as

$${}^5T_7^0T = {}^5T_6^6T = \begin{bmatrix} c_6c_7 & -c_6s_7 & s_6 & 0 \\ -s_7 & -c_7 & 0 & 0 \\ s_6c_7 & -s_6s_7 & -c_6 & 0 \\ 0 & 0 & 0 & 1 \end{bmatrix} \quad (6.17)$$

Equating elements (1,3) and (3,3) from both sides of the Equation 6.17, s_6 and c_6 are obtained. Therefore, η_6 is determined as

$$\eta_6 = \text{Atan2}(s_6, c_6) \quad (6.18)$$

Also, equating elements (2,1) and (2,2) from both sides of the Equation 6.17, one has s_7 and c_7 , and η_7 is obtained as

$$\eta_7 = \text{Atan2}(s_7, c_7) \quad (6.19)$$

The local joint angles of the model for subjects 7 and 8 during the tests were determined using the above relations, the positions of markers on the wrist and shoulder joints, and the subjects' anthropometric data. The linear and angular velocities and accelerations of the links of the model were calculated using outward iteration, in which i varies from 0 to 6.

Velocity propagation from link to link is obtained by [96]

$${}^i\omega_{i+1} = {}^i\omega_i + {}^iR_{i+1} \dot{\eta}_{i+1} {}^{i+1}\hat{Z}_{i+1} \quad (6.20a)$$

$${}^iV_{i+1} = {}^iV_i + {}^i\omega_i \times {}^iP_{i+1} \quad (6.20b)$$

$${}^{i+1}\omega_{i+1} = {}^{i+1}R^i {}^i\omega_i + \dot{\eta}_{i+1} {}^{i+1}\hat{Z}_{i+1} \quad (6.20c)$$

$${}^{i+1}V_{i+1} = {}^{i+1}R({}^iV_i + {}^i\omega_i \times {}^iP_{i+1}) \quad (6.20d)$$

where ${}^iV_{i+1}$ and ${}^i\omega_{i+1}$ are linear and angular velocities of link $i+1$ with respect to frame i , ${}^iP_{i+1}$ is the position of the origin of frame $i+1$ with respect to frame i , and $\dot{\eta}_{i+1}$ is the joint angular velocity of frame $i+1$.

Acceleration propagation is given by

$${}^{i+1}\dot{\omega}_{i+1} = {}^{i+1}R^i \dot{\omega}_i + {}^{i+1}R^i \omega_i \times \dot{\eta}_{i+1} {}^{i+1}\hat{Z}_{i+1} + \ddot{\eta}_{i+1} {}^{i+1}\hat{Z}_{i+1} \quad (6.21a)$$

$${}^{i+1}\dot{V}_{i+1} = {}^{i+1}R^i [{}^i\dot{\omega}_i \times {}^iP_{i+1} + {}^i\omega_i \times ({}^i\omega_i \times {}^iP_{i+1}) + {}^i\dot{V}_i] \quad (6.21b)$$

$${}^i\dot{V}_{C_i} = {}^i\dot{\omega}_i \times {}^iP_{C_i} + {}^i\omega_i \times ({}^i\omega_i \times {}^iP_{C_i}) + {}^i\dot{V}_i \quad (6.21c)$$

Where ${}^i\dot{V}_i$ and ${}^i\dot{V}_{C_i}$ are linear accelerations of origin of frame i and COM of link i with respect to frame i , ${}^i\dot{\omega}_i$ is the angular acceleration of link i with respect to frame i , and $\ddot{\eta}_{i+1}$ is the joint angular acceleration of frame $i+1$. The subscript C_i stands for the frame $\{C_i\}$, which has the same orientation as link frame i , and its origin is located at COM of the link i .

6.2.4 Kinetics of Wheelchair Propulsion

The net forces and moments in the upper limb joints of the users are calculated by using the inverse dynamics method. Figure 6.3 shows a generic link for modeling the limbs. The variables f_i , n_i , F_i , and N_i represents the force exerted on link i by link $i-1$, the moment exerted on link i by link $i-1$, the inertial force, and the moment acting at COM, respectively.

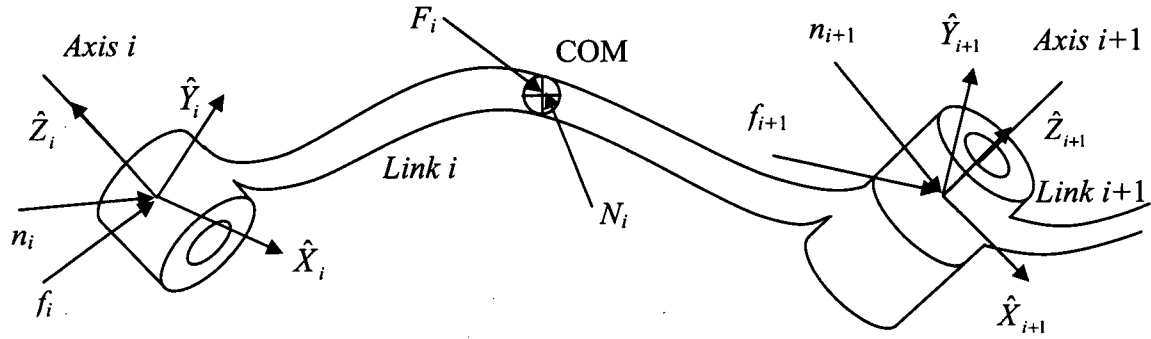


Figure 6.3 Forces, moments and inertial loads on a generic link i .

To calculate the net forces and moments in the upper limb joints, the applied forces and moments on the user's hand during MWP are required. These loads were measured by using the instrumented wheel in the tests. The forces and moments acting at COM of each link were calculated using Newton's and Euler's equations.

$${}^i F_i = m_i {}^i \dot{v}_{C_i} \quad (6.22a)$$

$${}^i N_i = {}^{C_i} I_i {}^i \dot{\omega}_i + {}^i \omega_i \times {}^{C_i} I_i \times {}^i \omega_i \quad (6.22b)$$

where ${}^i F_i$, ${}^i N_i$, ${}^i \omega_i$, and ${}^i \dot{\omega}_i$ are force, moment, angular velocity, and angular acceleration vectors of link i with respect to frame i . The variable m is mass of the link, ${}^i \dot{v}_{C_i}$ is linear acceleration vector of COM, and ${}^{C_i} I_i$ is the moment of inertia of the link i with respect to $\{C_i\}$.

The net forces and moment at joints are computed using inward iteration, in which i varies from 7 to 1:

$${}^i f_i = {}^i R^{i+1} f_{i+1} + {}^i F_i \quad (6.23a)$$

$${}^i n_i = {}^i N_i + {}^{i+1} R^{i+1} n_{i+1} + {}^i P_{C_i} \times {}^i F_i + {}^i P_{i+1} \times {}^{i+1} R^{i+1} f_{i+1} \quad (6.23b)$$

where ${}^i N_i$ and ${}^i n_i$ are moment vectors, ${}^i F_i$ and ${}^i f_i$ are force vectors and ${}^i P_{C_i}$ is the position vector of the COM with respect to the frame i .

6.3 Comparison of Methods I and II

The net loads at the upper limb joints of subjects 7 and 8 were calculated using Methods I and II. The results were compared to determine the utility and reliability of Method II.

The profiles of the applied force and moment on the wrist, elbow and shoulder joints are compared between the two methods in Figures 6.4 and 6.5, Figures 6.6 and 6.7, and Figures 6.8 and 6.9, respectively.

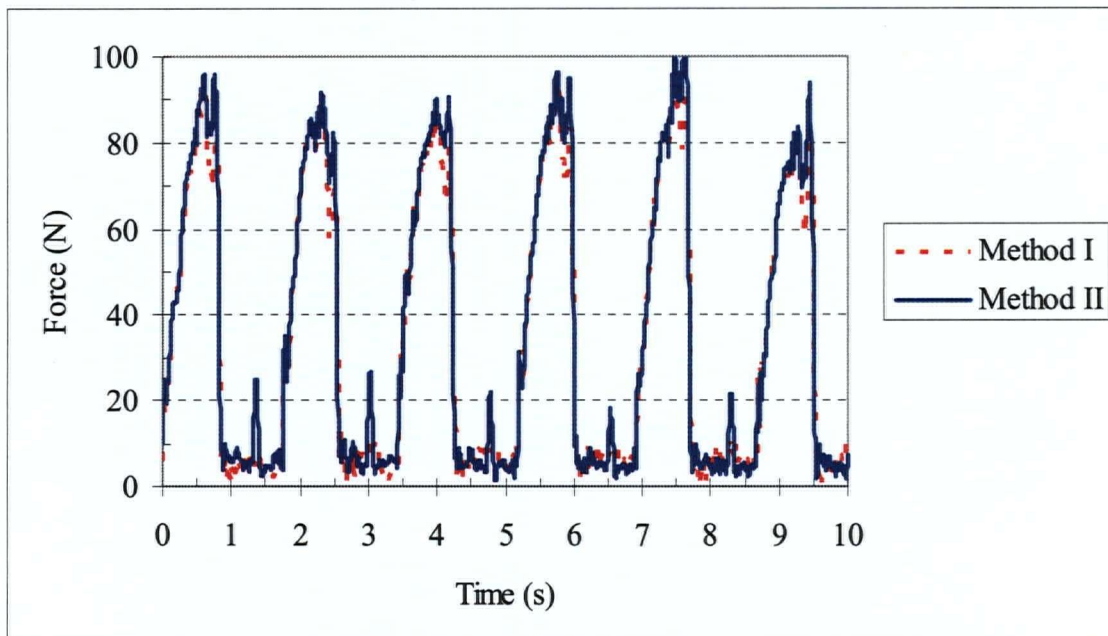


Figure 6.4 Total applied force on the wrist joint.

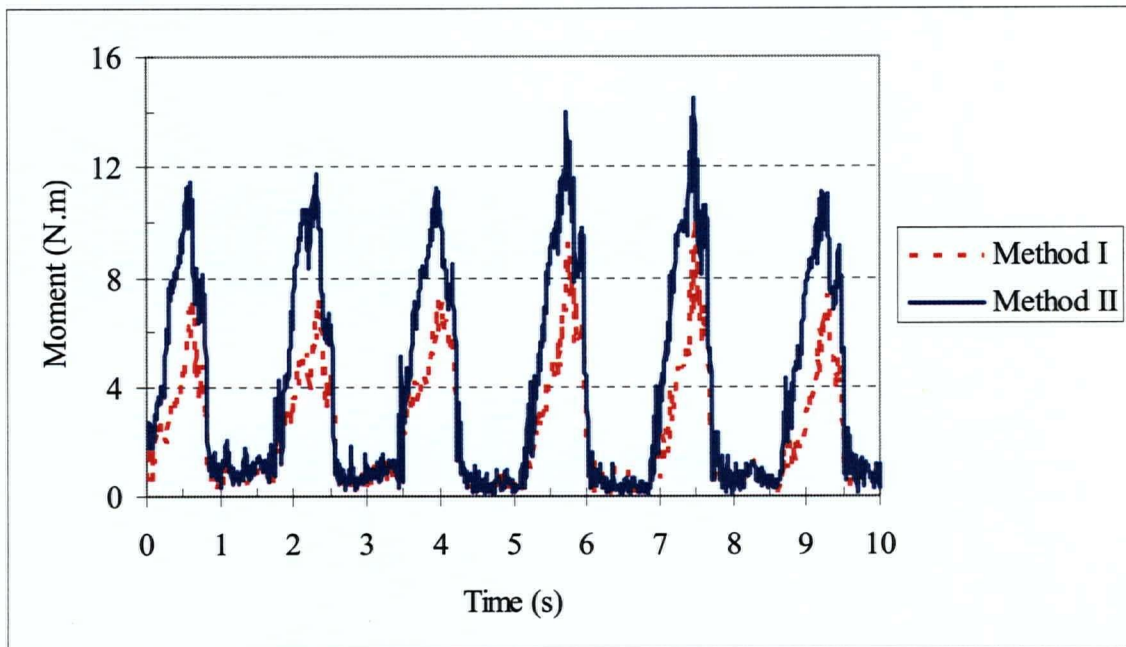


Figure 6.5 Total applied moment on the wrist joint.

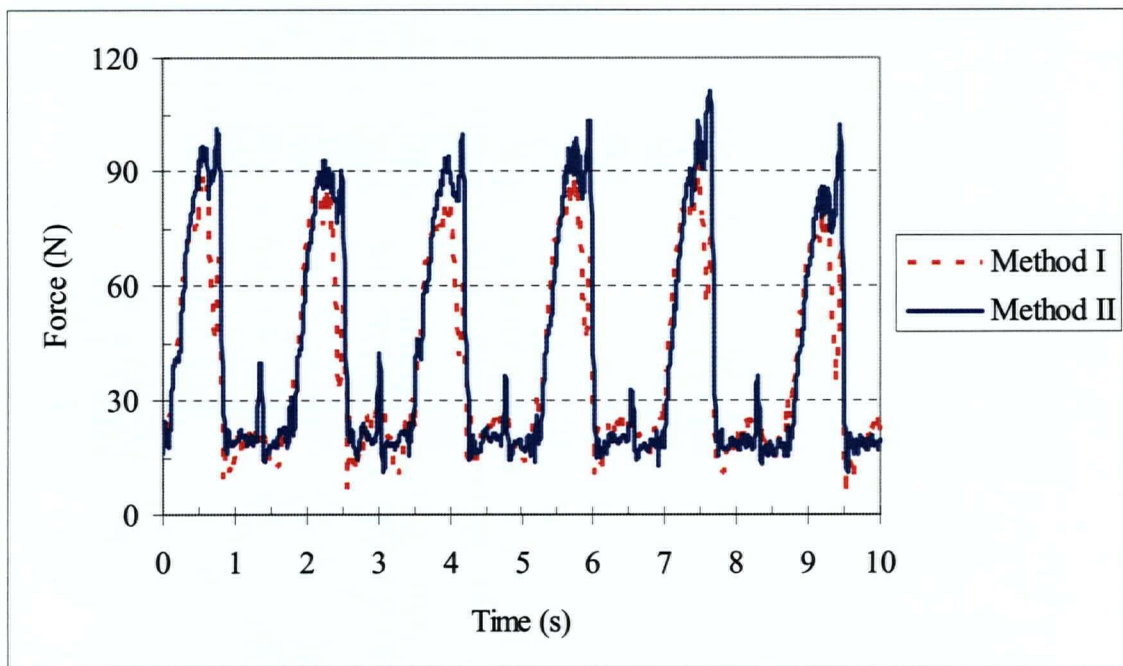


Figure 6.6 Total applied force on the elbow joint.

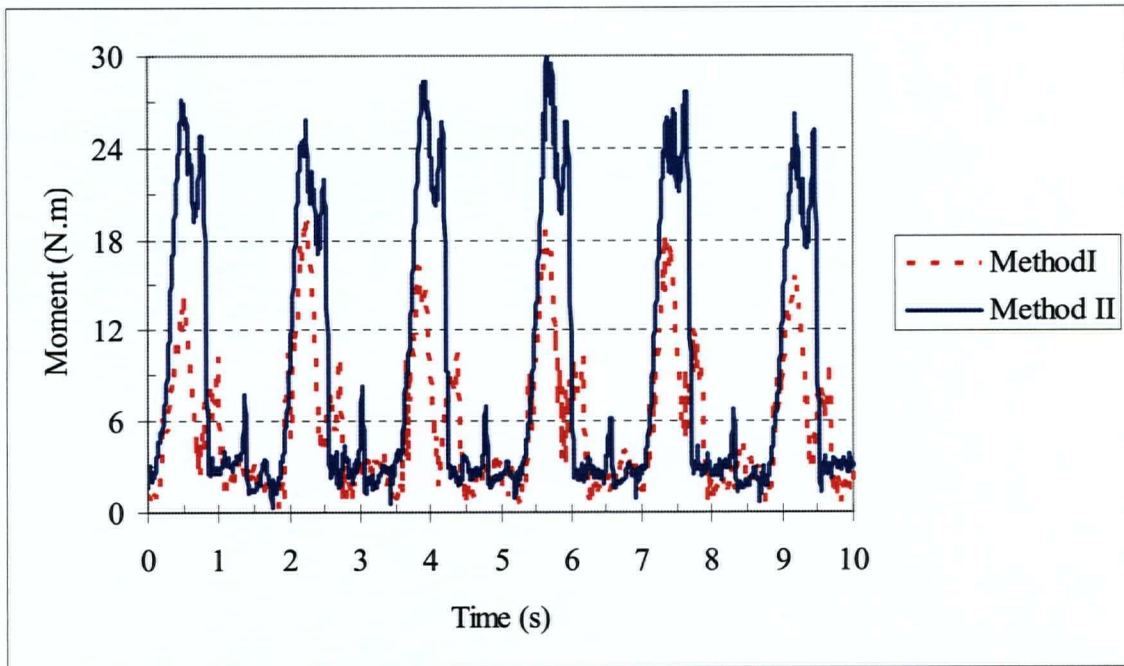


Figure 6.7 Total applied moment on the elbow joint.

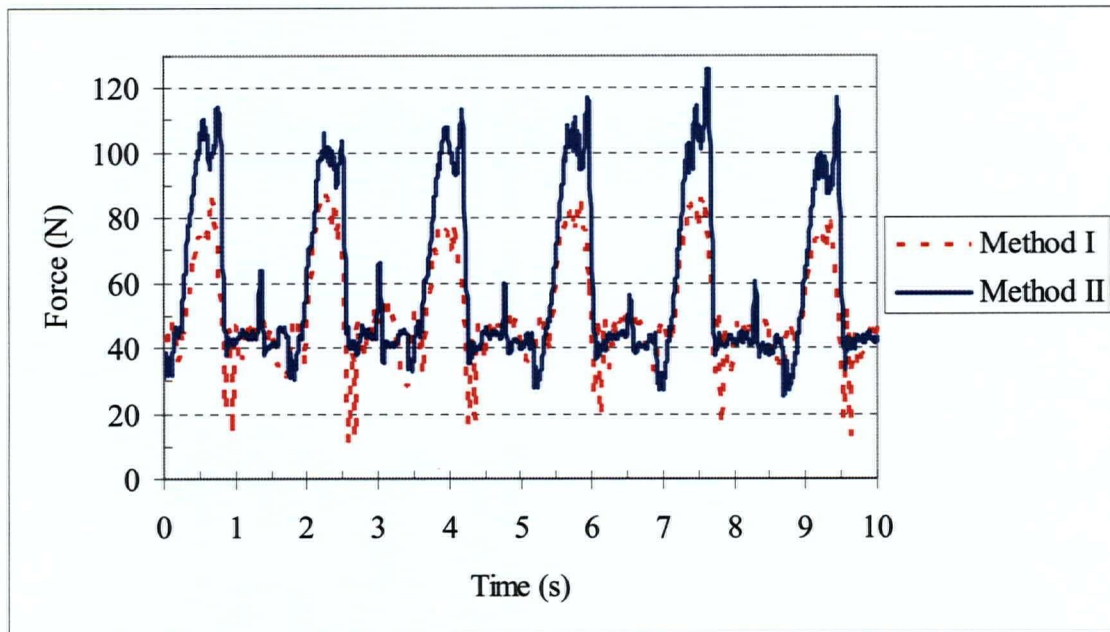


Figure 6.8 Total applied force on the shoulder joint.

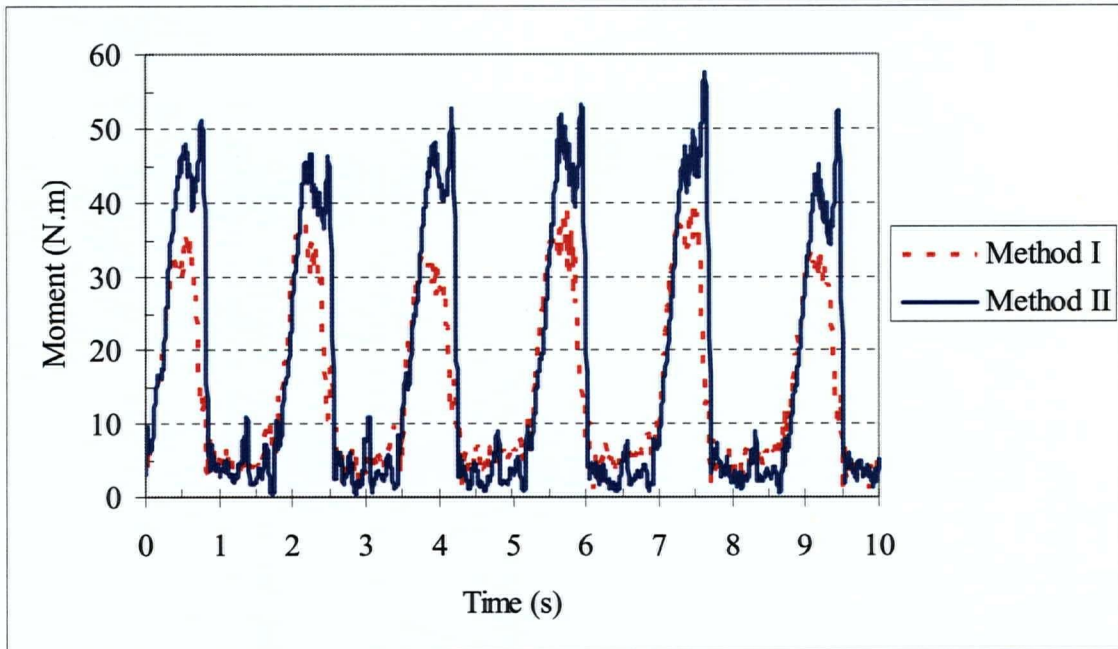


Figure 6.9 Total applied moment on the shoulder joint.

Comparing the profiles in the preceding figures indicates that the values calculated by Method II are over-estimated. The average degree of over-estimation of the loads over 5 consecutive cycles is determined according to Equations 6.24.

$$\text{Joint force over estimation} = \frac{\sum_{j=1}^n \frac{\sum_{i=1}^5 \frac{F_{Iij}}{F_{IIij}}}{5}}{n} \quad (6.24a)$$

$$\text{Joint moment over estimation} = \frac{\sum_{j=1}^n \frac{\sum_{i=1}^5 \frac{M_{Iij}}{M_{IIij}}}{5}}{n} \quad (6.24b)$$

where F_{Iij} and M_{Iij} are maximum joint force and moment of propulsion cycle i for subject j calculated using Method I, F_{IIij} and M_{IIij} are maximum joint force and moment of propulsion cycle i for subject j calculated using Method II, and n is the number of the subjects.

The average rate of over-estimation for joint loads are shown in Table 6.2.

Table 6.2 Average rates of over-estimation for upper limb joint loads.

Upper limbs' joint load	Average rate of over-estimation
Force at wrist	1.056
Force at elbow	1.209
Force at shoulder	1.321
Moment at wrist	1.499
Moment at elbow	1.936
Moment at shoulder	1.416

The calculated maximum loads using Method II were then corrected by multiplying them by the inverse of the over-estimation rate for the joint load. The relative errors for the corrected joint load were determined with respect to the loads obtained from Method I.

Table 6.3 shows the mean and Std. Dev. of the relative error of the maximum calculated load at upper limb joint using Method II. The forces showed lower mean error and Std. Dev. than the moments.

Table 6.3 Mean and Std. Dev. of the relative error (%) for upper limb joint loads.

Upper limbs'	Mean relative error	Std. Dev.
joint load	(%)	(%)
Force at wrist	2.886	1.456
Force at elbow	9.758	3.302
Force at shoulder	7.518	2.788
Moment at wrist	6.848	2.329
Moment at elbow	13.759	6.500
Moment at shoulder	11.870	5.603

6.4 Conclusions

In this chapter, a new method was developed to analyze the dynamics of the upper limb joints and to calculate the forces and moments during MWP. A robotic model was constructed using the inverse dynamic method. The local joint angles of the model were determined by using the inverse kinematic method. Three-dimensional net joint loads were calculated from kinetic, kinematic, and anthropometric data by using an inverse solution and the Newton-Euler method. The advantage of this method, which we refer to as Method II, is that one can perform inverse dynamic analysis using the kinematic data of only two markers on the arm.

The results calculated using Method II were compared with the results of Method I. The results showed an over-estimation for the calculated loads using the new method. The rates of the over-estimation were determined for the loads at the upper limb joints. As one investigates the over-estimated values from the wrist joint towards the shoulder

joint they increase because of accumulation of the kinematics deviations. However, the mean relative error was calculated as between 2.9 and 9.8 % for the maximum joint forces and between 6.9 and 11.9 % for the maximum joint moments, which appears to be acceptable for many studies.

Considering the ease of application of this method, it can be used in studies that are more related to the kinetics of motion of the similar models. One may decrease the relative errors by adjusting and modifying the assumptions for this model with more realistic ones. In any case, the overestimation can be considered as a conservative measure, which provides a further level of protection in any calculation of wheelchair-related parameters for manual wheelchair users.

CHAPTER 7

Conclusions

7.1 Introduction

This chapter summarizes the work performed in this dissertation and overall conclusions emerging from the research conducted are presented. The particular contributions relating to the fabricated instrumented wheel, proposed injury and efficiency indices, optimum seat position, and a new model for the analysis of the dynamics of the upper limb, are outlined. To motivate other interested researchers, possible future research directions and their scopes are proposed.

7.2 Conclusions

We hypothesized that an instrumented wheel fabricated by using a PY6 load sensor would prove to be a reliable and valid instrument for measuring 3D loads at the hub of a wheelchair during MWP, and that changing the seat position of the wheelchair

would change GME and upper limb joint loads of MWUs. Therefore, an instrumented wheel system was developed, fabricated and validated, and a method for determining the optimum wheelchair seat position for MWUs was determined.

To open the discussion about this research, the importance of the problems such as injury and pain associated with MWP for the users was emphasized, and the anatomy of the corresponding joints of the upper limbs was reviewed. The dynamic concepts of the MWP and the conflict concerning the direction of the applied load were explained, and the effects of the seat position on MWP factors were highlighted. The feasibility of using the heart rate instead of oxygen consumption to estimate MEE was investigated. The significance of using an instrumented wheel system developed in-house was emphasized. A literature review of previous work on the above topics was also presented.

7.2.2 Research Questions and Answers

The work carried out in this dissertation can be summarized by answering the following research questions.

- Is the PY6 load transducer a suitable and sufficiently accurate measuring device for determining 3D forces and moments at the handrim of a wheelchair during propulsion?

The PY6 load transducer was used in the fabricated instrumented wheel system. General uncertainty analysis as an analytical method was performed to verify the instrumented wheel. The results were compared with the reported results for the Smart^{wheel}, an instrumented wheel that is frequently referred in the literature. The results indicated that for our fabricated instrumented wheel, the uncertainty values for the

important load components, namely the planar forces and the axial moment, are low. The absolute error for hand-contact position was determined as $\pm 3^\circ$ or ± 1.5 cm along the rim, which is promising for a method that does not use cameras to calculate this angle.

The specifications of the instrumented wheel were determined using an experimental technique performed under different static and dynamic conditions. Both qualitative and quantitative analyses were performed. The tests showed high linearity with r above 0.9, Std. Dev. mostly close to zero, and overall mean coefficient of variation less than 4% for measured loads. These results indicated high repeatability, and a mean error of mostly less than 5% for all loads. The resultant specifications showed high linearity, high repeatability and a low percentage of errors. The overall results ensured the reliability of the system.

- How can the optimum seat position with respect to the wheel axle be determined for each wheelchair user?

To determine the optimum seat position a new method was introduced, and the test protocol and experimental setup were explained. In this method, the optimum seat position was determined by using the values of one of the three new indices proposed for efficiency and injury assessment.

EBI was proposed as a new index for efficiency assessment. This index was considered as a good alternative to estimate the GME of MWP because it uses the heart rate of the user to estimate the variation of MEE. As injury prevention is very important for the MWUs, two indices were proposed to measure possible injuries. The important factors that can affect the MWP are included in these indices. The indices can be used for injury assessment for a specific upper limb joint. One can compare the effects of BMI

and %BF in probable injuries using these indices. The values of the indices were calculated for each of the test subjects at different seat positions. By using these values, the optimum position for each individual was determined.

- Can one propose some generic rules to estimate the optimum seat position for various users?

To answer this question, a set of constant speed experiments was designed and performed at different seat positions for all subjects. The results of the fixed seat height experiments showed that $\overline{\text{EBI}}$ may increase by moving the seat forward ($p < 0.05$). The average value of the injury indices may decrease by moving the seat backward ($p < 0.05$). The statistical analysis estimated the Type I or Alfa error because of the small sample size of the subjects. Previous studies [12,35] confirm the finding for the injury indices. We were not able to find a similar case to compare the results for efficiency evaluation. One should consider the point that MWP is a combination of a human body and a device. There is no report that indicates the most efficient seat position should be necessarily the safest with less possibility of the injury. Therefore, it is not surprising that the optimum positions, which determined by using the efficiency and injury indices were different.

These results indicated that the average values of the injury indices and $\overline{\text{EBI}}$ can vary between 5.6–29.9% and between 5–27.5%, respectively. The higher variations mostly belong to the subjects whose index values changed significantly with respect to different seat positions, which indicates that the indices are indeed sensitive to seat position.

However, to determine the optimum seat position for each individual, the 3D response surfaces were determined for two subjects by using the BQF method. The

results indicated that the positions determined by using the efficiency and injury indices can be different.

The subjects with highest and lowest BMI and %BF at the time of experiments showed the maximum and minimum values, respectively, for injury indices for most of the propulsion phase. Therefore, one may conclude that BMI and %BF have significant effects on the probable injuries due to MWP that confirm the findings of the previous studies [23,70,71]. Also, the subjects with less wheelchair experience showed lower \overline{EBI} .

- Is there a relationship between the velocity and user injury?

To respond to this question, another set of experiments was designed and performed at a fixed seat position and three propulsion velocities. The results obtained by the average of primary relations for the injury indices and performing the repeated-measures ANOVA indicated that higher propulsion velocity will increase the risk of injury for all subjects significantly ($p < 0.001$). As this proved the direct effect of velocity on the injury indices, the equations of the injury indices were further modified to include \overline{V}_i as one of their parameters. This refinement allows each of the injury indices to be a promising stand-alone measure of wheelchair user joint injury.

- Is there a relationship between velocity and the propulsion efficiency of the manual wheelchair user?

The results from repeated-measures ANOVA on a group of experiments at a fixed seat position and three different propulsion velocities indicated that there was no significant relationship between \overline{EBI} and velocity. These results emphasize that each user

has his own efficient propulsion velocity, which is related to the physiological, anatomical and technical characteristics and limitations of his body. Different subjects can have different efficient propulsion velocity that should be determined individually. The results of this study compliment the report of Mukherjee et al. [38].

- How can one estimate the probable injuries to upper limb joints?

To answer this question, a generic model for dynamic analysis of the limbs was introduced to determine the joint loads, which we referred to as Method I. The injury indices for the upper limb joints of two subjects were calculated using the modified equations for the joints. The results showed that both injury indices determine almost the same optimum position for each joint of the user.

The subject with the lowest %BF showed that his response surfaces for \overline{WUJII} and \overline{WUJII}' are different in magnitude and pattern for each joint, whereas the response surfaces were almost the same for the subject who had a higher %BF. It could be concluded that two persons with different %BF may have the same values of \overline{WUJII} but the one with less %BF appears to have lower \overline{WUJII}' . This implies that \overline{WUJII}' may be a more suitable index to estimate probable injury than \overline{WUJII} , as it can evaluate the injury more realistically. The results indicated that the optimum seat position can vary depending on the general injury indices or specific joint used to calculate the injury indices.

- To what extent will a 3D simulation of the upper limb joints be reliable, if only two markers are used for the kinematic tracking and analysis?

Using concept drawn from robotics and inverse dynamics, a new method was developed to calculate the joint loads during MWP, which we call Method II. The inverse solution and Newton-Euler method were used to calculate the local joint angles, and the 3D net joint loads of the model. This method performs inverse dynamics by having the kinematic data of only two markers during the experiments as part of the required data.

Method II over estimates the results, therefore the rates of over-estimations were determined to correct the calculated loads. The mean relative errors for the maximum joint forces and moments were determined to be between 2.9 and 9.8 % and between 6.9 and 11.9 %, respectively. One can shorten the test procedure and the post-processing time by using Method II, which can be used in similar kinetic studies. Although overestimation of the joint loads increases the protection level, the relative errors may decrease by adjusting the assumptions in this method.

7.3 Limitations of the Study

With considerations given to natural limits on time and resources, and practical aspects of achieving results in reasonable time, this study had some limitations as follows:

- Small sample size of the subjects was considered because of the considerable exclusion criteria of this study. Eight subjects were recruited over about a year. More subjects can improve the level of statistical significance.
- In this study, male subjects with Spinal Cord Injury (SCI) and lesion level below T5 were used; therefore the results cannot be generalized for all MWUs.

- The subjects used the test wheelchair not their own because of the fixed instrumentation. The effects of the rolling friction on front wheels due to the changing the center of gravity does not exist in our tests. This can alter the natural performance of the subjects.
- One instrumented wheel was fabricated in this study; therefore we focused on analyzing the dominant hand. Using two instrumented wheel may provided more reliable results analyzing both arms of the user.
- Accurate measurement of the heart rate was challenging. During some of the tests there was no record for part of the test period that made us to perform the tests again.
- The propulsion techniques were not necessarily the same for all of the subjects.
- Seat position had limited range. Wider range may provide more significant relations between the indices and the seat position.
- Except the wheelchair user himself there was not any other control system to keep the speed at the determined value.
- Percentage of body fat was not determined by using the best methods like DEXA.

7.4 Contributions

The contributions of this study are as follows:

- Development and fabrication of a reliable instrumented wheel for MWP analysis, presenting significant specifications. This system is one of the most essential equipment for kinetic analysis of the MWP.

- Introducing theoretical and experimental methods for determining the uncertainties and specifications of an instrumented wheel. Validation and specification of the system are vital to ensure reliable data can be acquired during the tests.
- Development of a kinetic method to reliably determine the hand-contact angular position without the use of expensive cameras. The hand-contact angle can be used to calculate some of the important factors for the analysis of the dynamics of MWP.
- Proposing a new index for efficiency assessment during MWP that is sensitive to wheelchair seat position and velocity variation. An alternative method can help the probable studies that have limitation for measuring oxygen consumption.
- Proposing two new indices for injury assessment during MWP that are sensitive to wheelchair seat position and velocity changes. To our knowledge, this is the first time that all known parameters that affect the injury of the subject during the propulsion are considered for the injury assessment. These indices provided a new vision for MWP injury assessment and/or prevention.
- Introducing a novel method of determining the optimum seat position for MWUs, to reduce injury and/or increase GME. This method can be used for both rehabilitation and sport purposes.
- Establishing a novel method to prescribe the manual wheelchair seat position for a user that may decrease the probable injury in a specific upper limb joint during the propulsion. To our knowledge, this is the first time that such a specific procedure is used to prescribe the optimum seat position for each individual.

- Initiating a method that needs the kinematic data of only two markers on the arm of the user as part of the data required for analyzing the kinetics of the upper limb during MWP by using the inverse solution.

7.5 Future Research Directions

In this study, a novel methodology was developed for prescribing the optimum seat position for the MWU on the basis of the values of the proposed indices. Although, the indices proved to be practical, the injury indices could be modified to include the effect of muscle activities and the range of motion of the joint angles as factors to cover fatigue and ROM effects. Also, one may wish to consider a weight coefficient for the factors in the equation of the injury indices to scale their effects. The analysis of the propulsion frequency versus the applied loads on the handrim during MWP will be very helpful for improving the proposed indices and injury assessment.

The method proposed in this study can be improved if the anthropometric information and the kinetic and kinematic data from both upper limbs of the user during propulsion are obtained and used in the analysis. Providing two instrumented wheels can eliminate probable asymmetries because of differences in the wheelchair's wheels and improve the propulsion of the users. Although there are a number of obstacles to overcome, shortening the test procedure duration and increasing the number of the seat positions for the tests can lead to a more reliable response surfaces.

To improve the results of the generic rules about the optimum seat position, increasing the number of subjects can provide data that is statistically more significant. As an extension of this study, one may consider the muscle forces in the dynamic

analysis to calculate joints contact loads instead of the net joint forces and moments to yield a better estimation of probable injuries. Also, the maximum and minimum of the internal/external rotation angles of the joints during MWP can be determined to analyze their relationship to the seat position.

Potential opportunities for the extension of the application of the proposed indices to other areas do exist. In addition to rehabilitation wheelchairs, one may continue exploring the possible application of the indices for sports wheelchairs to improve the efficiency and productivity of disabled athletes. This method can be used to improve the design of the wheelchairs, as well.

Another possible extension of this research is the application of the proposed methodologies, Method I, and Method II to the kinetic and kinematic analysis of the upper or lower limbs of able-bodied subjects during different activities such as particular motions during sport or work, and also to clinical aspects such as gait analysis.

In this work, we collaborated with different departments at UBC and benefited from accessing their research laboratory equipment for data collection. Similar collaborations with other research teams can be considered in the future, which can lead to multi-disciplinary research projects in different aspects of manual wheelchair use such as rehabilitation or sport. A team composed of an orthopedist or an occupational therapist and a biomechanical engineer could be a good combination for the studies that deals with both clinical and engineering issues.

References

1. Shields, M., 2004, "Use of Wheelchair and other mobility support devices," Health Reports, **15**(3), pp. 37–41.
2. Bayley, J.C., Cochran, T.P., and Sledge, C.B., 1987, "The Weight Bearing Shoulder: the Impingement Syndrome in Paraplegics," J. Bone and Joint Surgery (AM), **69**(5), pp. 676–678.
3. United States Census Bureau, June 16, 2003 (1997 data) "American With Disabilities: Household Economic Studies," HearingLoss.org, http://www.hearingloss.org/html/item_coalition_tricare_comment.HTM#_end3, date of using the website: June 23, 2005.
4. Boninger, M.L., Cooper, R.A., Shimada, S.D., and Rudy, T.E., 1998, "Shoulder and Elbow Motion during Two Speeds of Wheelchair Propulsion: a Description Using a Local Coordinate System," Spinal cord, **36**, pp. 418–426.
5. Hoover, A.E., Cooper, R. A., Ding, D., Dvorznak, M., Cooper, R. Fitzgerald, S.G., and Boninger, M.L., 2003, "Comparing Driving Habits of Wheelchair Users: Manual vs. Power," RESNA 26th International Conference on Technology & Disability, Atlanta, GA, pp. 19–23.
6. Yassi, A., 1997, "Repetitive strain injuries," The Lancet, **349**(9056), pp. 943–947.
7. Boninger, M.L., Souza, A.L., Cooper, R.A., Fitzgerald, S.G., Koontz, A.M., and Fay, B.T., 2002, "Propulsion Patterns and Pushrim Biomechanics in Manual Wheelchair Propulsion," Arch. Phys. Med. Rehabil., **83**, pp. 718–723.

8. Veeger, H.E.J., vander Woude, L.H.V., and Rozendal, R.H., 1992, "Effect of Handrim Velocity on Mechanical Efficiency in Wheelchair Propulsion," *Med. Sci. Sports Exerc.*, **24**(1), pp. 100–107.
9. de Groot, S., Veeger, H.E.J., Hollander, A.P., and van der Woude, L.H.V., 2002, "Consequence of Feedback-Based Learning of an Effective Handrim Wheelchair Force Production on Mechanical Efficiency," *Clin. Biomech.*, **17**, pp. 219–226.
10. Guo, L., Su, F., Wu, H., and An, K., 2003, "Mechanical Energy and Power Flow of the Upper Extremity in Manual Wheelchair Propulsion," *Clin. Biomech.*, **18**, pp. 106–114.
11. Kotajarvi, B.R.K., Sabick, M.B., An, K., Zhao, K., Kaufman, K.R., Basford, J.R., 2004, "The effect of seat position on wheelchair propulsion biomechanics," *J. Rehabil. Res. & Dev.*, **41**(3B), pp. 403-414.
12. Cooper, R.A., 1995, "Rehabilitation Engineering Applied to Mobility and Manipulation," Institute of Physics Pub., Bristol, Philadelphia, Printed in USA.
13. Richter, W.M., 2001, "The Effect of Seat Position on Normal Wheelchair Propulsion biomechanics: a Quasi-Static Model –Based Approach," *Med. Eng. & Phys.*, **23**, pp. 707–712.
14. Medical Multimedia Group, LLC, < <http://www.medicalmultimedigroup.com> >, date of using the website: June 6, 2007.
15. Faller, A., Schuenke, M., Schuenke, G., 2004, "The Human Body- An Introduction to Structure and Function," Thieme, Stuttgart, Germany, pp. 157–160.
16. Faiz, O., Moffat, D., 2006, "Anatomy at a Glance," Blackwell, Printed in India.

17. Su, F.C., Chang C.C., Wu, H.W., An, K.N., 1999, "The effect of seat position on biomechanics of the upper extremity in the wheelchair propulsion" in: van der Woude, L., Hopman, M.T.E., van Kemenade (Eds.), 1999, "Biomedical Aspects of Manual Wheelchair Propulsion," IOS Press, Amsterdam, pp.122–125.
18. Boninger, M.L., Dicianno, B.E., Cooper, R.A., Towers, J.D., 2003, "Shoulder Magnetic Resonance Imaging Abnormalities, Wheelchair Propulsion, and Gender," *Arch. Phys. Med. Rehabil.*, **84**, pp. 1615–1620.
19. van der Woude, L.H.V., Veeger, D.J., Rozendal, R.H., 1989, "Seat height in handrim wheelchair propulsion," *J. Rehabil. Res. & Dev.*, **26**(4), pp. 31–50.
20. Veeger H.E., van der Woude L.H., Rozendal R.H., 1991, "Within-cycle characteristics of the wheelchair push in sprinting on a wheelchair ergometer," *Med. Sci. Sports Exerc.*, **23**, pp. 264–271.
21. Veeger, H.E., van der Woude L.H., Rozendal R.H., 1992, "A computerized wheelchair ergometer. Results of a comparison study," *Scand. J. Rehabil. Med.*, **24**, pp. 17–23.
22. Dallmeijer, A.J., Kappe, Y.J., Veeger, D.H., Janssen, T.W., van der Woude, L.H., 1994, "Anaerobic power output and propulsion technique in spinal cord injured subjects during wheelchair ergometry," *J. Rehabil. Res. Dev.*, **31**, pp. 120–28.
23. Boninger, M.L., Cooper, R.A., Baldwin, M.A., Shimada, S.D., Koontz, A., 1999, "Wheelchair Propulsion Kinetics: Body Weight and Median Nerve Function," *Arch. Phys. Med. Rehabil.*, **80**, pp. 910–915.
24. Gellman, H., Sie, I. and Waters R.L., 1988, "Late complications of the weight-bearing upper extremity in the paraplegic patient," *Clin. Ortho.*, **233**, pp. 132–135.

25. Pentland, W.E. and Twomey, L.T., 1991, "The weight-bearing upper extremity in women with long term paraplegia," *Paraplegia*, **29**, pp. 521-530.
26. Sie, L.H., Waters, R.L., Adkins, R.H. and Gellman, H., 1992, "Upper extremity pain in the postrehabilitation spinal cord injured patient," *Arch. Phys. Med. Rehabil.*, **73**, pp. 44-48.
27. Wylie, E.J., Chakern, T.M., 1988, "Degenerative joint abnormalities in patients with paraplegia of duration greater than 20 years," *Paraplegia*, **26**, pp. 101-106.
28. Aljure, J. Eltorai, I., Bradley, W.E., Lin, J.E. and Johnson B., 1985, "Carpal tunnel syndrome in paraplegic patients," *Paraplegia*, **23**, pp. 182-186.
29. Burnham, R.S. and Steadward, R.D., 1994, "Upper extremity peripheral nerve entrapments among wheelchair athletes: Prevalence, location and risk factors," *Arch. Phys. Med. Rehabil.*, **75**, pp. 519-524.
30. Davidoff, G., Werner, R. and Waring, W., 1991, "Compressive mononeuropathies of the upper extremity in chronic paraplegia," *Paraplegia*, **29**, pp. 17-24.
31. Gellman, H., Chandler, D.R., Petrusek, J., Sie, I., Atkins, R. and Walters, R., 1988, "Carpal Tunnel syndrome in paraplegic patients," *J. Bone & joint Surg.*, **70**, pp. 517-519.
32. Matias, A.C., Salvendy, G. and Kuczek, T., 1998, "Predictive models of carpal tunnel syndrome causation among VDT operators," *Ergonomics*, **41**(2), pp. 213-226.
33. Tun, C.G. and Upton, J., 1988, "The paraplegic hand: Electrodiagnostic studies and clinical findings," *J. Hand Surg.*, **13**, pp. 716-719.

34. Glaser, R.M., Sawka, M.N., Brune, M.F., and Wilde, S.W., "Physiological responses to maximal effort wheelchair and arm crank ergometry," *Journal of Applied Physiology*, 1980; **48**(6), pp. 1060–1064.
35. Boninger, M.L., Baldwin, M.A., Cooper, R.A., Koontz, A., 2000, "Manual Wheelchair Pushrim Biomechanics and Axle Position," *Arch. Phys. Med. Rehabil.*, **81**, pp. 608–613.
36. Wei, S., Huang, S., Chuan-Jiang J., and Chiu, J., 2003 "Wrist Kinematic Characterization of Wheelchair Propulsion in Various Seating position: Implication to Wrist Pain," *Clinical Biomechanics*, **18**, pp. 46–52.
37. Cooper, R. A., 1990, "A Force/Energy Optimization Model for Wheelchair Athletics," *IEEE Transaction on System, Man, and Cybernetics*, **20** (2), 444–449.
38. Mukherjee, G., Bhowik, P., Samanta, A., 2002, "Energy cost of manual wheelchair propulsion at different speeds," *Int. J. Rehabil. Res.*, **25** (1), 71–75.
39. Hood, V.L., Granat, M.H., Maxwell, D.J., Hasler, J.P., 2002, "A new method of using heart rate to represent energy expenditure: The total heart beat index," *Arch. Phts. Med. Rehabil.*, **83**, pp. 1266–1273.
40. Bot, S.D.M., Hollander, A.P., 2000, "The relationship between heart rate and oxygen uptake during non-steady state exercise," *Ergonomics*, **43**(10), pp. 1578–1592.
41. Natali, A., Santoro, D., Brandi, L.S., Faraggiana, D., Ciociaro, D., Pecori, N., Buzzigoli, G., Ferrannini, E., 1993, "Effect of acute hypercarnitinemia during increased fatty substrate oxidation in man," *Metabolism*, **42**, pp. 594–600.
42. Ijzerman, M.J., Gert baardman, P.T., van't Hof, M.A., Boom, H.B.K., Hermens, H.J., Veltink., P.H., 1999, "Validity and reproducibility of crutch force and heart rate

- measurements to assess energy expenditure of paraplegic gait," *Arch. Phys. Med. Rehabil.*, **80**, pp. 1017–1022.
43. Schmid, A., Huonker, M., Barturen, J., Stahl, F., Schmidt-trucksass, A., Konig, D., Grathwohl, D., Lehmann, M., and Keul, J., 1998, "Catecholamines, heart rate, and oxygen uptake during exercise in persons with spinal cord injury," *J. Appl. Physiol.*, **85**(2), pp. 635-641.
44. Sawatzky, B.J., Miller, W.C., and Denison, I., 2005, "Measuring energy expenditure using heart rate to assess the effect of wheelchair tyre pressure," *Clin. Rehabil.*, **19**, pp. 182–187.
45. Tolfrey, K., Tolfrey, V.L.G., and Campbell, I.G., 2001, "Oxygen uptake-heart rate relationship in elite wheelchair racers," *European J. Applied Physiology*, **86**, pp. 174–178.
46. Vrongistinos, K., 2001, "Dynamic Analysis and Biomechanical Modeling of Wheelchair Propulsion", Dissertation, Auburn.
47. Asato, K.T., Cooper, R.A., Robertson, and Ster, J.F., 1993, "SMART^{Wheel}: Development and Testing of a System for Measuring Manual Wheelchair Propulsion Dynamics," *IEEE Transaction on Biomedical Engineering*, **40**(12), pp. 1320–1324.
48. Wu, H.W., Berglund, L.J., Su, F.C., Yu, B., Westreich, A., Kim, K.J., and An, K.N., 1998, "An Instrumented Wheel for Kinetic Analysis of Wheelchair Propulsion," *Journal of Biomechanical Engineering*, **120**, pp. 534–535.
49. Cooper, R.A., Boninger, M.L., VanSickle, D.P., and DiGiovine, C.P., "Instrumentation for Measuring Wheelchair Propulsion Biomechanics," in: van der

- Woude, L., Hopman, M.T.E., van Kemenade (Eds.), 1999, "Biomedical Aspects of Manual Wheelchair Propulsion", IOS Press, Amsterdam, pp. 104–114.
50. Wang Y.T., Beale D., Moeinzadeh, M., 1996, "An electronic device to measure drive and recovery phases during wheelchair propulsion: a technical note," *J. Rehabil. Res. Dev.*, **33**(3), pp. 305–315.
51. Rodgers, M.M., Gayle, G.W., Figoni, S.F., Kobayashi, M., Junghsen, L. and Glaser, R.M., 1994, "Biomechanics of wheelchair propulsion during fatigue," *Arch. Phys. Med. Rehabil.*, **75**, pp. 85–93.
52. Cooper, R.A., Boninger, M.L., VanSicle, D.P., Robertson, R.N. and Shimada, S.D., 1997 "Uncertainty Analysis for Wheelchair Propulsion Dynamics," *IEEE Trans. Rehabil. Eng.*, **5**(2), pp. 130–139.
53. Mallakzadeh, M., Sassani, F., 2007 "Instrumented Wheel for Wheelchair Propulsion Analysis," Chapter 4 of the book: *Mechatronic System–Devices, Design, Control, Operation and Monitoring*, CRC Press, Taylor & Francis, Boca Raton, FL (in press).
54. Mallakzadeh, M., Sassani, F., 2007, "General Uncertainty Analysis for Manual Wheelchair Propulsion Dynamic and Development of an Instrumented Wheel," *ASME Journal of Medical Devices*, **1**(2), pp. 140–150.
55. Mallakzadeh, M., Sassani, F., 2007, "An Experimental Technique to Verify an Instrumented Wheelchair," *Journal of Experimental Techniques*, **31**(1), pp. 25–33.
56. Mallakzadeh, M., Sassani, F., Sawatzky, B.J., 2007 "Effect of Linear Wheelchair Velocity on a New Manual Wheelchair User Joint Injury Index," *American Society of Biomechanics (ASB) Annual Conference (International)*, Stanford University, USA, August 22–25, 2007, Number of pages:2.

57. Sharon, S., 2000, "The impact of seating and positioning on the development of repetitive strain injuries of the upper extremity in wheelchair athletes," *Work*, **15**, pp. 67-76.
58. Veeger, H.E.J., Lute, E.M.C., Roeleveld, K., and van der Woude, L.H.V., 1992, "Differences in performance between trained and untrained subjects during a 30-s sprint test in a wheelchair ergometer," *Eur. J. Appl. Physiol.*, **64**, pp.158-164.
59. van Kemenade, C.H., te Kulve, K.L., Dallmeijer, A.J., van der Woude, L.H.V., and Veeger, H.E.J., 1999, "Changes in wheelchair propulsion technique during rehabilitation," in: van der Woude, L., Hopman, M.T.E., van Kemenade (Eds.), 1999, "Biomedical Aspects of Manual Wheelchair Propulsion", IOS Press, Amsterdam, pp. 227-230.
60. Vansickle, D., Cooper, R.A., Boninger, M.L., Robertson, R.N., and Shimada, S.D., 1998, "A Unified Method for Calculating the Center of Pressure During Wheelchair Propulsion," *Annals of Biomedical Eng.*, **26**, pp. 328-336.
61. Coleman, H.W. and Steele, W.G., 1999, "Experimentation and Uncertainty Analysis for Engineers," Jhon Wiley & Sons press, New York, pp. 47-79.
62. Kline, S.J., and McClintock, F.A., 1953, "Describing Uncertainties in Single-Sample Experiments," *Mech. Eng.*, **75**, pp. 3-8.
63. Norusis, M.J., 2002, "SPSS[®] 11.0 Guide to Data Analysis," Prentice-Hall, New Jersey, 2002.
64. van der Woude, L.H.V., de Groot, G., Hollander, A.P., van Ingen, S., and Rozendal, R.H., 1986, "Wheelchair ergonomics and physiological testing of prototypes," *Ergonomics*, **29**(12), pp. 1561-1573.

65. van der Woude, L.H., Veeger, H.E., Rozendal, R.H., van Ingen Schenau, G.J., Rooth, F., and van Nierop, P., 1988, "Wheelchair racing: effects of rim diameter and speed on physiology and technique," *Clinical Biomechanics*, **18**, pp. 106–114.
66. Cooper, R.A., Horvath, S.M., Bedi, J.F., Drechsler-Parks, D.M., and Williams, R.E., 1992, "Maximal exercise response of paraplegic wheelchair road racers," *Paraplegia*, **30**, pp. 573-581.
67. Curtis, K.A., Roach, K.E., Brooks, E., Amar, T., Benbow, C.S., Genecco, T.D., and Gualano, J., 1995, "Development of the Wheelchair User's shoulder Pain Index (WUSPI)," *Paraplegia*, **33**, pp. 290–293.
68. Roach, K.E., Budiman-Mak, E., Songsiridej, N., and Lertratanakul, Y., 1991, "Development of a shoulder pain and disability index," *Arthritis Care Res.*, **4**, pp. 143–149.
69. Boninger, M.L., Dicianno, B.E., Cooper, R.A., Towers, J.D., Koontz, A.M., and Souza, A.L., 2003, "Shoulder Magnetic Resonance Imaging Abnormalities, Wheelchair Propulsion, and Gender," *Arch. Phys. Med. Rehabil.*, **84**, pp. 1615–1620.
70. van Drongelen, S., de Groot, S., Veeger, H.E.J., Angenot, E.L.D., Dallmeijer, A.J., Post, M.W.M., and van der Woude, L.H.V., 2005, "Upper extremity musculoskeletal pain during and after rehabilitation in wheelchair-using persons with a spinal cord injury," *Spinal Cord*, pp. 1–8.
71. Dicianno, B.E., Boninger, M.L., Cooper, R., Towers, J., 1999, "Relationship between Body Index of Manual Wheelchair Users and Shoulder Pain Injury," *Am. J. Phys. Med. Rehabil.*, **78**(2), pp. 177-178.

72. Desport, J.C., Preux, P.M., Guinvarch, S., Rousset, P., Salle, J.Y., Daviet, J.C., Dudognon, P., Munoz, M., and Ritz, P., 2000, "Total body water and percentage fat mass measurements using bioelectrical impedance analysis and anthropometry in spinal cord-injured patients," *Clinical Nutrition*, **19**(3), pp. 185–190.
73. Maggioni, M., Bertoli, S., Margonato, V., Merati, G., Veicsteinas, A., and Testolin, G., 2003, "Body composition assessment in spinal cord injury subjects," *Acta Diabetol*, **40**, pp. 183–186.
74. Hopman, M.T.E., Dallmeijer, A.J., Snoek, G., and van der Woude, L.H.V., 1996, "The effect of training on cardiovascular responses to arm exercise in individuals with tetraplegia," *Eur. J. Appl. Physiol.*, **74**, pp. 172–179.
75. Durnin, J. and Womersley, J., 1974, "Body fat assessed from total body density and its estimation from skinfold thickness: measurements on 481 men and women aged from 16 to 72 years," *Br. J. Nutr.*, **32**, pp. 77–97.
76. Jebb, S.A., Cole, T.J., Doman, D., Murgatroyd, P.R., and Prentice, A.M., 2000, "Evaluation of the novel Tanita Body-fat analyzer to measure body composition by comparison with a four-compartment model," *Br. J. Nutr.* **83**(2), pp. 115–122.
77. Conway, J.M., Norris, K.H., and Bodwell, C.E., 1984, "A new approach for the estimation of body composition: infrared interactance," *Am. J. Clin. Nutr.*, **40**, pp. 1123–1130.
78. Thomas, E.L., Saeed, N., Hajnal, J.V., Brynes, A., Goldstone, A.P., Frost, G., and Bell, J.D., 1998, "Magnetic resonance imaging of total body fat," *J. Appl. Physiol.*, **85**(5), pp. 1778–1785.

79. Tokunaga, K., Matsuzawa, Y., Ishikawa, K., and Tarui, S., 1983, "A novel technique for the determination of body fat by computed tomography," *Int. J. Obes.*, **7**(5), pp. 437-445.
80. Ellis, K.J., 1996, "Measuring body fatness in children and young adults: comparison of bioelectric impedance analysis, total body electrical conductivity, and dual-energy X-ray absorptiometry," *Int. J. Obes.*, **20**(9), pp. 866-873.
81. Vanlandewijck, Y., Theisen, D., and Daly D., 2001, "Wheelchair Propulsion biomechanics-Implication for Wheelchair Sports," *Sports Med.*, **31**(5), pp. 339-367.
82. Stankovits, S., 2000, "The impact of seating and positioning on the development of repetitive strain injuries of the upper extremity in wheelchair athletes," *Work*, **15**, pp. 67-76.
83. Samuelsson, K., Larsson, H., Thyberg, M., and Gerdle, B., 2001, "Wheelchair seating intervention. Results form a Client-centred approach," *Disabil. & Rehabil.*, **23**(15), pp. 677-682.
84. Aissaoui, R., Arabi, H., Lacoste, M., Zalzal, V., Dansereau, J., 2002, "Biomechanics of Manual Wheelchair Propulsion in Elderly - System Tilt and Back recline Angles," *Am. J. Phys. Med. Rehabil.*, **81**, pp. 94-100.
85. Masse, L.C., Lamontage, M., and O'Riain, M.D., 1992, "Biomechanical analysis of wheelchair propulsion for various seating positions," *J. Rehabil. Res. Dev.*, **29**(3), pp. 12-28.
86. Hughes, W.H., Weimar, P.N., and Brubaker, C.E., 1992, "Biomechanics of wheelchair propulsion as a function of seat position and user-to-chair interface," *Arch. Phys. Med. Rehabil.*, **73**, pp. 263-269.

87. Karlsson, A.K., Friberg, P., Lonroth, P., Sullivan, L., and Elam, M., 1998, "Regional sympathetic function in high spinal cord injury during mental stress and autonomic dysreflexia," *Brain*, **121**(9), pp. 1711–1719.
88. Arnold, J.M.O., Feng, Q., P., Delaney, G.A., and Teasell, R.W., 1995, "Autonomic dysreflexia in tetraplegic patients: Evidence for a adrenoceptor hyper-responsiveness," *Clinical Autonomic Research*, **5**(5), pp. 267–270.
89. Reeves, S.L., Varakamin, C., and Henry, C.J., 1996, "The relationship between arm-span measurement and height with special reference to gender and ethnicity," *Eur. Clin. Nutr.*, **50**(6), pp. 398–400.
90. Basse, E.J., 1986, "Demi-span as a measure of skeletal size," *Annals of Human Biology*, **13**(5), pp. 499–502.
91. Johnson, N.L. and Leone, F.C., 1977, "Statistics and Experimental Design- Volumes I and II," Jhon Wiley & Sons, Printed in the USA.
92. Clarke, G.M., 1980, "Statistics and experimental design," E. Arnold, London.
93. Zhang, J. and Foschi, R.O., 2004, "Performance-based design and seismic reliability analysis using designed experiments and neural networks," *Probabilistic Engineering Mechanics*, **19**, pp. 259-267.
94. Fausett, L., 1994, "Fundamentals of Neural Networks Architectures, Algorithms, and Applications," Prentice-Hall, Englewood Cliffs, NJ, USA.
95. Mead, R., and Pike, D.J., 1975, "A review of response surface methodology from a biometric viewpoint," *Biometric*, **31**, pp. 803–851.
96. Craig, J.J., 1986, "Introduction to Robotics Mechanics & Control," Addison-Wesley, Printed in USA.

97. Wittenburg, J., 1977, "Dynamics of Systems of Rigid Bodies," B.G. Teubner Stuttgart, Printed in Germany.
98. MacGill, D.J., and King, W. W., 1989, "Engineering Mechanics: An introduction to Dynamics," PWS-KENT Publishing Company, Printed in USA.
99. McKerrrow, P., 1991, "Introduction to Robotics," Addison-Wesley Publishing Company, Printed in Singapore.
100. Wolovich, W.A., 1987, "Robotics: Basic Analysis and Design," Holt, Rinehart and Winston Publishing Company, Printed in USA.

APPENDIX

ETHICS CERTIFICATE OF APPROVAL